

## ABSTRACT

Title of dissertation:       NUMERICAL SIMULATIONS  
                                  OF GRANULAR PHYSICS  
                                  IN THE SOLAR SYSTEM

Ronald-Louis G. Ballouz, Doctor of Philosophy, 2016

Dissertation directed by:  Professor Derek C. Richardson  
                                  Department of Astronomy

Granular physics is a sub-discipline of physics that attempts to combine principles that have been developed for both solid-state physics and engineering (such as soil mechanics) with fluid dynamics in order to formulate a coherent theory for the description of granular materials, which are found in both terrestrial (e.g., earthquakes, landslides, and pharmaceuticals) and extra-terrestrial settings (e.g., asteroids surfaces, asteroid interiors, and planetary ring systems). In the case of our solar system, the growth of this sub-discipline has been key in helping to interpret the formation, structure, and evolution of both asteroids and planetary rings. It is difficult to develop a deterministic theory for granular materials due to the fact that granular systems are composed of a large number of elements that interact through a non-linear combination of various forces (mechanical, gravitational, and electrostatic, for example) leading to a high degree of stochasticity. Hence, we study these environments using an  $N$ -body code, `pkdgrav`, that is able to simulate the gravitational, collisional, and cohesive interactions of grains. Using `pkdgrav`, I have studied

the size segregation on asteroid surfaces due to seismic shaking (the Brazil-nut effect), the interaction of the OSIRIS-REx asteroid sample-return mission sampling head, TAGSAM, with the surface of the asteroid Bennu, the collisional disruptions of rubble-pile asteroids, and the formation of structure in Saturn's rings. In all of these scenarios, I have found that the evolution of a granular system depends sensitively on the intrinsic properties of the individual grains (size, shape, and surface roughness). For example, through our simulations, we have been able to determine relationships between regolith properties and the amount of surface penetration a spacecraft achieves upon landing. Furthermore, we have demonstrated that this relationship also depends on the strength of the local gravity. By comparing our numerical results to laboratory experiments and observations by spacecraft we can begin to understand which microscopic properties (i.e., grain properties) control the macroscopic properties of the system. For example, we can compare the mechanical response of a spacecraft to landing or Cassini observations of Saturn's ring to understand how the penetration depth of a spacecraft or the complex optical depth structure of a ring system depends on the size and surface properties of the grains in those systems.

NUMERICAL SIMULATIONS OF  
GRANULAR PHYSICS IN THE SOLAR SYSTEM

by

Ronald Ballouz

Dissertation submitted to the Faculty of the Graduate School of the  
University of Maryland, College Park in partial fulfillment  
of the requirements for the degree of  
Doctor of Philosophy  
2016

Advisory Committee:  
Professor Derek Richardson, Chair/Advisor  
Professor Doug Hamilton  
Professor Jessica Sunshine  
Dr. Thomas Statler  
Professor Wolfgang Losert  
Dr. Olivier Barnouin

© Copyright by  
Ronald Ballouz  
2016

To my wife Kellie, my parents Eppie & Georges, my brothers Samir, Tony, and  
David, and to Maddie & Mickey.

## Acknowledgments

I owe so much gratitude to my advisor, Derek Richardson, for helping me throughout the last 5 years that we have been working together. I came into the Department of Astronomy at the University of Maryland thinking that I would pursue a career in galactic astronomy. When I came for a prospectives visit to the University of Maryland, one of the first people I talked to was Derek, and his kindness and intelligence left an impression on me. After he gave the first ever colloquium I attended at the department, I knew that I was going to switch to planetary sciences. Derek has been an engaging and supportive advisor. Above all else, I'd like to thank him for his patience.

I would also like to thank Patrick Michel for his hospitality during my months in Nice, and whose valuable insights into the field have shaped much of my thinking. I also owe him and Derek so much thanks for setting an excellent example, and developing a wonderful team of seasoned and burgeoning scientists who somehow all got interested in the mechanics of tiny grains on far-away worlds. Much of this thesis has come about from discussions with team members that I've had the luck and pleasure to coincide with: Kevin Walsh, Steve Schwartz, Yang Yu, Clara Maurel, and Yun Zhang.

I am grateful for my fellow graduate students, who have helped me survive and appreciate graduate school. Thank you Johnny, Vicki, Krista, Gabriele, Mahmuda, and Maggie, for sticking around, sharing a laugh, and encouraging me when I felt hopeless.

I also have to thank the members of my thesis committee who have stuck with me since the very beginning of my PhD work. Thank you Jess for reminding me to keep the science in focus. Thank you Doug for showing me how fun planetary dynamics can be. Thank you Tom for teaching me the importance of being cognizant of the scientific world outside one's own little bubble.

Finally, I'd like to thank my family. My parents for trusting me to make my own choices. My brothers for their encouragement. My wife for her constant love and patience, and our dogs for their unbridled enthusiasm.

# Table of Contents

List of Tables	viii
List of Figures	ix
List of Abbreviations	xi
1 Introduction	1
1.1 Evidence of Regolith and its Mobility on Asteroid Surfaces . . . . .	5
1.2 Numerical Simulations of Granular Physics . . . . .	12
1.3 <code>pkdgrav</code> . . . . .	12
1.3.1 Computational Resources . . . . .	16
1.3.2 Code Improvements: Fixed Search Ball . . . . .	17
1.4 Thesis Outline: Granular Physics in the Solar System . . . . .	21
1.4.1 Regolith Mobility on Asteroids . . . . .	21
1.4.2 Spacecraft-Regolith Interactions . . . . .	22
1.4.3 Catastrophic Disruption of Rubble-Pile Asteroids . . . . .	23
1.4.4 Structure Formation in Saturn’s B Ring . . . . .	24
1.4.5 Outlook and Future Work . . . . .	27
2 Size Segregation on Asteroid Surfaces: Brazil-nut Effect	28
2.1 Chapter Preface . . . . .	28
2.2 Background . . . . .	30
2.3 Methodology . . . . .	34
2.3.1 <code>pkdgrav</code> : PBC . . . . .	34
2.3.2 Friction parameters . . . . .	36
2.3.3 Simulation parameters and walls setup . . . . .	39
2.3.4 Initialization process and main simulations . . . . .	42
2.4 Results . . . . .	43
2.4.1 Earth-gravity cases: Walls versus PBC . . . . .	43
2.4.2 Earth-gravity cases: static and rolling friction . . . . .	50
2.4.3 Low-Gravity Cases . . . . .	55
2.5 Discussion . . . . .	66

2.5.1	Driving mechanisms	66
2.5.2	Interplay between gravity and rolling friction	73
2.6	Conclusion	76
3	Low-speed granular impacts: Modeling Spacecraft-Regolith Interactions	80
3.1	Chapter Preface	80
3.2	Background	81
3.3	Methodology	85
3.3.1	Inertial walls	86
3.3.1.1	TAGSAM specifications	88
3.4	Impact Experiments	92
3.4.1	Material Property	93
3.4.2	Penetration Depth Experiments	97
3.4.3	Gravity Dependence	100
3.5	OSIRIS-REx TAGSAM	107
3.5.1	Simulations	107
3.5.2	Penetration Depth	113
3.5.3	TAG Reconstruct	117
3.5.3.1	Force Profiles	117
3.5.3.2	S/C vertical speed	120
3.5.3.3	Spring Compression Time	122
3.6	Conclusions & Future Work	122
4	Catastrophic Disruption of Gravitational Aggregates	126
4.1	Chapter Preface	126
4.2	Background	127
4.3	Methodology	132
4.3.1	Rubble-Pile Model	132
4.3.2	Simulation Parameters and Collision Geometries	135
4.4	Results	136
4.4.1	Head-on Equatorial Collisions	137
4.4.2	Oblique Equatorial Collisions	143
4.4.3	Head-on Collisions with $\delta < 90^\circ$	146
4.5	Discussion	147
4.5.1	The “Universal” Law for Catastrophic Disruption	147
4.5.2	Rotation Dependence of Catastrophic Disruption	155
4.5.3	Dependence on Material Properties	159
4.6	Conclusions & Future Work	161
5	Large-scale Structure in Saturn’s B ring	171
5.1	Chapter Preface	171
5.2	Background	171
5.3	Methodology	175
5.3.1	Periodic Boundary Conditions & Patch Properties	175
5.3.2	Diagnostic Tools	179

5.3.2.1	Viscosity Calculation . . . . .	179
5.3.2.2	Physical Optical Depth Calculation . . . . .	182
5.4	Results . . . . .	187
5.4.1	Correlation between Friction and Viscosity . . . . .	190
5.4.2	Correlation with Density . . . . .	192
5.4.3	Physical Optical Depth Measurements . . . . .	194
5.4.4	Comparison with Cassini UVIS occultations . . . . .	196
5.5	Conclusions & Future Work . . . . .	198
6	Conclusions & Future Work . . . . .	203
6.1	Conclusions . . . . .	203
6.2	Future Work . . . . .	207
6.2.1	MASCOT lander . . . . .	208
6.2.2	The Plateaus in Saturn's C ring . . . . .	209
	Bibliography . . . . .	213

## List of Tables

1.1	High-Performance Computing Usage Summary . . . . .	17
2.1	Material Property Parameters . . . . .	38
2.2	Values of test statistics: Table 1 . . . . .	48
2.3	Values of test statistics: Table 2 . . . . .	48
2.4	Regression analysis results . . . . .	49
3.1	The physical properties of real granular materials. . . . .	94
4.1	Summary of Mass Loss Results: Table 1 . . . . .	165
4.1	Summary of Mass Loss Results: continued . . . . .	166
4.1	Summary of Mass Loss Results: continued . . . . .	167
4.1	Summary of Mass Loss Results: continued . . . . .	168
4.1	Summary of Mass Loss Results: continued . . . . .	169
4.2	Summary of $\chi^2$ analysis . . . . .	170
5.1	Summary of ring patch parameters and simulation results . . . . .	188
5.1	Summary of ring patch parameters and simulation results, continued	190

## List of Figures

1.1	Mosaic of small Solar System Bodies . . . . .	3
1.2	Granular Solid Liquids & Gas . . . . .	4
1.3	Regolith on the Surface of Itokawa . . . . .	7
1.4	Regolith Mobility on Asteroids: Surface Accelerations . . . . .	11
1.5	Saturn Optical Depth Structure . . . . .	25
2.1	Initial set up for a periodic boundary simulation. . . . .	35
2.2	Angle of repose example: Gravel . . . . .	38
2.3	Least square regression of mean rise speed: Earth Gravity Cases . . . . .	45
2.4	Regression line of mean rise speed: $\mu_s$ and $\mu_r$ in Earth Gravity . . . . .	51
2.5	Convection Pattern . . . . .	56
2.6	Rise Speeds in $10^{-2} g$ . . . . .	58
2.7	Regression lines of mean rise speeds: $10^{-4} g$ . . . . .	60
2.8	Regression lines of mean rise speeds: 1 mm oscillation comparison . . . . .	62
2.9	Height evolution of Brazil-nut: PBC vs. Walls . . . . .	67
2.10	PBC vs Walls: Clustering at different jump heights . . . . .	70
2.11	PBC vs. Walls: bed height dilation at different local gravity . . . . .	74
3.1	TAGSAM diagram . . . . .	89
3.2	TAGSAM diagram . . . . .	90
3.3	Diagram of a uni-axial compression test . . . . .	95
3.4	Young’s modulus measurement . . . . .	96
3.5	Young’s Modulus and Poisson ratio as a function of friction properties . . . . .	98
3.6	Comparison with Impact Experiments onto Dry Ottawa Sand . . . . .	101
3.7	Comparison with Impact Experiments onto Glass Beads . . . . .	102
3.8	Gravity Dependence of the Penetration Depth . . . . .	103
3.9	The dependence of the drag coefficient on gravity . . . . .	106
3.10	TAGSAM montage . . . . .	108
3.11	Changes in spacecraft and TAGSAM separation . . . . .	110
3.12	Force Profile on TAGSAM and resulting spacecraft dynamics . . . . .	111
3.13	TAGSAM penetration depth as a function of friction parameters . . . . .	114
3.14	Density maps of TAGSAM penetration . . . . .	116
3.15	Force profile for moderate friction cases . . . . .	119

3.16	Force profile for moderate friction cases . . . . .	120
3.17	Spacecraft vertical speed as a function of material property . . . . .	121
3.18	TAGSAM spring compression timings . . . . .	123
4.1	Schematic of two collision scenarios . . . . .	134
4.2	Mass Loss for head-on Equatorial Impacts . . . . .	138
4.3	Map projection of mass loss . . . . .	140
4.4	Mass loss distribution with impact longitude . . . . .	141
4.5	Mass loss distribution with latitude . . . . .	143
4.6	Mass loss distribution for oblique equatorial impacts . . . . .	144
4.7	Mass of the largest remnant vs. impact speed for pole-on impacts . . . . .	148
4.8	Comparison with universal law for head-on collisions . . . . .	149
4.9	$\chi^2$ analysis for determining $\alpha$ and $A$ . . . . .	153
4.10	$Q_R^A/Q_{RD}^*$ with adjusted interacting mass . . . . .	156
4.11	Semi-Analytic fit for $Q_{RD}^*$ . . . . .	160
4.12	$Q_{RD}^*$ for different material properties . . . . .	162
5.1	Diagram of a sliding-patch model for simulating a ring system . . . . .	177
5.2	Viscosity Calculation: Comparison with Literature . . . . .	183
5.3	Dependence of Optical Depth on Ring Geometry . . . . .	185
5.4	Ring Simulation Snapshots . . . . .	189
5.5	Viscosity and Toomre Q dependence with $\mu_s$ . . . . .	193
5.6	Dependence of Toomre Q on particle density and friction . . . . .	194
5.7	Physical optical depth variation with observing angle and friction . . . . .	197
5.8	Comparison with Cassini UVIS occultations . . . . .	199
6.1	MASCOT bouncing . . . . .	210
6.2	Radial profile of Saturn's C ring . . . . .	211

## List of Abbreviations

### General:

pkdgrav	parallel k-d tree gravity code
NASA	National Aeronautics and Space Administration
ESA	European Space Agency
JAXA	Japan Aerospace Exploration Agency
ApJ	Astrophysical Journal
MNRAS	Monthly Notices of the Royal Astronomical Society
P&SS	Planetary & Space Sciences

### Chapter 1:

NEAR – Shoemaker	Near Earth Asteroid Rendezvous – Shoemaker
NEA	Near-Earth Asteroid
SSDEM	Soft-Sphere Discrete Element Method
OSIRIS-REx	Origins, Spectral Interpretation, Resource Identification, Security, Regolith Explorer
TAGSAM	Touch and Go Sample Acquisition Mechanism

### Chapter 2:

BNE	Brazil-nut Effect
PBC	Periodic Boundary Condition(s)

### Chapter 3:

S/C	Spacecraft
-----	------------

### Chapter 4:

SSSBs	Small Solar System Bodies
-------	---------------------------

### Chapter 5:

UVIS	Ultraviolet Imaging Spectrograph
VIMS	Visual and Infrared Mapping Spectrometer

### Chapter 6:

MASCOT	Mobile Asteroid Surface Scout
DLR	Deutsches Zentrum für Luft - und Raumfahrt
CNES	Centre National d'Études Spatiales

## Chapter 1: Introduction

Granular material, in the form of regolith, is found in the uppermost layer of most solid bodies in our Solar System, from planets and their satellites to asteroids and comets. Regolith is loosely defined as broken up particulates that are present on the surface of a moon or other small solar system body. In the planetary science community, the terminology of sedimentary deposits is used to describe the range of sizes of these particulates. The terms pebble, cobble, and boulder describe individual particles of sizes ranging from 4 mm to 6.4 cm, 6.4 cm to 2.6 m, and  $> 2.6$  m, respectively (Miyamoto et al., 2007). Before the first spacecraft encounter with small solar system bodies, it was generally assumed that most of these bodies were monolithic rocks with bare surfaces (although, there was some discussion of alternatives: see Dollfus et al. 1977; Housen et al. 1979; Michel et al. 2001). Because of the low surface gravity on asteroids, it was assumed that regolith formation would not be possible since small grains that were created during a cratering event on a small body would then escape easily its gravitational influence (Chapman, 1976). However, the Galileo, NEAR and Hayabusa space missions revealed the asteroids Gaspra, Ida, Eros (Sullivan et al., 2002; Robinson et al., 2002) and Itokawa (Fujiwara et al., 2006) were covered entirely by a layer of regolith (see Fig. 1.1). Furthermore, the

regolith on the surface of these and other small bodies seemed to exhibit complex dynamics. The crater morphology on the asteroid Lutetia as observed by the Rosetta spacecraft is thought to be affected by dry granular flows and avalanches on the surface (Vincent et al., 2012). Meter-size boulders resting on the surface of tiny Itokawa pose a conundrum for the asteroid’s surface evolution. Furthermore, ground-based observations of near-Earth asteroids (NEAs) have revealed that the weathered surfaces of some asteroids appear to be “freshened” possibly by close encounters with planets (Binzel et al., 2010; Nesvorný et al., 2010). Astronomical observations of small bodies are, by their nature, limited to only surveying a body’s surface. Therefore, understanding how the surface behaves is critical for interpreting observations and for formulating coherent theories of their overall structure and evolution.

Granular physics is a relatively new sub-discipline of physics that attempts to combine principles that have been developed for both solid-state physics and engineering (such as soil mechanics) with fluid dynamics in order to formulate a coherent theory for the description of granular materials, which are found in both terrestrial (e.g., earthquakes, landslides, and pharmaceuticals) and extra-terrestrial settings (e.g., asteroid and terrestrial planet surfaces, asteroid interiors, and planetary ring systems). Granular matter behaves differently than any other familiar form of matter, such as solids, liquids or gases (Fig. 1.2). While the individual grains are solid, collectively granular matter can also behave as liquids or gases. Although constitutive equations exist for granular interactions on Earth, the inferred scaling to the gravitational and environmental conditions on other planetary bodies such

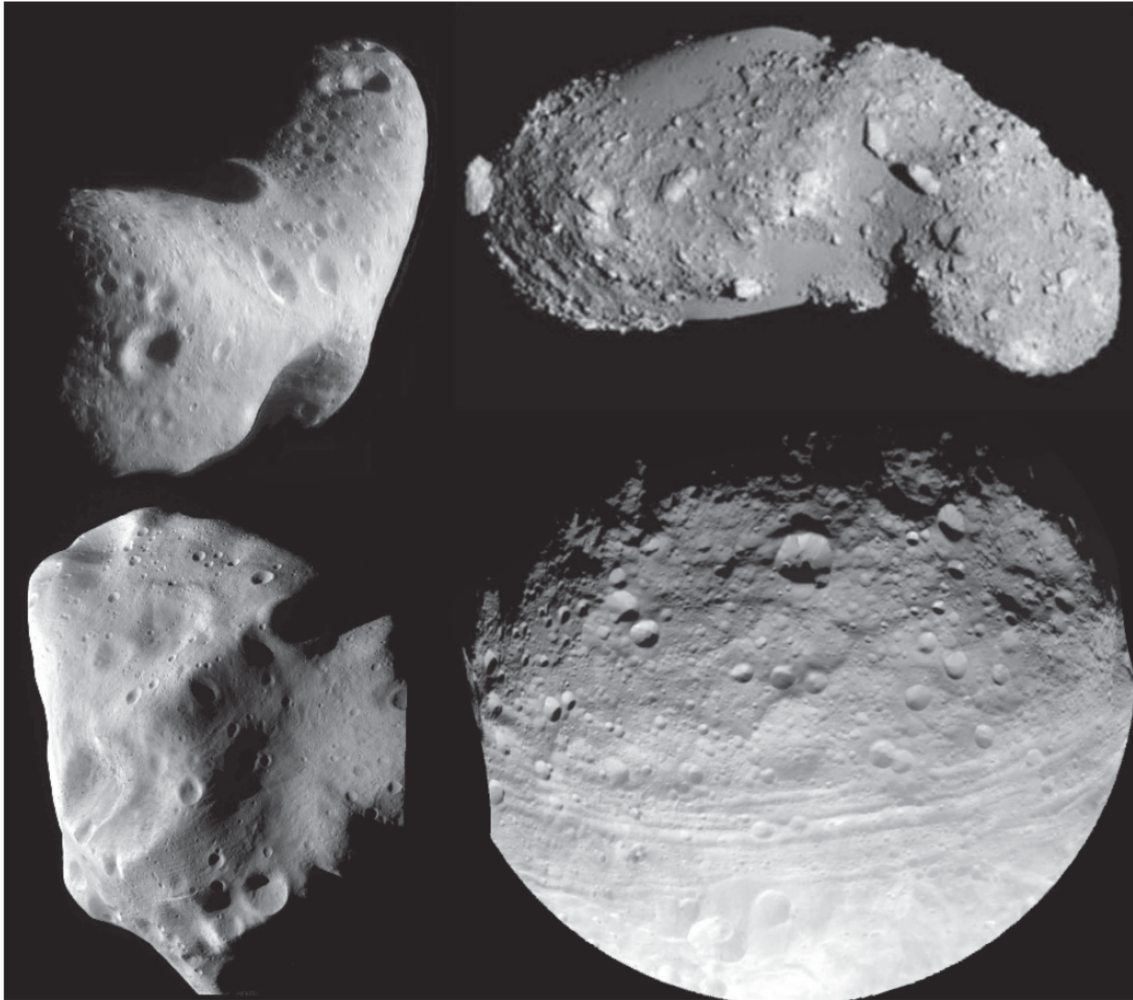


Figure 1.1: Images of asteroids visited by spacecraft. Clockwise from the top left: Eros, Itokawa, Vesta, Lutetia (not to scale). These asteroids span a wide range in surface gravity. Due to their elongated shapes and fast spins, small asteroids have surface gravities that can vary by nearly an order of magnitude. Compared to Earth gravity,  $g$ , the mean surface gravity on the small bodies shown here are  $2.5 \times 10^{-2}g$ ,  $5 \times 10^{-3}g$ ,  $6 \times 10^{-4}g$ , and  $10^{-5}g$  for Vesta, Lutetia, Eros, and Itokawa, respectively. Source: [Murdoch et al. \(2015\)](#).

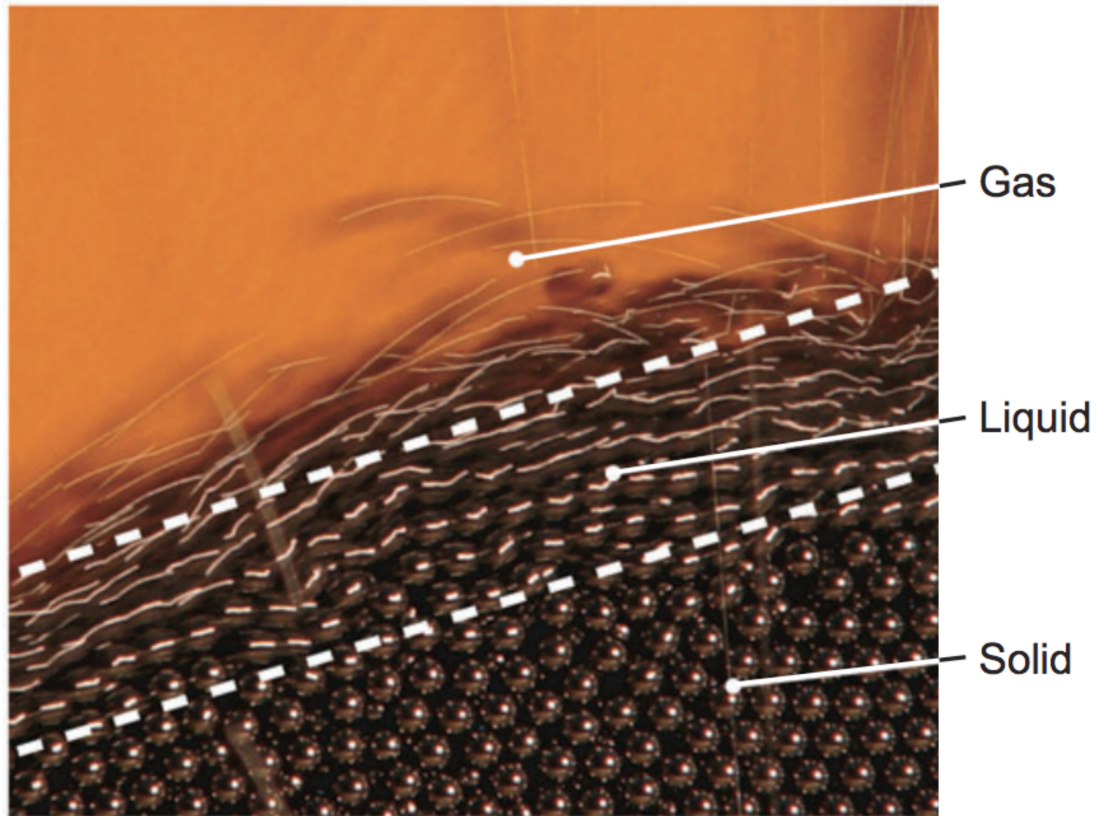


Figure 1.2: A pile of steel beads exhibiting avalanching behavior. Grains in the lower right portion of the image are static, behaving as solids. A phase transition occurs near the surface where grains begin to flow like liquids. Slightly above the surface, ballistic grains can attain gas-like qualities. source: [Forterre & Pouliquen \(2008\)](#).

as asteroids is currently untested. In the case of our Solar System, the growth of this sub-discipline has been key in helping to interpret the formation, structure, and evolution of environments that exhibit granular processes.

In this thesis, we apply the principles of granular physics to four different planetary science scenarios. We study the size segregation of granular material in an attempt to explain the presence of large boulders in spacecraft observations of asteroids. We explore low-speed impacts onto the surface of asteroids, in order to

better understand how a spacecraft might be able to land or interact with the surface of a small body. We study the collisions of rubble-pile asteroids, bodies that are a gravitationally bound granular system, in contexts relevant to planet formation. Finally, we study Saturn's B Ring, a unique granular system where the combined effects of dissipative collisions and self-gravity lead to the emergence of large-scale structures.

## 1.1 Evidence of Regolith and its Mobility on Asteroid Surfaces

Spacecraft visits to asteroids have discovered evidence of regolith on small asteroids. Furthermore, it is likely that this surface material is able to be mobilized. Surface images provide evidence of this motion, and understanding the underlying forces behind these phenomena allows us to gain insight into how a small body interacts with the space environment and how the asteroid itself functions as a physical system. Some examples of environmental factors that can influence an asteroid's structural evolution are micro-meteorite impacts, solar radiation pressure, and tidal interactions with larger bodies.

Close-up images of Itokawa by the Hayabusa mission show that the surface is covered with unconsolidated particles (Fig 1.3). These grains are typically found piled on each other without being buried by a fine layer of sediment. Furthermore, the position and orientation of the rocks appear to be stable against local gravity. Also, small impact craters on the surface are found to have partially disrupted rims, and the debris from these rims seems to drain towards the effective gravitational

potential lows of the asteroid (see the region highlighted by the white circle and arrows in Fig. 1.3). These features indicate that grains on the surface of the asteroid were likely reallocated after they were formed or reaccumulated on the surface. This implies that the surface has been subjected to global vibrations. The source of these vibrations could be micrometeoroid impacts (Garcia et al., 2015), tidal encounters with larger objects in the Solar System (Yu et al., 2014), or thermal fluctuations due to solar radiation (Delbo et al., 2014). Focusing on impacts, we can use analytical formulations for the expected surface accelerations due to an impact to better understand the phase space of possible seismic activity that can drive regolith mobility. Following Miyamoto et al. (2007), the maximum half-cycle amplitude,  $A$ , and seismic frequency,  $f$ , of a vibrating rock define the average seismic strain energy per unit volume of rock,  $e$ :

$$e = \rho_a \pi^2 f^2 A^2, \quad (1.1)$$

where  $\rho_a$  is the bulk density of the asteroid. The maximum acceleration magnitude that the rock experiences is:

$$a = 4\pi^2 f^2 A. \quad (1.2)$$

The total seismic energy density in the system is given as  $2e$  (Lay & Wallace, 1995); therefore, the total seismic energy,  $E_s$ , of an asteroid with radius  $D_a$  (assuming a spherical shape), is given as:

$$E_s = \frac{\rho_a D_a^3 a^2}{48\pi f^2}. \quad (1.3)$$

For a seismic event that is generated by an impact, the kinetic energy,  $E_i$ , imparted

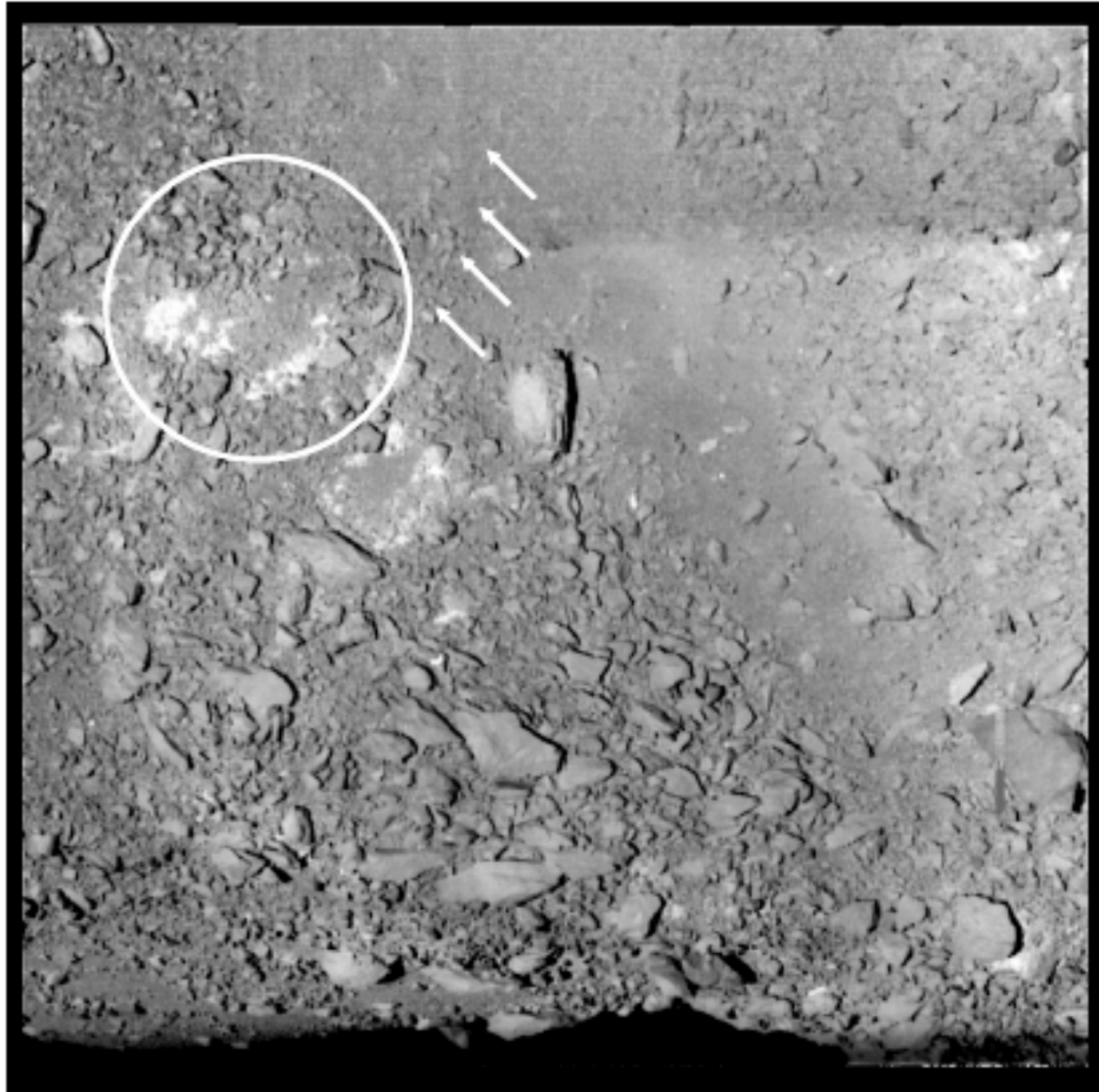


Figure 1.3: The Hayabusa mission's orbital survey showed regions on the surface of Itokawa that were very smooth, occupied by cm-size particles, and regions of rough terrain, occupied by boulders. Here, we have a closeup image of Itokawa's surface. The white circle indicates an impact crater, which has a collapsed rim. The material seems to drain towards the asteroid's effective gravitational potential low (indicated by the white arrows).

by the event is given by (Richardson et al., 2004)

$$E_i = \frac{1}{12} \pi \rho_i D_i^3 v_i^2, \quad (1.4)$$

where  $\rho_i$  is the density of the impactor,  $D_i$  is the diameters of the impactor, and  $v_i$  is the impact speed. Only a small fraction of the kinetic energy is transferred to seismic energy. Therefore, the actual seismic energy can be written as

$$E_s = \eta E_i, \quad (1.5)$$

where  $\eta$  is the seismic efficiency factor. Using Eq. 1.3, 1.4, and 1.5, the maximum acceleration can be written as

$$a = 2\pi v_i f \sqrt{\eta \frac{\rho_i}{\rho_a} \left(\frac{D_i}{D_a}\right)^3}. \quad (1.6)$$

The gravitational acceleration on the surface of a spherical body,  $g$ , is given as

$$g = \frac{2}{3} \pi G D_a \rho_a, \quad (1.7)$$

where  $G$  is the gravitational constant. Therefore, the maximum acceleration,  $a$ , relative to the local gravity can be written as

$$\frac{a}{g} = \frac{3f v_i}{G} \sqrt{\eta \frac{\rho_i D_i^3}{\rho_a^3 D_a^5}}. \quad (1.8)$$

While this equation may be useful for estimating the magnitude of surface accelerations due to seismic shaking for a monolithic spherical body, actual small bodies are likely rubble piles, collections of gravitationally bound boulders. A rubble-pile asteroid can have micro- and macro-porous interior structure Richardson et al. (2002), meaning their interiors have significant void spaces. The asteroid Itokawa is thought

to be very porous as it has a very low bulk density of  $1.9 \text{ g/cm}^3$  compared to its constituent rocks (which typically have densities  $> 2.7 \text{ g/cm}^3$ ). Such an interior structure would cause seismic waves to attenuate as they can be partially reflected and refracted off boulder-boulder and boulder-void boundaries. Therefore, a better estimate of the surface accelerations on a small asteroid should include the effects of seismic energy attenuation. A precise approach would require knowledge of the size distribution of the constituent “rubble” of a rubble-pile. Analytically, an estimate can be obtained by applying diffusive scattering theory. [Richardson et al. 2005](#) provide a prescription for including this effect, giving the seismic attenuation,  $A_t$ , of a wave as it propagates across a body:

$$A_t = \exp\left(\frac{-fD_a^2}{K\pi Q}\right), \quad (1.9)$$

where  $K$  is the seismic diffusivity and  $Q$  is the seismic quality factor. Therefore, the surface acceleration on the surface of a body due to an attenuated seismic wave can be written as:

$$\frac{a}{g} = \frac{3fv_i}{G} \sqrt{\eta \frac{\rho_i}{rho_a^3} \frac{D_i^3}{D_a^5}} \cdot \exp\left(\frac{-fD_a^2}{K\pi Q}\right). \quad (1.10)$$

Most of the parameters in Eq. 1.10 are difficult to determine, especially since the internal structure of any asteroid has never been directly measured through experiments. However, some general properties of asteroids that may be directly measured, such as size and bulk density, can give an indication of the general interior properties of an asteroid (i.e., whether it is likely to be a rubble pile or a solid monolithic body).

In order to get a sense of how surface accelerations driven by impacts might vary as a function of asteroid size and density, we adopt some nominal values for the impact and seismic parameters (Richardson et al., 2004). Fig. 1.4 shows the surface acceleration relative to gravity due to impacts (Eq. 1.10) as a function of the asteroid diameter, for different combinations of  $f$ ,  $D_i$  and  $\rho_a$ . The shaded regions show the magnitude of surface acceleration that is required to drive granular convection (which occurs at values over unity, Jaeger et al. 1996) or to destabilize the surface (which occurs at values over 0.2, Lambe & Whitman 1979). We see that the regolith on smaller asteroids can be mobilized by smaller impactors. For an Itokawa-sized body, an impactor that is 10 cm in size imparts sufficient seismic energy to drive granular convection on the asteroid’s surface.

The analysis here has assumed seismic properties of asteroids that might not actually reflect reality. In order to gain a better understanding of the plausibility of regolith motion by small impactors, a more accurate model of asteroid interiors needs to be obtained. Garcia et al. (2015) performed simulations of seismic wave propagation for different asteroid interiors and found that a naive approach, such as the one described here, can underestimate the seismic accelerations by a factor of  $\sim 50$ . While this encourages the picture of seismically driven regolith motion, direct simulations need to be performed to determine whether these seismic events are sufficiently energetic to mobilize regolith such that there are observable changes on the surface (this is the topic of Chapter 2).

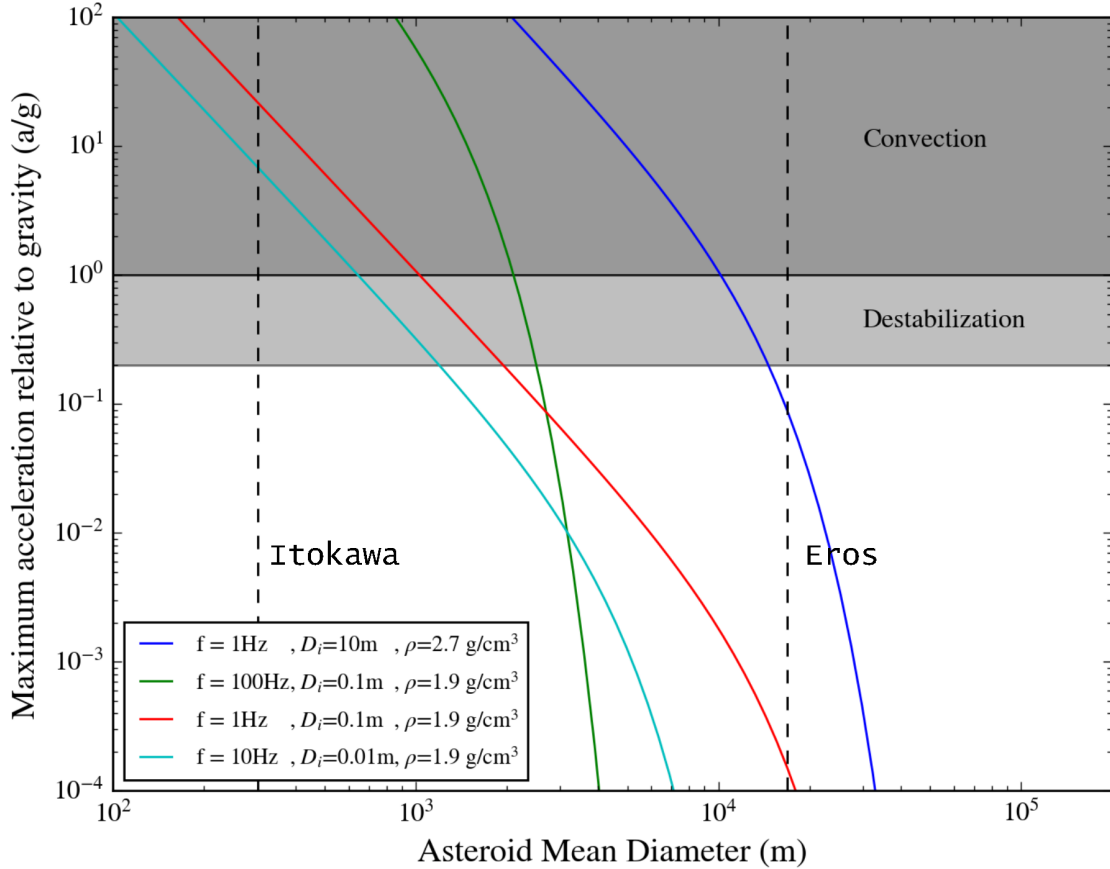


Figure 1.4: We use nominal values of the seismic and impact parameters to plot curves that may be representative of the expected surface accelerations for different asteroid sizes. We use values of  $Q = 200$ ,  $K=0.25$ ,  $\eta = 10^{-4}$ ,  $v_i = 4$  km/s, and  $\rho_i = 2.5$  g/cm<sup>3</sup>. Eros and Itokawa have bulk densities of 2.7 g/cm<sup>3</sup> and 1.9 g/cm<sup>3</sup>, respectively. We see that small impactors (down to 10 cm) can cause regolith to be mobilized on Itokawa’s surface. For the assumed seismic and impact parameters, regolith on the surface of Eros is unlikely to be mobilized by an impact.

## 1.2 Numerical Simulations of Granular Physics

It is difficult to develop a complete deterministic theory for granular materials due to the fact that granular systems are composed of a large number of elements that interact through a non-linear combination of various forces (mechanical, gravitational, and electrostatic, for example) leading to a high degree of stochasticity. A tool for the study of these complex system has been numerical simulations that model the different dynamical interactions (collisions, electrostatic forces, gravitational forces, etc) directly. For a study of Solar System objects, numerical simulations are invaluable as we can recreate extra-terrestrial conditions that would be very difficult or impossible in a laboratory setting, including micro-gravity and vacuum conditions. We approach our study with a combination of computational modeling and analytical tools. Where appropriate, we use observational data to constrain the very large parameter space involved with granular dynamics. The goal of each of these projects was to study the behavior of granular material in extreme conditions so that we may enhance our understanding of both astrophysical and granular systems.

## 1.3 `pkdgrav`

All the simulations presented in this thesis were conducted with the parallel  $N$ -body gravity tree code `pkdgrav` (Stadel, 2001), adapted to model collisions between solid spherical grains (Richardson et al., 2000, 2009, 2011). Originally collisions

in `pkdgrav` were treated as idealized single-point-of-contact impacts between rigid spheres. A soft-sphere option was added (Schwartz et al., 2012); with this option, particle contacts can last many timesteps, with reaction forces dependent on the degree of overlap (a proxy for surface deformation) and contact history. This allows us to model multi-contact and frictional forces. The code uses a 2nd-order leapfrog integrator, with accelerations due to gravity and contact forces recomputed each step.

The soft-sphere discrete element method (SSDEM) implementation in `pkdgrav` uses a spring/dash-pot to model the collisional forces between particles. In this model, a spherical particle overlapping with a neighboring particle feels a reaction force in the normal and tangential directions determined by spring constants ( $k_n$ ,  $k_t$ ). The normal restoring spring force,  $F_N$ , is generated according to Hooke’s law,

$$\mathbf{F}_{N,\text{restoring}} = -k_n x \hat{\mathbf{n}}, \quad (1.11)$$

where  $x$  is the amount of overlap between the two particles, and  $\hat{\mathbf{n}}$  is the unit vector that points from a particle’s center to its collider’s center. The tangential restoring force is given by

$$\mathbf{F}_{T,\text{restoring}} = -k_t \mathbf{S}, \quad (1.12)$$

where  $S$  is the tangential displacement from an equilibrium contact point, which is tracked over the entire duration of an overlap. The value of  $k_n$  determines the speed of propagation of a sound wave through a granular system. A “correct” value for  $k_n$  would depend on the sound speed of the material being simulated. In practice, a value of  $k_n$  is chosen to ensure that overlaps do not exceed 1% of the smallest

particle in a collision. There are two regimes that constrain this determination: one where the kinetic energy of the particles dominate, and another where the confining pressure of surrounding particles dominates. For the first regime,  $k_n$  is determined by considering the scenario where all of the energy of a collider with mass  $m$  traveling at a speed  $v_{\max}$  is input into a single spring. Limiting the fractional overlap,  $x_{\max}$ , we obtain the following prescription for  $k_n$ :

$$k_n = m \left( \frac{v_{\max}}{x_{\max}} \right)^2. \quad (1.13)$$

For the second regime, where the particle is in a dense static medium under the influence of a global potential (such as gravity), the potential energy of the entire medium is taken into consideration. In order to prevent overlaps exceeding values of  $x_{\max}$ , we require a spring with a strength that can resist the overburden pressure. For a system with height  $H$  under the influence of a gravitational acceleration  $g$ , and composed of particles with size  $s$  and density  $\rho$  that are packed so that the porosity of the system is  $\phi$ ,  $k_n$  is given by

$$k_n = \frac{\phi \rho g H s^2}{x_{\max}}. \quad (1.14)$$

In situations where both kinetic energy and confining pressure play a role, the largest value of  $k_n$  is the one chosen. Conventionally, the value of  $k_t$  is typically set to be  $\sim \frac{2}{7}k_n$ . The SSDEM implementation also allows optional damping effects. The damping parameters ( $C_n, C_t$ ) are related to the conventional normal and tangential coefficients of restitution used in hard-sphere implementations,  $\varepsilon_n$  and  $\varepsilon_t$ , by the spring constants  $k_n$  and  $k_t$  (see [Schwartz et al. 2012](#) for the full procedure). The

normal and tangential damping forces are given by

$$\mathbf{F}_{N,\text{damping}} = C_n \mathbf{u}_n, \quad (1.15)$$

$$\mathbf{F}_{T,\text{damping}} = C_t \mathbf{u}_t, \quad (1.16)$$

where  $\mathbf{u}_n$  and  $\mathbf{u}_t$  are the normal and tangential components of the relative velocity, respectively. We also include the effects that impose static, rolling, and/or twisting friction. For the studies presented in this thesis, only the static and rolling friction effects were used as these effects were found to dominate the behavior of particles in the relevant simulations. The static and rolling friction components are parameterized by dimensionless coefficients  $\mu_s$  and  $\mu_r$ , respectively. The coefficient of static friction determines the maximum amount of tangential force that can be supported by the contact point of two particles. This tangential force scales linearly with the normal force at the contact point. In the event that the tangential force exceeds the maximum value given by the static friction coefficient, the particles slip past one another, and the tangential force then is determined by the tangential spring constant and the tangential damping coefficient. The coefficient of rolling friction is used to determine the resulting torque due to two particles rolling against one another. Two particles are said to be rolling with respect to each other if their relative velocities are zero, but they have some relative rotational motion. The torque induced by the rotation scales linearly with the coefficient of rolling friction. In practical terms, a non-zero coefficient of rolling friction codifies some non-spherical shape information to our spherical particles. Plausible values for these various parameters are obtained

through comparison with laboratory experiments (Section 2.2).

This numerical approach has been validated through comparison with laboratory experiments; e.g. [Schwartz et al. \(2012\)](#) demonstrated that `pkdgrav` correctly reproduces experiments of granular flow through cylindrical hoppers, specifically the flow rate as a function of aperture size, [Schwartz et al. \(2013\)](#) demonstrated successful simulation of laboratory impact experiments into sintered glass beads using a cohesion model coupled with the soft-sphere code in `pkdgrav`, and [Schwartz et al. \(2014\)](#) applied the code to low-speed impacts into regolith in order to test asteroid sampling mechanism design.

### 1.3.1 Computational Resources

Our simulations were run on high-performance supercomputing facilities that are available to the Department of Astronomy at the University of Maryland, College Park. These include the `yorp` cluster operated by the Department of Astronomy, `deeptought` and its successor `deeptought2` operated by the University of Maryland, and the MARCC `bluecrab` cluster administered jointly by the University of Maryland and John Hopkins University and operated by John Hopkins University. Table 1 summarizes the usage of each cluster according to simulations done for each chapter by the total number of computational hours (service units, or SU's). In general, simulations that required a low number of cores ( $< 32$ ) or simulations that were done to prototype new code implementations were performed on the `yorp` cluster. Studies that required a large number of cores ( $> 32$ ) or a large parameter

space sweep (such as the cases presented in chap. 2) were performed using one of the supercomputing clusters (`deephought`, `deephought2`, or `MARCC bluecrab`).

Table 1.1: Usage summary by simulations done in each chapter, in kSUs (approximate).

	yorp	deephought	deephought2	MARCC bluecrab
Chapter 2	300	200	600	-
Chapter 3	300	1200	2200	-
Chapter 4	500	400	-	-
Chapter 5	100	-	1000	2000

### 1.3.2 Code Improvements: Fixed Search Ball

In this brief section, we detail code changes implemented during this thesis that resulted in faster run times for simulations. In `pkdgrav`, each particle maintains a list of its nearest neighbors in order to check for potential colliders. Rather than performing a collision check for each other particle in a simulation, which would take  $N^2$  time, a particle only performs a collision check on its nearest neighbors. The tree code implemented in `pkdgrav` provides nearest-neighbor lists in order  $N \log N$  time. The number of nearest neighbors that a particle has to search for in order to effectively determine whether it is in overlap with another particle largely depends on its size with respect to other particles. For equal-sized particles, the theoretical maximum number of neighbors that a single particle may be in contact with is 12. (Note: this is only true if the particles are “just touching” and not overlapping significantly.) In general, for a size distribution of particles, the maximum number

of overlaps that a single particle may experience is given by

$$\text{MAX\_NUM\_OVERLAPS\_PER\_PARTICLE} = 8 + 4 \left( \frac{R_{\text{max}}}{R_{\text{min}}} \right)^2, \quad (1.17)$$

where  $R_{\text{max}}$  and  $R_{\text{min}}$  are the maximum and minimum particle radii in the simulation, respectively.

Of vital importance to detecting neighbors, and therefore particle contacts, is the use of a search ball by each particle. The search ball of a particle defines the limited region around it where it will look for nearest neighbors. In the default implementations of `pkdgrav`, the search ball is dynamically constructed each time step. Years of practical use of the code have shown that this might not be the most efficient way to find nearest neighbors in all cases. Methods that generate a fixed search ball for each particle based on some prescription make the code run faster as the search ball does not need to be re-constructed each time step. Three different fixed-search-ball strategies were implemented in order to speed up processing time and ensure proper neighbor finding for certain `pkdgrav` scenarios. We outline these methods below, and best practices for using them.

- **Maximum diameter:** The size of the search ball of each particle is set to the diameter of the largest particle in the simulation. This option is optimal for equal-size particles, or a size distribution of particles with a relatively small size ratio ( $\frac{R_{\text{max}}}{R_{\text{min}}} \lesssim 3$ ). The advantage of this option is the speed-up in having a fixed search ball, while maintaining a relatively small memory requirement.
- **Sum of particle radius and mean radius:** The size of each particle's search ball is set to its own radius plus the mean radius of all particles in

the simulation. This allows each particle to have a unique search ball that depends on its own size. This option is especially useful for scenarios where a single very large particle interacts with a large number of small particles (of roughly equal size). This allows the large particle to efficiently detect all the small particles as nearest neighbors, while also limiting the size of the small particles' search ball. This reduces the number of nearest neighbors that each particle needs to check for overlaps. However, the disadvantage is the large memory requirement. Each particle needs to carry around an overlap list that can contain `MAX_NUM_OVERLAPS_PER_PARTICLE` number of particle IDs.

- **Sum of particle radius and next-largest particle radius:** The size of each particle's search ball is set to its own radius plus the radius of the next-largest particle in the simulation. This option is useful when there is a large and continuous size distribution of particles, or in the case of a single large intruder interacting with a continuous size distribution of particles. This optimizes the number of nearest neighbors a particle needs to check for overlaps. The disadvantage is the large memory requirements.

In all cases (including the default) it is also necessary to sort the particles in size order, either in increasing order for the default or maximum-diameter cases, or decreasing for the other two. This is because to save memory, a given particle only stores SSDEM contact information for neighbors with higher order numbers, and neighbors are determined by measuring distances between particle centers, not surfaces. For the increasing-size-order cases, the sort strategy ensures there is never

more than 12 possible contacts per particle (assuming overlaps are always small), keeping memory usage low. For the decreasing-size-order cases, the sort strategy ensures no contacts are missed (a large particle will see all possible neighboring small particles), at the expense of a larger memory requirement.

The most obvious advantage of a fixed search ball is that processors spend less time re-computing search balls each time step. The cost of using a fixed search ball is larger memory requirements for certain cases. Practically, we found that using a fixed search ball speeds up the computational time by a factor of 2 for cases where the simulated particles are of roughly equal size (within 10% in radius). For simulations with a large size difference between the smallest and largest particle (e.g., for a bed of target particles that are 1/30th the size of an impactor), we find an order of magnitude or more speed up.

The advantage of using the default search ball option is that it is general, and is low memory use (only 12 colliders ever need to be stored into memory). The disadvantage to this method is that the search ball needs to be regenerated every time step, and, for a very large size difference in particles, each particle will have to loop through `MAX_NUM_OVERLAPS_PER_PARTICLE` nearest neighbors to check for overlaps, which increases as the square of the size ratio. These two factors require a lot of processing time, and scale poorly with total number of particles.

## 1.4 Thesis Outline: Granular Physics in the Solar System

We used the code described above to study various scenarios related to Solar System dynamics that are connected by the fact that they all exhibit granular processes. Each study builds from and upon the others. Although these studies take place at rather different scales, they illustrate the importance of granular physics throughout the field of planetary science.

### 1.4.1 Regolith Mobility on Asteroids

In Chapter 2, we present a study related to regolith motion on Asteroids. Size segregation on asteroid surfaces can be driven by the the Brazil-nut Effect (BNE). The BNE is a process whereby repeated vibrations of a granular system causes large particles, embedded in a medium of smaller particles, to begin to rise against the direction of the local effective gravity in the system. This effect has been invoked in the past to explain the presence of large boulders on the surface of asteroids ([Matsumura et al., 2014](#)). The BNE is a physical process that has been studied extensively by granular physicists in the lab, and recently by planetary scientists through simulations. The BNE study is presented first as it is a relatively simple problem to conceptualize that provides a good introduction to the complexities of granular physics and its importance to the field of planetary science. The work presented here extends the current knowledge of the BNE by testing its efficiency for different boundary, gravity, and vibration conditions that closely resemble those found on asteroids.

## 1.4.2 Spacecraft-Regolith Interactions

In Chapter 3, we discuss impacts onto a granular medium, and studies related to the Touch-and-Go Sample Acquisition Mechanism (TAGSAM) on the OSIRIS-REx spacecraft. In the last two decades, the exploration of small-solar-system bodies has been advanced greatly by spacecraft missions that flyby (e.g., Rosetta at Šteins and Lutetia), orbit (e.g., Dawn at Vesta and Ceres), touchdown on the surface (e.g., NEAR at Eros), and/or return samples (e.g., Hayabusa at Itokawa). In particular, with the success of the Hayabusa mission, sample return has become an increasingly viable and popular option for the study of asteroids. Besides the incredible scientific value of a returned surface sample, the ability of such missions to directly interact with the surface provides a unique opportunity to test and validate models of small-body surface geotechnical properties (Biele et al., 2015). While there have been several missions that have touched down on a small-body surface (NEAR, Hayabusa, and Rosetta’s Philae lander), we still have a poor understanding of how regolith behaves in low-gravity environments. The study of hypervelocity impacts on asteroids (impacts at speeds of  $\geq 1$  km/s) has a rich literature (Michel et al., 2001; Housen & Holsapple, 2011); however, very little is known about the response of an asteroid surface to low-speed impacts ( $\sim 1$  m/s). This dearth of knowledge is due to the fact that there are no natural processes that produce  $\sim 1$  m/s impacts on asteroids. Therefore, in Chapter 3, we study low-speed impacts onto a granular medium by attempting to extend the current theory of impacts in Earth-gravity. Then, we focus our attention on the wholly anthropocentric activity of landing

on a small solar-system body. Specifically, we model the future touchdown of the OSIRIS-REx spacecraft on the surface of the asteroid Bennu.

### 1.4.3 Catastrophic Disruption of Rubble-Pile Asteroids

In Chapter 4, we move from discussions of cm-size particles on the surface or near-surface of small bodies to exploring the collisions of  $\sim 1$  km-sized rubble piles, gravitational aggregates of meter size objects. There is strong observational (Pravec et al., 2005) and theoretical (Richardson et al., 2002) evidence that some asteroids in our Solar System are rubble piles rather than solid monolithic bodies. Unlike monolithic objects, rubble piles have almost no tensile strength. A rubble pile does have shear and compressive strengths. The relative importance of each of these components depends on the surface properties of the constituent “particles” of the gravitational aggregate. What little tensile strength a rubble pile has comes from the cohesive forces between individual boulders. This cohesion likely comes from short-range Van der Waals and electrostatic forces between the smaller particles that make up the regolith layer on the surface of the boulders. The relatively recent discovery of the rubble-pile structure of asteroids has had important implications for understanding the evolution of asteroids undergoing physical processes that depend on the strength of these objects. In particular, computational studies of rotational-shape evolution of rubble piles (Cotto-Figueroa et al., 2015; Zhang et al., 2016) are changing our understanding of how asteroids spin-up through thermal re-radiation (i.e., the YORP effect, see Bottke et al. 2006) and how they might break apart

through rotational fission (Walsh et al., 2008; Sánchez & Scheeres, 2012). Furthermore, the internal structure of a planetesimal (km-size objects found in the early Solar System) affects the rate at which it can grow through mergers, an important step for the formation of planets. Numerical simulations are indispensable tools for probing the range of possible collisional outcomes (Leinhardt et al., 2000; Leinhardt & Stewart, 2012). In Chapter 4, we study the binary collisions of rubble piles in order to determine how the collisional parameters of the system affect the outcome. We focus on how the rotational properties of the system affect the rate at which planetesimals catastrophically disrupt (i.e., the rate at which a collision would result in an object losing more than half of its initial mass). Since a rubble-pile is inherently a gravitationally bound granular system, its behavior is dependent on the physical properties of its constituent particles. Therefore, accurately modeling rubble-pile dynamics requires carefully considering the material properties of the individual particles. Hence, we use knowledge of material properties developed by our study of granular physics on small scales (Yu et al., 2014) to better model larger-scale systems. Symbiotically, we can use large-scale systems as astronomical laboratories, where we can probe the physics of granular flow in extreme conditions.

#### 1.4.4 Structure Formation in Saturn’s B Ring

In Chapter 5, we continue our study of larger-scale granular systems by studying Saturn’s B ring. The rings are made up of meter-size particles composed mostly of ice. The B Ring is one of Saturn’s main rings, beginning  $\sim 92,000$  km away from

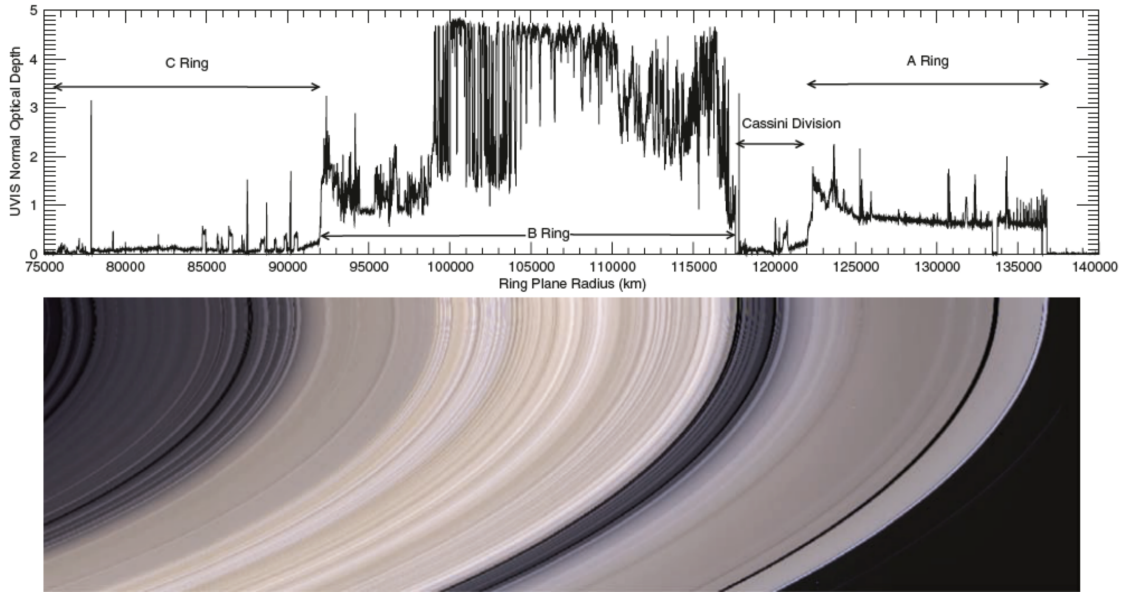


Figure 1.5: Optical depth pattern (top panel) and Cassini Image of Saturn’s main rings. The optical depth is derived from measurements of stellar occultation showing the A,B, C rings and Cassini Division (10 km radial resolution). source: [Colwell et al. \(2009\)](#).

Saturn and extending outwards for  $\sim 26,000$  km. It is also the brightest of Saturn’s rings as it has the highest optical depths. Fig. 1.5 shows an image of Saturn’s main rings (upper panel) and their optical depth structure (lower panel).

The B ring is divided into four subrings, from the innermost B1 ring to the outermost B4 ring. The normal optical depths range from  $\sim 0.7$  in the B1 ring to  $\sim 3$  in the B2 ring, and transmitted light is completely blocked in the the B3 ring. The Cassini mission has provided a wealth of high-resolution data that has revealed rich and varied structure in the rings (such as propellers and ridges, see [Tiscareno et al. 2010](#)). These structures vary in scale, from thousand-km structure clearly visible in images to small sub-km wake-like structure inferred through observations of stellar

occultations (Colwell et al., 2007). Wake-like structures are repeated variations in the optical depth with radial distance. The first indication of their presence was from the observing-geometry dependence of the B ring optical depth as the observing angle changed. This occurs because low opacity regions are obscured by the wake-like structures at certain observing angles. Two different mechanisms have been suggested to explain the presence of wakes: self-gravity and viscous overstability. Self-gravity wakes are produced by the continuous gravitational collapse and subsequent tidal disruption of ring-particle aggregates, causing the formation of unique extended structures that are typically tilted with respect to the direction of orbital motion. Viscous overstability results from the balance between the dissipation of energy due to ring particle collisions and the input of energy due to Keplerian shear. This process leads to the formation of overdense structures that are perfectly aligned with the direction of orbital motion. In Chapter 5, we present simulations of the formation of km-scale structure in the B-ring, and attempt to clarify the conditions necessary for the emergence of self-gravity wakes or viscous overstability structure. We find that the presence of each mechanism depends on the specific physical properties (density, surface properties) of the ring particles. By comparing with observational results, we are able to place constraints on the properties of the actual ring particles. This allows us to place some constraints on the mass of the B ring.

### 1.4.5 Outlook and Future Work

In Chapter 6, we conclude the thesis by summarizing the important findings of each of the granular-physics-related problems that we have studied. We also give a brief overview of other collaborative projects that are underway that extend and compliment the work presented here. Finally, we present perspectives for future work and detail the improvements in simulation software and data analysis necessary to build upon the results presented in this thesis.

## Chapter 2: Size Segregation on Asteroid Surfaces: Brazil-nut Effect

### 2.1 Chapter Preface

The work presented in this chapter was published in the Monthly Notices of the Royal Astronomical Society (MNRAS) as Maurel et al. (2017). The work was done jointly by Clara Maurel (a PhD student now at the Massachusetts Institute of Technology) and myself. Each of us gave a roughly equal amount of effort in performing the simulations, analyzing the results, and preparing the manuscript for publications. Clara’s efforts focused on performing simulations in Earth-gravity and conducting statistical analyses of these results. My contribution was updating the code to function properly for Periodic Boundary Conditions (PBC)—see discussion below—then performing simulations in low gravity. Furthermore, by performing post-simulation analysis on the output data, I was able to show that different mechanisms drove the Brazil-nut Effect (BNE) for different boundary conditions, and that these mechanisms depend on the local gravity. Roughly speaking, the first half of the chapter (pages 23–44), related to the procedures and generation of results in Earth gravity, was Clara’s work, while the latter half (pages 45–67), focusing on analysis and discussion of results, was my work.

In this chapter, we investigate numerically size segregation among regolith

grains, which is likely to occur after repeated shaking events induced by micro-shocks arising from micrometeorite impacts or other disturbances on asteroid surfaces. In particular, we are interested in the so-called Brazil-nut effect (BNE), i.e., the migration of a large intruder toward the top of a vertically shaken granular system. We go a step forward in simulating this segregation effect by implementing horizontal periodic boundary conditions (PBC) in the  $N$ -body code `pkdgrav`, with the aim of making the simulations more representative of the expected asteroid environment. Since previous simulations used walls as a boundary condition, which don't exist on asteroids. We study the influence of the PBC on the outcomes of a shaking simulation in Earth gravity and compare them to those obtained within a walled container. For both configurations, we also study the influence of static and rolling friction on the BNE. We observe the well-known convection mechanism that drives the BNE in the presence of walls. However, we find that a different mechanism, consisting of void filling, is responsible for the segregation of the “Brazil nut” with PBC, and we discuss its relevance in light of previous granular physics studies. By running similar simulations in  $10^{-4}g$ , we show that this void-filling mechanism remains relevant to explain the BNE with PBC in a low-gravity environment. However, depending on the gravity, the friction properties of particles influence the rise speed of an intruder differently. An increase in the rolling friction properties of the grains diminishes the void-filling mechanism in Earth gravity, while an increase enhances it in  $10^{-4}g$ . We speculate that this is likely due to a change in the granular flow timescales at different gravity regimes.

## 2.2 Background

Particle segregation is one of the processes that can play a critical role in the evolution of asteroid surface properties, and possibly internal ones (Murdoch et al., 2015). Main Belt collisional evolution models suggest that a majority of asteroids of size ranging from a few hundreds of meters to about 50 kilometers are of second generation at least, i.e., are born as a result of the collision between two parent bodies (Bottke et al., 2005, 2015). Numerical simulations of catastrophic disruption (Michel et al., 2001, 2015b) indicate that those second-generation bodies are generally gravitational aggregates, formed by reaccumulation of ejected fragments, and thus can be modeled as granular systems (Richardson et al., 2002). Moreover, the vast majority of their surfaces seem to be covered in regolith, another kind of granular medium, as suggested by thermal inertia measurements (Delbo' et al., 2007; Delbo et al., 2015)) and direct images (e.g., on Eros, Asphaug et al. 2001, and Itokawa, Miyamoto et al. 2007). The granular properties of regolith are still poorly understood, as well as the diversity of these properties among the asteroid population. For instance, the two near-Earth asteroids visited by spacecraft so far, i.e., the 17-km size Eros (NASA-Near-Shoemaker) and the 320-meter size Itokawa (JAXA-Hayabusa), possess thoroughly different regolith properties, despite their same S taxonomic type: a thick layer of fine grains was found on Eros, while a shallow layer of gravel-like grains was found on Itokawa (Yoshikawa et al., 2015). In addition to the asteroids' different dynamical and collisional histories, their different gravitational environments likely have a strong influence on the variety of their surface

properties. However, both Eros and Itokawa show big boulders on their surfaces (e.g., [Barnouin-Jha et al. 2008](#)) surrounded by smaller grains. This characteristic is particularly striking on Itokawa, whose gravity is so small that the common invocation of gravitational capture of ejecta after impact cratering can hardly explain the presence of large rocks at the surface. In fact, ejection speeds of excavated material are expected to exceed the escape speed of the asteroid (a few tens of cm/s). [Michel & Richardson \(2013\)](#) proposed that the boulders at the surface of Itokawa result from the asteroid's formation process: after the disruption of its parent body, Itokawa could have formed by gravitational re-accumulation of ejected fragments.

However, regolith segregation and more specifically the Brazil-nut effect or BNE ([Rosato et al., 1987](#)) may be another process responsible for the presence of big boulders at the surface of asteroids. The BNE consists of large particles rising up through a granular medium composed of smaller grains, when the latter is repeatedly shaken. On an actual asteroid, the occurrence of this effect could be the result of seismic shaking induced by thermal cracking ([Delbo et al., 2014](#)) or multiple micro-impacts experienced by the asteroid over its lifetime (e.g., [Cheng et al. 2002](#); [Richardson et al. 2004](#)). Seismic shaking, and the resulting motion of regolith material, was invoked to explain the paucity of small craters on Eros and Itokawa ([Richardson et al., 2004](#); [Michel et al., 2009](#)) as well as the formation of ponds on Eros ([Cheng et al., 2002](#)). In addition they may also cause particle segregation. This could explain the presence of big boulders at the surface, and also imply that an asteroid's interior could be composed of smaller particles than those observed at the surface, suggesting a variation of macroporosity with depth. Therefore, parti-

cle segregation and BNE might have important implications in the arrangement of asteroid surfaces and interiors.

Two issues arise with the BNE. First, the mechanism driving the BNE is still not fully established and doubts remain about its unicity (Kudrolli, 2004). In particular, granular convection is a process often invoked as the origin of granular segregation at the surface of asteroids (Miyamoto et al., 2007; Asphaug, 2007). However, granular convection is strongly dependent on the gravitational acceleration and it has been shown that a weak gravitational acceleration may reduce the efficiency of particle size segregation (Gray & Thornton, 2005; Murdoch et al., 2013). Moreover, recent numerical simulations and parabolic flight experiments show that the rising speed of a large intruder through a granular material decreases with the external gravity (Tancredi et al., 2012; Güttler et al., 2013; Matsumura et al., 2014). Therefore, asteroids with their low gravity should not be the most suitable place for such a process. However, as the typical lifetime of asteroids of similar or larger size than Itokawa is greater than tens of millions of years (e.g., Bottke et al. 2005), provided that the meteoroid flux is efficient enough to induce repeated shaking events, particle segregation may have time to occur despite the low-gravity conditions. The second issue is that the BNE is known to occur in a confined, walled environment (such as the one used by, e.g., Tancredi et al. 2012 and Matsumura et al. 2014), which does not seem to be the best representation of an asteroid interior or near-surface. A numerical study by Perera et al. (2016) showed that a rubble-pile asteroid, made up of a population of particles of two different sizes, will show size segregation for sufficiently high impact energies. Their study showed that size segregation can occur

on a global scale without the need of a confining wall; however, their simulations were limited to showing segregation of large 40-m and 80-m size particles. Thus, although these experimental and numerical studies greatly helped to improve our understanding of the size segregation process and its sensitivity to various parameters (e.g., gravity, friction coefficients), the conclusions need to be confirmed in an environment more consistent with the one expected on an actual asteroid surface.

The aim of this chapter is to accomplish a step towards this goal by numerically investigating the BNE in an unconfined environment, using periodic boundary conditions, or PBC. Particle size segregation is, in this case, not influenced by the confinement caused by walls of the container and the potential occurrence of the BNE will therefore only be due to the interaction among particles. If BNE occurs under such conditions, the possibility of an extrapolation to the asteroid environment will be strengthened. We investigate the differences in behavior of the large intruder when wall boundaries are either present or absent, and also specifically focus on the influence of the static and rolling friction properties of the grains. We also get closer to realistic asteroid environments by performing the same simulations in low gravity, such as those encountered on Itokawa-like asteroids. Understanding how a granular medium with a size distribution may segregate in an unconfined environment can allow us to better assess the porosity and grain distribution on asteroids.

Today, we only have direct access to global bulk densities through space missions (e.g., [Yeomans et al. 1997](#); [Fujiwara et al. 2006](#)), study of the Yarkovsky effect ([Chesley et al., 2003](#)) or binary asteroid observations ([Merline & Chapman, 2001](#)).

This new aspect of investigation may be of great value for indirectly estimating the density heterogeneity within asteroids. Considering the paucity of direct measurements, the community needs other means to derive information from indirect measurements, through, e.g., the modeling of different dynamical processes possibly contributing to the evolution of asteroids' internal structure. This chapter offers a contribution to this effort. In Section 5.3 we provide details on the various parameters investigated, with and without PBC. Results are presented and analyzed in Section 5.4, and are followed by complementary analysis, interpretation and discussion in Section 4.5. Conclusions and proposed future work are found in Section 2.6.

## 2.3 Methodology

### 2.3.1 `pkdgrav`: PBC

In our study, we make use of periodic boundary conditions (PBC). Doing so, we can study particle segregation for an ensemble of particles that are freely vibrating without a surrounding physical boundary. Periodic boundary conditions are imposed on a patch of particles by replicating the patch in the horizontal directions ( $x$ - $y$ ), perpendicular to the oscillating direction ( $z$ ). Each replicated patch contains ghost particles that match the relative positions of the original particles. Particles near the boundary edges may interact in collision with ghost particles. Figure 2.1 illustrates an initial set up with PBC.

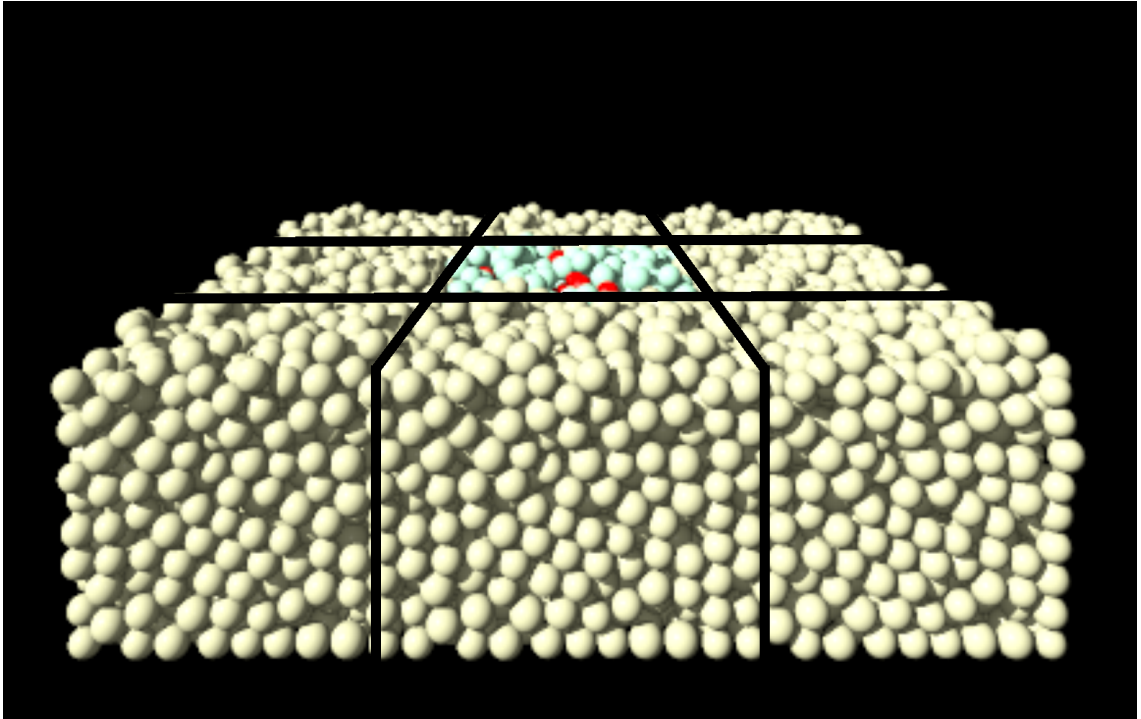


Figure 2.1: Initial set up for a periodic boundary simulation. Central pattern is surrounded by 8 replicas made of ghosts particles. Lines were added to help visualize the replicated patterns. The colors of the real particles are varied for better visualization.

### 2.3.2 Friction parameters

One aspect of this study is to analyze how material properties influence the outcomes of the simulations. Given the strong uncertainties concerning the granular properties of asteroids, we performed simulations using a broad spectrum of friction coefficients. Each grain in the system was simulated with the same set of coefficients. We made the choice to focus on materials of medium-to-high levels of static and rolling friction, starting in the range where the BNE is expected to occur with wall boundaries under Earth gravity, and pushing to levels where friction might impede this effect.

[Matsumura et al. \(2014\)](#) studied the influence of friction on the rise of the “Brazil nut” for static and rolling friction parameters, respectively  $\mu_s$  and  $\mu_r$ , between 0.0 and 0.9, using `pkdgrav` and cylindrical containers. Their results showed that certain values of friction parameters were more favorable to the BNE:  $\mu_s \gtrsim 0.5$  and  $\mu_r \lesssim 0.2$ . They obtained these thresholds with coefficients of restitution  $\epsilon_n = 0.5$ ,  $\epsilon_t = 0.5$  and for an amplitude and frequency of oscillation  $A = 1$  cm and  $\omega = 93.9$  rad s<sup>-1</sup>, respectively. We based the lower limit of the investigated range of friction on a set of parameters identified by [Matsumura et al. \(2014\)](#) as leading to the rise of a big intruder in an oscillating bed of small grains:  $\mu_s = 0.8$ ,  $\mu_r = 0.2$  and medium dissipation of the grains with  $\epsilon_n = 0.5$ ,  $\epsilon_t = 0.5$ . Note that this set may not necessarily reflect properties of a material existing on Earth. As an upper limit, we defined a gravel-like material ([Yu et al., 2014](#)), characterized by  $\mu_s = 1.3$ ,  $\mu_r = 2.0$ , and again  $\epsilon_n = 0.5$ ,  $\epsilon_t = 0.5$ . This very high friction aims

to represent the behavior of irregularly shaped grains that resist flow even though we are using spherical particles. If we were able to simulate true angular shapes, these coefficients would likely be smaller compared to their current values. We also implemented a “control” material, for which we did not expect to see the intruder rise. For this we used a set of parameters mimicking the behavior of glass beads, a low-friction material ( $\mu_s = 0.43$ ,  $\mu_r = 0.1$ ) with a very small amount of dissipation ( $\epsilon_n = 0.95$ ,  $\epsilon_t = 1.0$ ). This set of material parameters was calibrated against avalanche experiments by [Richardson et al. \(2012\)](#).

These three sets of material parameters were compared to the literature by carrying out angle-of-repose simulations. Grains of 0.5-cm radius were initially contained, at equilibrium, in a rectangular box. Then, by removing one side of the box, they were allowed to fall through an extended container, paved with a layer of similar grains glued to the floor (to create a rough surface). We recorded the evolution of the slope formed by the pile of particles and calculated the resulting slope angle, which converged to the value of the angle of repose once the equilibrium state was reached. [Figure 2.2](#) shows the equilibrium state for the gravel-like material and the corresponding angle of repose. The values of the angles of repose for the different materials are summarized in [Table 2.1](#). The angles obtained belong to the ranges that can be found in the literature:  $\phi(^{\circ}) \in [21,25]$  for glass beads (e.g., [Barabási et al. 1999](#)) and  $\phi(^{\circ}) \in [32,40]$  for gravel-like material (e.g., [Orlova 1962](#)).

We performed a series of simulations for equally distributed values of friction parameters ranging between moderate and the gravel-like values:  $\mu_s \in [0.8, 1.3]$  in steps of 0.1 and  $\mu_r \in [0.2, 2.0]$  in steps of 0.2, with  $\epsilon_n = 0.5$ ,  $\epsilon_t = 0.5$  throughout.

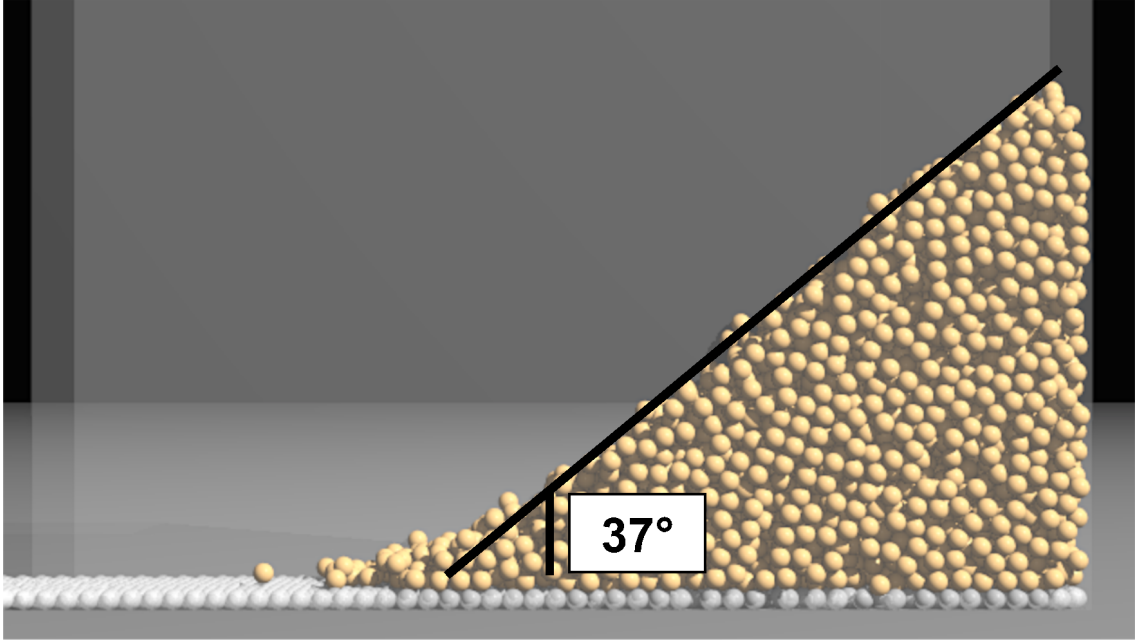


Figure 2.2: High-friction “gravel” material system at equilibrium after the release of the grains. Here the final achieved angle of repose is  $37^\circ$  (see Table 2.1).

Parameters	Glass beads	Moderate friction	Gravel-like
$\epsilon_n$	0.95	0.5	0.5
$\epsilon_t$	1.0	0.5	0.5
$\mu_s$	0.41	0.8	1.3
$\mu_r$	0.1	0.2	2.0
$\phi$ ( $^\circ$ )	19.5	27.5	37.0
Barabási et al. (1999)	[21,25]	-	-
Orlova (1962)	-	-	[32,40]

Table 2.1: Coefficients of restitution and friction of the simulated glass beads, and of the materials representing the lower and upper limits of the range of static and rolling friction investigated. These are compared to the ranges found in the literature.

Each of these simulations was repeated 10 times (3 times for the cases in a low-gravity environment—see Section 5.4 for details), with walls and PBC, each time starting with a new random initialization to ensure the independence of the simulations. In summary, we had a total of 60 simulations repeated 10 (or 3) times, for both walls and PBC cases, in addition to the control simulation with glass beads.

*Note* — The rolling friction model used for this study is the same as that in Yu et al. (2014) and Matsumura et al. (2014). The latest version of `pkdgrav` has an optional new rolling friction model that uses a rolling force spring (Zhang et al., 2016). This new model is particularly important to treat quasi-static problems. In our case, however, the BNE simulations are strongly dynamic and the conclusions should not suffer from a change in the rolling friction model. We tested this by conducting a limited number of runs comparing intruder rise speeds for the two models, using roughly equivalent material parameters and found no substantial differences. We refrain from using this model for the majority of our simulations as it adds to the computational cost of a simulation.

### 2.3.3 Simulation parameters and walls setup

In our simulations, two key parameters are the normal spring constant  $k_n$  (see Section 2.3.1) and the simulation timestep  $\delta t$ . The value of  $k_n$  was chosen so that the maximum overlap of particles was no more than 1% of the smallest particle radius for the entire simulation. The timestep was then chosen so that collisional loading and unloading of the spring takes at least 30 steps. This means the timestep

is always very small compared to the gravitational dynamical time of the system. In the present simulations, the acceleration of the bottom wall is several times the local gravity, and constrains the required timestep and normal spring constant necessary to properly resolve particle-particle and particle-wall collisions. The values of  $k_n$  and  $\delta t$  are given by:

$$k_n \approx m \left( \frac{v_{\max}}{x_{\max}} \right)^2 \quad ; \quad \delta t \approx \left( \frac{m}{k_n} \right)^{1/2}, \quad (2.1)$$

where  $m$  is the typical mass of the particles,  $v_{\max}$  is the maximum expected particle speed and  $x_{\max}$  is the maximum overlap when two particles collide, 1% of the smallest particle radius in this case (see [Schwartz et al. 2012](#)). The maximum 1% overlap criterion is sufficient to properly resolve collisions when the maximum speeds in the simulations are less than the sound speed of the simulated material. For our simulations, the maximum expected speeds are less than a third of the sound speed of the material. Therefore, by using a 1% maximum overlap criterion, we are able to resolve collisions correctly and in a computationally efficient manner.

The small bed particles in our simulations are spheres with a normal distribution of radii of mean  $r_p = 0.5$  cm, with a standard deviation 0.05 cm, and a cutoff at  $\pm 1$  standard deviation. The Brazil nut has a radius of  $r_{BN} = 1.5$  cm. These values were chosen for their convenience regarding computational time. Although BNE may involve meter-size boulders on actual asteroids, we expect the effect to scale to larger size, up to the limit where self-gravity becomes non-negligible. The density is  $\rho_P = 2700$  kg m<sup>-3</sup> for each particle, meaning the large intruder is 27 times more massive than a small particle in the granular bed. In order to estimate  $k_n$  and  $\delta t$ , we

used the mean bed-particle mass as the typical value for  $m$  and their mean size to evaluate  $x_{\max}$ . Also,  $v_{\max}$  is the speed of the oscillating wall (i.e.,  $v_{\max} = A\omega = 93.9$  cm s<sup>-1</sup>; see below). From this we derived the following values for  $k_n$  and  $\delta t$ :

$$k_n \approx 5 \times 10^5 \text{ kg s}^{-2} \quad ; \quad \delta t \approx 4 \times 10^{-6} \text{ s.} \quad (2.2)$$

With `pkdgrav`, particles are allowed to interact with each other as well as with walls. One of our main objectives is to compare walls cases and PBC cases. In order to make walls and PBC setups as similar as possible, every wall uses the same coefficients of restitution and friction as the grains. In every walls case, lateral walls form a parallelepiped open on the top of a  $10 \times 10$  cm base, which is high enough to prevent any escape of the particles once oscillations of the bottom plate start. The choice of a rectangular container is different from the one of [Matsumura et al. \(2014\)](#), who performed all their simulations with a cylindrical container. However, as PBC require rectangular boundaries, the walls cases have to be performed with a rectangular container to ensure a relevant comparison. In order to evaluate the influence of the container's geometry, we carried out pairs of simulations aiming to compare, under different conditions of friction, the outcomes of a simulation inside a cylinder and inside a parallelepiped. We found that in all cases, both geometries led to the same result (either no rise of the Brazil nut at all or full rise) within a comparable amount of time. Consequently, we assumed that for our purposes, the use of a parallelepiped container had no significant influence on the outcomes of the simulations compared to the use of a cylinder.

Finally, we set the oscillation of the bottom wall (and lateral walls if they

exist) to a frequency  $\omega = 93.9 \text{ rad s}^{-1}$  and an amplitude  $A = 1 \text{ cm}$ . These values match the fiducial choice of [Matsumura et al. \(2014\)](#) and represent a dimensionless acceleration of  $\Gamma = \frac{A\omega^2}{a_g} \approx 9$  for simulations under Earth gravity ( $a_g$  is the gravitational acceleration taken equal to  $1g$ ). This value of  $\Gamma$  will be kept the same throughout the study, even for simulations under low gravity, as another means of ensuring the validity of our comparisons.

### 2.3.4 Initialization process and main simulations

The initialization process was the same for the walls and PBC simulations. In order to avoid any bias due to a uniform placement of the grains, we generated randomly the particles inside an ellipsoidal volume large enough to avoid contacts between the grains. This volume was suspended above the parallelepiped container and particles were allowed to fall inside the container under Earth gravity. The Brazil nut was positioned a few millimeters above the floor of the container and small grains fell from a few tens of centimeters. This way, the large intruder was at the bottom of the system at the end of the filling phase. Once the particles were at equilibrium inside the container, we could either start walls cases or turn on the PBC and remove the lateral walls. The central patch of particles, in the latter case, was thus surrounded by a layer of replicas. The particles were then allowed to re-equilibrate before starting the main simulations.

As mentioned in Section [2.3.3](#), we gave the bed particles a small size distribution. This prevented artificial packing of the particles while filling the container or

during a main simulation. Fill-ups were performed separately for each configuration of  $(\mu_s, \mu_r)$ .

## 2.4 Results

In this section, we present the results of the various simulations described in the previous section. We first report on the results obtained under Earth gravity, by analyzing the differences in outcomes between PBC and walls cases, emphasizing on the influence on the BNE of static and rolling friction levels. In the second part, we present the results obtained in a low-gravity environment. Further analysis and discussions about the results are found in Section 4.5.

### 2.4.1 Earth-gravity cases: Walls versus PBC

The principal observation that can be made while running identical simulations performed with walls and PBC in Earth gravity is that final outcomes of both configurations are relatively similar. If the Brazil nut rises up with a walls case, it also rises in the associated PBC case, but if it does not rise in certain conditions, it will not rise with PBC either. For example, as already shown by [Matsumura et al. \(2014\)](#) with walls, the simulation involving glass beads resulted in no net ascension of the intruder, independent of the boundary conditions. Conversely, with grains of moderate friction ( $\mu_s = 0.8$  and  $\mu_r = 0.2$ ), the BNE occurred with walls as well as with PBC. Therefore, we confirm here that BNE does not necessarily require a confined environment to occur. However, although the system achieves a similar

final state in both cases, the mechanism driving the BNE is different. Here we present the relevant results, which are analyzed and contextualized in Section 4.5. As a means of comparison, we focus in this section on the rise speed of the Brazil nut. Doing so, we can include in the analysis the cases where the intruder starts rising but does not reach the top within the time of the simulation (arbitrarily fixed). The rise speed is measured in cm per oscillation (cm/osc). Recall from Section 2.3.2 that, to provide better statistics, we performed 10 times independently the 60 simulations derived from the chosen range of  $\mu_s$  values (from 0.8 to 1.3) and  $\mu_r$  values (from 0.2 to 2.0), each time with an independent initialization. Thus, for each value of  $\mu_s$ , we had  $10 \times 10 = 100$  cases (one for each value of  $\mu_r$ , for 10 simulations), and  $10 \times 6 = 60$  cases for each value of  $\mu_r$ . In total, we had 600 simulations for both walls and PBC configurations.

In this section, we are interested in comparing the global behavior of the walls cases to that of the PBC cases. To do so, we focus on the evolution of the rise speed with  $\mu_s$  for all values of  $\mu_r$  mixed up (i.e., independent of  $\mu_r$ ), and similarly, the evolution of the rise speed with  $\mu_r$ , for all the values of  $\mu_s$  mixed up. The question of the influence of  $\mu_r$  for a given  $\mu_s$  and vice versa will be addressed in Section 2.4.2. Figure 2.3 shows the least-squares regression lines obtained by fitting the 600 values of rise speed as a function of  $\mu_s$  (left panel) and  $\mu_r$  (right panel), for PBC and walls cases. For reasons of clarity, the 1200 individual scatterpoints are not plotted, but shaded areas show the 95% confidence intervals for the fits.

At first glance, the left panel of Fig. 2.3 suggests that, in both walls and PBC cases, the higher the value of  $\mu_s$ , the higher the mean rise speed of the Brazil

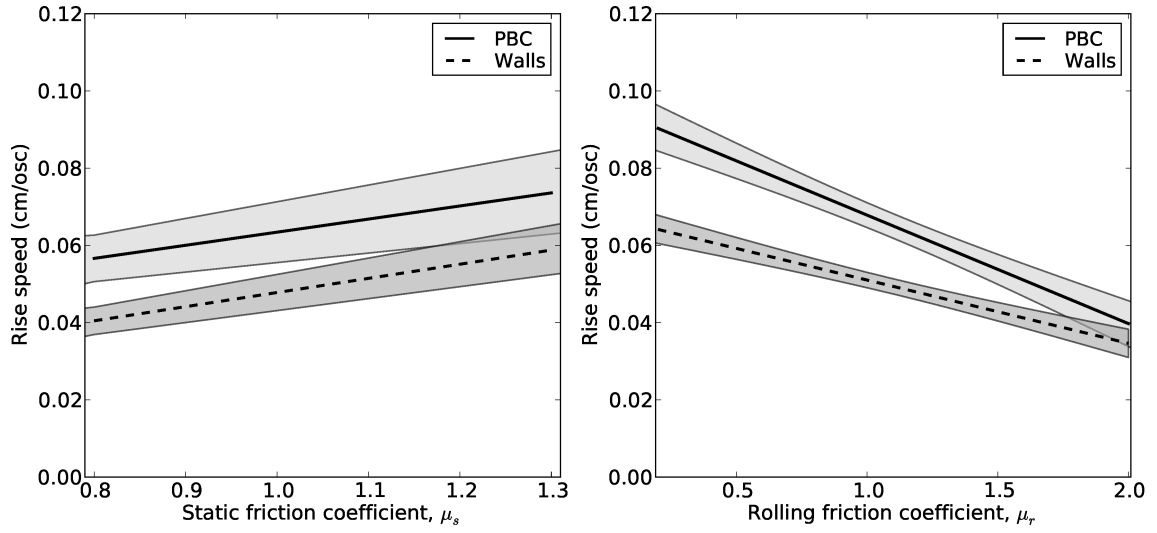


Figure 2.3: Least squares regression lines showing the evolution of the mean rise speed of the Brazil nut with  $\mu_s$  (left) and  $\mu_r$  (right), for walls cases (dashed line) and PBC cases (solid line). The lines are obtained by fitting the data of the series of 10 simulations, all values of  $\mu_r$  and  $\mu_s$  mixed up, respectively for left and right panel. Shaded areas show the 95% confidence intervals for the fits.

nut. In addition, this growing trend is similar in both cases. On the right panel of Fig. 2.3, the opposite trend appears. The mean rise speed of the intruder decreases with an increasing value of the rolling friction coefficient  $\mu_r$ . This time, a steeper slope is evident for PBC cases, meaning that with PBC, the rise of the intruder is more affected by the level of rolling friction than with walls. Finally, looking at both panels, the mean rise speed of the Brazil nut with PBC seems to be globally higher than with walls. This last observation would suggest that either the same mechanism is driving the BNE in both cases, but it is more efficient with PBC, or two different mechanisms are actually leading the BNE with walls and PBC. The difference in steepness of the slopes in the right panel of Fig. 2.3 would actually support the second hypothesis. However, before elaborating on this, we performed a series of statistical tests on the raw data to strengthen our forthcoming conclusions. For this, we used a variation of the Student  $t$ -test adapted to the study of the slope of regression lines. The objective was threefold: 1) ensure that the trends visible on Fig. 2.3 are not artifacts due to a linear regression made on dispersed data; 2) check whether the two slopes in the left panel of Fig. 2.3 are statistically equal and whether the two slopes of the right panel are significantly different; 3) assess whether the intercepts of the PBC and walls lines are statistically different from each other. We will first present the three tests and their results successively, before elaborating on the actual information we can get from these results.

Test 1) requires comparing the four slopes of linear regression in Fig. 2.3 to zero. If the corresponding test statistics are higher than a critical value, the null hypothesis is rejected, and the slopes would indeed have a significant steepness. To

compare a slope to zero, the following test statistic can be used:

$$t = \frac{|b|}{s_b}, \quad (2.3)$$

where  $b$  is the slope of the regression line considered, and  $s_b$  is a function of the standard deviation of the abscissa values ( $\mu_s$  or  $\mu_r$ ) and of the standard error of the estimate, which measures the accuracy of predictions made by the regression line. This  $t$ -value is then compared to a critical value  $t_{\text{crit}}$  found on Student's law table, which depends on the number of available data and on the desired confidence interval. Here, for  $600 \times 2$  available data and a 95% confidence interval, Student's law table gives  $t_{\text{crit}} \sim 1.96$ . The four calculated values of  $t$  are summarized in Table 2.2 (two for the evolution of the mean rise speed in walls and PBC cases with  $\mu_s$ , and the two others with  $\mu_r$ ). Each  $t$ -value of Table 2.2 being greater than  $t_{\text{crit}}$ , this test ensures that statistically, the mean rise speed of the Brazil nut is indeed affected by an increasing level of static and rolling friction, whether walls or PBC are turned on. However, Test 1) does not compare walls and PBC cases to each other.

Test 2) requires comparing the slopes of the PBC and walls regression lines to each other. The test statistic that can be used is given by

$$t = \frac{|b_w - b_{\text{pbc}}|}{\sqrt{s_{b_w}^2 + s_{b_{\text{pbc}}}^2}}. \quad (2.4)$$

Here,  $b_{w/\text{pbc}}$  is the slope of the corresponding regression line (walls or PBC), and  $s_{b_{w/\text{pbc}}}$  is the corresponding value of  $s_b$ . The critical value remains  $t_{\text{crit}} \sim 1.96$ , and

$t_{\text{crit}} = 1.96$				
t-value	Walls cases		PBC cases	
	RS = $f(\mu_s)$	RS = $f(\mu_r)$	RS = $f(\mu_s)$	RS = $f(\mu_r)$
	<u>6.04</u>	<u>9.39</u>	<u>3.34</u>	<u>9.92</u>

Table 2.2: Values of the test statistic obtained from Eq. 2.3. From left to right, the two first columns correspond to walls cases, and the other to PBC cases. The left column of each set of two (labeled “RS =  $f(\mu_s)$ ”) gives the  $t$ -value corresponding to the slope of the regression line shown in the left panel of Fig. 2.3. This  $t$ -value shows how significantly the walls and PBC cases are affected by an increase of the static friction level. The right column (labelled “RS =  $f(\mu_r)$ ”) gives the  $t$ -value corresponding to the lines in the right panel of Fig. 2.3, which characterize this time the effect of rolling friction level on the walls and PBC cases. The critical  $t$ -value for 95% confidence,  $t_{\text{crit}}$ , is given at the top of the table. The  $t$ -values are underlined if they are above  $t_{\text{crit}}$ .

$t_{\text{crit}} = 1.96$		
t-value	RS = $f(\mu_s)$	RS = $f(\mu_r)$
	0.17	<u>3.52</u>

Table 2.3: Values of the test statistic obtained from Eq. 2.4. These values show how significantly the evolution of the mean rise speed with respect to  $\mu_s$  (left column) and  $\mu_r$  (right column) differs from PBC to walls cases. The critical  $t$ -value for 95% confidence,  $t_{\text{crit}}$ , is given at the top of the Table. The  $t$ -values are underlined if they are above  $t_{\text{crit}}$ .

Table 2.3 shows the two  $t$ -values that compare the evolution of mean rise speed with  $\mu_s$  (left) and  $\mu_r$  (right) between walls and PBC cases. As expected from Fig. 2.3, this test ensures that statistically, the mean rise speed of the Brazil nut is similarly affected by the level of static friction (the slopes are statistically equal), whether walls of PBC are turned on ( $t_{\mu_s} < t_{\text{crit}}$ ). On the other hand, the effect of  $\mu_r$  on the mean rise speed of PBC cases is significantly different for walls and PBC cases.

To complete the set of statistical verifications, we want to assess whether the intercepts of the regression lines in each case (left and right panels of Fig. 2.3) are significantly different. For this, we subtract one regression line from the other

---


$$t_{\text{crit}} = 1.96$$

	RS = $f(\mu_s)$	RS = $f(\mu_r)$
Confidence interval	[-0.05 ; 0.02]	[-0.05 ; 0.002]

Table 2.4: For each panel of Fig. 2.3 (“RS =  $f(\mu_s)$ ” and “RS =  $f(\mu_r)$ ”) is given the confidence interval for the value of the intercept of the line corresponding to the walls-cases regression line subtracted from the PBC-cases regression line. The value zero belonging to both intervals, we cannot conclude that the intercepts of the walls and PBC cases are significantly different.

and find the confidence interval of the resulting predicted value when  $x = 0$  ( $y$ -intercept). If 0 belongs to the confidence interval, it means that the intercept of the line resulting from the subtraction can be zero, and therefore that the two intercepts cannot be significantly distinguished. Table 2.4 shows the confidence intervals for each panel of Fig. 2.3. Here, the visual interpretation was actually misleading, and we cannot say that the mean rise speeds of PBC cases are statistically higher than that of walls cases.

To summarize, Fig. 2.3 visually suggests that BNE could, under Earth gravity, be driven by a different mechanism with PBC compared to with walls. Our results suggest that whatever the mechanism is that drives the BNE for PBC, it has a similar dependence on the static friction as the mechanism driving the BNE with Walls. However, the BNE mechanism involved in PBC has a stronger dependence on the rolling friction than the BNE mechanism involved with Walls. The previous statistical tests, however, help us to qualify these first conclusions. So far, we know

that, for both PBC and walls cases, the mechanism driving the BNE is sensitive to the level of static friction (the mean rise speed increases with  $\mu_s$ ) and the level of rolling friction (the mean rise speed decreases with  $\mu_r$ ). Moreover, with PBC, the influence of  $\mu_r$  is significantly more important than with walls, whereas the influence of  $\mu_s$  is at first glance similar. Finally, we cannot conclude from the present analysis that the BNE mechanism with PBC is making the intruder rise faster than with walls, as the intercept of the regression lines on Fig. 2.3 are actually not significantly different.

At this point, further analysis is needed to discriminate the mechanisms driving BNE with PBC and walls, provided that they are different. For this, we no longer focus on the mean rise speed, but on the influence of the static and rolling friction at given values of  $\mu_r$  and  $\mu_s$  respectively.

#### 2.4.2 Earth-gravity cases: static and rolling friction

Figure 2.4 shows the regression lines obtained by fitting the data of the series of 10 simulations for PBC cases (top) and walls cases (bottom). However, unlike Fig. 2.3 where all values of friction parameters are mixed up, each line represents a certain level of rolling friction (left panels) and static friction (right panels). For clarity, the 95% confidence intervals are omitted from these plots. For PBC cases, these intervals are globally  $\pm 0.02$  for the top left panel and  $\pm 0.01$  cm/osc for the top right panel. For Walls cases on bottom left panel, we find a maximum of  $\pm 0.04$  cm/osc for confidence interval of the  $\mu_r = 0.2$  fitted line, while for all other lines we

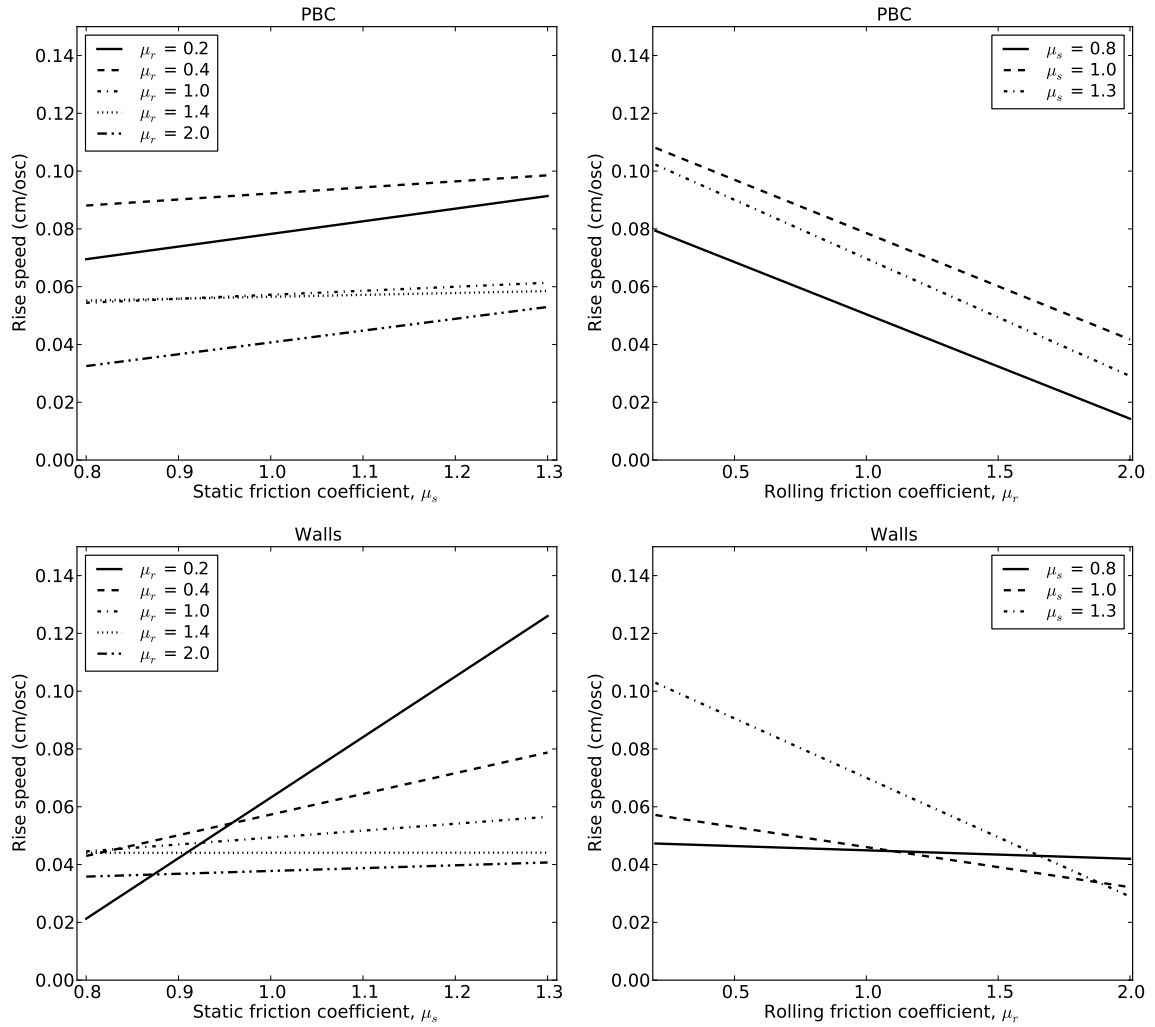


Figure 2.4: Regression lines obtained by fitting the data of the series of 10 simulations for PBC cases (top) and walls cases (bottom). Left panels represent the evolution of the rise speed with  $\mu_s$  for different values of  $\mu_r$ , while right panels show the evolution with  $\mu_r$  for different values of  $\mu_s$ .

have  $\pm 0.01$  cm/osc. On bottom right panel, we also find a larger confidence interval for the  $\mu_s = 1.3$  curve ( $\pm 0.02$  cm/osc) and  $\pm 0.01$  cm/osc otherwise. Interestingly, Figure 2.4 seems to imply an important difference in behavior of the Brazil nut between walls and PBC cases. Even in the worst case scenarios, the larger intervals found for Walls cases do not change the visible trends.

Let us first focus on walls cases (bottom panels). On the left panel, we see that the lower the value of  $\mu_r$ , the more important the influence of  $\mu_s$  on the rise speed of the intruder. For example, for  $\mu_r = 0.2$  (solid line), the least-squares linear regression shows that the rise speed can increase from approximately 0.02 cm/osc at  $\mu_s = 0.8$  to more than 0.12 cm/osc at  $\mu_s = 1.3$ , while for  $\mu_r = 2.0$  (dash-dot-dot line), the influence of  $\mu_s$  on the rise speed seems to be insignificant. Moreover, this trend is strongly correlated with the values of  $\mu_r$ . The influence of  $\mu_s$  decreases rapidly with increasing  $\mu_r$ , and then stagnates at almost zero. A clear trend is also visible in the bottom-right panel of Fig. 2.4. At low levels of static friction, the influence of  $\mu_r$  on the rise speed is hardly visible (solid line), however at high  $\mu_s$  (dash-dot line), the rise speed can decrease by approximately a factor of 10 between  $\mu_r = 0.2$  and  $\mu_r = 2.0$ , again with a correlation between the values of  $\mu_s$  and the importance of its influence on the rise speed. These observations were validated by the same statistical test as Test 2), in which we compared the slopes two by two. The results of this test were in agreement with the trend visible in Fig. 2.4.

On the other hand, the influence of static and rolling friction levels in PBC cases is not so clearly brought out by the top panels of Fig. 2.4. Neither the influence of  $\mu_s$  on the rise speed of the intruder nor the influence of  $\mu_r$  seem to be

correlated with an increase or decrease of  $\mu_r$  and  $\mu_s$ , respectively. In fact, the slope of each regression line in the left and right panels looks relatively similar. This was confirmed by performing Test 2) again: no clear trend and no significant difference between a majority of slopes was found. In addition, the values of the intercepts of the regression lines are also not clearly correlated to an increase of  $\mu_r$  or  $\mu_s$ . Figure 2.4 might suggest the existence of an efficiency threshold for values of  $\mu_r$  and  $\mu_s$  respectively around 0.4 and 1.0 (which give the highest intercept), but more data would be required to confirm or refute this hypothesis.

In light of the above-mentioned results, we claim that a different mechanism is driving the BNE with walls compared to with PBC. In fact, with walls, the efficiency of the process (characterized here by the rise speed of the Brazil nut) is highly dependent on the values of  $\mu_r$  and  $\mu_s$ : at low rolling friction levels, the process is catalyzed by an increasing level of static friction. However, a higher level of rolling friction completely inhibits this effect. In contrast, at low levels of static friction, the influence of  $\mu_r$  on the rising process is almost non-existent, whereas for a higher  $\mu_s$ , an increase of the rolling friction level impacts drastically and negatively the rise speed of the intruder. It is well known that, under certain conditions (level of friction, frequency and amplitude of the oscillations), friction between particles and walls engenders a convective motion (e.g., [Knight et al. 1993](#)), with particles rising through the center of the container and sinking along the walls. The results presented above seem to adequately characterize such a mechanism. The convective motion needs a certain level of static friction between the walls and the small grains to take place. As this level gets higher, the convection rolls form more and more

easily (very likely until a certain limit, apparently not reached in our simulations). However, all this depends on the level of rolling friction. If particles are hardly able to roll on each other, the whole inward stream (inside the layer of particles that are in contact with the walls) is inhibited and the intruder rises more slowly.

With periodic boundary conditions, the very different behavior of the Brazil nut for the same static and rolling friction conditions strongly suggests that BNE is driven by a mechanism different from convection. This mechanism is marginally affected by the level of static friction but is, however, more dependent on the level of rolling friction. In addition, the top panels of Fig. 2.4 show a more stochastic behavior of the rise speed than for walls cases, for which the correlation between rise speed,  $\mu_s$  and  $\mu_r$  is demonstrated. To further strengthen the suspicion that convection is not the leading mechanism for BNE when PBC are turned on, we analyzed the flow of particles for several simulations, with walls and PBC, as illustrated in Fig. 2.5. This figure was created by considering a 5-particle-wide cross-section of the center of the container (the selection was done along the  $y$ -direction). A grid consisting of cells that are 1 particle wide is superimposed on the  $x$ - $z$  plane. For every cell, the average displacement of particles from that cell to adjacent cells is tracked and plotted. In order to properly visualize the flow of particles, it is necessary to isolate the relative displacement of a particle with respect to other particles from the overall shaking motion of the entire medium. This is accomplished by only considering particle positions at the same phase of an oscillation cycle. We chose the zero phase of the oscillation, where the bottom plate has zero displacement and is moving in the positive  $z$ -direction. Figure 2.5 shows a snapshot of this average motion of par-

ticles. The right panel, representing a walls case, clearly shows a convective motion of particles, as a thin particle-wide layer is forced downwards along the walls. This forces the center of the bed and the Brazil nut to move upwards. This pattern of granular convection is apparent throughout all walls simulations. The left panel does not show a similar convective motion for the PBC cases. Rather, we find that most PBC cases show more-randomized and less-uniform motion. There are some cases where the convective pattern visible on the right panel is seen intermittently in PBC cases; however, it only lasts for a few forcing cycles before it disappears. Hence, due to the absence of boundaries, convection cycles do not appear strongly when PBC are turned on, and despite that, we do see the Brazil nut rising. A further analysis of the leading mechanism for BNE in the absence of confining walls is proposed in Section 4.5.

### 2.4.3 Low-Gravity Cases

A key objective was to see how our findings might extend to a realistic asteroid gravity environment. For this we performed a suite of simulations with a local gravity set to  $10^{-4}$  times Earth gravity ( $10^{-4}g$ ), which is equivalent to the surface gravity on an Itokawa-sized body (Michikami et al., 2008). We re-initialized the grains in the low-gravity environment and allowed them to settle as explained in Section 2.3.4. This was again done for walls and PBC cases. To accurately compare these low-gravity simulations to those done in  $1g$ , we modified the shaking frequency of the granular bed such that  $\Gamma$  remains the same ( $\Gamma \approx 9$ ; see end of Section 2.3.3).

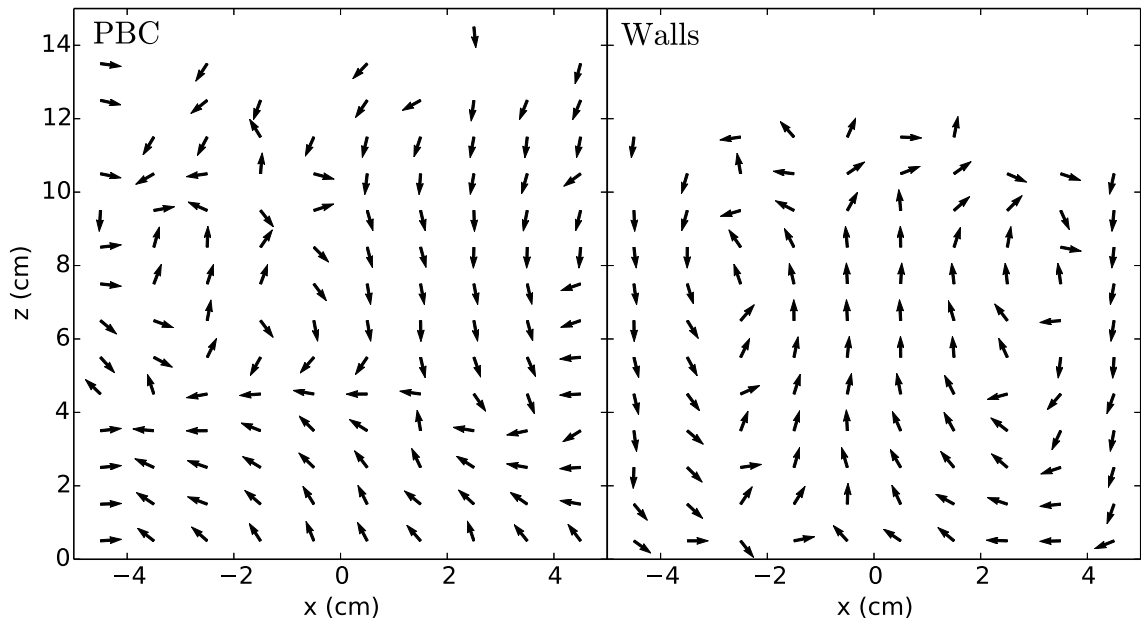


Figure 2.5: By tracking the change in particle positions over a single forcing period, we can visualize the convective motion of grains in simulations with wall boundaries (**right**) and the lack of convective motion in simulations with periodic boundaries (**left**). Both of these cases are for grains with friction parameters  $\mu_s = 0.9$  and  $\mu_r = 1.4$  (relatively high friction).

As a consequence, we first adopted a shaking frequency of  $0.939 \text{ rad s}^{-1}$ , while keeping the amplitude of the oscillation at 1 cm. This allowed us to use a timestep of  $\delta t \approx 3.7 \times 10^{-4} \text{ s}$  for these low-gravity simulations. We maintained a maximum possible fractional overlap of  $\sim 1\%$  by adjusting the value of  $k_n$  to  $\approx 42 \text{ kg s}^{-2}$ . The value of  $k_t$  was then  $\frac{2}{7}k_n \approx 12 \text{ kg s}^{-2}$ . This adjustment in the values of the spring constants is done for the sake of computational efficiency. If we were to maintain the same value of  $k_n$  as that used in the Earth-gravity simulations, the total time taken to complete each of the low-gravity simulations would increase by 2 orders of magnitude.

In order to ensure that this change in the value of  $k_n$  does not have a considerable impact on the outcome of our simulations, we ran a suite of simulations in a local gravity of  $10^{-2}g$ , where the value of  $\Gamma$  is again kept constant. Half of the simulations were done with a  $k_n$  and  $k_t$  that is the same as that used in the  $1g$  cases, and the other half were done with a  $k_n$  and  $k_t$  chosen to maintain a maximum possible overlap of  $1\%$  (based on a vibrating bed with an oscillation frequency of  $9.39 \text{ rad s}^{-1}$  and an oscillation amplitude of 1 cm). The local gravity of  $10^{-2}g$  was chosen with consideration for time constraints, since the slower simulations (those with spring constants similar to the  $1g$  cases) were only 1 order of magnitude slower than simulations with spring constants chosen to maintain  $1\%$  overlaps. We performed simulations with wall boundaries and chose three different values of  $\mu_s$  (0.8, 1.0, 1.2) and five different values of  $\mu_r$  (0.2, 0.6, 1.0, 1.4, 1.8). This small suite of simulations allows us to efficiently determine the magnitude of  $k_n$ 's influence in the rest of our simulations. The results of this test are shown in Fig. 2.6. Here we show

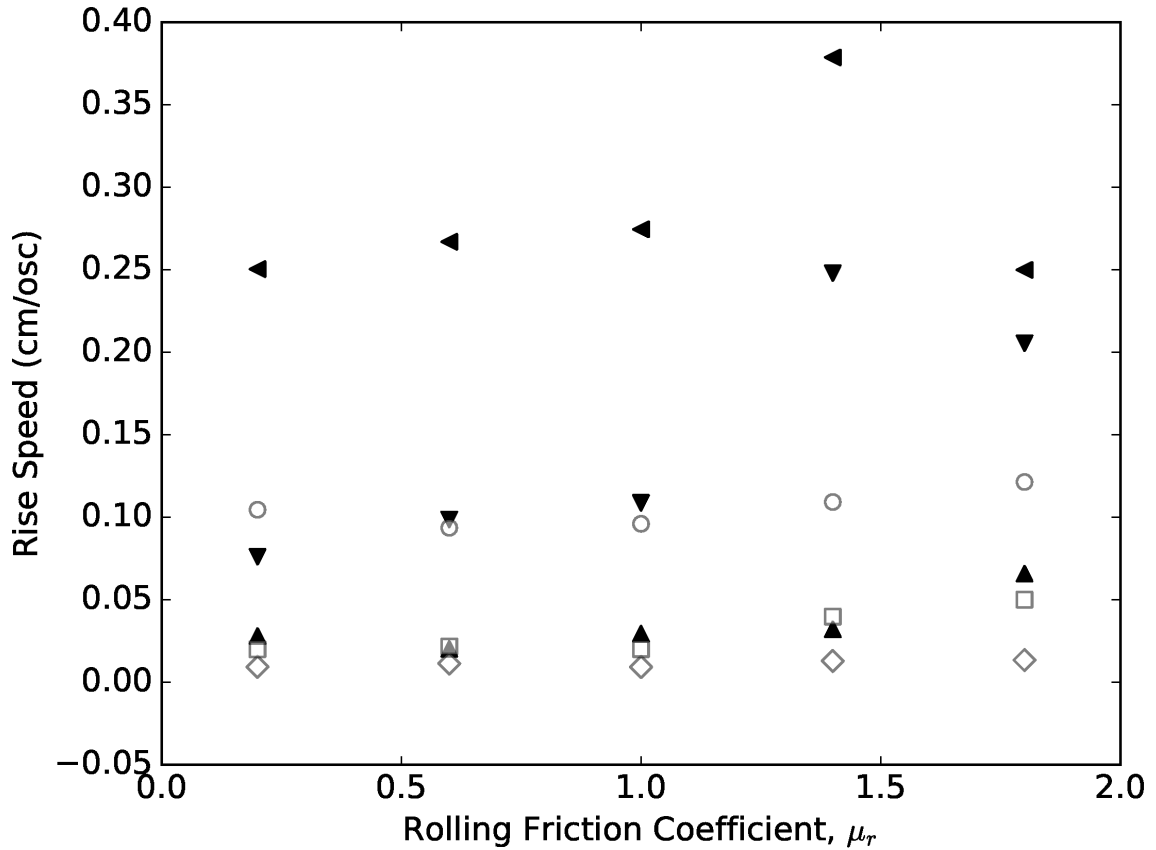


Figure 2.6: Rise speeds of the Brazil nut for simulations with a local gravity of  $10^{-2}g$ . The open symbols represent simulations where the particle collisions are resolved with spring constants similar to those in the  $1g$  simulations, with  $\mu_s = 0.8, 1.0,$  and  $1.2$  represented by diamonds, squares, and circles, respectively. The spring constants and the time-step used in these simulations are very conservative values. The filled triangles represent simulations where the spring constants are chosen based on maintaining a maximum possible fractional overlap of 1%, with  $\mu_s = 0.8, 1.0,$  and  $1.2$  represented by up-, down-, and left-facing filled triangles, respectively. The time-step varies by 1 order of magnitude between these two cases (with the filled symbols having a greater time-step).

the variation in the time taken for the intruder to rise to the top of the granular bed. We find that for a wide range in  $\mu_r$ , the rise speeds for various  $\mu_s$  have similar magnitudes and variances for the two spring constant cases. For both cases, we find that the “brazil” nut rises with fairly similar speeds, the cases with a smaller  $k_n$  and larger time-step (filled triangles) bracketing the cases with a larger  $k_n$  and smaller time-step (open symbols). We conclude that, while there is some possible effect in the change of the particle spring constants, this effect is quite small. Furthermore, we find that both cases lead to similar trends across friction parameters, e.g., under  $10^{-2} g$ , the rise-speed increases as  $\mu_s$  increases, independently of  $\mu_r$ . Therefore, using a spring constant that allows for a faster computational time, while maintaining a small maximum fractional overlap, is acceptable for the current simulation setup.

For the cases with a local gravity  $10^{-4}g$ , the range of considered friction levels was similar to that described in Section 2.3.2:  $\mu_s$  ranged from 0.8 to 1.3, and  $\mu_r$  from 0.2 to 2.0. Again, we attempted to minimize any stochasticity that might arise from sample preparation by performing three separate simulations (with separate initializations) for each  $\mu_s$  and  $\mu_r$  pair. In total we performed 360 simulations in the low-gravity regime (3 initializations, 2 boundary conditions, and 60 unique friction pairs).

Overall, for a shaking amplitude of 1 cm and both PBC and walls scenarios, we were still able to observe the BNE occurring in almost all the simulations. Every walls case showed the intruder rising to the top of the granular bed in the time of the simulation, whereas for PBC simulations, it occurred in approximately 84% of the cases (152 out of 180). The PBC cases that did not lead to a complete rise

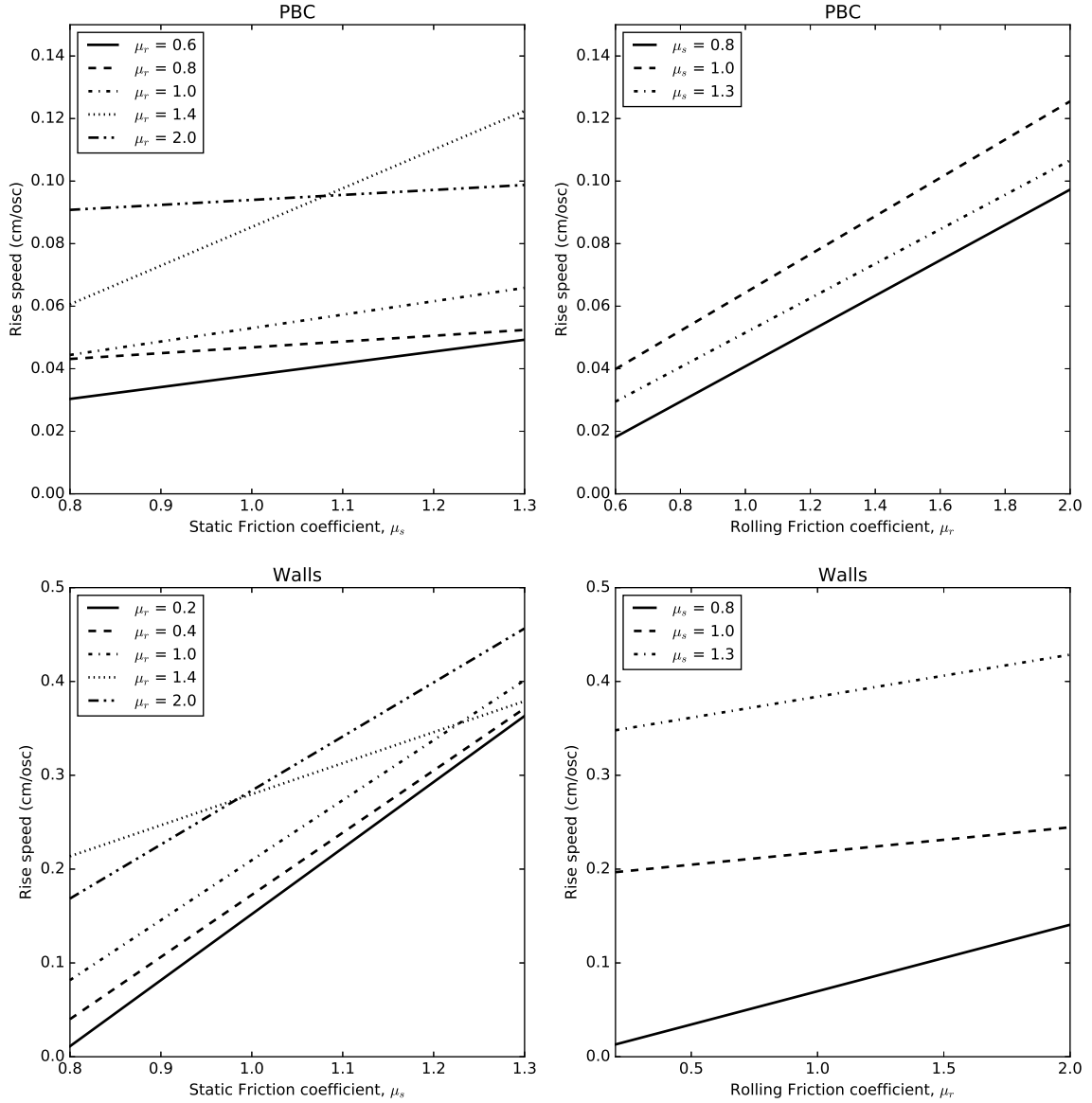


Figure 2.7: Rise speeds of the Brazil nut for simulations with a local gravity of  $10^{-4}g$ . The panels show lines that represent the linear trend of the rise speed with  $\mu_s$  for different values of  $\mu_r$  (left) and vice versa (right) with data extracted from three independent suites of simulations. The top panels show the results for cases with PBC, while the bottom panels show the results for walls cases.

tended to be cases with low values of the rolling friction parameters ( $\mu_r < 0.6$ ). In addition, these low-friction cases that did not result in a BNE tended to have the intruder begin to rise, but eventually stall at a system height lower than the barycenter of the system. These cases were omitted from subsequent analysis of rise speeds. Figure 2.7 shows the average rise speeds for PBC (top panels) and walls (bottom panels) cases as a function of  $\mu_s$  (left panels) and  $\mu_r$  (right panels). The curves represent linear fits of 3 independent simulations (3 different initializations of the granular bed). Like previous studies (Tancredi et al., 2012; Güttler et al., 2013; Matsumura et al., 2014), we find that, at moderate friction values, the rise speeds in a lower-gravity environment are comparable to those under Earth gravity. Here, we also show that this result still holds even when PBC are used. However, unlike these previous studies, we have performed an exploration of the friction parameter (a proxy for material property) phase-space in low gravity. This has resulted in some surprising outcomes.

For the PBC cases, we find that the magnitude of rise speeds in  $10^{-4}g$  are similar to the  $1g$  cases. Furthermore, similar to Earth gravity, we find that both the walls and PBC cases show a positive correlation with  $\mu_s$  (see left panels of Fig. 2.7). However, the walls cases seem to have a stronger correlation with  $\mu_s$  than the PBC cases. This likely points to a difference in the mechanism driving the BNE in each case, which is discussed further in Section 4.5. Furthermore, contrary to the Earth-gravity cases, we find that the rise speed in both PBC and walls cases is positively correlated with rolling friction,  $\mu_r$  (compare right panels of Figure 2.4 to Figure 2.7). This positive correlation appears to be stronger for the PBC cases than the walls

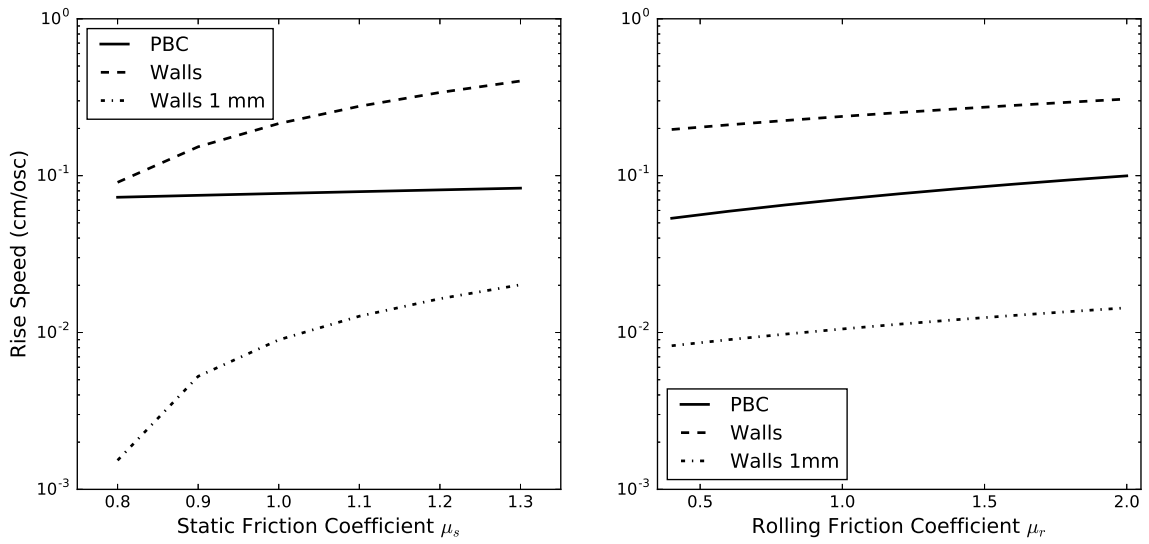


Figure 2.8: Average rise speeds of the Brazil nut for all simulations with a local gravity of  $10^{-4}g$ . The left and right panels show the rise speed as a function of  $\mu_s$  and  $\mu_r$ , respectively. Mean rise speeds are shown for simulations with an oscillation amplitude of 1 cm with PBC (solid line) and walls (dashed line). Oscillation amplitudes of 1 mm are also shown for walls cases (dot-dashed).

cases. For these PBC cases, we speculate that, in a low-gravity environment, the grains are lofted over a much longer period than under Earth gravity. This larger lofting period may give the grains more time to reconfigure, allowing for the entire system to re-settle with more voids (i.e., a smaller filling factor), as particles with a larger rolling friction can more easily maintain larger void spaces (in the other extreme, frictionless particles are more easily compacted into tighter spaces). As we will discuss in Section 4.5, larger void spaces in a granular system are important for the BNE to occur in a PBC system.

Previous studies (e.g., [Matsumura et al. 2014](#)) showed that the rise speed is generally constant across gravitational regimes (when scaling for the number of oscillations). In an absolute sense, [Matsumura et al. \(2014\)](#) showed that for a constant  $\Gamma$ , the rise speed of a system scales with the square root of the gravity of the system. In this study, we find that for low friction values, the magnitude of the rise speeds is consistent with this result, and that across 4 orders of magnitude in gravity, a variation of exactly 2 orders of magnitude in the oscillation frequency results in rise speeds that are within an order of magnitude of each other (in terms of cm/osc). Moreover, again at low friction values, comparable to those used in [Matsumura et al. \(2014\)](#), the rise speeds for the walls cases are very similar to that found in their  $10^{-4}g$  case. However, this picture becomes challenged when varying the friction parameters toward higher values.

In  $1g$  walls cases, we found that increasing  $\mu_s$  from 0.8 to 1.3 leads to a factor of  $\sim 6$  increase in the rise speed (for low  $\mu_r$ ). In the  $10^{-4}g$  cases, a comparable variation in  $\mu_s$  leads to an increase in the rise speed by a factor of  $\sim 20$ . For highly

frictional particles, the efficiency of granular convection engendered by the presence of walls is enhanced in low-gravity. We speculate that this may be due to differences in the packing of the granular bed (see Section 2.3.4) in low gravity. With a smaller overburden pressure on the grains at the bottom of the bed due to gravity, the upward ratcheting effect of granular convection may proceed much faster. While we can only speculate on an enhancement mechanism at this point, it is interesting to note that the data clearly show that the behavior of the grains differs in a low-gravity environment. By varying the material properties of the grain, we can begin to probe the limits of possible behavior of a granular system in micro-gravity.

To further mimic an actual asteroid environment, we deemed it necessary to test the effect of varying the frequency and amplitude of the oscillation to levels that might correspond to seismic shaking on a real asteroid. Several authors (e.g., [Cheng et al. 2002](#) and references therein) claim that the seismic shaking that occurs on an asteroid may have frequencies of the order of a few Hertz for millimeter-size amplitudes. In our case, the amplitude of the oscillation is 1 cm, which may still be an upper limit corresponding to more extreme shaking situations, but may not be representative of the vibrations induced by micro-meteorite impacts. [Garcia et al. \(2015\)](#) even find seismic wave amplitudes of the order of a few microns. Taking this information into account, we tested the effect of a smaller amplitude (always keeping the same value of  $\Gamma$ ) and ran simulations with an amplitude of 1 mm and an oscillation frequency of  $2.96 \text{ rad s}^{-1}$ . This was done for a unique initialization of the granular bed. The 1 mm value was preferred to a smaller one, because a lower amplitude would have certainly resulted in poor results, as it would have represented

less than  $1/10^{\text{th}}$  of a grain diameter.

Our initial expectation was that none or very few of the low-amplitude cases would actually exhibit the BNE, as previous studies (Matsumura et al., 2014) underlined the sensitivity of the BNE to the amplitude and frequency of the oscillation. According to their study, even amplitudes of half the grain size could lead to the disappearance of the BNE, even at high oscillation frequencies. For these smaller-amplitude cases, approximately 60% of the walls cases resulted in a full rise of the intruder, while only 6% resulted in a BNE for PBC. Both boundary conditions showed a strong dependence of BNE occurrence on friction properties. For the Wall cases, only cases with  $\mu_s > 0.9$  exhibited the BNE. For PBC, the few cases (5 in total) that did exhibit BNE had high static and rolling friction ( $\mu_s > 1.0$  and  $\mu_r > 1.6$ ). In Fig. 2.8 we show the average rise speeds as a function of  $\mu_s$  (left) and  $\mu_r$  (right), for the three different types of simulation in  $10^{-4}g$ : PBC cases with 1-cm amplitude (solid line), walls cases with 1-cm amplitude (dashed line) and walls cases at 1-mm amplitude (dot-dashed line). Due to a lack of rising Brazil nut obtained with some PBC cases with 1-mm amplitude cases, the corresponding average rise speeds were not included. We found that the number of oscillations required for the intruder to rise to the top is much greater for the 1-mm amplitude than for the 1-cm amplitude cases (about an order of magnitude greater). This was expected, as the particle displacement at each oscillation is much smaller. While there is no strong correlation of the average rise speeds with  $\mu_r$ , there is a rapid increase in the rise time with  $\mu_s$  for cases that exhibit the BNE. This is similar to the effect seen for the 1-cm amplitude cases.

## 2.5 Discussion

### 2.5.1 Driving mechanisms

In light of the results presented in Section 5.4, we investigate the mechanisms that might be responsible for generating the BNE in a medium that is not confined by lateral walls. To analyze the differences in the way the BNE is driven, we consider the evolution of the height of the Brazil nut for both PBC and walls cases, for the same range of friction parameters as before ( $\mu_s = 0.8$  to 1.3 in increments of 0.1 and  $\mu_r = 0.2$  to 2.0 in increments of 0.2).

The evolution in time of the height of the Brazil nut (solid curve) is plotted in Fig. 2.9, for one set of friction parameters ( $\mu_s = 0.8$  and  $\mu_r = 0.4$ ). We compare this evolution to the changes in the standard deviation of the entire bed's height (dotted curve). This latter parameter shows oscillations driven by the periodic motion of the bottom plate. More interestingly, large spikes in the standard deviation indicate an event where the system significantly dilates, creating void spaces in the medium. If we compare the top panel of Fig. 2.9 (PBC case) with the bottom panel (walls case), we can see that the BNE takes place in both cases. However, while the walls case shows a gradual increase in the height of the Brazil nut, the PBC case shows a more sporadic growth with some isolated jumps in the Brazil nut's height that are correlated with spikes in the standard deviation of the bed's height.

The difference in the evolution of the height of the Brazil nut in the two cases visible here is evident in most of the simulations. It suggests a systematic

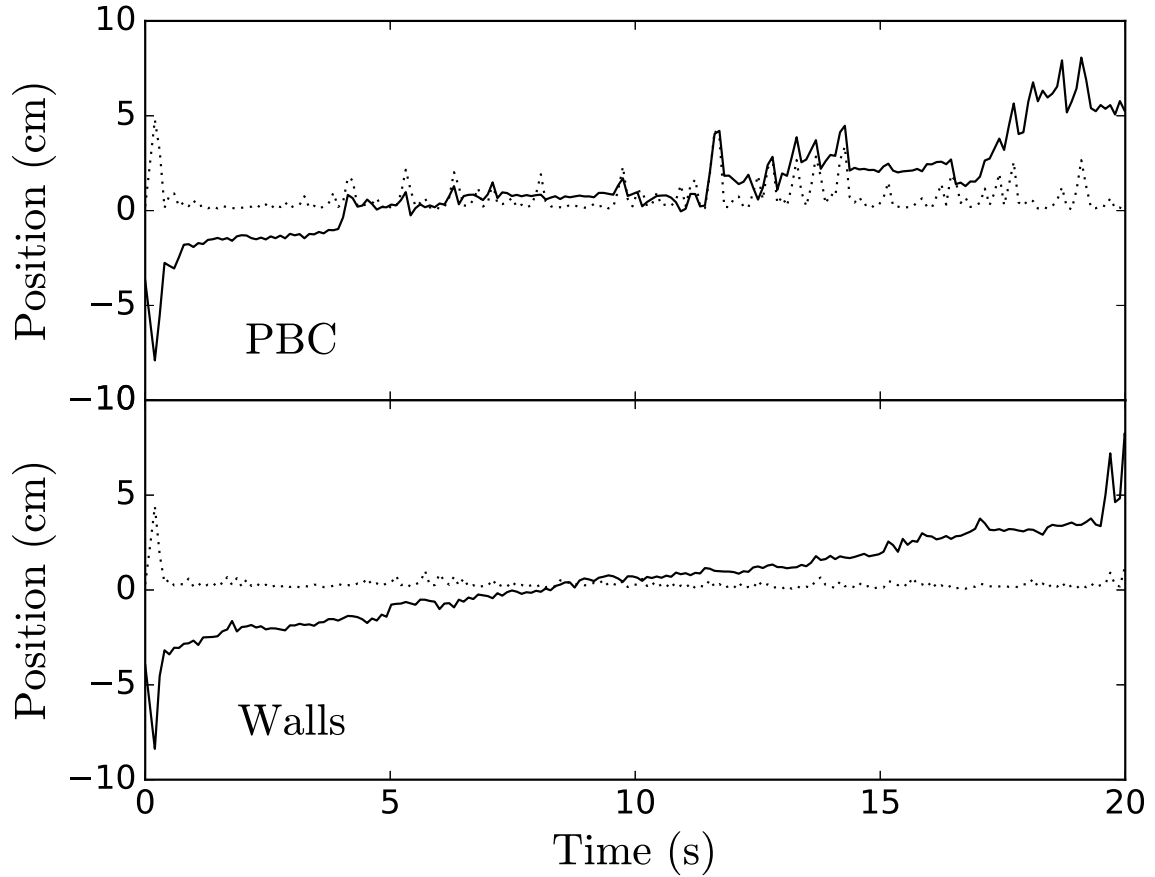


Figure 2.9: The height evolution of the Brazil nut (solid curve) differs for the PBC case (top) compared to the walls case (bottom). The dotted line represents the standard deviation in the height of the grains in the system. For PBC cases, the Brazil nut experiences jumps in its height, which are directly associated with the spikes in the standard deviation of grain heights. These spikes in the standard deviation represent expansions in the granular medium and the creation of voids. These two cases are for systems where the particles have friction parameters of  $\mu_s = 0.8$  and  $\mu_r = 0.4$ .

difference in the mechanism driving the BNE depending on the presence of walls, that was hinted at in the previous section (e.g., see Section 2.4.1). For the walls cases, the steady increase in the height of the BNE suggests that a classical convection mechanism takes place, as shown by previous authors (e.g., Knight et al. 1993). The convection mechanism is driven by particle-wall interactions which force a downward stream of particles along the walls, while interior particles are driven upwards. The size of this downward stream is limited by the size of the small grains, therefore the Brazil nut is not able to entrain itself into the downward flow and remains at the top (see right panel of Fig. 2.5 for an example of this downward stream). For the PBC cases, the sporadic height evolution of the Brazil nut might suggest a possible random walk of the particle to the top. However, comparing the rise speeds of the PBC cases to the walls cases in  $1g$ , we find that they rise at similar speeds (see Fig. 2.3). This does not support the idea of a random walk, which would likely result in longer rise speeds than that found in convection-driven walls cases. Since large “jumps” in the height of the Brazil nut are correlated with spikes in the standard deviation of the grains’ height, we suggest that with PBC a void-filling mechanism (Pöschel & Herrmann, 1995) drives the BNE. When a vibration lofts the material such that void space is created underneath the Brazil nut, the surrounding particles have a larger probability of filling the void space than the Brazil nut due to their smaller size. This geometric effect is able to drive the BNE, as subsequent vibration-driven lofting events further cause small particles to lodge themselves underneath the Brazil nut. In order to show that this mechanism is indeed responsible for causing the BNE in PBC cases, we analyze the standard deviation of the grains

height for all simulations.

For each simulation where a full BNE cycle occurs (a Brazil nut is able to move to the top and never sinks), we use a conventional peak-finding algorithm to pick out each spike in the standard deviation of the bed’s height and measure the corresponding change in the height of the Brazil nut due to this void-filling event,  $\Delta z_{vf}$ . In each panel of Fig. 2.10, we show the sum of these changes in height due to void-filling events,  $\Sigma\Delta z_{vf}$ , normalized by the bed depth  $h_{total}$  (each panel represents a unique initialization of the granular bed). PBC cases are represented on the left of each panel and walls cases on the right. We see that the PBC cases have systematically higher values of  $\Sigma\Delta z_{vf}$ , indicating that the “jumps” of the entire bed are much more significant and frequent than with walls. This supports our claim that the BNE, under Earth gravity, is mostly driven by void-filling events with PBC, while with walls this mechanism has only some slight contribution. Since the outcome of each simulation can be highly influenced by the starting conditions, we measure the  $\Delta z_{vf}$  in each simulation for four different initializations to show that the difference between the two cases persists regardless of initial conditions (Fig. 2.10 top-right, bottom-left and -right panels). The difference in the mean of  $\Sigma\Delta z_{vf}$  for the two populations (represented on the plot by a light dot-dashed line) is shown in the top right corner of each panel.

In the top panels of Fig. 2.11, we compare the mean of the standard deviation spikes ( $\bar{\sigma}_{z,vf}$ ), normalized by the grain radius, for each simulation (one initialization). This figure shows that void-filling events in PBC cases are driven by large fluctuations in the system height that are present in PBC cases. For walls cases,

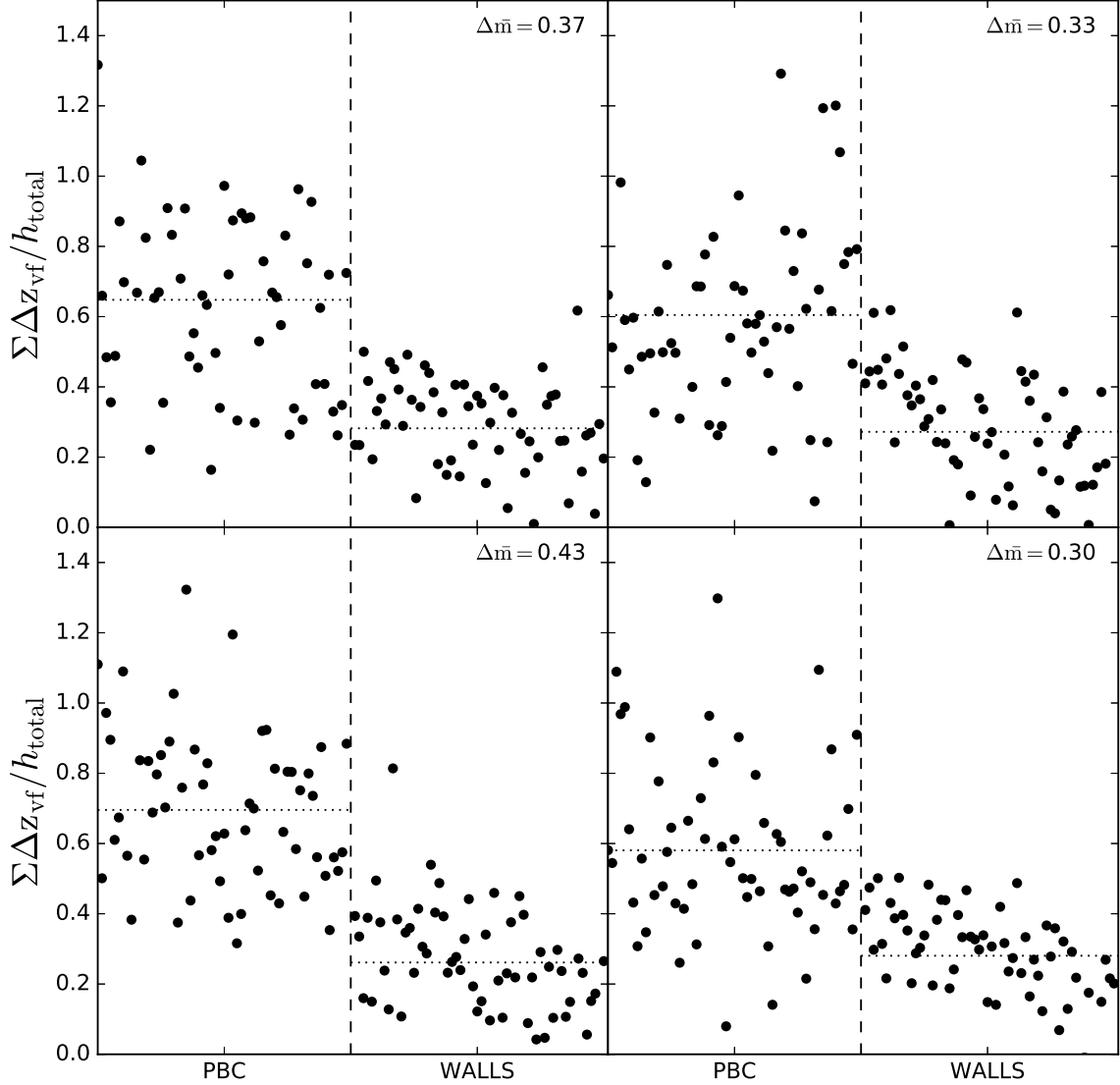


Figure 2.10: Sum of the changes in Brazil nut height due to void-filling events for 4 different initializations of the granular bed. Each point represents a single simulation. Each simulation results in a BNE (the intruder rises to the top of the granular system). For each simulation the change in the intruder height due to a void-creating event is tracked. The thick vertical dashed lines separate simulations with PBC and simulations with wall boundaries. The dot-dashed lines represent these mean values of  $\Sigma \Delta z_{vf}$  for each boundary condition, and  $\Delta \bar{m}$  is the difference in the mean values. The values here represent the total net change in the intruder's height over the course of the entire simulation. Points for PBC cases cluster at high values, while points for walls cases cluster at low values. Evidently, two different mechanisms drive the BNE for these two different setups.

these fluctuations are limited due to particle-boundary interactions, which restrain the amount of possible system dilation.

We performed the same analysis for low-gravity simulations (amplitude of 1 cm and frequency of  $0.939 \text{ rad s}^{-1}$ ), in order to assess whether or not the void-filling mechanism is also responsible for the BNE effect in PBC cases at low gravity. The ratio  $\bar{\sigma}_{z,vf}$  over grain radius obtained under these conditions for one suite of simulations is shown in the bottom panels of Fig. 2.11. We find a similar clustering of standard deviation spikes at high values in the PBC cases compared to the Wall cases, which supports the idea that void-filling remains, under low gravity, the principal mechanism driving the BNE when PBC are used.

The lower incidence of BNE in PBC cases at low gravity and low friction values (16% of the cases showed a brazil-nut incapable of rising) might be due to an attenuation in the efficiency of the void-filling mechanism compared to convection. We speculate that this might come about from a diminution of the energy transmitted to the granular bed by the bottom plate. In fact, as we keep the same value of  $\Gamma$  and the same amplitude as in the  $1g$  simulations for the low-gravity ones, we introduce a factor of  $10^{-4}$  in the kinetic energy transmitted to the grains compared to the  $1g$  cases. With an energy four orders of magnitude lower than the one involved in Earth gravity, we can expect smaller dilation spikes, thus smaller voids created under the intruder at low friction values, and lower efficiency of the void-filling process compared to  $1g$ . However, Fig. 2.11 shows that the mechanism is still active in low gravity.

The void-filling mechanism has been previously studied with PBC by [Schröter et al.](#)

(2006). The authors showed that a system bounded by walls can have a BNE driven by convection, while a PBC case is likely driven by void-filling events. However, these authors speculated that the vibrations that induce void-filling events are much smaller than those that drive convection. Here, we show that for the same vibrational energy, two different mechanisms arise due to differences in the boundary conditions.

The results presented here marks the first attempt at showing that a void-filling mechanism may be responsible for size-segregation of large grains on an asteroid. By using boundary and gravity conditions that more closely resemble an asteroid environment, we suggest that vibrations are able to drive a boulder to the surface of an asteroid. Furthermore, the void-filling mechanism is also enhanced by a larger size ratio between particles, and, unlike the convection mechanism seen with walls, it does not depend on the bed depth (Schröter et al., 2006). Previous studies (e.g., Taguchi, 1992) have shown that convection-driven mechanisms are limited to the upper 10 or so grain heights of a system. After a certain depth, convection can no longer efficiently drive BNE. Since the void-filling mechanism occurs independently of bed depth, a boulder entrained deep below the surface may still be able to segregate upwards. Finally, the void-filling mechanism is characterized by independent lofting events and does not necessarily require a continuity in the seismic shaking. Thus it can be driven by independent shocks undergone by an asteroid over its lifetime. All of these facts make the void-filling mechanism particularly relevant to the asteroid environment.

## 2.5.2 Interplay between gravity and rolling friction

Unlike previous studies, we have attempted to clarify the influence of material property on the rise speed of the Brazil nut for different boundary conditions and different gravity regimes. As Section 2.4.3 shows, a low-gravity system changes the dynamical effects of rolling friction. In Earth gravity, PBC cases showed a negative correlation with  $\mu_r$ ; meanwhile, a positive correlation was found in low gravity. Furthermore, an inspection of Fig. 2.6 shows that at intermediate gravity,  $10^{-2} g$ , there seems to be no correlation with  $\mu_r$  at all. These clues hint at a variation in the granular flow of this system across different gravity regimes.

The PBC simulations in Fig. 2.11 are uniquely identified based on the static friction coefficient of the grains. On each panel, grains are grouped by increasing values of  $\mu_s$  (from left to right), and each of these  $\mu_s$  groupings are sorted in order of increasing  $\mu_r$  (again from left to right), when the data are available. We plotted, for each  $\mu_s$  group, the regression line that best fits the dependence of  $\bar{\sigma}_{z,vf}$  with  $\mu_r$  for that particular group. We find that for Earth-gravity conditions,  $\bar{\sigma}_{z,vf}$  clearly decreases with  $\mu_r$  for every value of  $\mu_s$ . At  $10^{-4}g$ , the trend reverses, and  $\bar{\sigma}_{z,vf}$  increases with  $\mu_r$  for every value of  $\mu_s$ .

These trends suggest that, in Earth-gravity conditions, rolling friction diminishes dilation events in the system. Grains have a more difficult time flowing past one another as the system locks up. Even if voids are created, the grains are incapable of flowing into these voids. In low gravity, rolling friction enhances the strength of dilation events in the system. The larger average value of  $\bar{\sigma}_{z,vf}$  (dot-dashed hori-

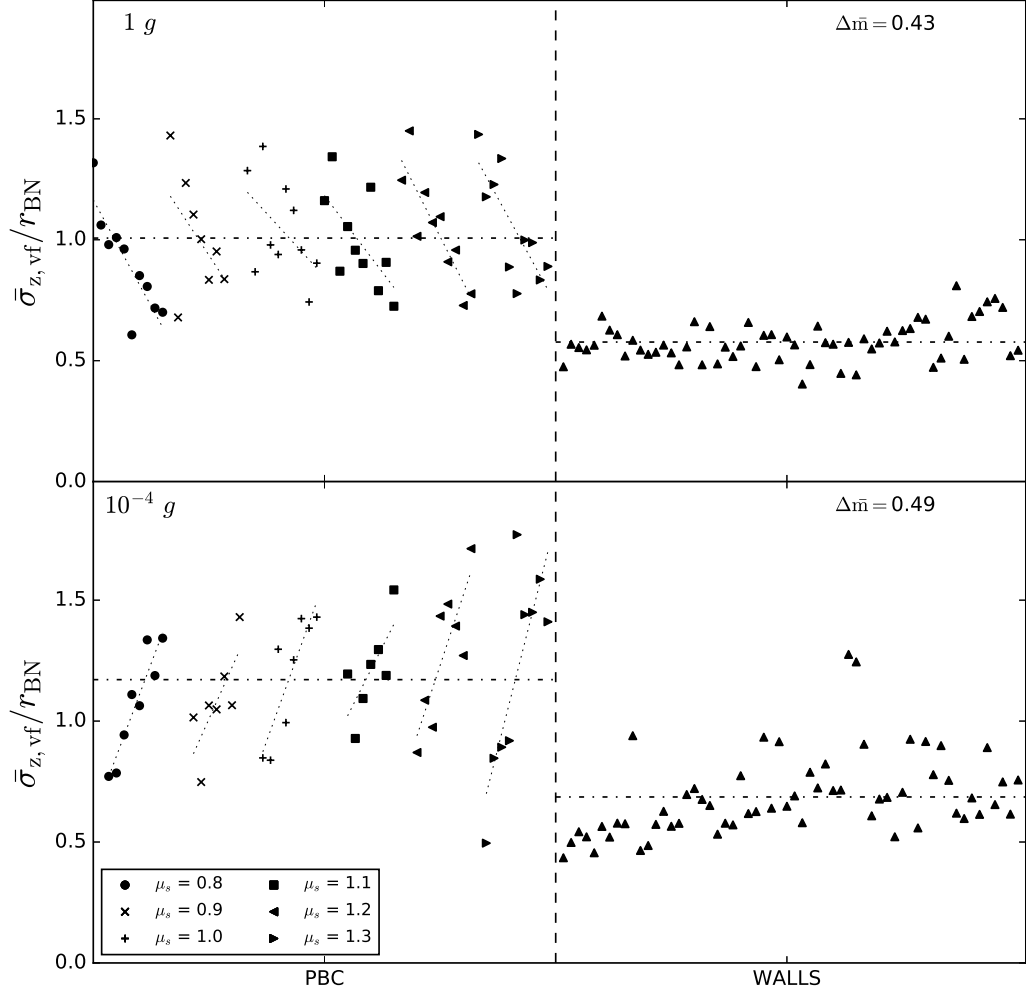


Figure 2.11: Mean of the grain height standard deviation during void-filling events. The thick vertical dashed lines separate simulations with PBC and simulations with wall boundaries. The horizontal dot-dashed lines represent the mean values of  $\bar{\sigma}_{z,\text{vf}}$  for each boundary condition, and  $\Delta\bar{m}$  is the difference in mean values. The granular systems in these two setups behave differently in response to the periodic forcing. For PBC cases, the grains are more free to dilate and create voids. For walls cases, the walls inhibit the grains from expanding too much. Hence, the standard deviation in the height of the grains is systematically larger for PBC cases than it is for walls cases. We plot the PBC cases with unique scatter points based on the static friction value,  $\mu_s$ , used in each simulation. Simulations with  $\mu_s$  of 0.8, 0.9, 1.0, 1.1, 1.2, and 1.3 are represented by circles, x-marks, crosses, squares, left-facing triangles, and right-facing triangles, respectively. Each of the 6 groups of  $\mu_s$  values are sorted in order of increasing rolling friction,  $\mu_r$ . The dotted lines for each  $\mu_s$  group represent regression lines establishing the dependency of  $\bar{\sigma}_{z,\text{vf}}$  with  $\mu_r$  for each unique  $\mu_s$ .

zontal lines in Fig. 2.11) for PBC cases suggests that the system is lofted higher and for a longer time in a lower-gravity environment. Systems with high-friction grains will be able to create larger void spaces, as the system is able to dilate due to stronger contact forces. This stronger force network may further feed into longer lofting times as subsequent impulses from the bottom plate are more efficiently transmitted upwards. Thus, rather than diminishing the BNE, high rolling friction, combined with longer lofting times, may create large enough void spaces that the void-filling mechanism is enhanced. Therefore, while these rougher grains typically inhibit granular flow, they can create larger void spaces that allow grains to move more freely in low-gravity.

While a full physical model of this process is beyond the scope of this study, we can begin to see its outlines. Namely, there are two important dynamical timescales involved in this process, whose predominancy seems to reverse with gravity; namely, the first being a gravitational timescale, and the second being a granular flow timescale. The gravitational timescale is well known, being simply determined by the size of the system and the local gravitational acceleration. The granular flow timescale is more elusive to determine, as there are combined non-linearities that come into play in a granular system. However, it is clear that what will chiefly determine the efficiency of granular flow, and the possibility of BNE in a semi-boundless system, is the incidence of voids in that system.

## 2.6 Conclusion

We performed numerical simulations of vibration-driven grains. We attempted to advance the current understanding of size segregation among asteroid regolith grains in low gravity by performing simulations with realistic grain physical properties, boundary conditions, and gravity environment. Previous studies that used simulations of the BNE in the context of asteroids ran simulations with walls. Here, we wanted to better mimic the asteroid environment by removing these lateral boundaries, which are probably not the most appropriate representation of an asteroid interior. Instead, we implemented periodic boundary conditions (PBC). We were able to show that for a wide range in friction properties, the BNE occurs even when PBC are used. We also explored a broad range of friction levels, from medium to high, which led us to the conclusion that a different mechanism drives the BNE in walls compared with PBC cases. While granular convection is well known to drive the BNE with walls, we have shown that a void-filling mechanism is actually predominant when PBC are turned on. The void-filling mechanism occurs when a vibration causes the granular system to dilate, creating void spaces in the medium. In Earth gravity, a sufficiently fluid granular system allows the creation of void spaces that affords an opportunity for large-scale displacement of particles. Due to the size difference between the large intruder and the surrounding grains, the smaller grains have a higher probability of filling the void space created below the intruder. This allows the BNE to occur in a system without confining wall boundaries, which are required for granular convection to occur.

For a better representation of the asteroid environment, we also studied the BNE in low gravity ( $10^{-4}g$ ). We found that both convection for walls cases and the void-filling mechanism for PBC cases are still able to occur, however with striking differences compared to the  $1g$  simulations. For walls cases, we found that convection is counterintuitively enhanced for higher friction and speculate that the lower packing in low-gravity cases may be responsible for this behavior. For PBC cases, we found that the void-filling mechanism is still able to occur, and that the total number of forcing cycles in the lower-gravity environment is comparable to that in Earth gravity. However, our exploration of a broad range of rolling friction levels highlighted major differences in the effect of this rolling friction on the BNE. Unlike for the  $1g$  cases, where a higher rolling friction freezes the void-filling mechanism (the grains are no longer able to fill the voids), low-gravity cases show a reverse trend, where a higher rolling friction level actually enhances the BNE. We suggest that this difference comes from a change in the predominant time scale for the system. In  $1g$ , the gravity does not allow long lofting time and therefore, the higher the rolling friction, the greater the inhibition of the grains' reorganization, which occurs on a different time scale, the granular flow time scale. Conversely, in low gravity, the granular flow time scale becomes more important as the gravity allows much longer lofting time, enabling frictional particles to fill the voids anyway. In addition, a higher rolling friction results in the creation of more voids to be filled by the particles, which results in the inversion of the trend of the rise speed with  $\mu_r$  for Earth- and low-gravity cases. We propose that the transition between the predominancy of one regime or another may occur around  $10^{-2}g$ , as the influence

of  $\mu_r$  on the rise speed is for this case almost non-existent.

Finally, we also studied small-amplitude vibrations, where the amplitude is much smaller than the size of the grains. We found that the BNE is less likely to occur. This is especially true for cases with PBC. The PBC cases require sufficiently large void spaces to be created during the vibration in order to drive the BNE. If the shaking amplitude is much smaller than a grain size, then the subsequent voids are likely to be small as well. Hence, the grains are unable to fill in voids created underneath the intruder. Despite this, we find that a few PBC cases are able to exhibit the BNE. These are cases where both the static and rolling friction are high. It is possible that in these cases the friction between grains is sufficient to allow voids to slowly grow between subsequent shakes until they become large enough for a small particle to occupy them. Furthermore, a real asteroid will have grains that span a wider size distribution. It is possible that grains with a size smaller than the oscillation amplitude might be able to self-segregate efficiently, influencing the segregation process at larger scales.

The void-filling mechanism is a promising mechanism to explain features on actual asteroids. Images and radar observations collected during space missions indicate the presence of boulders at the surface of asteroids. In fact, a boulder is the target of the Asteroid Retrieval Mission (ARM) under study at NASA, which aims at collecting a boulder from the surface of the asteroid 2008 EV5 and placing it on a cis-lunar orbit for later rendezvous by astronauts sent to interact with it ([Abell et al., 2015](#)). The physical properties of boulders present on asteroid surfaces are intimately related to their origin and history. Determining the mechanism bringing them to

the surface (BNE or any other mechanism) can provide valuable clues to determine their physical properties. Future work could build on the simulations performed in the present study and explore a larger parameter space, always with the aim of characterizing asteroid interiors and environments more realistically.

## Chapter 3: Low-speed granular impacts:

### Modeling Spacecraft-Regolith Interactions

#### 3.1 Chapter Preface

Some of the work presented in this chapter is in preparation as “Calibrating Granular Mechanics Codes for a Range of Granular Materials at Very Low Gravity” by R.-L. Ballouz, D. P. Sánchez, K. J. Walsh, H. C. Connolly Jr., D. S. Lauretta, D. C. Richardson, and D. J. Scheeres, for publication in *Icarus*. This chapter presents a suite of simulations that were performed for the upcoming NASA OSIRIS-REx mission to the asteroid Bennu. As the work has progressed, it has been presented in three science team meetings and one American Astronomical Society Division of Planetary Sciences meeting, and has been written up as quarterly internal reports for the OSIRIS-REx team. The goal of this work is to determine how the granular surface of an asteroid might respond to the intrusion of a spacecraft. By conducting low-speed impact experiments on to a variety of granular material types, we are able to determine the range of possible regolith behavior that a spacecraft might encounter as it touches down on an asteroid.

## 3.2 Background

NASA's third New Frontiers mission, OSIRIS-REx, will rendezvous in 2018 with a primitive near-Earth asteroid, (101955) Bennu. After being inserted into orbit around the body and conducting measurements, which includes the creation of a global surface map, a Touch-And-Go-Sample Acquisition Mechanism (TAGSAM) will be deployed to collect material from the asteroid's surface (Berry et al., 2016). The TAGSAM consists of a sampler head with an articulated pogo-stick-like arm. The sampling strategy is to force nitrogen gas into the regolith thereby entraining some material into the sampling device. However, the interaction of a sampling mechanism with a regolith surface in the low gravity environment of a small body is difficult to predict, even if the physical conditions on the surface of an asteroid are well known. This is because the response of granular material to low-speed impacts is poorly understood.

Hitherto, most studies of impacts onto asteroid surfaces have focused on developing scaling relations for predicting the outcome of cratering processes. Lab experiments typically study impacts onto cohesive and non-cohesive grains by impactors traveling at speeds of the order of 100 to 1000 m/s (Schmidt & Housen, 1987; Housen & Holsapple, 2011). In such studies, the fate of the impactor is largely ignored. In the context of planetary science, the study of low-speed impact collisions (impacts at speeds of  $\sim 1$  m/s or less) in low-gravity conditions were performed to investigate collisions between planetary ring particles (e.g., Colwell 2003). However, there is a rich literature in the granular physics community of

studies of granular impact cratering in Earth-gravity conditions (e.g., [Uehara et al. 2003](#); [Katsuragi & Durian 2007](#)). [Uehara et al. \(2003\)](#) attempted to develop scaling of the crater depth as a function of impactor density, impact speed, and the material type of the target. They suggested that the crater depth,  $d$ , formed by a low-velocity impact onto granular material should scale as

$$\frac{d}{a} = \frac{0.175}{\tan(\phi)} \left(\frac{\delta}{\rho}\right)^{1/2} \left(\frac{ga}{v^2}\right)^{-1/3}, \quad (3.1)$$

where  $a$  is the impactor radius,  $\phi$  is the granular target's angle of friction,  $\delta$  is the impactor density,  $\rho$  is the target density,  $g$  is the gravitational acceleration, and  $v$  is the impact speed. While Eq. 3.1 does imply a scaling with gravity, there were no experiments performed to verify if this were true. Subsequent work by [Katsuragi & Durian \(2007\)](#) extended this work by conducting impact experiments of 1-inch steel spheres onto 250-350  $\mu\text{m}$  glass beads. [Katsuragi & Durian \(2007\)](#) proposed a unified force law for granular impact cratering, where the force on a projectile by the granular target is composed of the sum of a velocity-dependent inertial drag and a depth-dependent friction term. While this study did develop a theoretical model to describe the complex response of granular materials to impact, it did not include the effect of the local gravity on the outcome.

Driven by spacecraft missions, such as OSIRIS-REx and Hayabusa-2, that will interact with the asteroid surface, the study of low-speed impacts on to regolith in low-gravity environments has only recently emerged (e.g., [Nakamura et al. 2013](#)). [Nakamura et al. \(2013\)](#) built upon the work of [Katsuragi & Durian \(2007\)](#)

by conducting laboratory experiments and numerical simulations of 6 mm plastic projectiles impacting 50  $\mu\text{m}$ -size glass beads. They studied the deceleration profiles of the impactors and isolated the effects of three different components to the deceleration of a projectile: a depth-dependent lithostatic pressure term, a velocity-dependent viscous-like drag term, and a velocity-squared-dependent inertial-drag term. Of these three components, only the first, the lithostatic pressure term, has a gravity dependence. By measuring the contributions of each term to the deceleration of the impactor, [Nakamura et al. \(2013\)](#) found that the gravity-dependent lithostatic-pressure term has a very marginal effect on the deceleration compared to the other effects. The lithostatic-pressure term was measured to have a magnitude that was 1/40th of the inertial-drag term. This suggested that the local gravity has a negligible influence on the outcome of a cratering impact. [Altshuler et al. \(2014\)](#) conducted impact experiments at gravities ranging from  $0.4g$  to  $1.2g$ , and found a similar lack of dependence of the penetration depth of an impactor with the local gravity. While these studies suggest little to no gravity dependence on the outcome of a granular impact, the range of gravities were limited to values of no more than  $\sim 0.1g$  ( $\sim 10^4 \times$  the gravity on Itokawa). It is unclear whether this description of granular impacts is still valid at very low gravities.

Spacecraft missions that have interacted with the surface of a small solar system body have resulted in rather unpredictable outcomes. These range from soft landings (NEAR-Shoemaker at Eros, e.g., [Dunham et al. 2002](#) to meter-high bouncing (Hayabusa at Itokawa, see [Yano et al. 2006](#)) to spacecraft displacements of 100's of meters (Philae at Comet 67P/Churyumov-Gerasimenko, see [Biele et al. 2015](#)).

The different outcomes of these touchdown attempts are likely due to difference in the material properties of the surface (fluffy vs. strong material) and the gravitational environment (which ranges from milli-g's on Eros to micro-g's on Itokawa). In collaboration with the OSIRIS-REx mission, we studied granular impacts in low-gravity environments using numerical simulations. Firstly, we calibrated our code by conducting simulations of granular impacts in  $1g$  and compared the outcomes to laboratory experiments by [Holsapple \(2016\)](#). Then we extended our simulations to low-gravity environments, in order to compare our simulations with theoretical predictions. Finally, we carried out simulations of the intrusion of a realistic physical model of the sampling device (TAGSAM) into a bed of cm-size spherical particles to estimate the extent to which the granular material resists the load applied by the device.

The exact nature of the surface of Bennu (OSIRIS-REx's target asteroid ) is unknown. For that reason, it is necessary to study impacts and penetration experiments over a large range of possible conditions and materials. Our goal is to identify the governing physical parameters of that surface, and to assess how they determine the outcome. Many important questions, especially that of the role of the near-zero gravity, cannot easily be answered with physical experiments. Physically simulating such a wide range of possible interaction scenarios on Earth is difficult and expensive. Therefore, numerical simulations are an ideal tool to explore possible sampling scenarios, in order to better understand the dynamics of the sampler and determine any possible difficulties that the mission may encounter. By generating an “atlas” of possible outcomes, we are able to provide the mission with a tool

to reconstruct the actual sampling attempt. This is accomplished by producing synthetic inertial measurement unit (IMU) data that we will be able to compare with actual spacecraft data. Furthermore, once the actual sampling attempt happens, our atlas may be used to infer the physical properties of the surface.

The rest of the chapter proceeds as follows. First, we introduce the code updates that were implemented in order to model the collisional interaction of a non-spherical body with spherical particles. Afterwards, we compare granular impact simulations with laboratory experiments that were performed to calibrate our code. Then, we discuss the simulations that were performed to generate an atlas of possible outcomes that will be used to reconstruct the TAGSAM sampling attempt and that can possibly characterize the properties of the surface grains on Bennu. Finally, we conclude this chapter by summarizing our study and discussing the applicability of the methods developed here for future space missions that will either interact with a small solar system body's surface or deploy a lander.

### 3.3 Methodology

The study presented here uses a soft-sphere discrete element method code to solve collisions between spherical particles (see Chapter 1 for details). The same integrator also solves collisions between a spherical particle and a geometric primitive (termed a wall) that either provides a boundary condition (such as a container that holds particles) or an object that can collide with a particle. Non-inertial walls that serve as boundaries were introduced in code developments by [Richardson et al.](#)

(2011). Here, we describe the developments that were implemented that allow us to combine geometric primitives (spheres, rectangles, cylinders, etc.) to construct arbitrary shaped inertial objects that can collide with spherical particles.

### 3.3.1 Inertial walls

In `pkdgrav`, inertial walls are geometric primitives with a finite mass that can react to impulses by spherical particles (but not other inertial walls). These walls can be combined to form a single assembly of walls that collectively react to impulses as a single rigid body. An inertial wall has the following key properties that allow it to behave as a rigid body: a mass, a center of gravity, a spin vector, a moment of inertia tensor, and an orientation matrix.

When an inertial wall overlaps with a particle, the reaction force is calculated using the usual Hooke's law spring force that is used for particle-particle collisions. The resulting accelerations are solved using the leap-frog integrator and are applied to the center of gravity of the inertial wall, similar to the method used for particle collisions. The resulting change to the spin vector and orientation, however, requires the rigid-body Euler equations to be solved. The changes to the spin are found by solving the following differential equations,

$$\begin{aligned}
 I_1 \dot{\omega}_1 - \omega_2 \omega_3 (I_2 - I_3) &= \mathbf{N}_1 \\
 I_2 \dot{\omega}_2 - \omega_3 \omega_1 (I_3 - I_1) &= \mathbf{N}_2 \\
 I_3 \dot{\omega}_3 - \omega_1 \omega_2 (I_1 - I_2) &= \mathbf{N}_3
 \end{aligned}
 \tag{3.2}$$

where  $I_k$  are the principal moments of inertia of the body,  $\omega_{\mathbf{k}}$  are the spin components

in the body frame, and  $\mathbf{N}_k$  are the net torque components in the body frame (for  $k = 1,2,3$ ). The principal moments of inertia are user supplied information based on the internal mass distribution of the wall assembly. The net torque components are calculated by summing up the individual torques from each particle-wall collision. Each individual torque,  $N$ , is given by

$$\mathbf{N} = \mathbf{N}_n + \mathbf{N}_t - \mathbf{N}_{\text{particle}}, \quad (3.3)$$

where  $\mathbf{N}_{\text{normal}}$  and  $\mathbf{N}_{\text{tangential}}$  are the normal and tangential torques, respectively, found by

$$\mathbf{N}_{n,t} = \mathbf{r}_{p-w} \times \mathbf{F}_{n,t}, \quad (3.4)$$

where  $\mathbf{r}_{p-w}$  is the moment arm, calculated as the vector from the wall assembly's center of gravity to the particle's center, and  $\mathbf{F}_{n,t}$  is the normal and tangential force by the particle on the wall assembly.  $\mathbf{F}_n$  and  $\mathbf{F}_t$  are found by taking the negative of the normal and tangential force on the particle by the wall assembly, which have already been calculated.  $\mathbf{N}_{\text{particle}}$  is the torque on the particle due to the static, rolling, and tangential friction forces that the particle feels by interacting with the wall. The changes to the orientation, as reflected in the principal axes components, are found by solving the following equations,

$$\begin{aligned}
\dot{\hat{\mathbf{p}}}_1 &= \omega_3 \hat{\mathbf{p}}_2 - \omega_2 \hat{\mathbf{p}}_3 \\
\dot{\hat{\mathbf{p}}}_2 &= \omega_1 \hat{\mathbf{p}}_3 - \omega_3 \hat{\mathbf{p}}_1 \\
\dot{\hat{\mathbf{p}}}_3 &= \omega_2 \hat{\mathbf{p}}_1 - \omega_1 \hat{\mathbf{p}}_2
\end{aligned} \tag{3.5}$$

where  $\hat{\mathbf{p}}_k$  denote the principal axes. Both sets of equations (Eq. 3.2 and Eq. 3.5) are solved using a 5th-order time-adaptive Runge-Kutta integrator during the update of particle positions. We use a Runge-Kutta integrator instead of a leap-frog integrator because these equations are not easily adapted to the leapfrog integrator.

### 3.3.1.1 TAGSAM specifications

The head will contact the surface of the Bennu asteroid with an initial approach speed of about 10 cm/s. After a certain interval of time ( $< 5$  seconds) of positive deceleration of the spacecraft, nitrogen gas will flow through an annular nozzle around the lower part of the collector head. This will mobilize the surrounding regolith, allowing it to flow into the TAGSAM and be retained inside it. It will be stored there until it is returned to Earth for laboratory analysis.

Fig. 3.1 is a diagram of the TAGSAM. We attempt to replicate its geometry as close as possible by combining 6 geometric primitives (3 cylinders and 3 disks, see Fig. 3.2). The collector head is made out of an outer hollow cylinder with a diameter of  $\sim 30$  cm and an inner hollow cylinder with a diameter of  $\sim 15$  cm. Interior to the main cylindrical housing is a smaller cylinder that tapers downwards. The first disk has a hole and is used to cover the gap between the bottom of the cylinder, the

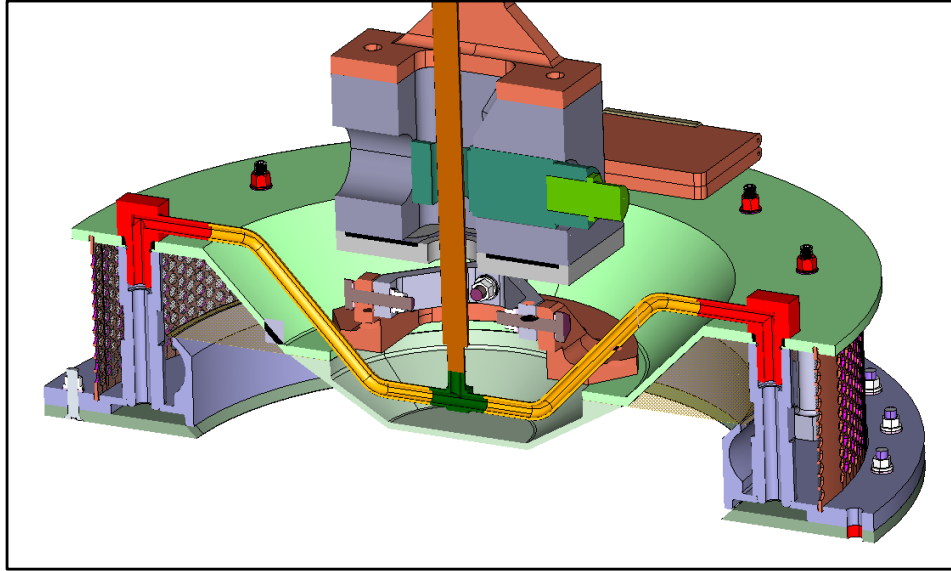


Figure 3.1: Diagram of the TAGSAM. The collector head has an outer diameter of about 30 cm, and an inner diameter of about 15 cm.

second disk covers the bottom of the tapered cylinder, and the last disk is used to completely cover the top of the two cylinders. The total mass of the TAGSAM is 20 kg. It is attached to a spacecraft (represented by a 1,280 kg sphere) by a pogo-stick like arm (represented by a cylinder). The TAGSAM head can move with six degrees of freedom as a single rigid body. The spacecraft and TAGSAM dynamics are coupled by the arm, which contains a constant-force spring that is designed to begin compressing when the TAGSAM head feels a force that exceeds 67 N. The spring ensures that the force felt by the spacecraft does not exceed 67 N.

In order to produce realistic acceleration profiles of the spacecraft-TAGSAM assembly, we included a spring force model that modulated the system's dynamics as it penetrated the regolith bed. Our spring force model took the following into account:

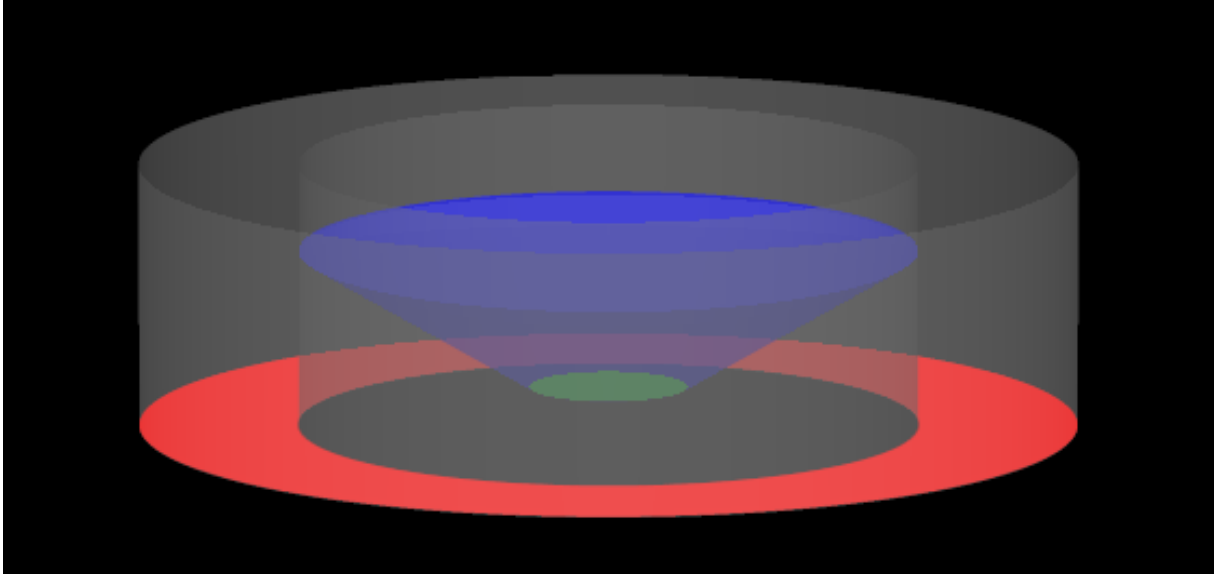


Figure 3.2: The TAGSAM used in the simulations. A disk covers the top, but is left out of this image.

- If the ground force,  $F_{\text{ground}}$ , as felt by the approaching TAGSAM assembly, is below the 67 N threshold, then both the TAGSAM and the spacecraft (S/C) feel a force,

$$F_{\text{S/C}} = F_{\text{TAGSAM}} = F_{\text{ground}}, \quad (3.6)$$

where  $F_{\text{S/C}}$  is the force on the spacecraft and  $F_{\text{TAGSAM}}$  is the force on the TAGSAM.

- If the ground force exceeds the 67 N threshold, then the spring is engaged. The S/C feels a force equal to the spring force, and the TAGSAM feels a force equal to the difference between the ground and spring force,  $F_{\text{spring}}$ .

$$F_{S/C} = F_{\text{spring}} \quad (3.7)$$

$$F_{\text{TAGSAM}} = F_{\text{ground}} - F_{\text{spring}}. \quad (3.8)$$

This force configuration is kept as long as the spring is compressed (i.e. the change in the separation between the TAGSAM and the S/C with respect to their initial separation is  $\leq 0$ ). The spring is designed to not compress more than 15 cm. Furthermore the spring may not extend beyond its initial equilibrium length. We treat these two boundary conditions as a perfectly inelastic collision between the S/C and the TAGSAM. In the event one of these hard-stops is reached, the TAGSAM's position is set to where it should be for a 15 cm or 0 cm separation, and the TAGSAM and S/C velocity is determined based on conservation of momentum for a perfectly inelastic collision:

$$v_{\text{new}} = \frac{m_{S/C}v_{S/C} + m_{\text{TAGSAM}}v_{\text{TAGSAM}}}{m_{S/C} + m_{\text{TAGSAM}}}, \quad (3.9)$$

where  $m_{S/C}$  is the mass of the spacecraft,  $v_{S/C}$  is the speed of the spacecraft,  $m_{\text{TAGSAM}}$  is the mass of the TAGSAM, and  $v_{\text{TAGSAM}}$  is the speed of the TAGSAM. Since the mass of the S/C is much larger than that of the TAGSAM, this new velocity will typically match the S/C's old velocity. This choice in a hard stop interaction would cause a slow down for a downward moving S/C for the case of a 15 cm hard stop (the TAGSAM is pushing up against the S/C) and a slow down for an upward moving S/C for the case of a 0 cm hard stop (the TAGSAM is pulling down on the S/C). This makes physically intuitive sense for such a configuration of a massive object attached to a much smaller object by a rigid spring.

Finally, rather than being constant, in actuality, the spring force increases the more the spring is compressed. Furthermore, the spring force discontinuously changes depending on whether it is compressing or expanding. We model the spring force as,

$$F_{\text{spring}} = -k\Delta z + F_{\text{spring},0}, \quad (3.10)$$

where  $k$  is a spring constant that changes depending on whether the spring is compressing or expanding,  $\Delta z$  is the change in spring length (or change in separation between the TAGSAM and S/C), and  $F_{\text{spring},0}$  is the spring force at zero compression or expansion. For a compressing spring, the force ranges from 67 N at 0 compression to 81 N at 15 cm compression. Therefore we can write the spring force as:

$$F_{\text{spring}} = -\frac{14}{15}\Delta z + 67 \quad (3.11)$$

with  $\Delta z$  in cm. For an expanding spring, the force ranges from 47 N at 0 compression to 49 N at 15 cm compression. Therefore we can write the spring force as:

$$F_{\text{spring}} = -\frac{2}{15}\Delta z + 47 \quad (3.12)$$

### 3.4 Impact Experiments

In order to use our code to test the response of a granular bed on the surface of an asteroid to a spacecraft landing, we must first ensure that our code can accurately predict the dynamics of a granular medium in Earth-gravity. In this section, we first present two collections of simulations that were conducted to ensure that our grains behave similarly to realistic materials. The first part of the calibration

involves measuring the bulk macroscopic properties of a granular medium as a function of its microscopic properties (elastic and friction properties). In the second part, we compare numerical simulations of impact experiments to laboratory results by [Holsapple \(2016\)](#) for grains with similar macroscopic properties. After we have demonstrated the ability of our code to accurately predict impact outcomes in Earth gravity, we perform simulations in low-gravity environments to check whether our results are in line with theoretical predictions of gravity-dependence ([Nakamura et al., 2013](#); [Altshuler et al., 2014](#)). Following the presentation of the code calibration results, we describe the simulations that were conducted to model the TAGSAM's interaction with the granular bed.

### 3.4.1 Material Property

Before comparing cratering simulations with lab experiments, we first verify that the macroscopic properties of a granular bed can indeed be accurately measured. The materials we are attempting to simulate are glass beads and dry sand, whose macroscopic properties are listed in [Table 3.1 \(Holsapple, 2016\)](#). The relevant properties of the material that we find through simulations are the Young's modulus and the Poisson ratio. The Young's modulus measures the stiffness of the granular assembly; the Poisson ratio measures the relative amount of expansion of the granular material in the direction perpendicular to the direction of compression. We also measure the angle of friction of the material, through the angle of repose landslide measurements described in [Chapter 2](#).

Table 3.1: The physical properties of real granular materials.

Material	Dry Ottawa Sand	Coarse Solid Glass Beads
Density (g/cm <sup>3</sup> )	1.5	1.5
Grain Radius ( $\mu\text{m}$ )	600-850	600-850
Sound Speed (m/s)	200	140
Poisson's ratio	0.25	0.25
Young's modulus (MPa)	135	70
Angle of Friction	35°	22°

The Young's modulus and Poisson ratio can be measured through uni-axial compression tests on a packed granular medium. We conduct these simulations by first filling a 4 cm  $\times$  4 cm  $\times$  2 cm box with 4000 mm-size particles. Fig. 3.3 shows the setup for these simulations. The right wall of the box moves inward, compressing the granular assemblage. This results in stresses to all the walls of the confining box. The pressure on each wall of the box is tracked throughout the entire length of the simulation. The Young's modulus is measured by taking the ratio of the pressure on the forcing wall to the fractional change in the size of the granular system. The Poisson's ratio is typically measured as the ratio of the tangential strain to the normal strain (fractional changes in the size of the granular assembly due to compression). Since we use non-moving walls, we instead measure the ratio of the tangential pressure to the normal pressure. Fig. 3.4 shows an example of the stresses measured in one of our simulations.

In our simulations, the sound speed of the material is determined by the elastic properties of the grains, set by the normal spring constant  $k_n$ . Therefore, this parameter is tuned so that the sound speed of the simulated grains match that of

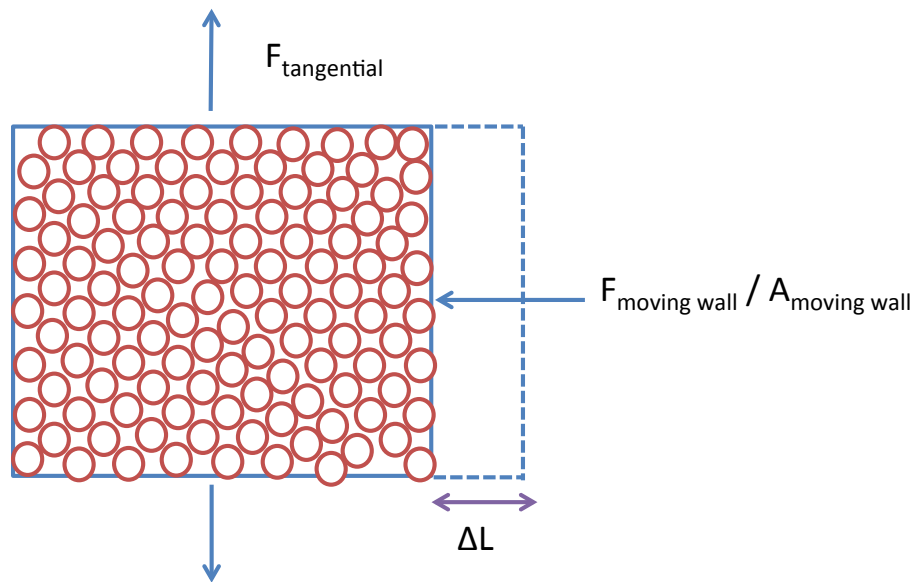


Figure 3.3: The setup for a simulation to perform uni-axial compression tests on grains. The uni-axial compression tests allow us to measure changes in the macroscopic properties of grains (Young's modulus and Poisson ratio), based on microscopic properties (friction and elastic properties of individual grains).

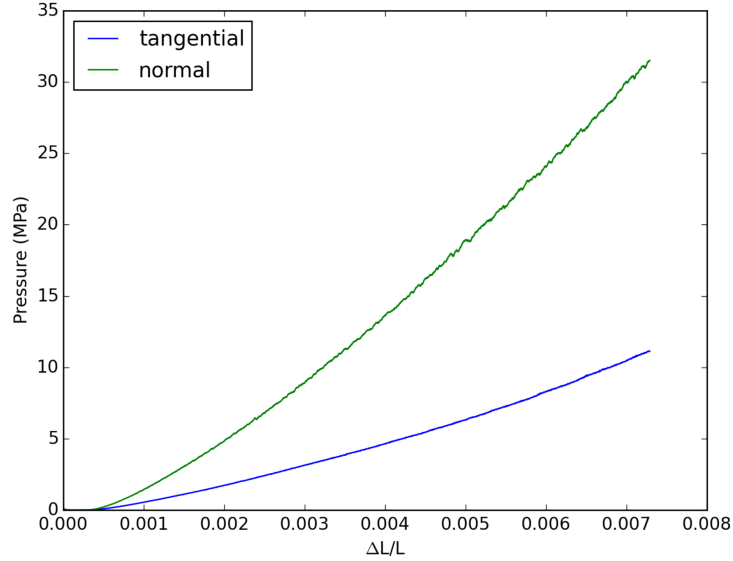


Figure 3.4: The resultant pressures on the right compressing wall (green) and a tangential wall (blue) are shown as a function of the fractional change in the length of the system (strain).

the actual material.

We ran uni-axial compression tests for walls moving at 0.2 and 2 m/s, for coefficients of normal and tangential restitution of 0.5 and 0.9, for static,  $\mu_s$ , coefficients of friction ranging from 0.0 to 1.0, and for rolling,  $\mu_r$ , coefficients of friction of 0, 0.1, and 0.2. Fig. 3.5 shows the result of sweeps of the two friction parameters that control the surface roughness of the spherical grains, for the case of a confining wall moving at 0.2 m/s, and for restitution coefficients of 0.9. We see that both the Young’s Modulus and Poisson ratio are mainly controlled by the static friction. The rolling friction has little to no effect on the outcomes of these experiments. The Young’s moduli range from 50–200 MPa, and the Poisson ratios range from  $\sim 0.2$  to 0.8.

We performed a consistency check by increasing the compression rate to 2 m/s, and found no significant difference in the outcome. For smaller restitution coefficients (0.5) we find that the Young’s modulus is slightly different: the range of possible values is smaller (100–200 MPa).

By matching values of Young’s modulus and Poisson’s ratio, We find that dry sand is best simulated with grains that have a  $\mu_s$  of 0.8 and a  $\mu_r$  of 0.2, while glass beads are best simulated by grains that have a  $\mu_s$  of 0.4 and a  $\mu_r$  of 0.1. The compression tests have shown that the only time we have realistic Poisson ratios ( $< 0.4$ ), is for moderately high friction coefficients ( $\mu_s > 0.3$ ). This highlights the point that in order to produce realistic outcomes in SSDEM simulations, realistic friction parameter values must be used.

### 3.4.2 Penetration Depth Experiments

After tuning our collision parameters to values that can accurately model realistic materials, we used this information to conduct simulations of impact experiments. By comparing with laboratory results by [Holsapple \(2016\)](#), we can show the level of accuracy our simulations are able to achieve in predicting the outcomes of impact experiments. These experiments also serve as a data set that can verify the accuracy of the code calibration described in the previous section.

The impact experiments are set up by filling a cylinder with a 10 cm radius and 9.2 cm height (with a covered bottom) with  $\sim 400,000$  spherical particles. The spheres have a normal distribution of radii with a mean of 1 mm, and a standard

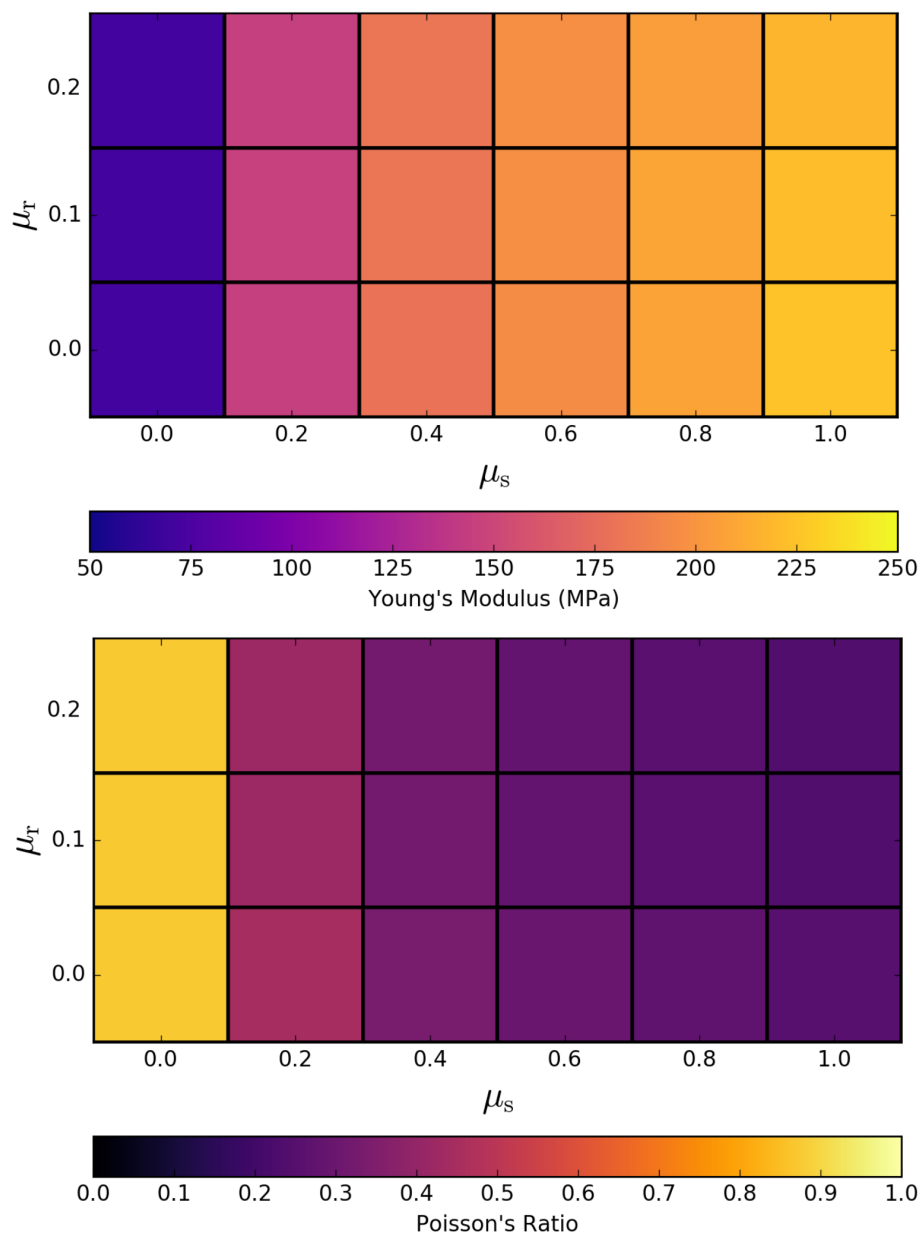


Figure 3.5: These plots show the measured macroscopic properties of grains under uni-axial stress for the case of a confining wall moving into the material at 0.2 m/s, and for restitution coefficients of 0.9. The top plot shows the range in Young's moduli that we find as a function of friction parameters. The bottom plot shows the corresponding Poisson's ratio for each combination of friction parameters. The static friction coefficient has a stronger influence on both macroscopic properties of the grains.

deviation of 0.1 mm. The distribution is cut off at 1 standard deviation. This is done to prevent the grains from crystallizing or packing too closely together. The spring constant of each grain is set such that the typical propagation speed of an impact matches that listed in Table 3.1 across the grain. This is consistent with previous impact simulations that use a soft-sphere approach (Wada et al., 2006).

We conducted low-speed impact cratering simulations onto two different granular materials: glass beads and dry sand. For impact experiments onto glass, we use coefficients of restitution parameters derived from previous studies (Schwartz et al., 2013):  $\epsilon_n$  and  $\epsilon_t \sim 0.9$ . Based on the uni-axial compression tests and matching the friction angle of  $22^\circ$ , we use  $\mu_s = 0.4$ , and  $\mu_r = 0.1$ . The simulated glass beads have a Young's modulus  $\sim 150$  MPa and a Poisson ratio of 0.31. For impact experiments onto dry sand, we use coefficients of restitution parameters similar to that of gravel (Yu et al., 2014):  $\epsilon_n$  and  $\epsilon_t \sim 0.55$ . Based on the uni-axial compression tests and matching the friction angle of  $35^\circ$ , we use  $\mu_s = 0.8$ , and  $\mu_r = 0.2$ . The simulated dry sand has a Young's modulus  $\sim 200$  Mpa and a Poisson ratio of 0.23. These values are slightly different than those reported by Holsapple (2016). Any divergences of our simulations with the lab experiments may result in part from these differences. The impactor has a diameter of 2.54 cm. Its density is varied between that of steel, aluminum, and nylon (7.6, 2.7, and 1.15 g/cm<sup>3</sup>, respectively).

Fig. 3.6 shows the outcome of our impact simulations onto dry sand. The shape of each data point represents whether it is a simulation (x's) or lab (circles) result. The colors map the impactor's material type (density). For each case (unique impact speed and projectile material), we performed three separate simulations with

different initializations of the granular bed in order to obtain some measure of the uncertainty of our predictions. The error bars plotted here represent 1 standard deviation in our measurements for each unique case. For the lab experiments, the data provided has 5 to 6 cases for each impactor density and impact speed. For each case, the mean value of the measured penetration depths is plotted. The error bars show the standard deviation of the data. Overall we find that our results match the lab experiments fairly well. The penetration depths that we measure trend in the same manner as that of the lab experiments. For the nylon and aluminum cases we find very close matches. However, for the steel cases we find that the simulated projectiles penetrate deeper. In general, we demonstrate that we can reliably match the penetration depths to within a few mm for these cases at  $1g$ .

In Fig. 3.7 we compare simulation results of impacts onto glass beads to the corresponding lab experiments. For almost all cases we see a good match between the simulation outcome to the lab data. The general trends in the data are similar to that of the lab experiments. As expected, higher impactor densities and higher impact speeds result in larger penetration depths. The one data point that deviates wildly from the experiments is the 4.38 m/s case for nylon.

### 3.4.3 Gravity Dependence

Since we have shown that we can match the experimental data in  $1g$ , we proceeded to run a suite of simulations in low gravity for the case of an aluminum impactor on dry sand. We performed simulations for a range of impacts speeds at

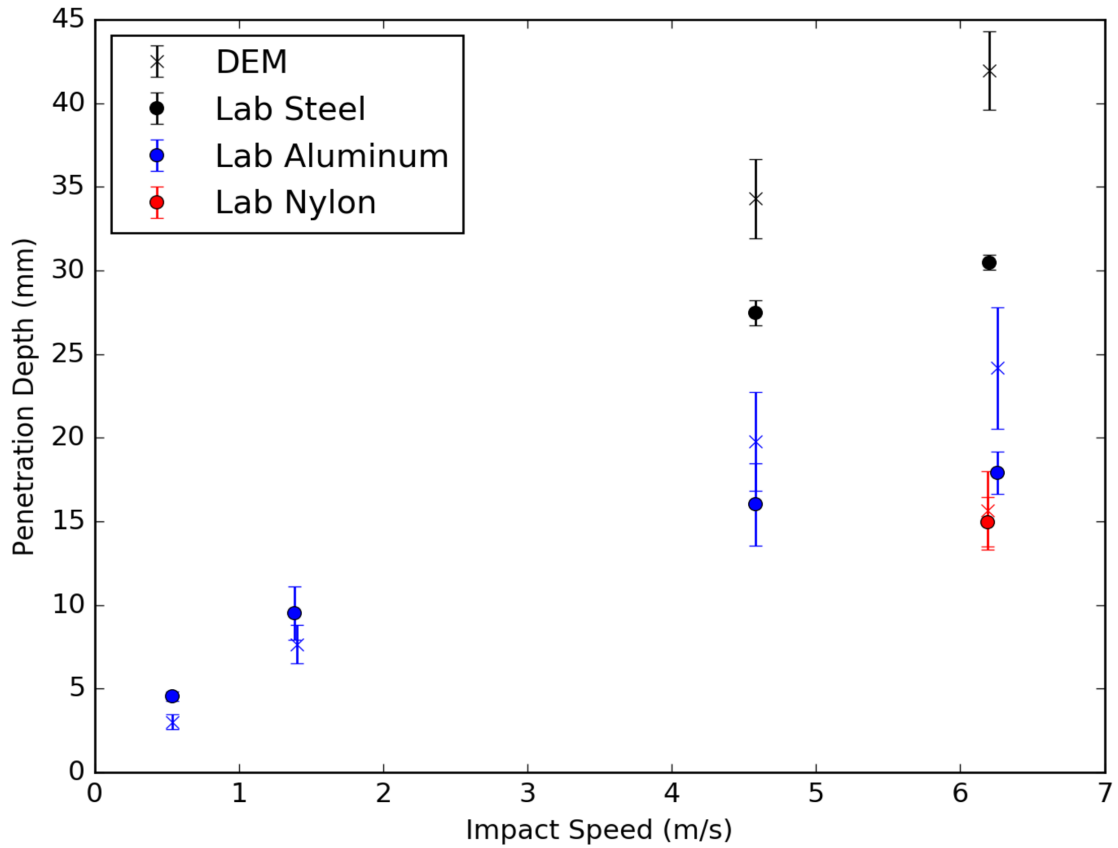


Figure 3.6: Comparison of simulations (x's) to laboratory experiments (circles) of a spherical impactor dropped in to a bed of dry sand. The black, blue, and red circles represent the penetration depth of steel, aluminum, and nylon impactors, respectively. The black, blue, and red x's are the corresponding outcomes of numerical simulations.

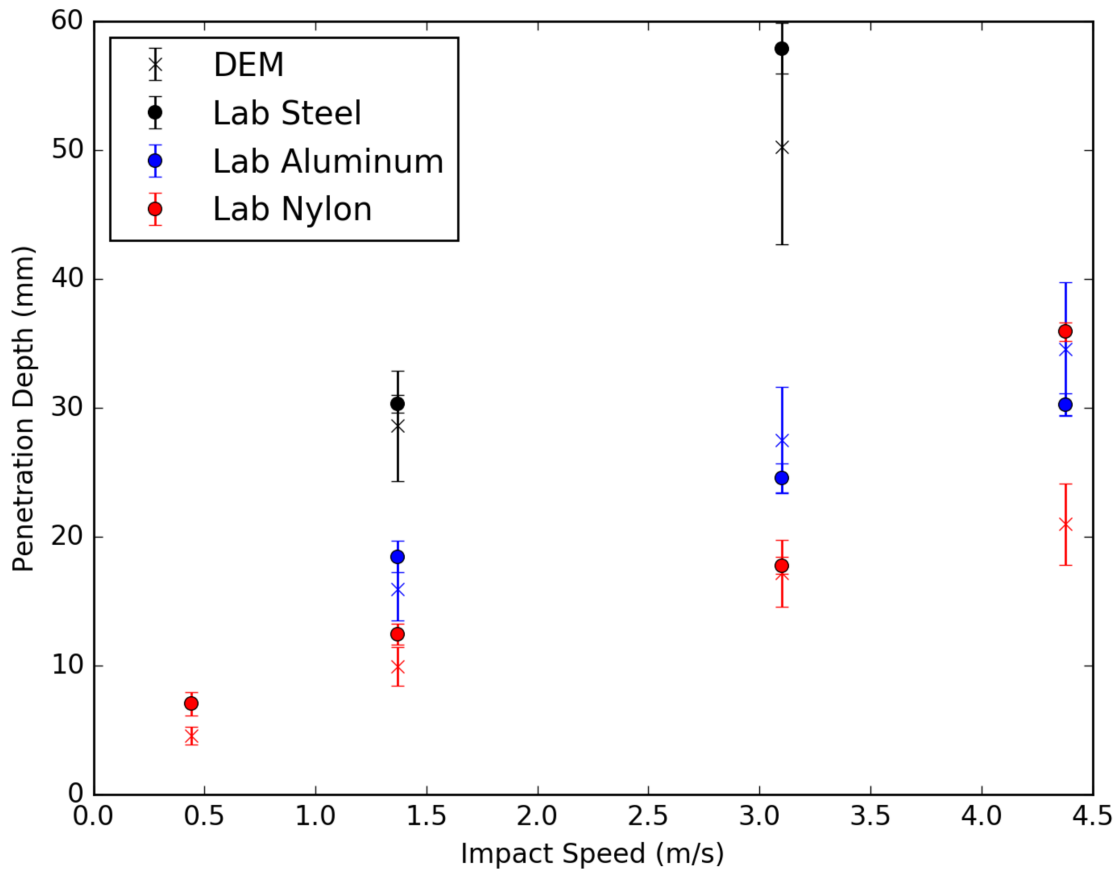


Figure 3.7: Comparison of simulations (x's) to laboratory experiments (circles) of a spherical impactor dropped into a bed of glass beads. The black, blue, and red circles represent the penetration depth of steel, aluminum, and nylon impactors, respectively. The black, blue, and red x's are the corresponding outcomes of numerical simulations.

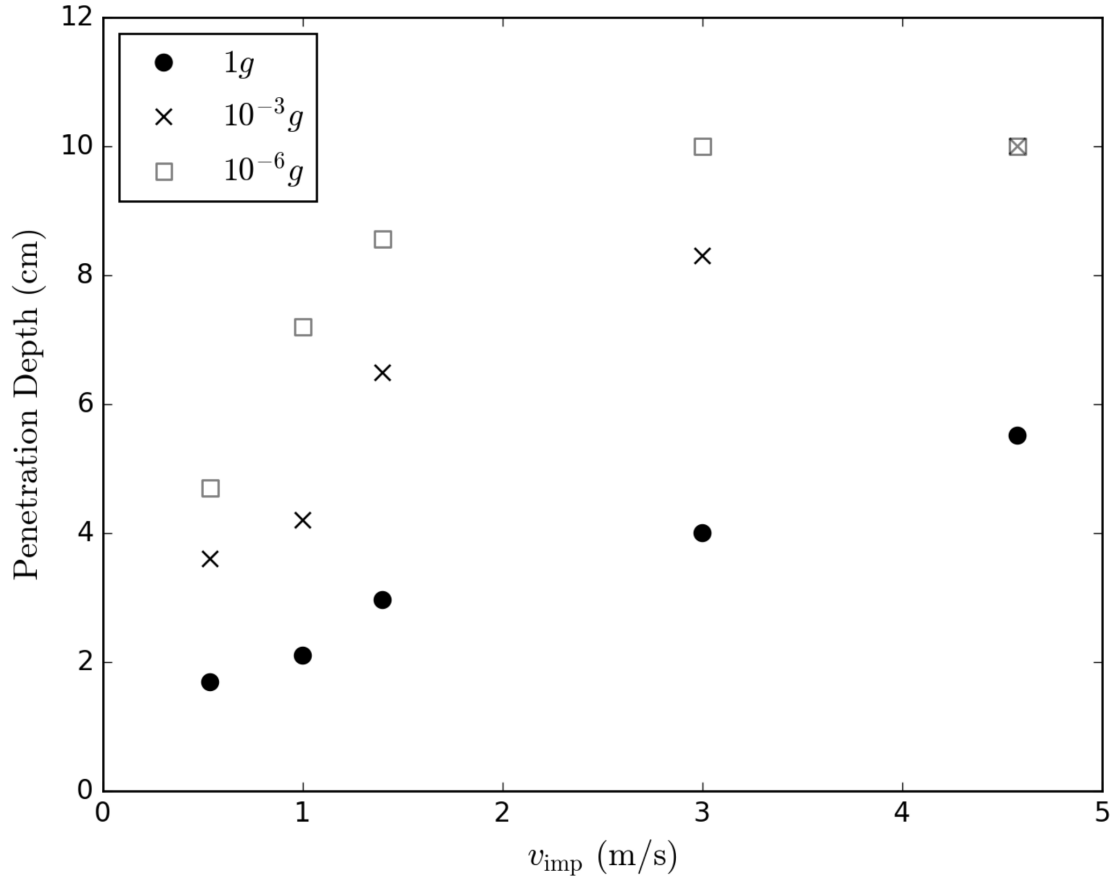


Figure 3.8: Simulations of an aluminum impactor onto dry sand at different gravities. For the low-gravity cases, the impactor reaches the very bottom of the container for the highest impact speed.

$1g$ ,  $10^{-3}g$ , and  $10^{-6}g$ . Fig. 3.8 plots the final penetration depth of the impactor as a function of impact speed for the three gravity cases. There is a clear indication from our simulations that penetration depth increases as the local gravity decreases. At higher penetration depths, the impactors start interacting with the bottom of the cylindrical container and reach the very bottom. Nevertheless, the low-speed impacts show a clear trend with gravity that contradicts recent results by Nakamura et al. (2013) and Altshuler et al. (2014).

According to [Nakamura et al. \(2013\)](#), the deceleration of a projectile may be described as

$$F = -k_0 S \rho g z - k_1 v - \frac{1}{2} C_d \rho S v^2, \quad (3.13)$$

where  $F$  is the force on the impactor by the granular medium,  $\rho$  is the density of the granular material,  $z$  is the depth of the impactor,  $C_d$  is the drag coefficient,  $S$  is the cross-sectional area of the impactor,  $k_0$  is a dimensionless parameter that encodes the physical characteristics of the grains (porosity, grain size, and surface roughness), and  $k_1$  is a constant that represents the viscous characteristics of the grains. The three components of the force law represent a depth-dependent lithostatic pressure term (first term), a speed-dependent viscous-like drag term (second term), and a speed-squared-dependent inertial-drag term (third term). Of these three components, only the first, the lithostatic pressure term, has a gravity dependence. By measuring the contributions of each term to the deceleration of the impactor, [Nakamura et al. \(2013\)](#) found that the lithostatic pressure term contributes only 1/40th of the pressure compared to the inertial drag term. This suggested that there should be no gravitational dependence for the penetration depth, since the lithostatic pressure has a negligible effect even at  $1g$ . Therefore, at even lower gravities, the difference in the penetration depth should be minimal.

However, our simulations do show that there is indeed a difference in the penetration depth with gravity. We postulate that the likely cause of this phenomenon is a change in the granular flow properties of grains in a low-gravity environment. This is likely caused by a dependence of the drag term  $C_d$  or the viscous term  $k_1$  on

gravity.

To test this idea, we can measure the force on the projectile as it penetrates through the granular medium. If the resistance to penetration is dominated by an inertial drag effect, then the magnitude of the force on the impactor is described by the third term on the right hand side of Eq. 3.13:

$$F = \frac{1}{2}C_d\rho Sv^2. \quad (3.14)$$

Fig. 3.9 shows the force on the aluminum impactor as a function of its speed for two different impact speeds (1.4 and 4.58 m/s) and gravity strengths ( $1g$  and  $10^{-3}g$ ). We also plot Eq. 3.14 for 5 different cases of the drag coefficient,  $C_d$ . We see that both cases have similar slopes initially. However, after some deceleration, large differences begin to emerge. For both cases, the  $1g$  case is better described by a drag force with a higher drag coefficient than the  $10^{-3}g$  case. The  $1g$  cases are best-fit by a drag coefficient  $C_d$  between 1.5 and 2.0, while the  $10^{-3}g$  cases are described by a drag force with a drag coefficient between 0.25 and 0.5. The data for  $10^{-6}g$  cases (not shown here for clarity) are best fit with  $C_d$  between 0.1 and 0.15. These results suggest that the drag properties of a granular system depend on the local gravity. We propose that the drag coefficient varies as  $\log(g)$ . This functional form suggests that changes in granular flow properties of regolith only begin to manifest in the very low-gravity environments of small bodies. This also explains the results of previous authors (Nakamura et al., 2013; Altshuler et al., 2014) who found virtually no dependence of the penetration depth with gravity because their studies were limited to local gravities of at most  $10^{-1}g$ .

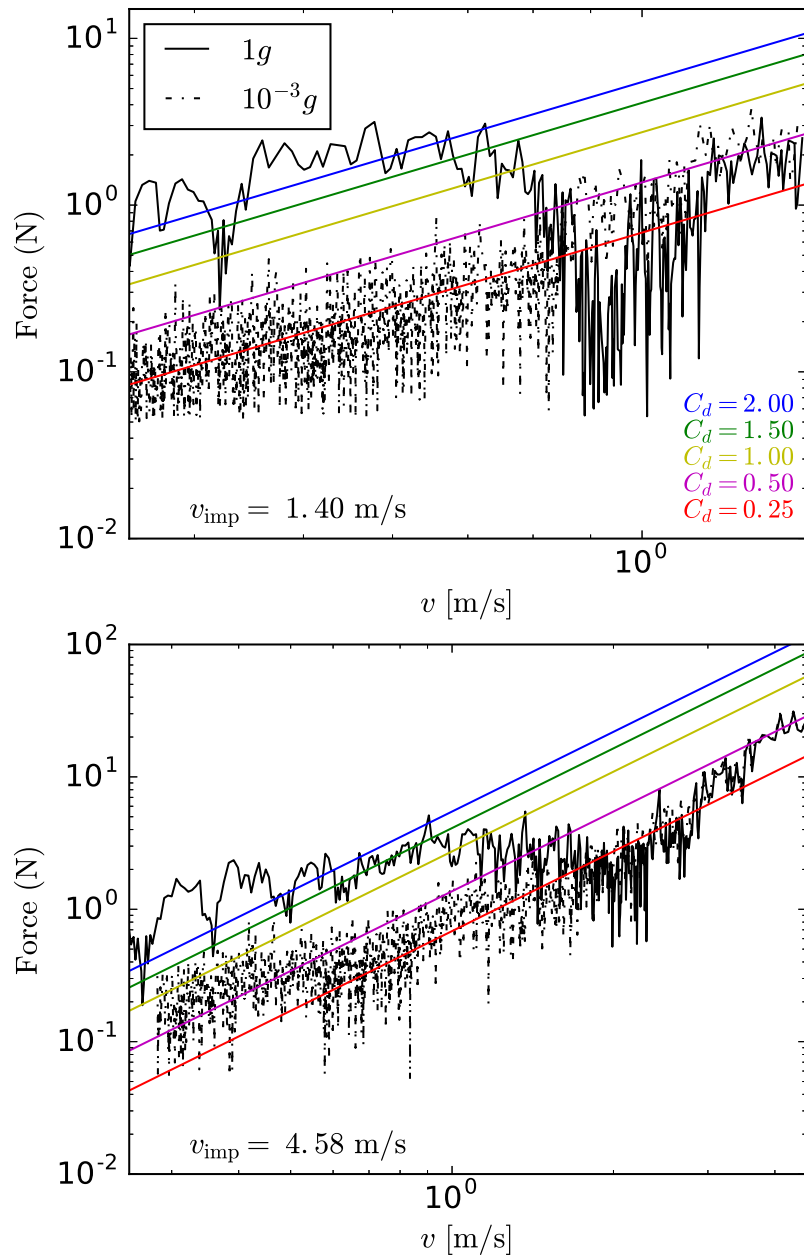


Figure 3.9: These plots show the force on an impactor as a function of its instantaneous speed. The top panel shows the cases for an impact speed,  $v_{\text{imp}}$ , of 1.4 m/s, while the bottom panel shows the cases with a  $v_{\text{imp}}$  of 4.58 m/s. The solid black curves represent impactors at  $1g$ , while the dot-dashed curve represent impactors at  $10^{-3}g$ . The blue, green, yellow, magenta, and red lines are Eq. 3.14 for a drag coefficient,  $C_d$ , of 2.0, 1.5, 1.0, 0.5, and 0.25, respectively.

### 3.5 OSIRIS-REx TAGSAM

In this section, we describe simulations of the TAGSAM penetrating a bed of granular material. The goal of this study was to construct an atlas of simulation results that can be used to detail the range of possible outcomes of a sampling attempt. This atlas of results has multiple uses. First, by comparing IMU data from the actual sampling attempt to our simulation results, we will be able to reconstruct what occurs to the S/C and TAGSAM during the sampling attempt. Second, we will be able to characterize the regolith since the response of the S/C and TAGSAM depends on the physical properties of the surface grains. Finally, observations during the orbital survey of Bennu will measure some of the surface properties of the grains, such as their mean size, size distribution, and mineralogy. If these characteristics are well constrained, then the sampling attempt can also act as a useful and rare impact experiment onto grains in a very-low-gravity setting. Based on the S/C's reaction, we may be able to make a measurement of the granular flow properties of grains in low gravity.

#### 3.5.1 Simulations

Fig. 3.10 shows snapshots of the TAGSAM penetrating a bed of grains. Our simulations are set up by first filling a cylindrical container with a height of 60 cm and a radius of 60 cm with  $\sim 150,000$  grains and allowing them to settle in low gravity ( $20 \mu\text{m}/\text{s}^2$  or  $\sim 2 \mu g$ ). Then, the actual touch-down simulation is conducted by placing the TAGSAM  $\sim 4$  cm from the surface of the granular bed. The TAGSAM has an

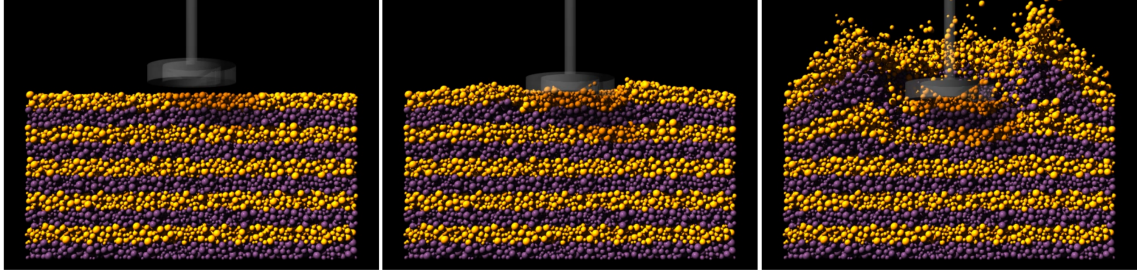


Figure 3.10: A model TAGSAM (visualized with some slight transparency) penetrates a bed of  $\sim 150,000$  particles (seen in cross-section) with an initial downward vertical speed of 10 cm/s in the microgravity environment of Bennu ( $g = 20 \mu\text{m} / \text{s}^2$ ). The cylindrical container has a height and radius of 60 cm.

initial downward speed of 10 cm/s. The total simulation time is 5 s, and the time step is  $10^{-5}$  s. Each grain has a density of  $2.7 \text{ g/cm}^3$ , typical of basalt. The regolith is composed of a power-law distribution of spherical particles (power-law index -2.5) with a minimum radius,  $R_{\min}$ , of 0.5 cm, and a maximum radius,  $R_{\max}$ , of 1.5 cm. We explored the effect of variations in the friction of the grains. However, we kept the normal and tangential coefficients of restitution constant at 0.55. These were the values adopted for dry sand in the uni-axial compression simulations described earlier.

An important aspect in these simulations was modeling the effect of the spring force between the TAGSAM and the S/C. The spring modulates the force that the S/C feels from the ground. It only engages when the TAGSAM feels a force greater than 67 N. The equations governing the effect of the spring were described previously in Eq. 3.6 and Eq. 3.8. Fig. 3.11 shows how the spring force is tracked (cyan curves), and its effect on the displacement between the TAGSAM and the

S/C (black curve), for a case with particles that have properties similar to that of dry sand. The numbered regions indicate key events in the dynamical interaction between the S/C, the spring, and the TAGSAM:

1. The TAGSAM feels a force from the ground that exceeds the 67 N threshold and the spring engages and starts compressing (time  $\sim 0.5$  s).
2. As the spring is further compressed, the spring force ramps up (as described by Eq. 3.11), until the displacement reaches a minimum, then begins increasing (time  $\sim 1.7$  s).
3. Afterwards, the spring expands, and the spring force is described by Eq. 3.12 instead. This continues until we reach the 0 cm hard stop (time  $\sim 3.3$  s).
4. At this point the spring is no longer engaged and the ground force is below the spring threshold. The spring force remains at zero until the end of the 5-second simulation.

In order to put some more context into the behavior of this dynamical system, we analyzed the time evolution of the ground force. Fig. 3.12 shows the magnitude of the force imparted by the grains on the TAGSAM head (red scatter points, right axis). Furthermore, we show the vertical distance from the surface of the S/C (purple curve) and TAGSAM (blue curve, left axis).

Overall, the force profile begins with a sharp peak and then proceeds in a constant-force-step profile. The magnitude of the force at each step is roughly equal to the spring force as determined by Eq. 3.11 and Eq. 3.12. The numbered regions

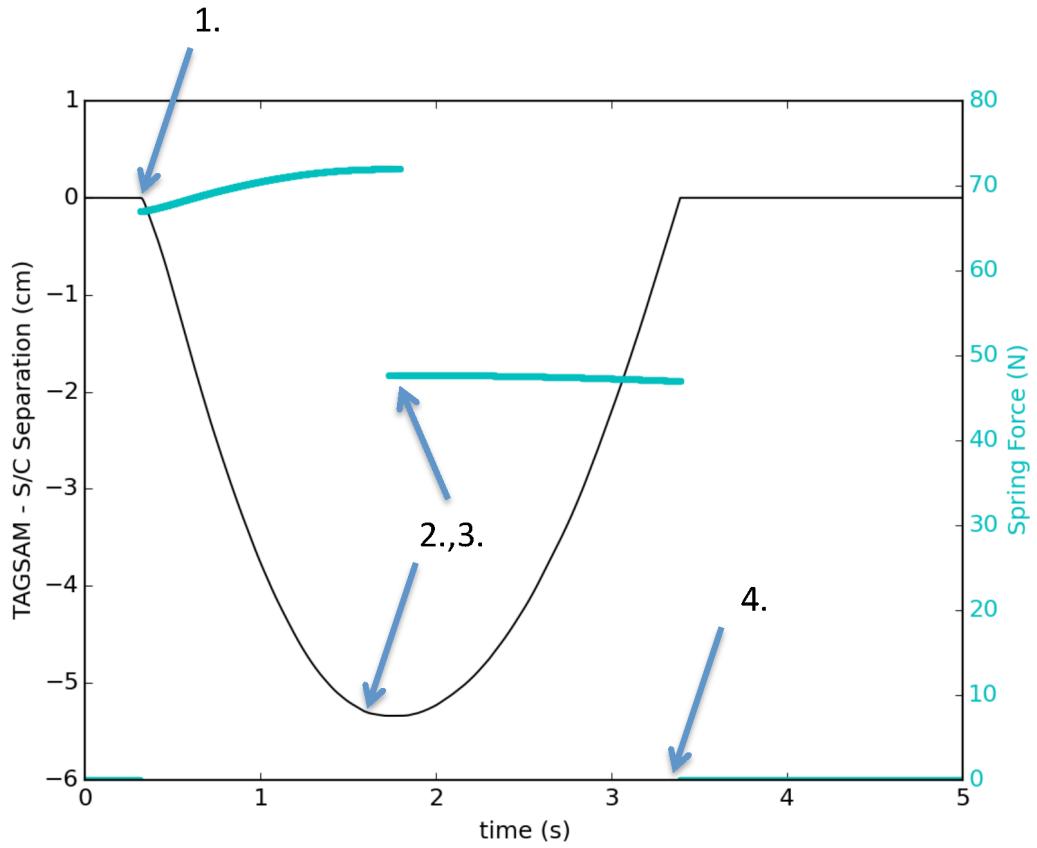


Figure 3.11: Plot of the displacement between the S/C and TAGSAM (black curve) as a function of time. Changes in the relative positions of the S/C and TAGSAM are driven by the spring that connects the two objects. The spring force (cyan curve) engages after the TAGSAM feels a ground force that exceeds 67 N. The force by the spring depends on whether it is undergoing compression or expansion. This behavior is described by Eq. 3.11 and Eq. 3.12. See text for details on numbered key events.

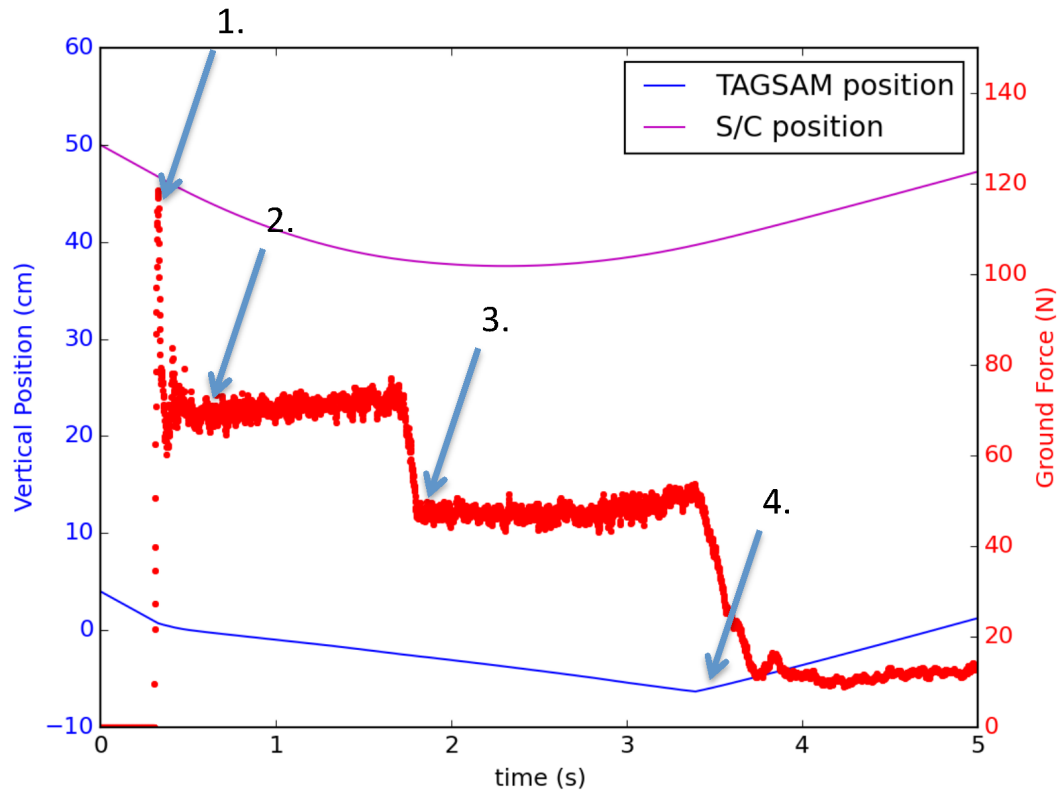


Figure 3.12: Plot of the ground force on the TAGSAM (red scatter points, right axis). On the same plot, we show the vertical distance from the surface of the TAGSAM (blue curve, left axis) and the S/C (purple curve, left axis). See text for details on numbered key events.

on the plot indicate key events:

1. At  $t \sim 0.5$  s, the TAGSAM makes contact with the ground and experiences a sharp impulse of  $\sim 120$  N. The spring immediately engages as the force threshold of 67 N is exceeded.
2. The spring engagement causes a force balance between the downward moving TAGSAM and the ground. The force by the ground on the TAGSAM is roughly at the spring threshold (67 N). The TAGSAM has a slight downward speed of 2 cm/s. Due to the force balance this remains roughly constant.
3. Once the S/C stops moving downwards, the spring begins to expand. This causes the spring force to drop to the 47–49 N range (Eq. 3.12). Since the TAGSAM is forced downward by the spring, it continues to interact with the ground in this force range. The ground pushes back at the TAGSAM with an equal force. The TAGSAM remains in force balance.
4. Once the S/C begins to move up, the spring expands to the 0 cm hard stop. At this point we have a perfectly inelastic collision between the TAGSAM and S/C (Eq. 3.9). The S/C drags the TAGSAM upwards with it.

Fig. 3.11 and Fig. 3.12 show how the spring dictates the dynamical interaction between the TAGSAM and the S/C, as well as modulating the total force that the TAGSAM feels during the sampling attempt. In the following section, we discuss how we model this interaction for different surface mechanical properties and how we will be able to infer these properties from the spacecraft’s response.

### 3.5.2 Penetration Depth

In order to quantify the effect that different materials might have on the sampling attempt, we conducted simulations that explore a wide parameter space of two material friction coefficients (static and rolling). These parameters combine to provide a proxy for material roughness (a parameter that may also be influenced by grain size, size distribution, shape, etc.). Fig. 3.13 shows a map of the penetration depth of the TAGSAM as a function of the rolling and static coefficients of friction.

We see that the penetration depth of the TAGSAM depends sensitively on the friction properties of the grains. When the static friction coefficient is low ( $< 0.4$ ) or when there is no rolling friction, the granular bed offers almost no resistance and the S/C - TAGSAM assembly is able to sink into the granular bed almost unimpeded. A final penetration depth of  $\sim 50$  cm would signify a freely falling spacecraft. If the regolith surface were made of material with friction properties similar to glass beads ( $\mu_s = 0.4$ , and  $\mu_r \sim 0.1$ ), the spacecraft would feel very little resistance, and sink deeper than  $\sim 20$  cm after 5 s. If instead the material were like dry sand ( $\mu_s = 0.8$ , and  $\mu_r \sim 0.2$ ), the spacecraft would feel a strong response from the granular bed, and only penetrate 2–3 particle diameters into the granular bed ( $\sim 4$  cm). While we show that there can be a wide range of responses to the penetration, the results clearly segregate into two general categories: almost unimpeded penetration (yellow squares) and strong resistance (light and dark red squares). Realistic materials will almost always have friction properties that would place them in one of these red squares, whose lowest friction value corresponds to a material with an angle of

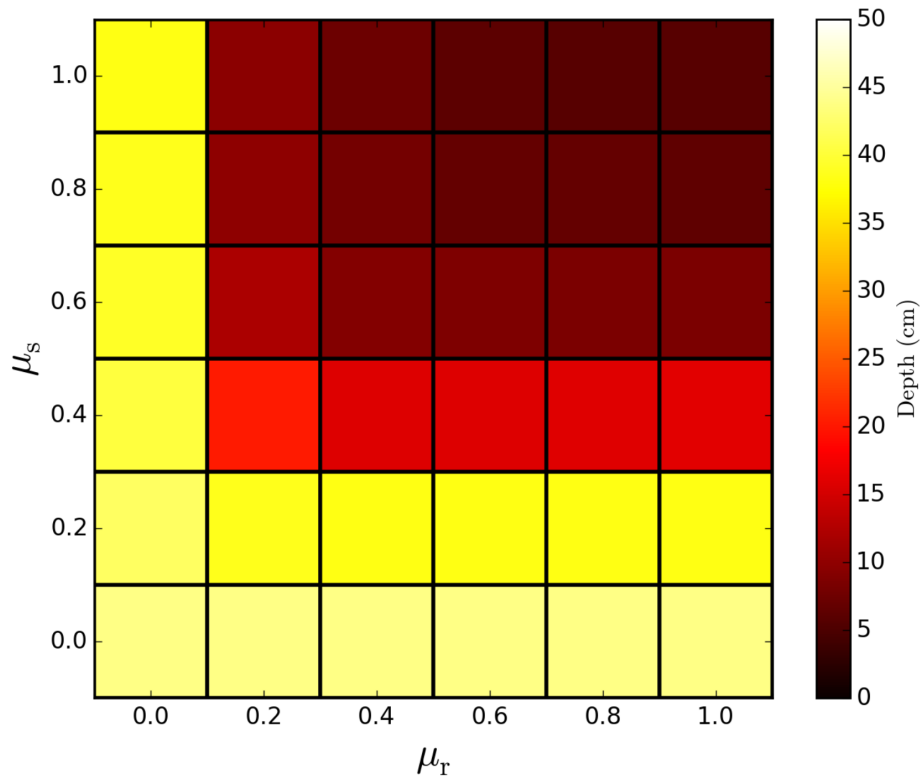


Figure 3.13: A map of the maximum penetration depth that the TAGSAM reaches for each combination of static and rolling friction parameters. Whiter/yellow colors signify more penetration, and red-der/blacker colors signify less penetration.

friction of  $\sim 22^\circ$ . Therefore, the outcome of the actual sampling attempt will likely result in the TAGSAM penetrating into at most 20 cm of the regolith bed.

In order to understand why the penetration depth depends so sensitively on the friction properties of the grains, we can draw comparisons with recent studies into shear-thickening fluids (Mukhopadhyay et al., 2014). Mukhopadhyay et al. (2014) conducted studies on granular material (cornstarch) suspended in fluids. Such fluid suspensions have the surprising property of resisting heavy loads when the impact speed of the projectile is sufficiently high. As a projectile impacts a fluid suspension, a shock wave travels through the suspension that causes the entire medium to dilate, leading to the interlocking of nearby grains.

It is possible that a granular material in low gravity can behave like grains suspended in a fluid. Once the sampler makes contact with the surface, the material underneath the sampler shear-thickens. As the material underneath the sampler expands, the highly frictional grains form more particle contacts. This creates a transition where the grains move from fluid-like flow to a solid-like response. Fig. 3.14 shows snap-shots of the end of two simulation. The top row shows a case with high friction ( $\mu_s, \mu_r = 0.8$ ), and the bottom row shows a case with low friction ( $\mu_s, \mu_r = 0.2$ ). The figures on the right show the change in the column density of grains from the beginning of the simulation. The large swaths of dark blue show regions where particles have been excavated. While the case with low friction shows regions of over-densities (red), the case with high friction sees some slight under-densities. This suggests that particles with high friction are able to shear-thicken by dilating. This results in more grain-grain contacts, and stronger force chain networks

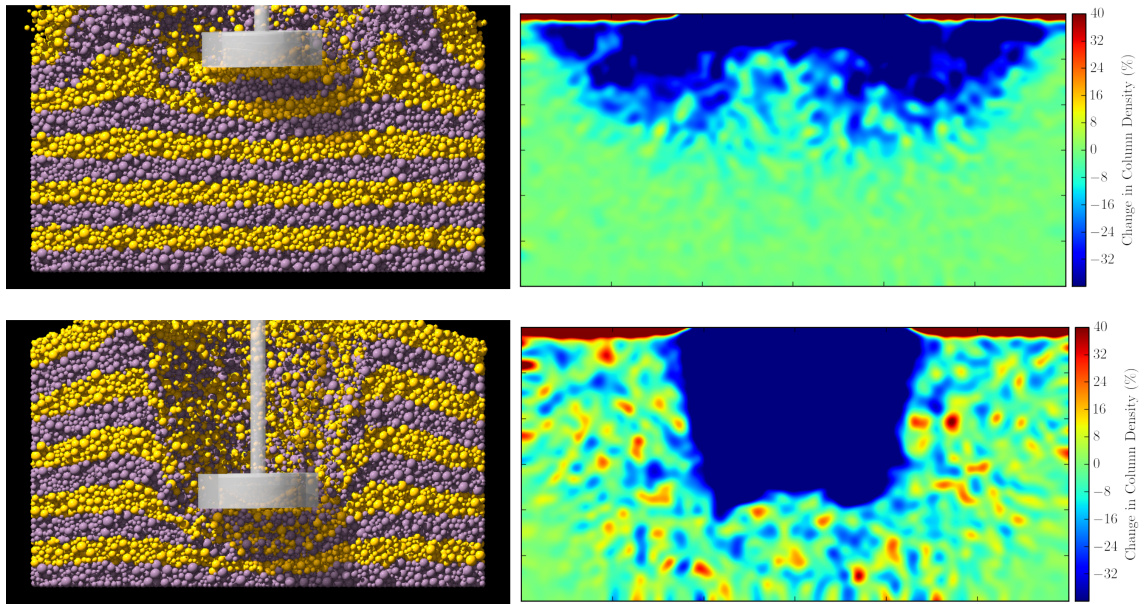


Figure 3.14: The plots on the left show the difference in the penetration depth of the TAGSAM for a case with high friction (top) and low friction (bottom) 5 seconds after initial contact. The plots on the right are corresponding maps of the column density through the granular bed. Bluer colors correspond to under-densities with respect to the initial density distribution of grains. Redder colors correspond to over-densities.

throughout the system, leading to an overall stronger material. For the other case, insufficient frictional contact causes the material to behave like a fluid in microgravity. The sampler plunges through, creating transient gaps and clusters.

### 3.5.3 TAG Reconstruct

We have demonstrated that friction properties of the grains play a crucial role in determining the final penetration depth of the TAGSAM. However, for most cases that mimic realistic grains, the range in penetration depths we find is relatively narrow. For grains with angles of friction similar to that of typical terrestrial rocks or sand ( $> \sim 30^\circ$ ), we expect the penetration depth to be  $< 10$  cm after 5 s. Therefore, in order to differentiate the outcomes for realistic materials, we analyze three different indicators: the force profile on the TAGSAM-S/C assembly, the change in the S/C speed, and the duration of spring compression. Using these indicators might allow us to more accurately reconstruct the sampling attempt, and determine the properties of the surface grains.

#### 3.5.3.1 Force Profiles

Since onboard accelerometers are limited to the S/C bus (no such devices will be on the TAGSAM head), our only indication of the type of material we will be interacting with (and the regolith's reaction to the sampling attempt) will be the data from S/C accelerometers. Therefore, any difference in the measured deceleration due to different materials would only be detected before the spring

has engaged. We analyzed four different profiles that span the range of expected material properties,  $\mu_s = 0.4\text{--}1.0$  and  $\mu_r = 0.4\text{--}1.0$ , to test whether any difference in the force profiles can be detected before the spring is engaged. Fig. 3.15 shows two cases with moderate friction. The left panel shows a case where both  $\mu_s$  and  $\mu_r = 0.4$ . The right panel shows a case where both  $\mu_s$  and  $\mu_r = 0.6$ . Both of these cases also exhibit a “stepped” force profile similar to that shown in Fig. 3.12. The “stepped” regions of the force profile indicate times when the spring is engaged. Therefore, the only valuable information that can be extracted is from the peak of the force profile. These two cases do show some differences in their overall force profile. In the left panel, the “steps” are shorter. For this case, the spring doesn’t compress very much and extends back to its original length relatively quickly. Once it does so, the TAGSAM and S/C dynamics are coupled again, and the reaction force on this assembly becomes much lower due to the drastic decrease in their downward speed. Thus, they are able to penetrate further into the granular bed. By the time the simulation ends, the S/C is close to stopping its downwards trajectory. The case with  $\mu_s, \mu_r = 0.6$  is slightly different. The spring is compressed for a longer time, allowing the S/C to slow down sufficiently to begin an upward trajectory that eventually leads to a 0 cm hard stop that drags the TAGSAM upwards. Furthermore, the initial impulse that the TAGSAM feels upon first contact is higher. Therefore, the TAGSAM is able to penetrate less in this case. Once the 0 cm hard stop is reached and the S/C-TAGSAM assembly begins moving upwards, the TAGSAM is embedded close to 10 cm into the regolith bed.

For even higher values of the friction coefficient, Fig. 3.16 shows that the force

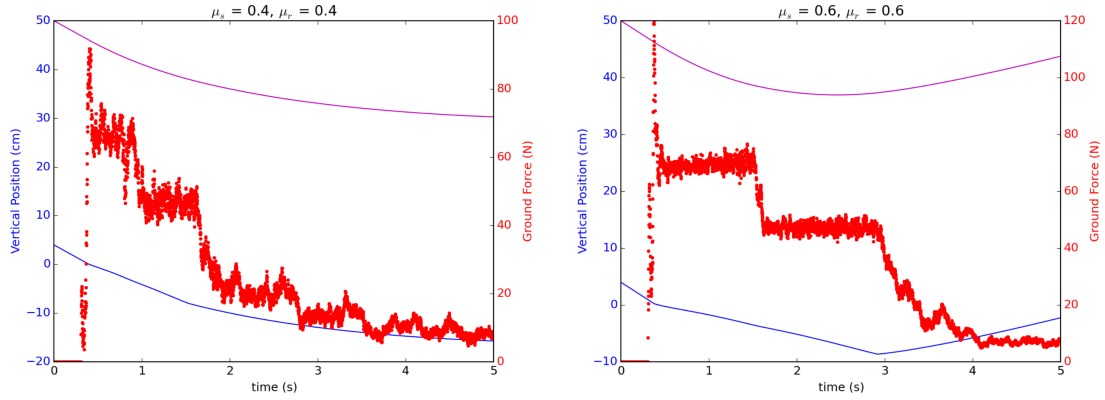


Figure 3.15: Force profiles for two cases with different friction properties. The left panel shows a case where both  $\mu_s$  and  $\mu_r = 0.4$ . The right panel shows a case where both  $\mu_s$  and  $\mu_r = 0.6$ . The ground force on the TAGSAM (red scatter points, right axis), the vertical distance from the surface of the TAGSAM (blue curve, left axis), and the S/C (purple curve, left axis) are shown.

profiles still have the “three-stepped” pattern. The left panel shows a case where both  $\mu_s$  and  $\mu_r = 0.8$ . The right panel shows a case where both  $\mu_s$  and  $\mu_r = 1.0$ . One key feature that differentiates these two cases is the peak of the force profile. The case with  $\mu_s, \mu_r = 1.0$  has a peak force (at  $\sim 130$  N) that is about 30 N higher than the case with  $\mu_s, \mu_r = 0.8$  (at  $\sim 100$  N). The lowest friction case presented here ( $\mu_s, \mu_r = 0.4$ ) follows this trend, as it has a peak force of  $\sim 90$  N. However, the case with  $\mu_s, \mu_r = 0.6$  (which has a peak force of 120 N) does not follow the general trend. Overall, a measurement of the peak force could be an indicator of the frictional properties of the granular matter. However, a calibration study with the actual instrument would be required if this technique were to be used for a measurement of the grain properties.

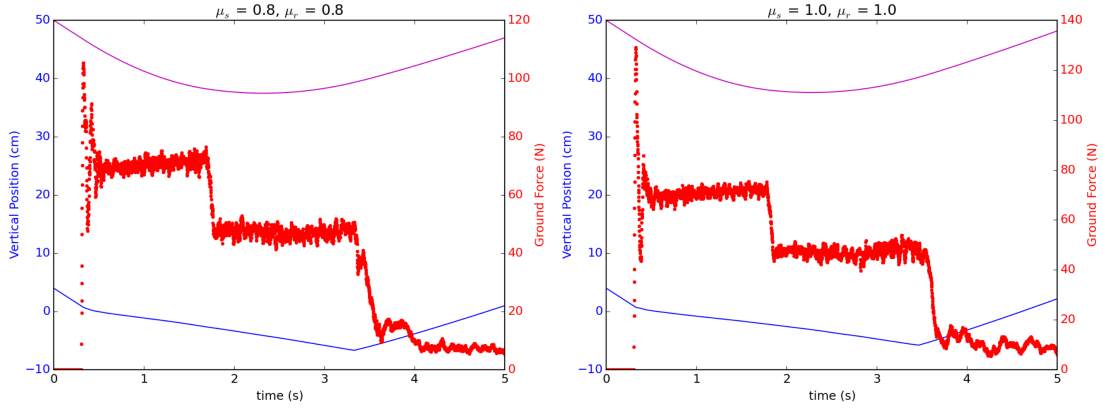


Figure 3.16: Force profiles for two cases with different friction properties. The left panel shows a case where both  $\mu_s$  and  $\mu_r = 0.8$ . The right panel shows a case where both  $\mu_s$  and  $\mu_r = 1.0$ . The ground force on the TAGSAM (red scatter points, right axis), the vertical distance from the surface of the TAGSAM (blue curve, left axis), and the S/C (purple curve, left axis) are shown.

### 3.5.3.2 S/C vertical speed

Since we will have no inertial measurements from the TAGSAM itself, a useful indicator for different regolith dynamics may be the behavior of the S/C. Fig. 3.17 compares the time evolution of the S/C's vertical speed for the range of material parameters discussed in the last section. Here, we clearly see that there is a marked difference in the S/C's deceleration for different material properties. The black and purple lines represent the upper end of our friction spectrum where things begin to behave in a similar manner (similar penetration depths and TAGSAM ground force profiles). At a simulation time of about 2 seconds (or about 1.5 seconds after initial contact), the effect of different materials on the deceleration profile becomes very noticeable (in order of increasing friction, the vertical speeds are:  $-3.7$ ,  $-1.7$ ,  $-1.2$ ,

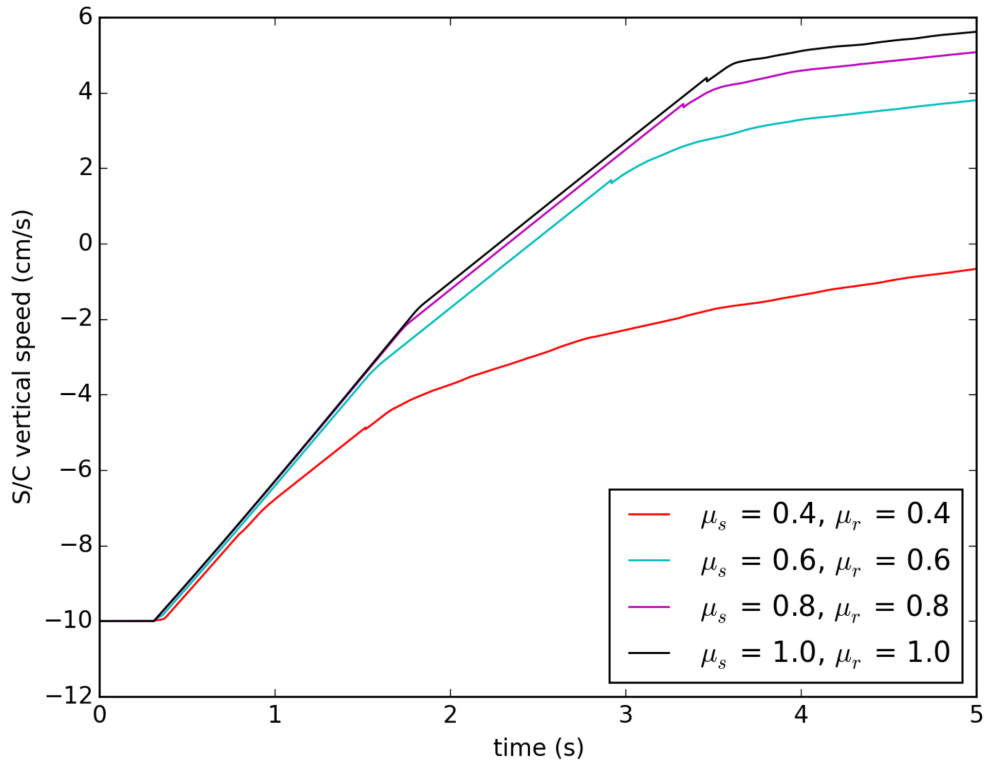


Figure 3.17: The vertical speeds of the spacecraft as a function of time. The red, cyan, magenta, and black curves represent cases where the grains have friction coefficient  $\mu_s$  and  $\mu_r = 0.4, 0.6, 0.8,$  and  $1.0,$  respectively. For different material types, the S/C will decelerate differently. The difference in deceleration becomes very noticeable  $\sim 2$  seconds after contact.

and  $-0.99$  cm/s). Therefore, by tracking the deceleration profile of the S/C, we may be able to determine the properties of the regolith itself. Furthermore, since each deceleration profile is unique, we would also be able to link this to the behavior of the TAGSAM, effectively reconstructing the sampling attempt.

### 3.5.3.3 Spring Compression Time

Finally, another possible indicator that would allow us to reconstruct the sampling attempt and determine regolith properties is the total amount of time the spring remains in a compressed state. Fig. 3.18 is a map of the total time a spring is compressed for each combination of  $\mu_s$  and  $\mu_r$ . By comparing the total time the spring compression time for different material properties, we see that there is some correlation with the rigidity of a material. This can be a useful diagnostic tool if the amount of compression can be measured in real time.

## 3.6 Conclusions & Future Work

This chapter presented a study of low-speed impacts onto granular material. While low-speed impacts have been studied by the granular science community (e.g., [Katsuragi & Durian 2007](#)) for some time now, the study of low-speed granular impacts on small solar system bodies has only recently emerged due to interest generated from spacecraft missions to asteroids and comets. The study of granular material in a low-gravity environment is still in its infancy. It is difficult to develop a deterministic theory for granular materials in any environment due to the fact that granular systems are composed of a large number of elements that interact through a non-linear combination of various forces (mechanical, gravitational, and electrostatic, for example) leading to a high degree of stochasticity. Therefore, numerical simulations are important for placing constraints on the range of possible behaviors that can be expected from a granular system.

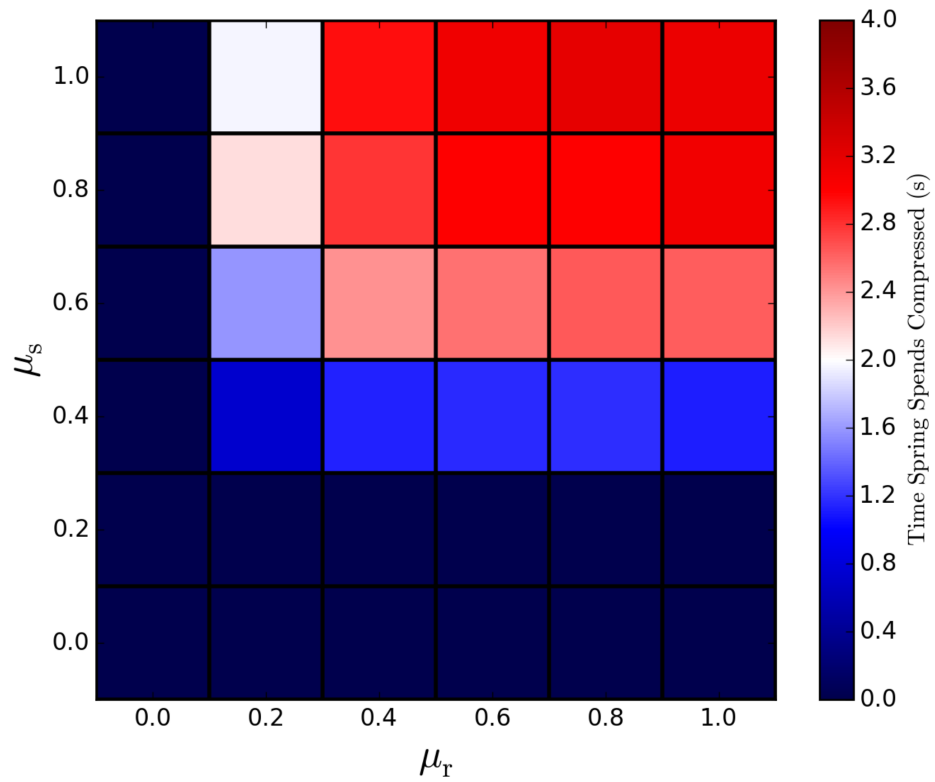


Figure 3.18: A map of the total time the spring between the S/C and TAGSAM is compressed. Redder colors signify more time, and bluer colors signify less time.

The OSIRIS-REx mission to Bennu will provide the community with a very unique low-speed impact experiment. We have demonstrated that the outcome of a sampling attempt by the TAGSAM can vary depending on the properties of the regolith. Granular material behaves more fluid-like in a low-gravity environment, and does not resist penetration as much as it would in  $1g$ . This was also demonstrated through low-speed impact experiments of an aluminum sphere onto dry sand. We first calibrated our simulation to the behavior of real granular material, and showed that we can replicate the results of laboratory experiments. Extending our simulations to low-gravity conditions, we showed that the penetration depth has a dependence on the local gravity. However, unlike previous results, which suggested that changes in penetration depth are likely due to the lack of lithostatic pressure in low gravity, we showed that it is more likely that it is a change in the granular flow properties of the material in low gravity that causes a change in the final penetration depth.

A key goal in this study was to demonstrate the ability of our simulation software to predict the outcome of a spacecraft's interaction with a regolith surface. We were able to create an "atlas" of simulation results that the future sampling attempt can be compared against. This "atlas" will be able to reconstruct the sampling attempt and possibly help determine the properties of the regolith. We studied the usefulness of three different indicators that might allow us to better utilize our atlas. The S/C deceleration profile and the spring compression time are promising metrics that might allow us to better constrain the regolith properties.

Future work will include extending the results presented here for grains with

non-zero cohesion. We expect the dynamical influence of cohesion to be similar to that of friction. Furthermore, we intend to use the software that was developed for this task on future space missions to small-body systems. In particular, we can simulate the dynamics of the MASCOT lander on Hayabusa-2 and the MASCOT-2 lander on the proposed Asteroid Impact Mission (AIM) under study at the European Space Agency (ESA).

## Chapter 4: Catastrophic Disruption of Gravitational Aggregates

### 4.1 Chapter Preface

The work presented in this chapter was published in the *Astrophysical Journal* (ApJ) as Ballouz et al. (2014), and in the *Planetary and Space Sciences Journal* as Ballouz et al. (2015). In this chapter, we carry out a systematic exploration of the effect of pre-impact rotation on the outcomes of low-speed collisions between planetesimals modeled as gravitational aggregates. A rotating body has lower effective surface gravity than a non-rotating one and therefore might suffer more mass loss as the result of a collision. What is less well understood, however, is whether rotation systematically increases mass loss on average regardless of the impact trajectory. This has important implications for the efficiency of planet formation via planetesimal growth, and also more generally for the determination of the impact energy threshold for catastrophic disruption (leading to the largest remnant retaining 50% of the original mass), as this has generally only been evaluated for non-spinning bodies. We find that for most collision scenarios, rotation lowers the threshold energy for catastrophic dispersal. For head-on collisions, we develop a semi-analytic description of the change in the threshold description as a function of the target’s pre-impact rotation rate, and find that these results are consistent with the “uni-

versal law” of catastrophic disruption developed by [Leinhardt & Stewart \(2009\)](#). Using this approach, we introduce re-scaled catastrophic disruption variables that take into account the interacting mass fraction of the target in order to translate oblique impacts into equivalent head-on collisions. Furthermore, we analyze how rubble pile of different material types catastrophically disrupt. We find that material with higher dissipative and friction properties requires larger impact energy to catastrophically disrupt. However, we find that the increase in mass loss due to pre-impact rotation is constant across different material types.

## 4.2 Background

Much of the evolution of small Solar System bodies (SSSBs) is dominated by collisions, whether from the initial build-up of planetesimals ([Lissauer, 1993](#)) or the subsequent impacts between remnant bodies that exist today ([Michel et al., 2004](#)). Outcomes of collisions between SSSBs are divided into two regimes: those dominated by material strength and those dominated by self-gravity ([Holsapple, 1994](#)). The transition from the strength to the gravity regime may occur at body sizes as small as a few kilometers or less for basalt ([Benz & Asphaug, 1999](#); [Jutzi et al., 2010](#)). After their formation, planetesimals interacted with one another in a dynamically cold disk ([Levison et al., 2010](#)). This allowed planet-size objects to form through collisional growth.

Since the dominant source of confining pressure for planetesimal-size SSSBs is self-gravity, rather than material strength, they can be assumed to be gravitational

aggregates (Richardson et al., 2002). Hence, the collisions can often be treated as impacts between rubble piles, the outcomes of which are dictated by collisional dissipation parameters and gravity (Leinhardt et al., 2000; Leinhardt & Richardson, 2002). Understanding the effects that contribute to changes in the mass (accretion or erosion) of gravitational aggregates is important for collisional evolution models of the early solar system (Leinhardt & Richardson, 2005; Weidenschilling, 2011). The outcomes of impacts in these models are parameterized through a catastrophic disruption threshold  $Q_D^*$  (Benz & Asphaug, 1999), which is the impact energy per unit mass (termed the specific impact energy) required to gravitationally disperse half the total mass of the system, such that the largest remnant retains the other half of the system mass. However, few studies have accounted for the effect of pre-impact rotation on the size evolution of SSSBs.

A rotating body has lower effective surface gravity than a non-rotating one (with the difference being greatest for surface material at the equator and decreasing for material closer to the rotation axis). Therefore, a rotating body might suffer more mass loss as the result of a collision. A recent laboratory study by Morris et al. (2012) suggests this is true for solid bodies. What is less well understood, however, is whether rotation systematically increases mass loss on average regardless of the impact trajectory.

In order to explain the collisional evolution of rotation rates of asteroids, Dobrovolskis & Burns (1984) evaluated analytically the sensitivity of mass loss to rotation for cratering impacts on rigid bodies. They found that the angle-averaged mass loss for cases with rotation is enhanced by factors of  $\sim 10\text{--}40\%$  compared to

cases without rotation for rotation speeds  $\sim 40\text{--}80\%$  of the critical spin rate (see their Fig. 2). Analytic and numerical work by [Cellino et al. \(1990\)](#) showed that catastrophic disruptions, rather than cratering events, were a bigger contributor to the rotational evolution of asteroids through an angular momentum “splash” process; however, they and subsequent authors [Love & Ahrens \(1996\)](#) focused on the effects of spin-state evolution change rather than mass loss.

Other authors have included pre-impact rotation in their numerical simulations of planetesimal and protoplanet collisions; however, except for [Takeda & Ohtsuki \(2009\)](#) none have systematically studied its contribution to mass loss in the dispersive regime. Using a hard-sphere model, [Leinhardt et al. \(2000\)](#) performed numerical simulations of collisions of equal-size bodies with pre-impact rotation; however, their work focused on the effect of rotation on the shape of the largest remnant. [Canup \(2008\)](#) studied the effect of pre-impact rotation on lunar formation; however, the work focused on a non-dispersive collision regime. Using a soft-sphere collision code, [Takeda & Ohtsuki \(2009\)](#) performed simulations of hyper-velocity impacts on rotating  $\sim 10\text{-km}$  size bodies. They found that mass loss is only sensitive to rotation when the target has an initial spin period close to break-up; otherwise, the collisional energy needed to disrupt a rubble-pile object is not affected by initial rotation. They argued that, upon collision, the ejection speeds of fragments in the hemisphere rotating away from the projectile (prograde direction) are accelerated by the initial rotation, but this is balanced by fragments in the hemisphere rotating toward the projectile (retrograde direction) being decelerated. However, their analysis was restricted to targets with initial rotations of 2.6 and 4.6 revolutions

per day (9.23 and 5.58 hours, respectively). Furthermore, their work focused on the efficiency of angular momentum transfer in catastrophic collisions.

In this chapter, we expand upon the work of previous authors by performing a systematic study of the effect of pre-impact rotation on the energy required to disperse material from km-size gravitational aggregates rotating with spin periods of 3, 4.5, and 6 hours. We solve numerically the outcomes of rubble-pile collisions using our soft-sphere discrete element method (SSDEM) collisional code and the numerical gravity solver, which is needed to accurately model the reaccumulation stage. SSDEM has the numerical resolution to determine the mechanics involved in enhancing or diminishing the amount of mass loss associated with collisions onto a rotating target. SSDEM permits realistic modeling of multi-contact and frictional forces between discrete indestructible particles. Thus, it is well suited to study low-speed (a few to tens of  $\text{m s}^{-1}$ ) impacts, as it can robustly model collisions that do not produce irreversible shock damage to material (as in hypervelocity,  $\text{km s}^{-1}$  impacts). In the quasi-steady-state collisional system generally present in a protoplanetary disk, impact speeds are typically on the order of the escape speed of the largest body in the vicinity. Until the largest body becomes protoplanet sized, impacts will be typically at speeds less than the sound speed of the assumed rocky material. Hence, we limit our study to collisions that occur at subsonic speeds. Most significant collisions today occur at supersonic speeds; however, studies of supersonic collisions require the use of shock physics codes, which include the effects of irreversible shock deformation.

Furthermore, we attempt to revise the dependence of catastrophic disruption

on the impact parameter  $b = \sin \theta$ , where  $\theta$  is the angle between the projectile’s path and the target’s center at impact (see Section 4.3.2). Previous studies (Canup, 2008; Leinhardt & Stewart, 2012) have shown that the increase in the threshold for catastrophic disruption for oblique impacts is due to a reduction in interacting projectile mass. These authors provide a formulation parameterized by the fraction of interacting mass,  $\alpha$ . We show that this does not account adequately for the increase in the catastrophic dispersal threshold for impacts with  $b \neq 0$  but  $\alpha \sim 1$  (impacts where most of the projectile interacts with the target). We discuss a possible revision to the formulation of the catastrophic disruption variables that includes the effective interacting target material. By only taking into account the mass of material that interacts in the collision, oblique impacts are rescaled into equivalent head-on collisions such that they are well described by the so-called “universal” law for catastrophic disruption (Leinhardt & Stewart, 2012).

Our results have important implications for the efficiency of planet formation via planetesimal growth, and for the determination of the impact energy threshold for catastrophic disruption, as this has generally only been evaluated for non-spinning bodies. In Section 4.3 we explain the computational methods and outline the parameter space that we explore. In Section 4.4 we provide our results. In Section 4.5 we discuss these results in the context of the “universal” law for catastrophic disruption and formulate a semi-analytic description of the dependence of catastrophic disruption on pre-impact rotation. We summarize and offer perspectives in Section 4.6.

## 4.3 Methodology

### 4.3.1 Rubble-Pile Model

Our simulations consist of two bodies with a mass ratio of  $\sim 1 : 10$ : a stationary target with mass  $M_{\text{targ}}$  and a projectile with mass  $M_{\text{proj}}$  ( $M_{\text{proj}} = 0.1M_{\text{targ}}$  for this work) which impacts the target at a speed of  $v_{\text{imp}}$ . Both the target and projectile are gravitational aggregates of many particles bound together by self-gravity. The particles themselves are indestructible and have a fixed mass and radius. In most of the simulations reported here, the only friction that is modeled is static friction, for which we assume  $\mu_s = 0.5$ , corresponding to an internal angle of friction of  $\tan^{-1}(\mu_s) \sim 27^\circ$ . However, we do discuss the dependence on material properties and SSDEM parameters in Section 4.5.3.

The rubble piles are created by placing equal-sized particles randomly in a spherical cloud and allowing the cloud to collapse under its own gravity with highly inelastic particle collisions. Randomizing the internal structure of the rubble piles reduces artificial outcomes due to the crystalline structure of hexagonal close packing (Leinhardt et al., 2000; Leinhardt & Richardson, 2002). Due to symmetry lines and planes in crystalline packing, there is a dependency of the collision outcome on the initial orientation of the target’s principal axes. To test the dependence of the collision outcome on initial orientation for a spherically collapsed rubble pile, a series of simulations was performed where the simulation parameters were kept constant except for the initial orientation of the target’s equatorial principal axes,

which were varied by increments of  $45^\circ$  about its polar axis. The results of these simulations show that, for a spherically collapsed rubble pile, the dependence of collision outcome on initial orientation is small (mass loss deviations of less than 1% from the mean).

For the simulations presented here, the target had an average radius of  $R_{\text{targ}} \sim 1.0$  km and bulk density of  $\rho_{\text{targ}} \sim 2$  g cm $^{-3}$ . The projectile had an average radius of  $R_{\text{proj}} \sim 0.5$  km and bulk density of  $\rho_{\text{proj}} \sim 2$  g cm $^{-3}$ . In order to determine accurately the physical properties (size, shape, mass, angular momentum) of the target after the collision, the rubble piles were constructed with a relatively high number of particles ( $N_{\text{targ}} = 10^4$ ,  $N_{\text{proj}} = 10^3$ ).

The collisional properties of the constituent particles are specified prior to each simulation. These values were fixed at  $\epsilon_n = 0.8$  (mostly elastic collisions with some dissipation) and  $\epsilon_t = 1.0$  (no sliding friction). Furthermore, since SSDEM models treat particle collisions as reactions of springs due to particle overlaps, the magnitude of the normal and tangential restoring forces are determined by the spring constants  $k_n$  and  $k_t = \frac{2}{7}k_n$ , respectively. For rubble-pile collisions, the value of  $k_n$  is given by

$$k_n \sim m \left( \frac{v_{max}}{x_{max}} \right)^2, \quad (4.1)$$

where  $m$  corresponds to the typical mass of the most energetic particles,  $v_{max}$  is the maximum expected speed in the simulation, and  $x_{max}$  is the maximum fractional particle overlap, which we set to be  $\sim 1\%$ . Thus, for our rubble-pile collisions with speeds  $\leq 10$  m s $^{-1}$ ,  $k_n \sim 4 \times 10^{11}$  kg s $^{-2}$ . The initial separation of the projectile and

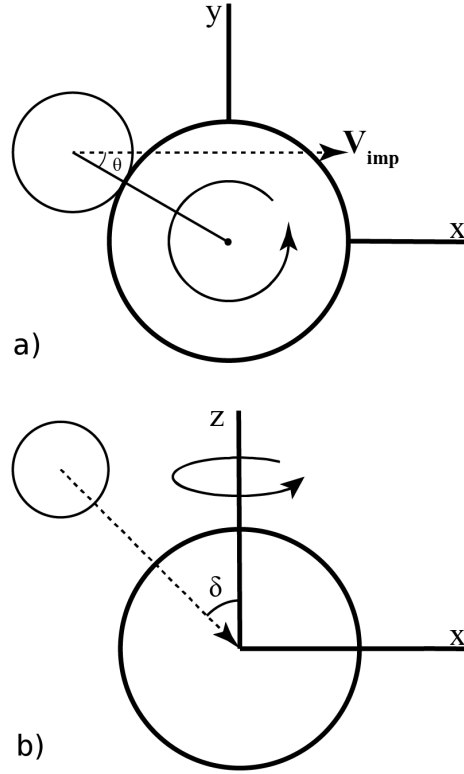


Figure 4.1: Schematic of two collision scenarios. Panel (a) shows a target impacted in its equatorial plane by a projectile moving left to right with speed  $v_{\text{imp}}$ . The impact angle  $\theta$  is the angle between the line connecting the centers of the two bodies and the projectile's velocity vector, at the time of contact. Panel (b) shows a projectile that impacts a target at an angle  $\delta$  between the rotation axis ( $z$ ) and the projectile's velocity vector.

target,  $d$ , for all cases was  $\sim 4R_{\text{targ}}$ , far enough apart that initial tidal effects were negligible. In order for the post-collision system to reach a steady state, the total run-time was set to  $\sim 3\times$  the dynamical time for the system,  $1/\sqrt{G\rho_{\text{targ}}} \sim 2$  hours. Furthermore, a time-step  $\Delta t \sim 3$  ms was chosen on the basis of the time required to sample particle overlaps adequately, for the choice of  $k_n$  and  $x_{\text{max}}$  given above.

### 4.3.2 Simulation Parameters and Collision Geometries

In order to probe the effect of rotation on collision outcome, simulations with the target rubble pile having an initial spin period  $P_{\text{spin}}$  of 3, 4.5, and 6 hours (values well above the spin break-up limit for a rubble pile of bulk density  $\sim 2 \text{ g cm}^{-3}$ ), were compared against runs with the target having no initial spin. For every spin period, simulations were done with a range of impact speeds such that there was adequate coverage of the gravitational dispersal regime (collisions that result in a system losing 0.1–0.9 times its total mass).

Furthermore, three different collision geometries were explored in this work, each of which depended on two different collision parameters. The first was the impact parameter  $b = \sin \theta$ , where  $\theta$  is the angle between the line connecting the centers of two bodies and the projectile’s velocity vector (see Fig. 4.1a). The second parameter was the angle  $\delta$ , which is the angle between the target’s rotation axis and the projectile’s velocity vector (see Fig. 4.1b). In this study, the effect of each parameter on the collision outcome was studied separately and compared against the standard case of a head-on collision. In a head-on collision, the projectile’s velocity vector is normal to the target’s rotation axis and is directed towards its center ( $b = 0$  and  $\delta = 90^\circ$ ).

For oblique impacts, the impact parameter  $b \neq 0$ . The impact parameter has a significant effect on the collision outcome because the total mass of the projectile may not completely intersect the target when the impact is oblique (Yanagisawa & Hasegawa, 2000; Canup, 2008; Leinhardt & Stewart, 2012). Thus,

when the projectile is large enough compared to the target, a portion of the projectile may shear off and only the kinetic energy of the interacting fraction of the projectile will be involved in disrupting the target. For any given collision speed, an oblique impact will erode less mass than a head-on collision. In this study, four values of  $b$  were used,  $\pm 0.5$  and  $\pm 0.7$ . For  $b > 0$ , the projectile impacts the target on the hemisphere that rotates towards the projectile, which we define as the retrograde hemisphere (see Fig. 4.1a). For  $b < 0$ , the projectile impacts the target on the hemisphere that is rotating away from the projectile, the prograde hemisphere. Hence, if the collision outcome is sensitive to initial rotation, then it is expected that the sign of  $b$  will also affect the amount of mass that is dispersed.

For non-equatorial impacts, the polar angle  $\delta < 90^\circ$  (see Fig. 4.1b). If the collision outcome is sensitive to the target's pre-impact rotation, then material from the target's equator may preferentially be dispersed due to its lower specific binding energy. However, it is uncertain whether the projectile more efficiently transfers its energy to the target's equator or to its poles upon impact. Hence, this study tests the effect of three different polar impact angles:  $\delta = 90^\circ$  (collisions directed at the target's equator),  $\delta = 45^\circ$ , and  $\delta = 0^\circ$  (collisions directed at the target's pole). In reality, most collisions will have a combination of non-zero values for both  $b$  and  $\delta$ .

## 4.4 Results

The collision of two rubble-pile objects typically results in either net accre-

tion, where the largest remnant has a net gain in mass compared to the mass of the target, or net erosion, where the target has lost mass. Alternatively, a collision could result in no appreciable net accretion or erosion (Leinhardt & Stewart, 2012). These latter types of collisions, called hit-and-run events, typically occur for grazing impacts that have an impact parameter,  $b$ , that is greater than a critical impact parameter  $b_{\text{crit}}$  (Asphaug, 2010), where  $b_{\text{crit}} = R_{\text{targ}}/(R_{\text{proj}} + R_{\text{targ}})$ . In this chapter, we focus on the dispersive regime, where impact velocities,  $v_{\text{imp}}$ , are greater than the escape speed from the surface of the target,  $v_{\text{esc}}$  (assuming no rotation). The impact speeds in our simulation range from 4–30  $v_{\text{esc}}$ , where  $v_{\text{esc}} \sim 1 \text{ m s}^{-1}$  is the escape speed from a spherical object with mass  $M_{\text{tot}} = M_{\text{proj}} + M_{\text{targ}}$  and density  $\rho_1 = 1 \text{ g/cm}^3$ . At impact speeds of 4–30  $v_{\text{esc}}$ , the mass of the largest remnant in each simulation,  $M_{\text{LR}}$ , ranges between 0.2–0.8  $M_{\text{tot}}$ . The amount of mass loss at the end of a simulation is found by measuring the final mass of the largest remnant and all material gravitationally bound to it (material with instantaneous orbital energy  $\leq 0$ ). Furthermore, we analyze the mechanics behind rotation-dependent mass loss by comparing the number of escaping particles that originate from different regions of the target. The result of each simulation is summarized in Table 4.1.

#### 4.4.1 Head-on Equatorial Collisions

For the nominal case of an equatorial-plane head-on collision,  $b = 0$  and  $\delta = 90^\circ$ . Fig. 4.2 shows that the amount of mass dispersal increases monotonically

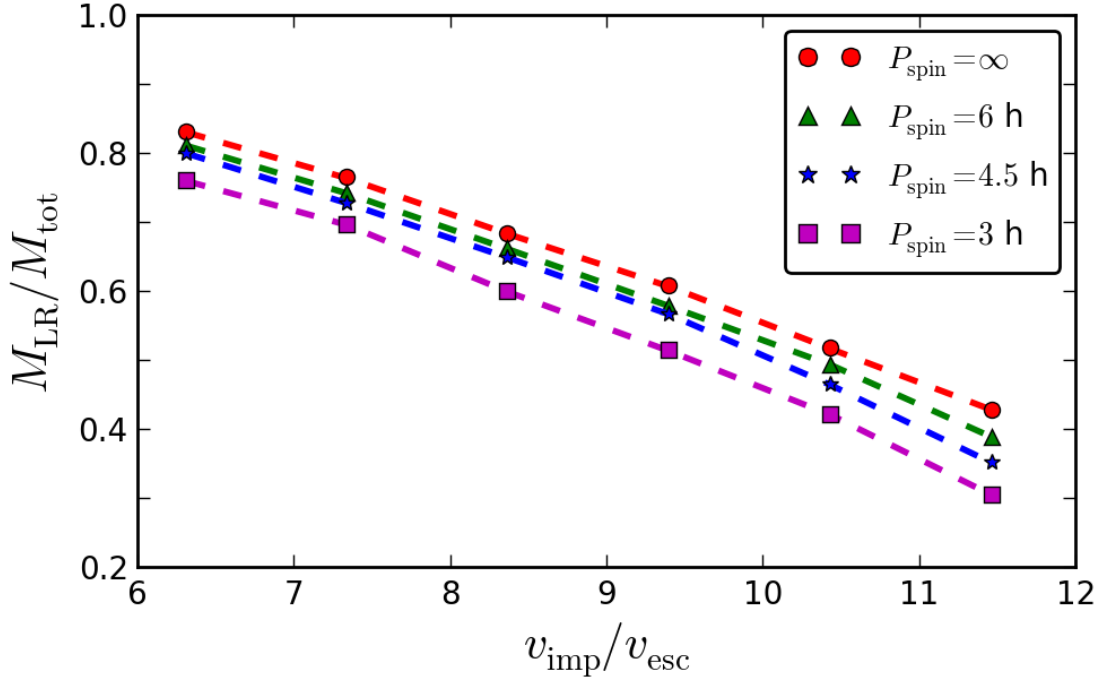


Figure 4.2: Mass loss for head-on equatorial impacts ( $b = 0$ ,  $\delta = 90^\circ$ ) is sensitive to pre-impact rotation. The amount of mass that is gravitationally dispersed is proportional to the impact speed. Green triangles, blue stars, and purple squares represent impacts where the target has a pre-impact spin period of 6 h, 4.5 h, and 3 h, respectively. Red-filled circles represent impacts where the target has no pre-impact spin. For head-on equatorial collisions, we derive the dependence of the reduced mass catastrophic disruption threshold,  $Q_{RD}^*$ , on the target's pre-impact rotation rate in Section 4.2.

cally with collision speed, and that, for head-on equatorial collisions, the amount of mass dispersal is sensitive to initial rotation, as cases with shorter spin periods systematically result in more mass loss. Furthermore, the collision outcomes for the target with an initial period of 6 hours approach the outcomes where the rubble pile initially has no spin. Since the spin limit for cohesionless rubble piles of this size and density is  $\sim 2.3$  hours, these results are fairly representative of all possible head-on collisions with initial spin (for  $\mu_s = 0.5$ ). Through a simple linear regression of the mass loss as a function of impact speed, we find that the catastrophic disruption threshold  $Q_D^*$  decreases by a range of  $\sim 10\text{--}30\%$  for the cases with pre-impact spin studied here. Since the transition from merging to catastrophic disruption may occur over a difference in energy of  $\sim 30\%$  (Leinhardt & Stewart, 2012), our results show that pre-impact spin can play a crucial role in the formation of planetesimals and protoplanets.

In order to obtain a better understanding of the underlying mechanics of rotationally enhanced mass loss, we considered the geometrical effects associated with a collision. By tracking the provenance of escaping particles originating from the target, we studied the likelihood of a particle’s escape as a function of its initial longitudinal and latitudinal point of origin on the target. Fig. 4.3 shows a mass-loss map for the case of a head-on collision with specific impact energy close to catastrophic disruption ( $v_{\text{imp}} = 9 \text{ m s}^{-1}$ ). The collision creates an extended impact region proportional to the projectile’s size ( $R_{\text{proj}} \sim 0.5 \text{ km}$ ), shown in Fig. 4.3 as the black region in the middle of the map. Material within this region is retained by the largest remnant as it is enclosed between the incoming projectile and the target’s

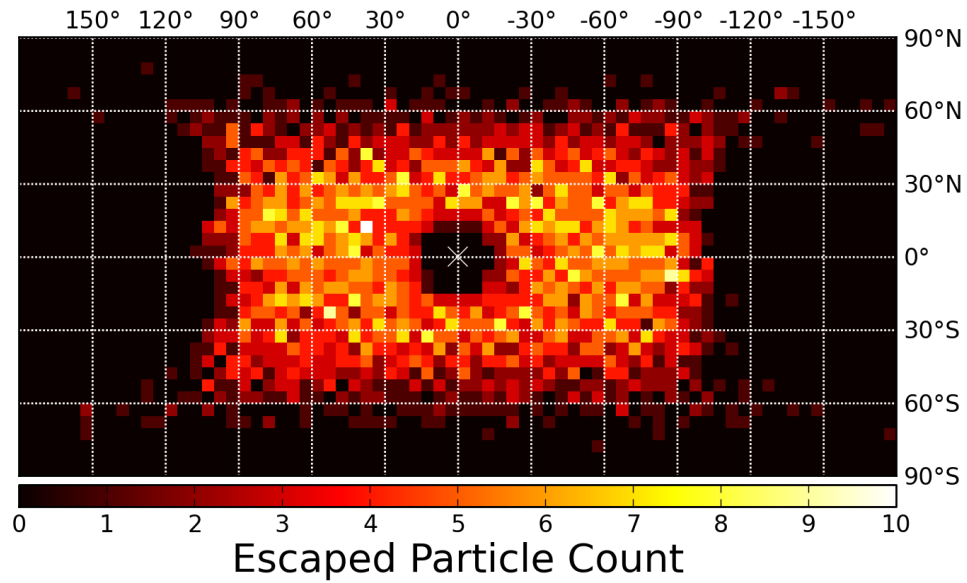


Figure 4.3: The cylindrical equi-distant map projection of the areas of mass loss from the head-on equatorial impact with  $v_{\text{imp}} = 9 \text{ m s}^{-1}$ . For an impactor of finite size, the regions near the impact point [coordinates  $(0^\circ, 0^\circ)$ ] do not experience mass loss as they are confined between the antipodal material and the incoming projectile during the collision. Rather, a ring of material surrounding the extended impact region is ejected (here shown as a rectangular region due to the distortion of the map projection).

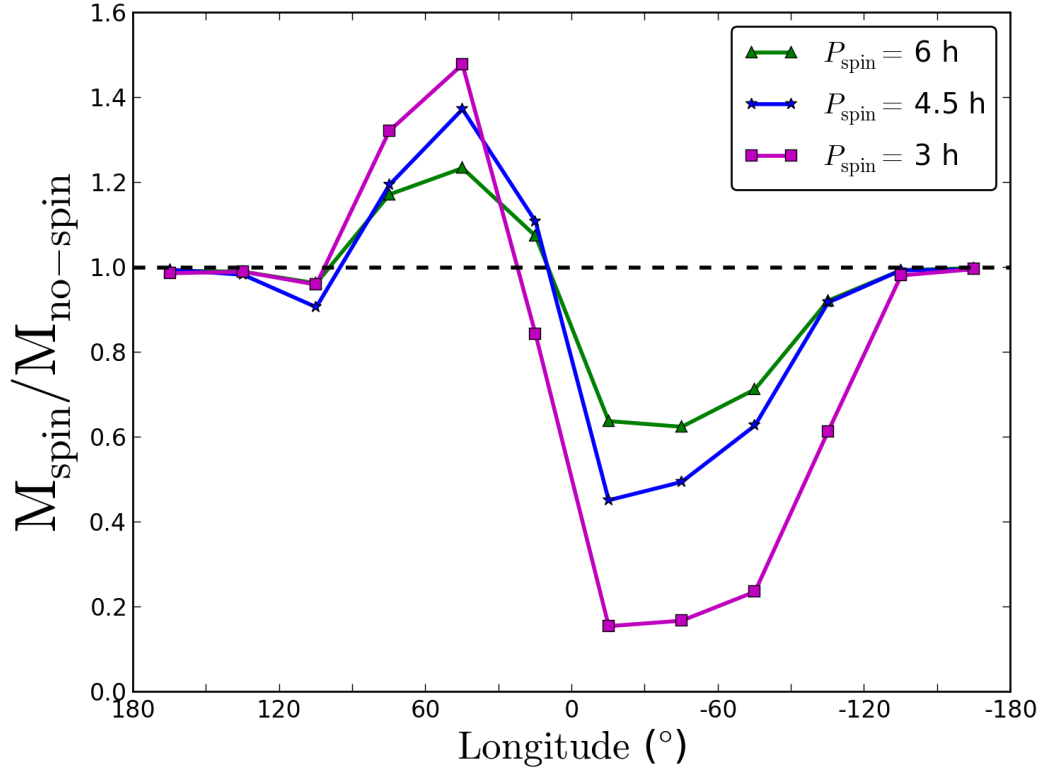


Figure 4.4: The mass loss distribution with impact longitude of cases with pre-impact spin normalized by the case without spin for the near-catastrophic impact speed,  $v_{\text{imp}} = 9 \text{ m s}^{-1}$ .  $M_{\text{spin}}$  is the mass in the largest remnant originating from a given longitude range of the target. The value of  $M_{\text{spin}}$  at each longitude bin is normalized by the case with no pre-impact rotation,  $M_{\text{no-spin}}$ . The sensitivity of mass loss to pre-impact rotation exists due to an enhancement in the amount of escaping material from the prograde hemisphere, which more than compensates for a corresponding greater retention of material from the retrograde hemisphere.

antipodal region (material  $180^\circ$  from the impact point). The escaping material originates from a nearly symmetrical ring about the impact region. Closer inspection of this escaping material reveals that the enhancement in mass loss is due to a preferential escape of material from prograde (negative) longitudes (Fig. 4.4). For this analysis, particles in the initial rubble-pile target were binned into  $30^\circ$  longitudinal spherical wedges. Since the target is nearly spherically symmetric, we consider longitudinal bins of equal size. Fig. 4.5 shows the number and sign convention that is used. The  $0^\circ$  longitude point is defined as the meridian of the target aligned with the impactor's velocity vector at the beginning of the simulation. Fig. 4.4 shows the mass distribution of the largest post-impact remnant as a function of the particle origin. When a target has pre-impact spin, material located in the retrograde longitudes (positive values) is preferentially retained by the largest remnant, and material located in the prograde longitudes preferentially escapes. This is due to retrograde material having angular velocities that are anti-aligned with the impact velocity vector, and prograde material having angular velocities that are aligned. However, there is a slight imbalance between these two outcomes, which favors a net increase in escaping mass. This can be seen in the increase in the amplitude of the troughs of Fig. 4.4 compared to the peaks. This phenomenon is observed in all cases of pre-impact spin. It is this process that eventually determines the total net enhancement in mass loss as a function of increasing pre-impact spin seen in Fig. 4.2.

However, head-on collisions are not the most likely collision geometry; rather, a collision with  $b = 0.7$  ( $\theta = 45^\circ$ ) is the most common on average (Love & Ahrens,

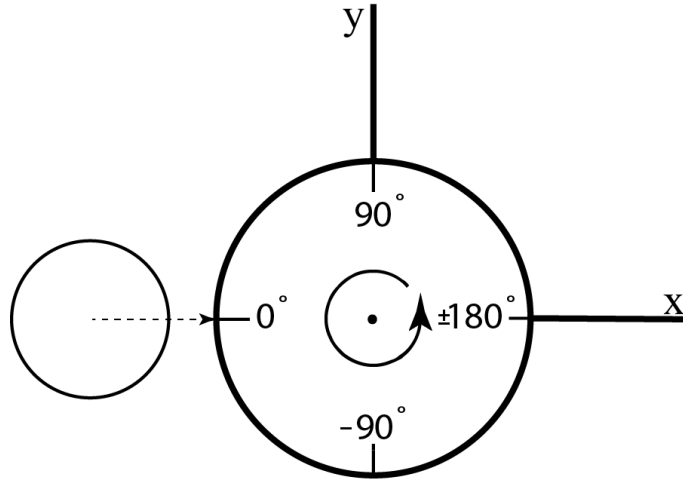


Figure 4.5: In order to determine the longitudinal origin of escaping particles, the target is divided into equal-size bins of longitudes. Following the right-hand rule, negative values of the longitude correspond to negative values along the  $y$ -axis when the spin-angular momentum vector is aligned with the positive  $z$ -axis.

1996). Furthermore, the mechanics of mass-loss enhancement due to pre-impact spin appears to be linked directly with the manner in which loading on the target occurs. Therefore, we extend our analysis to study the dependence of mass loss with the combined effects of non-zero  $b$  and  $\delta$  by studying each in isolation.

#### 4.4.2 Oblique Equatorial Collisions

Previous studies have shown that the catastrophic disruption criterion is highly sensitive to the impact parameter (Leinhardt et al., 2000; Leinhardt & Stewart, 2012). For oblique impacts, the energy of the projectile may not completely intersect the target. For certain values of  $b$ , a segment of the projectile may be able to shear off, and, consequently, this material does not interact with the target, effec-

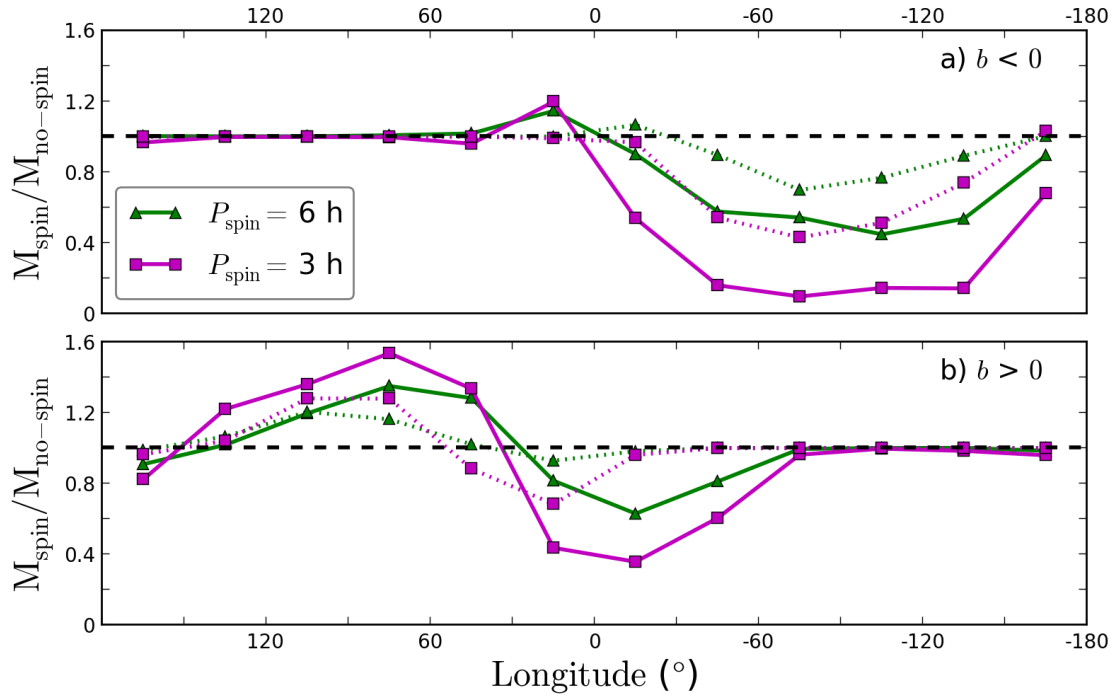


Figure 4.6: Mass loss distribution for oblique equatorial impacts for  $v_{\text{imp}} = 15 \text{ m s}^{-1}$ . Panel (a) shows the distribution for impacts onto the prograde hemisphere (negative  $b$ ), where the solid lines are for collisions with  $b = -0.5$ , and dotted lines are for  $b = -0.7$ . Panel (b) shows the distribution for impacts onto the retrograde hemisphere (positive  $b$ ), where the solid lines are for collisions with  $b = +0.5$ , and dotted lines are for  $b = +0.7$ . See text for discussion.

tively lowering the specific impact energy. Hence, a greater impact speed is required to reach catastrophic disruption compared to a head-on collision. Previous studies used a simple geometric model to determine the fraction of interacting projectile mass (Canup, 2008; Leinhardt & Stewart, 2012). The revised mass is then used in scaling the catastrophic disruption criteria (Leinhardt & Stewart, 2012).

We find that mass dispersal is only sensitive to pre-impact rotation when  $b < 0$ , for the range in  $b$ -values considered. For  $b > 0$ , the projectile impacts the target on its retrograde hemisphere; hence, the angular velocities of rotating particles are either anti-aligned or perpendicular to the impact velocity vector. Fig. 4.6 shows the mass distribution as a function of longitudinal origin for  $v_{\text{imp}} = 15 \text{ m s}^{-1}$ . The solid and dotted curves are for  $b \pm 0.5$  and  $b \pm 0.7$ , respectively. Fig. 4.6a shows that, for collisions onto the prograde hemisphere, pre-impact rotation systematically increases mass loss. This is similar to the results found for head-on collisions in Section 4.4.1. Conversely, Fig. 4.6b shows that collisions onto the positive retrograde hemisphere result in a rough balance between mass retention and mass-loss enhancement when pre-impact spin is introduced (i.e., the integrals under the curves are approximately zero). Hence, the net effect is that, for prograde impacts, pre-impact spin does not enhance mass loss very much. Furthermore, for the oblique impacts considered here, the rubble pile is efficient at dissipating the impact energy such that gravitational dispersal is localized to the hemisphere of the target that was impacted, rather than being a global effect.

### 4.4.3 Head-on Collisions with $\delta < 90^\circ$

Since the effective acceleration of a particle on a rotating body is a function of its colatitude, we would expect that the amount of mass loss a rubble pile experiences is a strong function of the latitude of impact. Fig. 4.7 shows the mass dispersal as a function of impact speed for two different values of the polar impact angle,  $\delta$ . Contrasting with the head-on equatorial case, for low collision speeds, pre-impact rotation does not systematically increase the amount of mass loss. However, for near- and super-catastrophic speeds, the amount of mass loss is greatly enhanced. For such energetic collisions, a target with a 3 h pre-impact spin period experiences  $\sim 25\%$  (for  $\delta = 45^\circ$ ) and  $\sim 50\%$  ( $\delta = 0^\circ$ ) more mass loss than a non-spinning target. On average, a pole-on impact onto a spinning target requires  $\sim 15\%$  less specific impact energy to reach catastrophic disruption compared to an equatorial head-on impact ( $\delta = 90^\circ$ ,  $b = 0$ ).

The enhancement in mass loss for near-polar impacts is due to the escape of equatorial surface particles. As discussed in Section 4.4.1 and shown in Fig. 4.3, the material that escapes originates from a ring about the extended impact region. For the case of pole-on and near-pole-on impacts, this dispersal region extends to the equator, where the effective pre-impact acceleration of particles is greatest. Unlike equatorial impacts ( $\delta = 90^\circ$ ), material at the equator is not confined by impacting projectile material. Instead, for polar impacts, polar material is trapped by the merging projectile material, and the collisional wave disperses material outside the immediate polar region. For highly energetic collisions, this mechanical wave

extends to the equator, where particles are unhindered and more readily escape. Hence, for the cases of near- and super-catastrophic collisions, the vertical transfer of impact energy (from the pole to the equator) leads to the ejection of low-latitude particles. Experiencing a lower effective gravitational potential at higher rotation rates, these particles escape more easily. This leads to the enhancements in mass loss seen in Fig. 4.7.

## 4.5 Discussion

### 4.5.1 The “Universal” Law for Catastrophic Disruption

In order to account for the dependence of mass ratio on catastrophic disruption criteria, [Leinhardt & Stewart \(2009\)](#) introduced new variables into their formulation for predicting collision outcomes: the reduced mass  $\mu \equiv M_{\text{proj}}M_{\text{targ}}/M_{\text{tot}}$ , the reduced-mass specific impact energy  $Q_R \equiv 0.5\mu v_{\text{imp}}^2/M_{\text{tot}}$ , and the corresponding reduced-mass catastrophic dispersal limit  $Q_{RD}^*$ . Through this new formulation, [Leinhardt & Stewart \(2009\)](#) showed that the outcome of any head-on collision, regardless of projectile-to-target-mass ratio, can be described by a single equation that they call the “universal” law:

$$M_{\text{LR}}/M_{\text{tot}} = -0.5(Q_R/Q_{RD}^*) + 0.5, \quad (4.2)$$

where the prime ( $\prime$ ) notation in  $Q_{RD}^*$  was introduced by [Leinhardt & Stewart \(2012\)](#) to denote a collision that could have a non-zero impact parameter. [Leinhardt & Stewart](#)

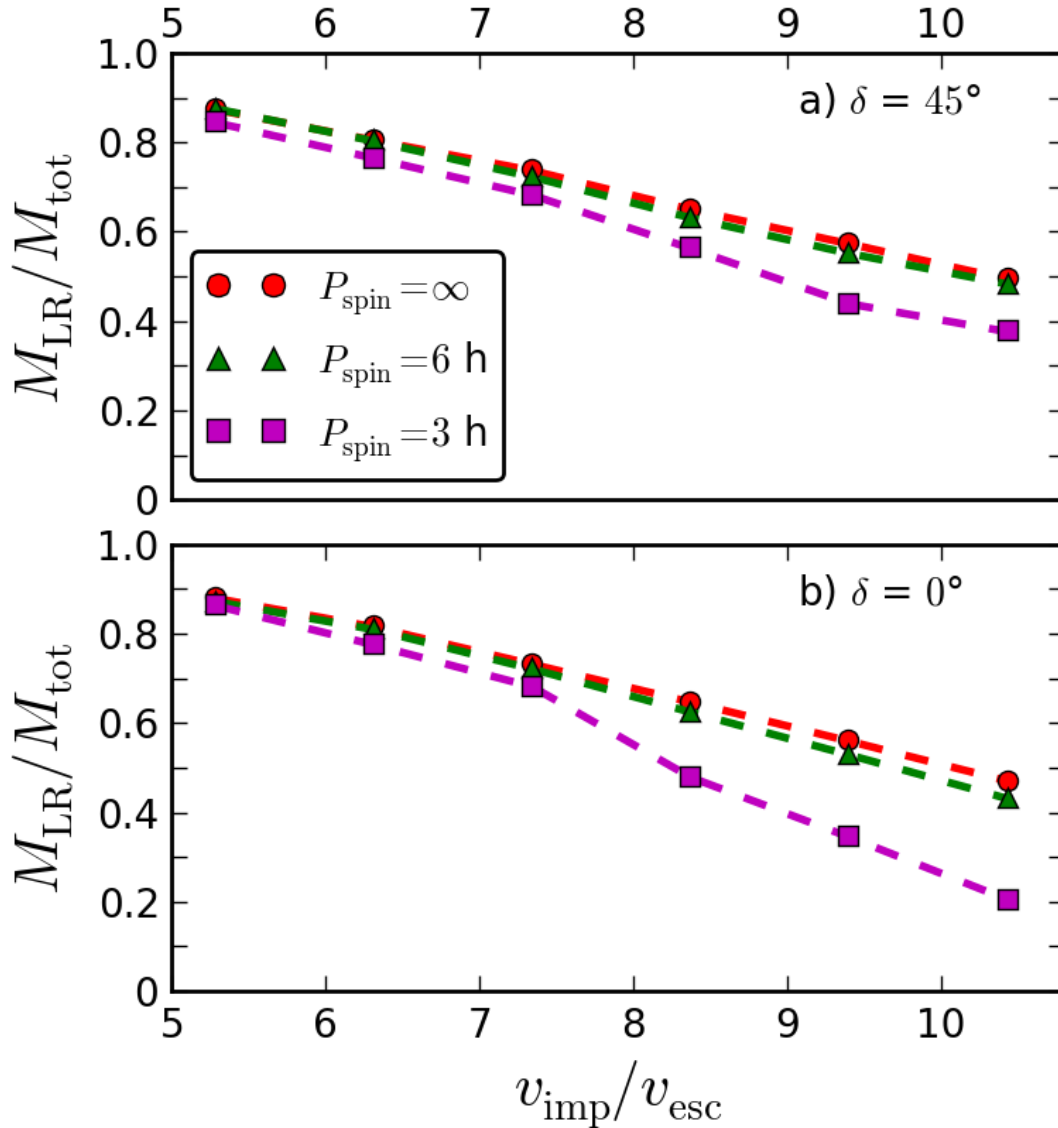


Figure 4.7: Mass of the largest remnant as a function of impact speed for cases with  $\delta < 90^\circ$ . Significant enhancements in mass loss only occur for near-catastrophic and super-catastrophic collisions. See text for discussion.

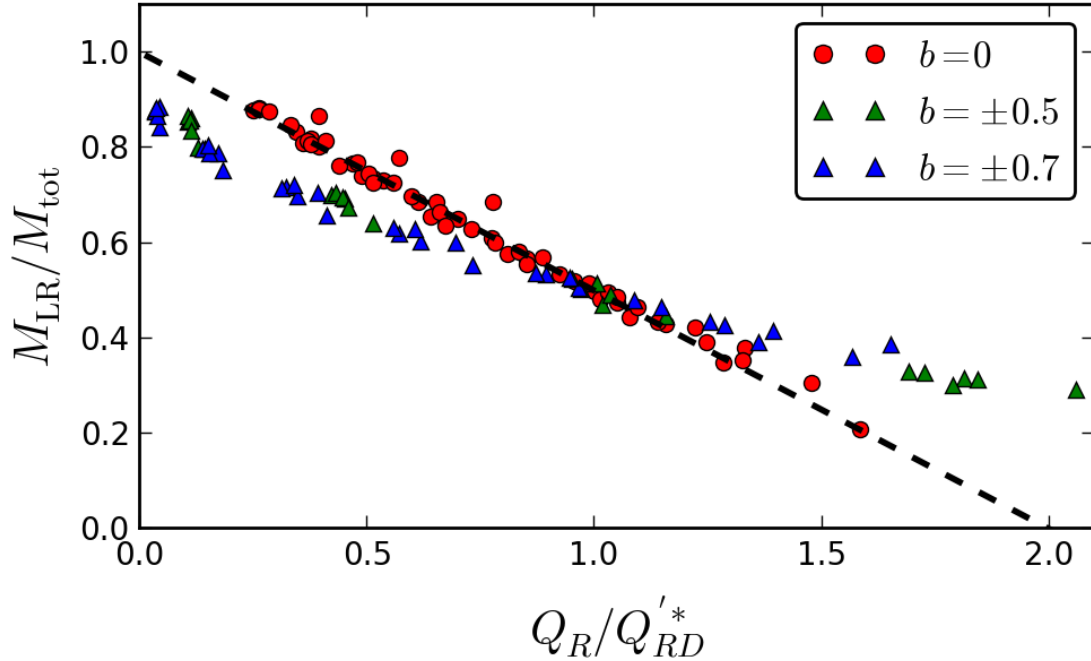


Figure 4.8: Head-on collision outcomes are described well by the “universal” law for catastrophic disruption, Eq. 4.2 (dotted-line). Most head-on collisions (red circles) show  $< 1\%$  deviations from the universal law. Non-equatorial impacts ( $\delta < 90^\circ$ ) onto rotating targets, show deviations of up to  $\sim 10\%$  due to non-linear effects present when collisions are near- and super-catastrophic (see text for discussion). Oblique impacts (filled triangles) systematically deviate from the universal law.

(2009) verified that, for head-on impacts ( $b = 0$ ), Eq. 4.2 agrees well with results from both laboratory experiments and numerical simulations of binary collisions with a range of mass ratios and material properties. Leinhardt & Stewart (2012) found that their numerical simulations showed deviations in  $M_{\text{LR}}/M_{\text{tot}}$  of  $\sim 10\%$  for near-normal impacts ( $b = 0$  and  $b = 0.35$ ), and larger and more varied deviations for more oblique impacts. In order to compare our results (summarized in Table 4.1) to those of Leinhardt & Stewart (2012), the outcomes of each group of collisions ( $M_{\text{LR}}$  as a function of  $Q_R$ ) were fit with a linear function to determine

empirically the value of  $Q_{RD}^*$  (collision groups are uniquely identified by single values of  $b$ ,  $\delta$ , and  $P_{\text{spin}}$ .) For most collision scenarios the results are well described by the linear fit. In these cases, deviations from the model were less than 1%. For non-equatorial collisions ( $\delta < 90^\circ$ ) onto a rotating target, we showed in Section 4.4.3 the existence of two different mass loss outcome regimes. For near- and super-catastrophic collisions, enhanced mass dispersal from the equator causes a non-linear increase in mass loss. Hence, for these cases, a single linear fit to determine  $Q_{RD}^*$  leads to deviations of  $\sim 10\%$ .

The results of our simulations are presented in Fig. 4.8, superimposed on the universal law for catastrophic disruption. For collisions with  $b = 0$ , we observe that the law predicts accurately the mass of the largest remnant (deviations  $< 10\%$ ). Furthermore, varying the polar-impact angle,  $\delta$ , or the spin period,  $P_{\text{spin}}$ , does not affect the mass of the largest remnant if the specific impact energy is normalized by  $Q_{RD}^*$ .

Cases of  $b = \pm 0.5, \pm 0.7$  seem to be better fit by a shallower slope. For oblique impacts, [Leinhardt & Stewart \(2012\)](#) introduced a parameter  $\alpha \equiv m_{\text{int,proj}}/M_{\text{proj}}$ , which accounts for the mass of the projectile that interacts with the target, such that the appropriate reduced mass is

$$\mu_\alpha \equiv \frac{\alpha M_{\text{proj}} M_{\text{targ}}}{\alpha M_{\text{proj}} + M_{\text{targ}}}. \quad (4.3)$$

For the case of a 1:10 mass ratio and  $b = \pm 0.5$ , we find  $\alpha \sim 1.0$ . Yet, we observe in our experiments that the specific impact energy required for catastrophic disruption is much greater than that for a head-on collision. Therefore, there must be some

other mechanism that accounts for this discrepancy in required specific impact energy.

During a collision, a compressive wave travels through the projectile, and upon encountering the projectile's edge, is reflected as a tensile wave that travels through the contact points and disrupts and disperses target (as well as projectile) material (Ryan, 2000). The width of this wave depends on a number of physical parameters such as the strain loading rate, the type of material, and the size ratio of the projectile and target. We hypothesize that the size of this wave determines what fraction of the target interacts in the collision. For cases with non-zero  $b$ , we observe that the particles that are able to escape are mostly localized to the same hemisphere of the collision; hence, some of the material in the opposite hemisphere of the target shears off and is not involved in the collision. For head-on collisions, the dispersive wave would originate near the center and propagate symmetrically through the target, maximizing the amount of material affected by the collision. The exact wave mechanics involved in computing the fraction of the target that does interact during the collision is difficult to determine accurately analytically. For now, we attempt to find an empirical determination of this interacting target mass by adjusting the disruption criteria variables to include this effect. Hence, we introduce a further revised reduced mass:

$$\mu_A \equiv \frac{\alpha M_{\text{proj}} A M_{\text{targ}}}{\alpha M_{\text{proj}} + A M_{\text{targ}}}, \quad (4.4)$$

where  $A \equiv m_{\text{int,targ}}/M_{\text{targ}}$ , the fraction of the mass of the target that interacts in the collision. Thus, the equivalent head-on specific impact energy is  $Q_R^A =$

$0.5\mu_A v_{\text{imp}}^2/M_{\text{tot}}$ . Furthermore, the mass of the largest remnant is now normalized by a total interacting mass,  $M_{\text{tot}}^A \equiv \alpha M_{\text{proj}} A M_{\text{targ}}$ . Using these new variables, we rescale the oblique impacts into equivalent head-on impacts. By using a  $\chi^2$ -minimization routine, we determined the best-fit values for  $\alpha$  and  $A$  (Fig. 4.9) that rescale the oblique impact results such that they fit the universal law for catastrophic disruption. We consider two cases,  $b = \pm 0.5$  and  $b = \pm 0.7$ . Since the effect is considered to be purely geometric, it is independent of the sign of  $b$ . For both cases of  $b$ , we find single  $1/\chi^2$  peaked regions in the parameter space. Possible values of  $A$  are well constrained between 0.8 and 0.9 for both cases of  $b$ . The best-fit values of  $\alpha$  differs for the two  $|b|$  cases, with  $b = \pm 0.5, \pm 0.7$  peaked at  $\alpha \sim 0.7, 0.75$ , respectively.

In order to constrain the possible values of  $\alpha$  and  $A$ , we also determined the interacting mass fraction of the projectile,  $\alpha_{\text{geom}}$ , through a simple geometric model. Following [Leinhardt & Stewart \(2012\)](#), we determine  $\alpha_{\text{geom}}$  by considering the volume of the projectile whose cross section intersects with the target. The volume of a spherical cap can be expressed as:

$$V_{\text{int,proj}} = \frac{\pi l^2}{3}(3r - l), \quad (4.5)$$

where  $l$  is the height of the spherical cap, and  $r$  is the radius of the sphere. For an oblique impact,  $l$  is the projected length of the projectile overlapping the target, and can be expressed as

$$l = (1 - b)(R_{\text{targ}} + R_{\text{proj}}). \quad (4.6)$$

Therefore,

$$\alpha_{\text{geom}} = \frac{m_{\text{int,proj}}}{M_{\text{proj}}} = \frac{V_{\text{proj}}}{V_{\text{int,proj}}} = \frac{3rl^2 - l^3}{4r^3}. \quad (4.7)$$

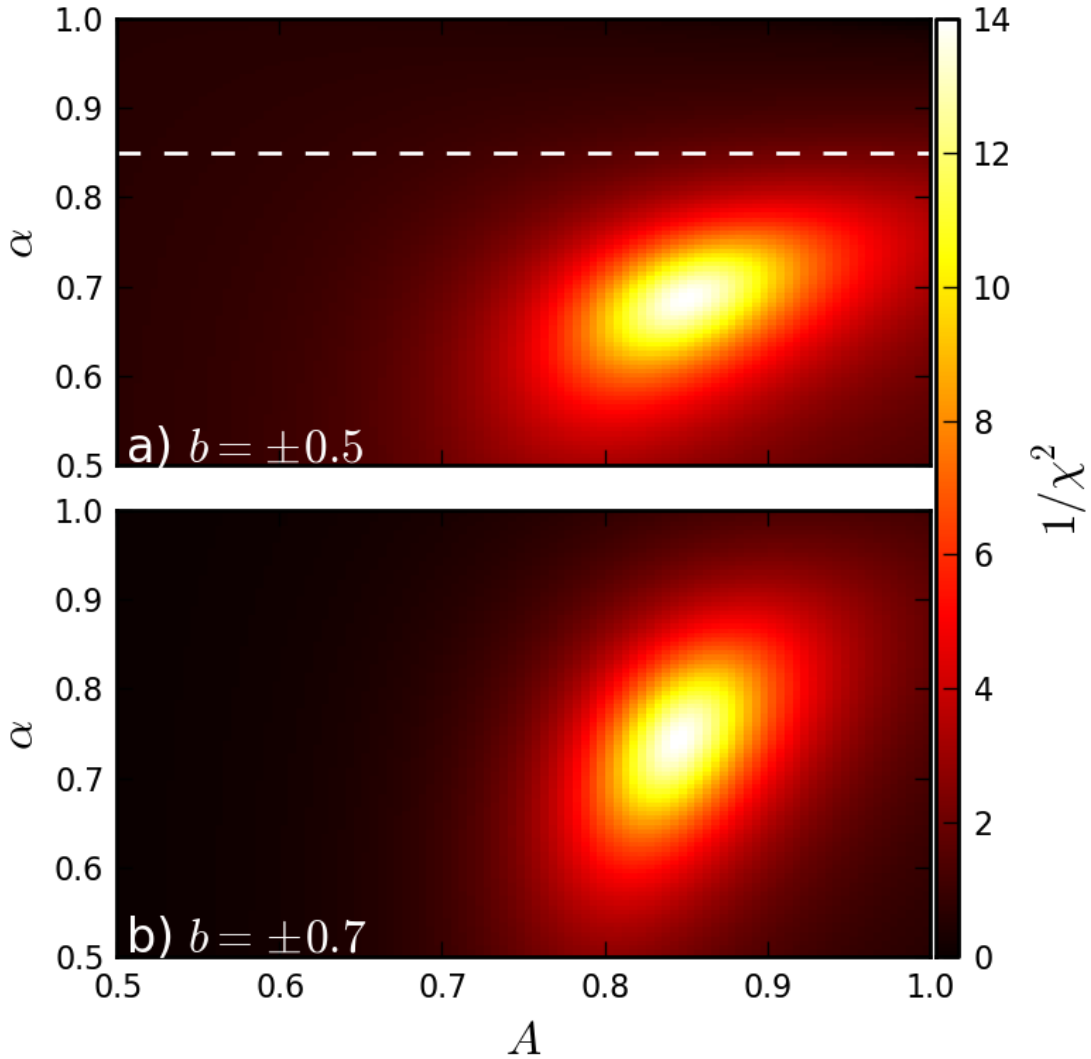


Figure 4.9: Using a  $\chi^2$  analysis, we determined the best values of  $\alpha$  and  $A$  that adjust the catastrophic disruption variables such that oblique impacts are well modeled by the universal law for catastrophic disruption. The white dashed line is the geometric constraint placed by  $\alpha_{\text{geom}}$ . For  $b = \pm 0.7$ ,  $\alpha_{\text{geom}} = 0.44$ . The  $\chi^2$  analysis shows that the geometric model may be underestimating the fraction of interacting projectile material (see text for discussion).

The value of  $\alpha_{\text{geom}}$  gives a lower boundary to the possible value of  $\alpha$ , since it is expected that the minimum amount of interacting material would be the mass that overlaps the target geometrically. We determined the best values of  $\alpha$  and  $A$  as constrained by the geometric model, and find that as  $|b|$  increases,  $\alpha$  and  $A$  decrease (Table 4.2). This trend is expected, since more projectile and target material can shear off when the impact is close to grazing. For the cases with  $b = \pm 0.7$ , we find that the best-fit value of  $\alpha$  (0.745) is much greater than  $\alpha_{\text{geom}}$  (0.44). This suggests that the simple geometric model underestimates the value of  $\alpha$ . A fraction of the projectile whose cross section does not overlap with the target does not completely shear off; rather, it is involved in the collision process, contributing to the impact energy delivered to the target.

For the cases with  $b = \pm 0.5$ , we find that the best-fit values for  $\alpha$  and  $A$  are excluded when  $\alpha$  is imposed to be greater than or equal to  $\alpha_{\text{geom}}$ . If the geometric constraint is not considered, then a combination of  $\alpha = 0.685$  and  $A = 0.845$  gives the minimum  $\chi^2$ . However, this would imply that the cases of  $b = \pm 0.5$  have a lower value for  $\alpha$  than the cases of  $b = \pm 0.7$  ( $\alpha = 0.745$ ). This is unlikely, as a larger fraction of projectile material is expected to interact when a collision is closer to head-on.

Hence, while our  $\chi^2$  analysis does a good job of fitting the data to the universal law, the results are unphysical unless they are constrained by a geometric model. Therefore, more work must be done in order to verify whether the energetics of oblique impacts are affected by the interacting fractional mass of both the target and the projectile as we suggest here. In Fig. 4.10, we show that oblique

impacts follow the linear universal law if the axes are changed to our rescaled catastrophic disruption variables. However, we find that for super-catastrophic collisions, the data points seem to tail-off rather than follow a linear relationship. Laboratory experiments (Matsui et al., 1982; Kato et al., 1995) and disruption simulations (Korycansky & Asphaug, 2009; Leinhardt & Stewart, 2012), have shown that the mass of the largest remnant follows a power law with  $Q_R$  for super-catastrophic collisions. At these high energies, mass dispersal results in the formation of a large number of fragments of roughly equal size, rather than a single large remnant, such that for incrementally higher impact energies, the largest remnant remains constant. This may explain the discrepancy that we see between the high-energy collision outcomes and the universal law.

#### 4.5.2 Rotation Dependence of Catastrophic Disruption

Since rotation decreases the effective gravitational binding energy of a body, we first describe the size-dependence of catastrophic disruption so that we may be able to formulate an analytic description of the dependence on pre-impact rotation. The catastrophic disruption criterion is a function of radius, with two regimes: a strength-dominated regime and a gravity-dominated regime (Housen & Holsapple, 1990). For rocky bodies, the transition from strength to gravity occurs at a radius of  $\sim 100$  m (Leinhardt et al., 2008). In the strength regime, the catastrophic disruption criterion decreases with increasing radius; this is due to multiple factors, such as the increase in the size of the largest internal crack and the total number of flaws

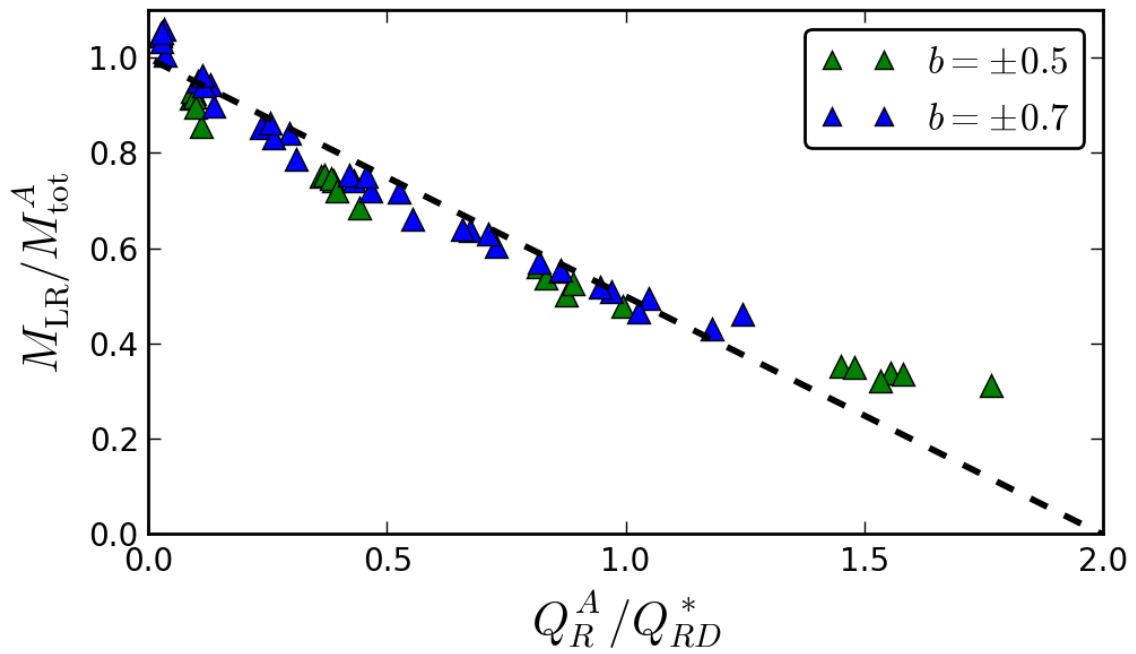


Figure 4.10: Adjusting our results for the correct interacting projectile and target produces a better fit for oblique impacts, for low  $Q_R^A / Q_{RD}^*$  (cf. Fig. 4.8). The corrected interacting mass fractions are summarized in Table 4.2.

with target size. In the gravity regime, disruption increases as the radius increases since disruption requires shattering and gravitational dispersal, and the gravitational binding energy of a body,  $U$ , is proportional to the square of the body's radius. For a binary collision, the gravitational binding energy can be approximated as,

$$U = \frac{3GM_{tot}}{5R_{C1}} = \frac{4}{5}\pi\rho_1GR_{C1}^2, \quad (4.8)$$

where  $G$  is the gravitational constant and  $R_{C1}$  is the spherical radius of the combined projectile and target masses at a density of  $\rho_1 = 1 \text{ g cm}^{-3}$ . [Leinhardt & Stewart \(2009\)](#) introduced  $R_{C1}$  in order to compare collisions of different projectile-to-target-mass ratios.

By determining the dependence of mass ratio on the catastrophic disruption criterion, [Leinhardt & Stewart \(2012\)](#) found that, in the gravity regime, the disruption criterion for equivalent equal-mass impacts,  $Q_{RD}^*$ , of different materials all fall along a single curve that scales as the radius squared. Since catastrophic disruption and the gravitational binding energy scale similarly with radius, the authors define a principal disruption curve, where  $Q_{RD}^*$  is a scalar multiple of  $U$ . They defined a dimensionless material parameter,  $c^*$ , that represents this offset, such that

$$Q_{RD}^* = c^*U. \quad (4.9)$$

For bodies with a diverse range of material properties (strengthless hydrodynamic targets, rubble piles, ice, and strong rock targets) and with  $0.5 \text{ km} < R_{C1} < 1000 \text{ km}$ , [Leinhardt & Stewart \(2012\)](#) found that the threshold for catastrophic disruption is defined by a single principal disruption curve with  $c^* = 5 \pm 2$ . They find that

a similar curve can describe the disruption of planet-size bodies ( $R_{C1} > 3000$  km) with  $c^* = 1.9 \pm 0.3$ .

In order to formulate a description of the dependence of catastrophic disruption on rotation, we first consider a rotating fluid body that has an effective specific gravitational binding energy,  $U_{\text{eff}}$ , given by

$$U_{\text{eff}} = U - \frac{|\boldsymbol{\omega} \times \mathbf{r}|^2}{2}, \quad (4.10)$$

where  $\boldsymbol{\omega}$  is the constant angular velocity of the body, and  $\mathbf{r}$  is the position vector of a particle relative to the center of the target. Similarly, we propose that in a binary head-on equatorial collision with pre-impact rotation, the catastrophic disruption criterion,  $Q_{\text{RD,rot}}^*$ , is a function of the angular speed of the target,  $\omega_{\text{targ}}$ . For a head-on equatorial collision with pre-impact rotation (collision geometry with no dependence on  $b$  and  $\delta$ ), this is represented by a subtraction of a latitude-averaged centrifugal term as in Eq. 4.10 such that

$$Q_{\text{RD,rot}}^* = Q_{\text{RD,no-rot}}^* - \omega_{\text{targ}}^2 R_{\text{targ}}^2, \quad (4.11)$$

where  $Q_{\text{RD,no-rot}}^*$  is the catastrophic disruption criterion without pre-impact spin. For non-equatorial or oblique impacts, we expect that the change in the catastrophic disruption criterion is a more complicated function of collisional angular momentum and the efficiency of its transfer. For the purposes of this chapter, we restrict our analysis to the simpler equatorial head-on collisions. Dividing Eq. 4.11 by  $Q_{\text{RD,no-rot}}^*$ , and substituting from Eq. (9), we find

$$\frac{Q_{\text{RD,rot}}^*}{Q_{\text{RD,no-rot}}^*} = 1 - K \left( \frac{\omega_{\text{targ}}}{\omega_{\text{crit}}} \right)^2; \quad (4.12)$$

$$K \equiv \frac{5}{3} \frac{R_{C1}}{R_{\text{targ}}} \frac{M_{\text{targ}}}{M_{\text{tot}}} \frac{1}{c^*},$$

where  $\omega_{\text{crit}} \equiv (GM_{\text{targ}}/R_{\text{targ}}^3)^{1/2}$  is the spin break-up limit of the target. We fit Eq. 4.12 with the empirically derived catastrophic disruption values (described in Section 4.5.1) for the three different pre-impact spin cases normalized by the spinless case (Fig. 4.11). We find a best-fit value of  $K = 0.3814$  (maximum deviations were  $\sim 3\%$ ), corresponding to a value of  $c^* = 4.83$ . Our value of  $c^*$  falls within the range for small bodies ( $R < 1000$  km in size) that [Leinhardt & Stewart \(2012\)](#) find.

Eq. 4.12 predicts that for pre-impact rotations close to break-up, the catastrophic disruption criterion can decrease by a factor of  $\sim 40\%$ . In reality, a spherical target spinning close to break-up would reach a new fluid-equilibrium shape, and the nature of its ellipsoidal shape will likely affect the catastrophic disruption criterion. In our simulations, the impacts occur quickly enough that the target does not reach a fluid equilibrium before disrupting. Future work could study the dependence of catastrophic disruption on the pre-impact shape of the target body.

### 4.5.3 Dependence on Material Properties

Finally, we measure the dependence of  $Q_{\text{RD}}^*$  on material properties. Our previous simulations kept the frictional properties of the particles constant. Here, we wish to examine the range of possible  $Q_{\text{RD}}^*$  that may be obtained by varying the friction coefficient values. We model three different types of materials: smooth par-

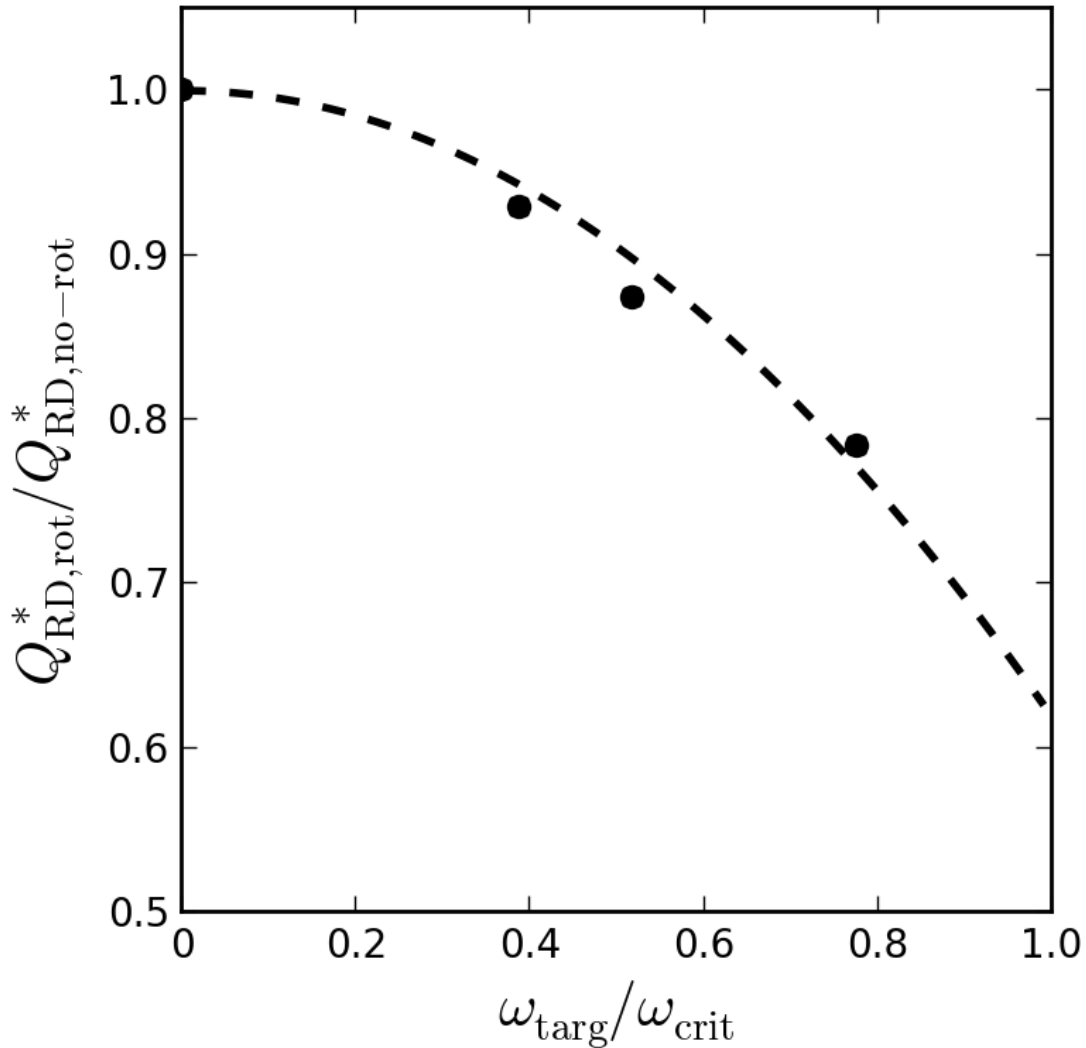


Figure 4.11: Head-on equatorial impacts have catastrophic disruption thresholds that are sensitive to pre-impact spin. We develop a semi-analytic description of  $Q_{RD}^*$  as a function of the pre-impact spin-rate of the target,  $\omega_{\text{targ}}$  (see text), and find that our data imply a value of  $c^* = 4.83$  for the dimensionless material parameter of the principal disruption curve. The dashed curve is the best-fit function (of the form described by Eq. 4.12) to the catastrophic disruption thresholds with pre-impact rotation normalized by the case with no rotation (circles).

ticles, glass beads, and gravel. The properties of glass beads were determined by [Schwartz et al. \(2013\)](#) in impact experiments. The properties of gravel were determined by [Yu et al. \(2014\)](#) in landslide experiments. The dissipation and friction parameters that correspond to each material were previously discussed in Chapter 2 and are shown in Table. 2.1. We performed simulations of binary collisions where we varied the material property of the rubble pile and the pre-impact spin rate of the target. In Fig. 4.12, we show that a rubble pile made up of rougher and less elastic material has a higher catastrophic disruption threshold. Furthermore, we also see that regardless of the material property type, the decrease in  $Q_{RD}^*$  due to some non-zero pre-impact spin is constant. Therefore, we expect that the semi-analytic prescription developed in the previous section to be valid for a rubble pile made up of particles of any material property.

## 4.6 Conclusions & Future Work

We have studied the effect of initial rotation on the outcome of rubble-pile collisions by analyzing the properties of the largest remnant and material that is gravitationally bound to it. By simulating different collision geometries and speeds, we have begun to explore a parameter space that is wide enough that we can formulate a phenomenological description of collision outcomes. Our main conclusion is that mass dispersal is a function of initial rotation period, with faster-rotating rubble-pile targets dispersing more mass. By analyzing the initial spatial distribution of the gravitationally bound masses, we have shown that there is an enhancement of mass

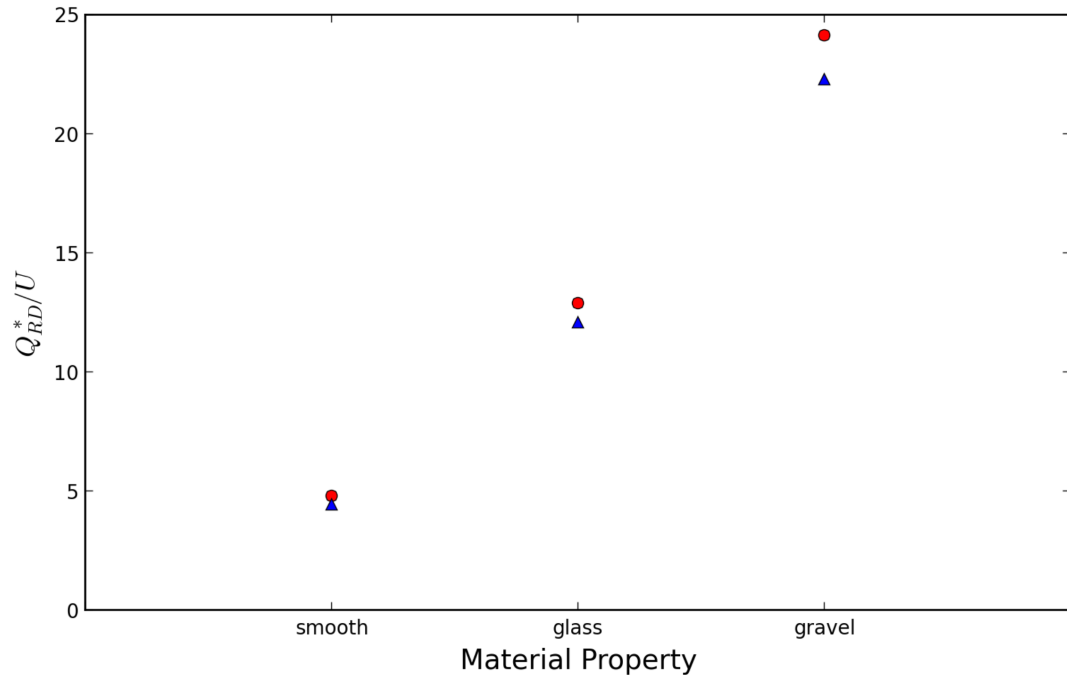


Figure 4.12: The reduced-mass catastrophic disruption threshold  $Q_{RD}^*$ , normalized by the gravitational binding energy,  $U$ , for the three material properties studied here. Red circles represent collisions with no pre-impact spin. Blue triangles represent collisions where the target has a pre-impact spin of 6 hours. Spin systematically decreases  $Q_{RD}^*/U$  by  $\sim 6\%$ .

loss when the impact energy is efficiently transferred to the prograde hemisphere of a rotating rubble pile. For head-on impacts onto regions near the pole, the collision efficiently disperses equatorial material for near- and super-catastrophic collisions, and fast rotation increases mass loss by factors of up to 50%. The mass of the largest remnant of head-on impacts is well described by the “universal law” for catastrophic disruption first put forward by [Leinhardt & Stewart \(2009\)](#), independent of initial pre-impact rotation. Hence, for a given impact speed, pre-impact rotation decreases  $M_{\text{LR}}/M_{\text{tot}}$ , and the corresponding decrease in  $Q_{RD}^*$  can be described by the universal law. However, oblique impacts follow a linear relationship with a shallower slope than the universal law. When the interacting mass fraction of the projectile and target are factored into the catastrophic disruption variables, the outcomes for oblique impacts can be rescaled for a better match to the universal law.

By subtracting a centrifugal term from the catastrophic disruption criterion of the case with no pre-impact rotation, we developed a prescription that describes the change in the catastrophic disruption criteria of head-on equatorial impacts onto a rotating target. We independently find a dimensionless material parameter,  $c^* = 4.83$ , that agrees with the principal disruption curves of [Leinhardt & Stewart \(2012\)](#) for small bodies. Our simplified description does not take into account the effects of angular momentum transfer in oblique impacts or the mechanism for enhanced mass loss from near- and super-catastrophic polar impacts described in Section 4.4.3. These effects will have to be further studied so that the change in the catastrophic disruption criterion can be determined for any impact trajectory.

Lastly, we calculated the catastrophic disruption threshold for three different

material types. We found that higher friction and dissipation values increase the catastrophic disruption threshold by about half a magnitude. Furthermore, we find that pre-impact rotation systematically increases mass loss on average, regardless of the target’s internal configuration.

In the future, a wider parameter space should be explored in order to strengthen the conclusions drawn here. In particular, the effectiveness of rotation in enhancing mass loss must be studied for different projectile-to-target-mass ratios. Since mass loss is sensitive to rotation, the spin-up or spin-down of the post-impact largest remnant plays an important role in the size evolution of a population of km-size bodies. Furthermore, the change in spin likely has an effect on the reaccumulation process, changing the final mass. In some cases, spin-up may lead to a remnant crossing the rotational disruption threshold ( $P_{\text{spin}} \sim 2.3$  h, for  $\rho \sim 2$  g cm<sup>-3</sup>). In order to understand how rotation affects the long-term size, shape, and spin evolution of a population of SSSBs, a semi-analytic description of the dependence of  $Q_{RD}^*$  on the parameters explored here must be formulated, such that  $M_{LR}$  can be determined for any given collision. Therefore, future work will also need to study the sensitivity of mass loss on rotation for larger ( $> 1$  km) bodies. It is unclear whether the collisional dynamics explored here scales to larger bodies. This will help inform future planet-formation studies by giving a more accurate prescription for collision outcomes, a necessary component for models that study the collisional growth of planetesimals.

Table 4.1: Summary of Collision Geometries and Mass Loss Outcomes.  $b$  is the impact parameter,  $\delta$  is the polar impact angle,  $P_{\text{spin}}$  is the spin period of the target,  $v_{\text{imp}}$  is the impact speed of the projectile, and  $M_{\text{LR}}/M_{\text{tot}}$  is the mass of the largest remnant normalized by the total mass of the system.

$b$	$\delta$ ( $^\circ$ )	$P_{\text{spin}}$ (h)	$v_{\text{imp}}$ (m s $^{-1}$ )	$M_{\text{LR}}/M_{\text{tot}}$
0	90	$\infty$	6.0	0.831089
0	90	$\infty$	7.0	0.764666
0	90	$\infty$	8.0	0.683734
0	90	$\infty$	9.0	0.607632
0	90	$\infty$	10.0	0.517345
0	90	$\infty$	11.0	0.428664
0	90	6	6.0	0.811708
0	90	6	7.0	0.742641
0	90	6	8.0	0.661843
0	90	6	9.0	0.579304
0	90	6	10.0	0.494084
0	90	6	11.0	0.389184
0	90	4.5	6.0	0.800477
0	90	4.5	7.0	0.728418
0	90	4.5	8.0	0.649403
0	90	4.5	9.0	0.567309
0	90	4.5	10.0	0.464814
0	90	4.5	11.0	0.351837
0	90	3	6.0	0.760627
0	90	3	7.0	0.696922
0	90	3	8.0	0.599811
0	90	3	9.0	0.514277
0	90	3	10.0	0.421599
0	90	3	11.0	0.305056

Table 4.1: Summary of Collision Geometries and Mass Loss Outcome, continued.

$b$	$\delta$ ( $^\circ$ )	$P_{\text{spin}}$ (h)	$v_{\text{imp}}$ (m s $^{-1}$ )	$M_{\text{LR}}/M_{\text{tot}}$
0	45	$\infty$	5.0	0.876133
0	45	$\infty$	6.0	0.807526
0	45	$\infty$	7.0	0.739923
0	45	$\infty$	8.0	0.652526
0	45	$\infty$	9.0	0.575735
0	45	$\infty$	10.0	0.496087
0	45	6	5.0	0.877857
0	45	6	6.0	0.805796
0	45	6	7.0	0.725621
0	45	6	8.0	0.634082
0	45	6	9.0	0.554188
0	45	6	10.0	0.485355
0	45	3	5.0	0.846789
0	45	3	6.0	0.767449
0	45	3	7.0	0.684930
0	45	3	8.0	0.565474
0	45	3	9.0	0.441618
0	45	3	10.0	0.378795
0	0	$\infty$	5.0	0.881670
0	0	$\infty$	6.0	0.817889
0	0	$\infty$	7.0	0.734517
0	0	$\infty$	8.0	0.649638
0	0	$\infty$	9.0	0.562160
0	0	$\infty$	10.0	0.472488

Table 4.1: Summary of Collision Geometries and Mass Loss Outcome, continued.

$b$	$\delta$ ( $^\circ$ )	$P_{\text{spin}}$ (h)	$v_{\text{imp}}$ (m s $^{-1}$ )	$M_{\text{LR}}/M_{\text{tot}}$
0	0	6	5.0	0.874406
0	0	6	6.0	0.812157
0	0	6	7.0	0.724058
0	0	6	8.0	0.627248
0	0	6	9.0	0.531327
0	0	6	10.0	0.433020
0	0	3	5.0	0.865095
0	0	3	6.0	0.777822
0	0	3	7.0	0.684112
0	0	3	8.0	0.481345
0	0	3	9.0	0.347406
0	0	3	10.0	0.206721
-0.5	90	$\infty$	5.0	0.855201
-0.5	90	$\infty$	10.0	0.694707
-0.5	90	$\infty$	15.0	0.513617
-0.5	90	$\infty$	20.0	0.299089
-0.5	90	6	5.0	0.834180
-0.5	90	6	10.0	0.671891
-0.5	90	6	15.0	0.490690
-0.5	90	6	20.0	0.312836
-0.5	90	3	5.0	0.797677
-0.5	90	3	10.0	0.638241
-0.5	90	3	15.0	0.445009
-0.5	90	3	20.0	0.289541

Table 4.1: Summary of Collision Geometries and Mass Loss Outcome, continued.

$b$	$\delta$ ( $^\circ$ )	$P_{\text{spin}}$ (h)	$v_{\text{imp}}$ (m s $^{-1}$ )	$M_{\text{LR}}/M_{\text{tot}}$
+0.5	90	$\infty$	5.0	0.852571
+0.5	90	$\infty$	10.0	0.699535
+0.5	90	$\infty$	15.0	0.540372
+0.5	90	$\infty$	20.0	0.327492
+0.5	90	6	5.0	0.865060
+0.5	90	6	10.0	0.702961
+0.5	90	6	15.0	0.511956
+0.5	90	6	20.0	0.326386
+0.5	90	3	5.0	0.860442
+0.5	90	3	10.0	0.690634
+0.5	90	3	15.0	0.481739
+0.5	90	3	20.0	0.315096

Table 4.1: Summary of Collision Geometries and Mass Loss Outcome, continued.

$b$	$\delta$ ( $^\circ$ )	$P_{\text{spin}}$ (h)	$v_{\text{imp}}$ (m s $^{-1}$ )	$M_{\text{LR}}/M_{\text{tot}}$
-0.7	90	$\infty$	5.0	0.876840
-0.7	90	$\infty$	10.0	0.796897
-0.7	90	$\infty$	15.0	0.715336
-0.7	90	$\infty$	20.0	0.619042
-0.7	90	$\infty$	25.0	0.532207
-0.7	90	$\infty$	30.0	0.424618
-0.7	90	6	5.0	0.863776
-0.7	90	6	10.0	0.786793
-0.7	90	6	15.0	0.695417
-0.7	90	6	20.0	0.601023
-0.7	90	6	25.0	0.504266
-0.7	90	6	30.0	0.414065
-0.7	90	3	5.0	0.840861
-0.7	90	3	10.0	0.750761
-0.7	90	3	15.0	0.656733
-0.7	90	3	20.0	0.551418
-0.7	90	3	25.0	0.462672
-0.7	90	3	30.0	0.386483
+0.7	90	$\infty$	5.0	0.874388
+0.7	90	$\infty$	10.0	0.795250
+0.7	90	$\infty$	15.0	0.712159
+0.7	90	$\infty$	20.0	0.628877
+0.7	90	$\infty$	25.0	0.534306
+0.7	90	$\infty$	30.0	0.432360
+0.7	90	6	5.0	0.880263
+0.7	90	6	10.0	0.804069
+0.7	90	6	15.0	0.720063
+0.7	90	6	20.0	0.628323
+0.7	90	6	25.0	0.525654
+0.7	90	6	30.0	0.390580
+0.7	90	3	5.0	0.884772
+0.7	90	3	10.0	0.787585
+0.7	90	3	15.0	0.702943
+0.7	90	3	20.0	0.599283
+0.7	90	3	25.0	0.477597
+0.7	90	3	30.0	0.359355

Table 4.2: Summary of  $\chi^2$  analysis: best-fit interacting mass fractions.  $b$  is the impact parameter,  $\alpha$  and  $A$  are the interacting mass fraction of the projectile and target, respectively, found the the  $\chi^2$  minimization technique.  $\chi^2$  is a goodness-of-fit parameter, and  $\alpha_{\text{geom}}$  is the interacting mass fraction of the projectile found by comparing the cross-sections of the the projectile and the target.

$b$	$\alpha$	$A$	$\chi^2$	$\alpha_{\text{geom}}$
$\pm 0.5$	0.85	0.94	0.61	0.85
$\pm 0.7$	0.745	0.845	0.68	0.44

## Chapter 5: Large-scale Structure in Saturn’s B ring

### 5.1 Chapter Preface

The work presented in this chapter has been submitted for publication to the *Astrophysical Journal* (ApJ) as Ballouz et al. (2017). In this chapter, we study the B ring’s complex optical depth structure. The source of this structure may be the intricate dynamics of the Keplerian shear and the self-gravity of the ring particles. The outcome of these dynamic effects depends sensitively on the collisional and physical properties of the particles. Two mechanisms can emerge that dominate the macroscopic physical structure of the ring: self-gravity wakes and viscous overstability. Here we study the interplay between these two mechanisms through simulations of a local ring patch.

### 5.2 Background

Observations have shown that Saturn’s rings exhibit rich and varied structure. Images from the Cassini spacecraft show that this structure exists on many different scales, from 100’s of meters to 100’s of kilometers (Porco et al., 2005; Colwell et al., 2007). The B ring, in particular, exhibits a varied and complex structure as uncov-

ered by physical optical depth measurements (Colwell et al., 2009). This structure likely comes about from the combined effects of ring particle collisions, ring self-gravity, and tidal forces of Saturn. For the origin of structure of sub-km scales, two mechanisms have been proposed.

The first of these mechanisms is the formation of gravitational wakes in the dense rings. Self-gravity causes the ring particles to clump, forming transient structures that are quickly disrupted by the background shear. These wakes have typical wavelengths of a few 100's of meters (the wavelength is defined as the average radial separation between two wakes) , and they are chiefly characterized by their pitch angle of  $20^\circ$ – $30^\circ$ , the angle that the opaque clumps form with respect to the azimuthal direction of motion. While they have never been imaged directly, their presence have been inferred from Cassini Ultraviolet Imaging Spectrograph (UVIS), Visual and Infrared Mapping Spectrometer (VIMS), and radio occultation optical depth measurements of the A and B rings (Colwell et al., 2006; Hedman et al., 2007).

The self-gravitational interactions of the particles create a dense packing of particles that are able to dissipate energy through inelastic collisions, leading to an increase in the angular momentum transport in the ring. For a sufficient number of dissipative collisions, the viscosity of the ring may evolve to the point that a viscous overstability develops (Salo et al., 2001). This allows particles in over-dense regions to flow towards under-dense regions. As particles flow radially away to under-dense regions, the opacity of the ring patch is temporarily smoothed out as particles don't preferentially occupy any region of space. However, this smoothing process overshoots as particles moving radially inward towards Saturn from an

overdense structure collide with particles moving radially outwards from an adjacent structure. This allows new over-dense regions to develop. These pulsations in ring density generate a wave pattern characterized by axisymmetric over-dense regions (regions of high vertical coherence, see [Hedman et al. 2014](#)). Similar to gravity wakes, these opaque clumps have sub-km wavelength, typically  $\sim 100$  m ([Salo et al., 2001](#); [Daisaka et al., 2001](#); [Rein & Latter, 2013](#)). Recent Cassini infrared occultation measurements of the B ring ([Hedman et al., 2014](#)) show that sub-km structure exists and appear to be structurally stable and axisymmetric at scales of up to 3,000 km, many orders of magnitude larger than the radial overstability wavelength, suggesting that such overstable structures do indeed exist in the B ring.

The development of the viscous overstability depends sensitively on the collisional dynamics of the ring particles. Initially, a viscous instability was hypothesized to explain the structure in the B-Ring. In this scenario, particle collisions were assumed to be highly elastic, which results in the dynamic shear viscosity of the ring to decrease with density, and the particle flux will be directed towards regions of high density. This results in an amplification of density fluctuations. However, laboratory experiments by [Bridges et al. \(1984\)](#) showed that collisions between frictionless and spinless icy spheres at impact speeds typical of Saturn's dense rings (a few mm/s) are highly inelastic. Subsequent laboratory and numerical studies showed the first hints that the viscous overstability could be possible in planetary rings ([Borderies et al., 1985](#); [Salo et al., 2001](#)). These laboratory experiments ([Bridges et al., 1984](#); [Borderies et al., 1985](#)) revealed that the restitution coefficient of the ice spheres was a function of the impact speed. This functional dependence

of the restitution coefficient with the impact speed predicts an energy equilibrium that allows for the viscous diffusion of ring material.

The study of the self-gravity and viscous overstability mechanisms has been advanced through numerical simulations using  $N$ -body integrators that simulate the collisional and gravitational evolution of some 100,000 particles in a co-moving patch (e.g., [Salo 1992](#); [Yasui et al. 2012](#); [Rein & Latter 2013](#)). These studies adapt the functional dependency of the dissipative parameters on the impact speeds found in [Bridges et al. \(1984\)](#) to model the collisions of hard-sphere particles. In the hard-sphere method, particle collisions occur as pair-wise interactions and are resolved instantaneously. These simulations have predicted that the viscous overstability may only develop when the internal density of ring particles is low (200-300 kg/m<sup>3</sup>), implying highly porous ring material or rubble-pile like structure. At larger particle densities, the viscosity of the ring is insufficient to keep it stable against self-gravitational perturbations, and gravity wakes develop. Studies have shown that both viscous overstability and self-gravity wakes may co-exist for certain ring physical and collisional properties ([Salo et al., 2001](#)). However, the exact nature of the relationship between these two mechanisms is not well known.

In this study, we perform direct numerical simulations of a patch of particles in Saturn's dense B ring. Our  $N$ -body code allows us to study the collisional and gravitational dynamics in high optical depth regions in Saturn's rings. The collisional method we employ in this study, which allows multi-contact and frictional forces ([Schwartz et al., 2012](#)), has never before been used in studies of Saturn's rings. This state-of-the-art numerical modeling enables a better understanding of

the interplay between the two mechanisms that create the structure of Saturn’s B ring. The goal of this study is to generate a library of synthetic observations of the optical depth structure mapped to particle physical and collisional properties. By comparing these synthetic observations with actual data, we may be able to also determine the physical properties of ring particles.

### 5.3 Methodology

We simulate the collisions of ring particles in Saturn’s B ring, a distance of 100,000 km away from Saturn. The typical collision speeds of particles due to Keplerian shear is expected to be of the order of a few times  $\Omega_0 r_p$ , where  $\Omega_0$  is the Keplerian orbital angular frequency for an object orbiting Saturn at 100,000 km ( $\sim 2 \times 10^{-4} \text{ s}^{-1}$ ), and  $r_p$  is the typical radius of the ring particles. Thus, for our ring simulations, particles typically collide at relative speeds of  $\sim 0.5 - 1 \text{ mm s}^{-1}$ . Therefore, in order to maintain overlaps that are  $\leq 1\%$ , we set  $k_n \sim 4.71 \text{ kg s}^{-2}$  and the time step  $\delta t \sim 1.5 \text{ s}$ .

#### 5.3.1 Periodic Boundary Conditions & Patch Properties

We perform local simulations of ring particles by restricting the computational volume to a small region (a “patch”) of the entire ring. Particles are modeled in a co-moving patch frame (Perrine & Richardson, 2012). The linearized equations of motion, called the Hill’s equations, are (Hill, 1878):

$$\ddot{x} = F_x + 3\Omega^2 x + 2\Omega\dot{y},$$

$$\ddot{y} = F_y - 2\Omega\dot{x},$$

$$\ddot{z} = F_z - \Omega^2 z,$$

where  $F$  is the acceleration due to particle self-gravity,  $x$ ,  $y$ , and  $z$  are the coordinates of the particle in the local coordinate system (whose origin is located at the center of the patch), and the derivatives are with respect to time. We use periodic boundaries at the radial and azimuthal edges of the patch. Periodic boundary conditions (PBCs) allow us to simulate a patch of the disk with a computational feasible number of particles. PBCs are imposed on a patch of particles by replicating the patch in the radial ( $x$ ) and azimuthal ( $y$ ) directions. Each replicated patch contains ghost particles that match the relative positions of the original particles. Figure 5.1 illustrates the PBC setup. Particles in the central patch feel the gravitational effects of ghost particles, and can collide with ghost particles at the boundaries. The azimuthal and radial extents of the patch are small compared to the orbital distance to the planet, but large compared to the radial mean free path of the particles inside the patch. Particles exiting one side of the azimuthal or radial boundary reappear on the other side, preserving their general properties (mass and spin). When a particle crosses the radial boundary, its azimuthal speed is modified to account for the Keplerian shear. Therefore, depending on whether it crosses over from a smaller radial position to a larger one or vice versa, its azimuthal speed will be adjusted by  $\pm\frac{3}{2}\Omega L_x$ , where  $L_x$  is the radial width of the patch.

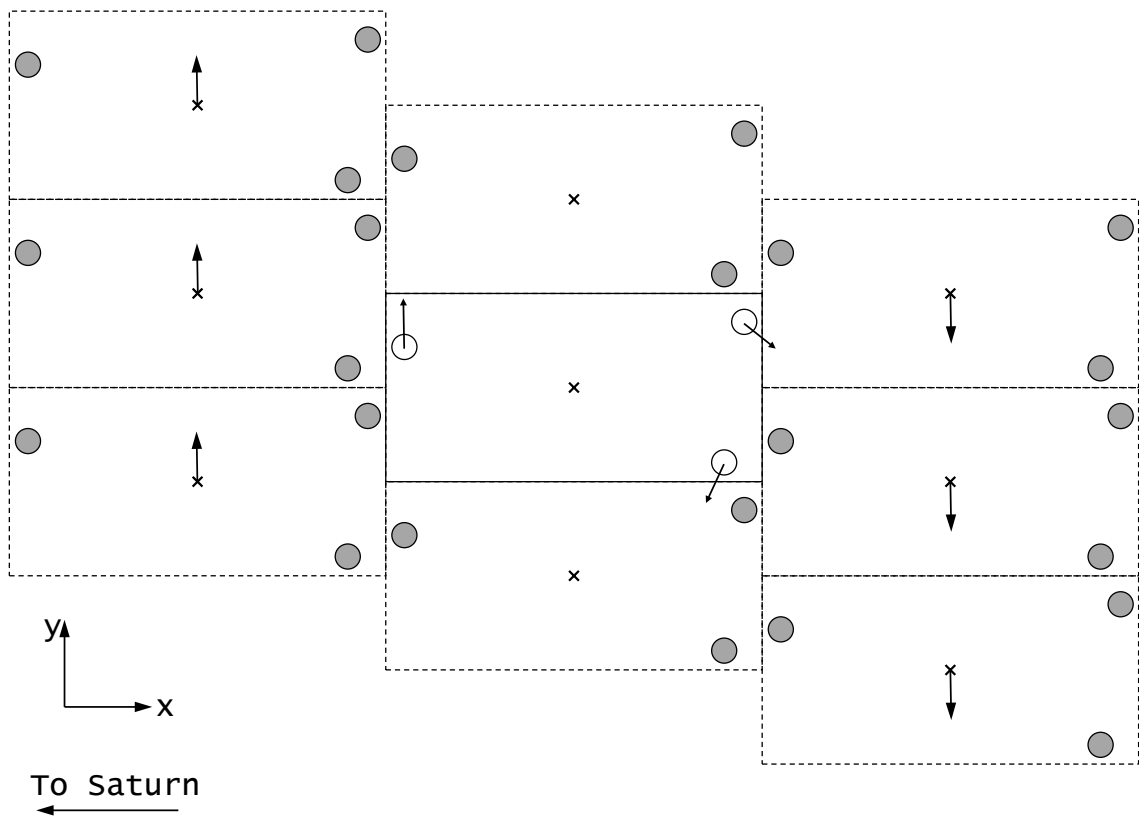


Figure 5.1: A schematic diagram of a local sliding-patch model with shearing periodic boundary conditions. The three white particles in the center solid box are the simulated particles; grey particles are in replicated patches (dashed boxes) that provide boundary conditions. The  $x$  coordinate is the radial direction, with Saturn located in the negative  $x$  direction;  $y$  is the azimuthal direction, and the entire patch orbits Saturn in the positive  $y$  direction.  $z$  points out of the page, forming a right-handed coordinate system. The simulation is carried out in the orbital frame of the center of the patch, so particles to the left shear upward (positive  $y$  direction); on the right, they shear downward (negative  $y$  direction). The replicated patches similarly shear past the center box in Keplerian fashion; each bold X marks the center of each patch, with the bulk motion of each patch indicated by black arrows.

We simulate a patch of the B ring that has a dynamic optical depth of 1.4 and a surface density of  $840 \text{ kg m}^{-2}$ . We choose this value of the optical depth as it is typical of the B ring, and it corresponds to a number of particles that can be feasibly simulated in a timely fashion using our code. The value of the surface density is well within the range found through analysis of density waves (400–1400  $\text{kg m}^{-2}$ , [Hedman & Nicholson 2016](#)). In order to ensure that we allow sufficient space for the formation of large-scale structures, we simulate a patch that is at least  $20 \lambda_{cr}$  in the radial direction and  $4 \lambda_{cr}$  in the azimuthal direction, where  $\lambda_{cr}$  is the Toomre wavelength, and is defined as:

$$\lambda_{cr} = \frac{4\pi^2 G \sigma}{\Omega}, \quad (5.1)$$

where  $G$  is the gravitational constant and  $\sigma$  is the surface density. Previous simulations ([Salo, 1992](#); [Daisaka & Ida, 1999](#)) have shown that the typical wavelengths of wakes is close to  $\lambda_{cr}$ .

For each simulation, we choose a single combination of a particle density and particle radius that corresponds to a constant optical depth of 1.4 and a patch surface density of  $840 \text{ kg m}^{-2}$ . This is done in order to keep  $\lambda_{cr}$  constant across all simulations, allowing us to draw more accurate comparisons of simulation outcomes across different particle density cases. Therefore, a simulation can contain particles with densities of 0.45, 0.60, 0.75, or  $0.90 \text{ g/cm}^3$  that have radii of 1.0, 0.75, 0.6, and 0.5 m, respectively. The number of particles in our simulations range from  $\sim 120,000$  to  $\sim 500,000$  particles (see [Table 5.1](#))

### 5.3.2 Diagnostic Tools

We develop diagnostic tools to study the bulk behavior of the particles in the patch and to compare our results to observations. Firstly, in order to measure the different contributions to the angular momentum transport in the ring, we describe how we calculate the viscosity of the patch. This is important for characterizing the influence of the individual ring properties to the larger-scale dynamics, and it allows us to directly compare our results to previous theoretical treatments of ring dynamics. Secondly, we describe a Monte Carlo ray-tracing algorithm that measures the physical optical depth of our simulations. This allows us to directly compare the outcome of our simulations to Cassini results by producing synthetic stellar occultation data.

#### 5.3.2.1 Viscosity Calculation

In a planetary ring system, the viscosity of the disk describes how efficiently the system is able to transport angular momentum from interior parts to its exterior. In its simplest sense, viscosity is a measure of a fluid system's resistance to stresses, either shearing or tensile. For a ring system such as Saturn's, there are three components that contribute to the viscosity in a disk: translational viscosity, collisional viscosity, and gravitational viscosity (Daisaka et al., 2001). The first is the translational component due to Keplerian shear,  $\nu_{trans}$ . This can be calculated

by measuring the radial velocity dispersion in the ring patch, and is defined as:

$$\nu_{\text{trans}} = \frac{2}{3\Omega\Sigma_i m_i} \Sigma_i m_i \dot{x}_i \dot{y}_{r,i}, \quad (5.2)$$

where  $\Sigma_i m_i$  is the sum of all particle masses,  $\dot{x}_i$  is the  $x$ -component of the velocity, and  $\dot{y}_{r,i} = \dot{y}_i + (3/2)\Omega x_i$  is the  $y$ -component of the velocity relative to the mean shear speed at radial position  $x_i$ .

The second component of the viscosity is due to the transfer of angular momentum due to collisions. Previous authors ([Wisdom & Tremaine, 1988](#); [Daisaka et al., 2001](#)) have relied on event-driven hard-sphere collision codes. Thus, they calculate the exchange in momentum in the azimuthal direction for each discrete collision. The collisional component of the viscosity is given by:

$$\nu_{\text{coll}} = \frac{2}{3\Omega M \delta T} \Sigma \delta p_y (x_{>} - x_{<}), \quad (5.3)$$

where  $M$  is the total mass in the patch, and the summation is over all pairwise collisions that occur during the time interval  $\delta T$ , which results in an exchange of momentum  $\delta p_y$  in the  $y$  (azimuthal) direction to the particle in the exterior orbit with radial distance  $x_{>}$  whose collisional partner has an interior orbit with radial distance  $x_{<}$ .

The last component of the viscosity is due to the self-gravitational interaction of ring particles. While this is an important contribution to the overall viscosity of a ring system, we do not measure this component in this study. Rather, the focus of this study is on how collisional interactions of the disk are effected by different physical properties of the particles. We refer the reader to [Daisaka et al. \(2001\)](#) for a full discussion on gravitational viscosity.

Since our soft-sphere code treats collisions as finite duration with possible multiple simultaneous contacts and frictional forces, we must revise this formulation. Following the treatment in [Wisdom & Tremaine \(1988\)](#), we can reformulate the exchange of momentum between two particles from the collisional force balance calculated in our soft-sphere collision method, so the collisional viscosity becomes:

$$\nu_{coll} = \frac{2}{3\Omega M} \Sigma F_{y>}(x_{>} - x_{<}), \quad (5.4)$$

where  $F_{y>}$  is the collisional force in the azimuthal direction on a particle due to its colliding partner(s). Formulated in this way, we are able to take into account multi-contact and frictional forces.

Another method that involves measuring the change in orbital elements due to collisions has been devised to measure the total viscosity (sum of translational, collisional, and gravitational viscosity) in the ring patch ([Tanaka et al., 2003](#)). [Yasui et al. \(2012\)](#) recently used this method to calculate the viscosity of spinning self-gravitating particles in planetary rings. They were also able to take the first steps in measuring the effect of friction on the viscosity by including the effects of a tangential restitution coefficient. [Yasui et al. \(2012\)](#) were able to demonstrate the validity of their calculation by performing simple tests to measure the viscosity in a small patch and compare their results to those found by [Wisdom & Tremaine \(1988\)](#).

In order to validate our re-formulation of the [Wisdom & Tremaine \(1988\)](#) prescriptions for calculating the collisional viscosity, and to ensure that our code is capable of replicating results found in recent numerical simulations of ring systems, we performed a simple simulation test similar to that done by [Yasui et al. \(2012\)](#).

Using a square  $125 \text{ m} \times 125 \text{ m}$  ring patch made up of  $1 \text{ m}$  particles, we ran ring simulations with a speed-dependent normal coefficient of restitution,  $\epsilon_n$ , based on laboratory impact experiments (Bridges et al., 1984), given by:

$$\epsilon_n(v) = \min\{0.32(v/v_c)^{-0.234}, 1\}, \quad (5.5)$$

where  $v$  is the relative speed between colliding particles at the moment of first overlap, and  $v_c$  is a normalization equal to  $1 \text{ cm s}^{-1}$ . We performed these simulations for ring patches with optical depths ranging from 0.4 to 1.6, and for values of  $\epsilon_t$  of 0.5 and 1.0. These runs had the self-gravity between particles turned off since we are only interested in the equilibrium viscosity achieved through ring particle collisions. This also speeds up the calculation. The simulations were run until the particles reached collisional equilibrium (a few 10's of orbits), determined when the patch reaches a steady radial velocity dispersion. We find excellent agreement between the viscosities we measure and those found in Yasui et al. (2012) (see Figure 5.2).

### 5.3.2.2 Physical Optical Depth Calculation

The dynamical optical depth  $\tau_{\text{dyn}}$  of a ring is defined as

$$\tau_{\text{dyn}} = \int \pi s^2 n(s) ds, \quad (5.6)$$

where  $s$  is the particle radius and  $n(s)$  is the surface number density of ring particles whose sizes are between  $s$  and  $s + ds$ .

The physical normal optical depth  $\tau_{\text{phys}}$  is defined as (e.g., Colwell et al. 2007)

$$\tau_{\text{phys}} = -\sin |B| \log\left(\frac{I}{I_0}\right), \quad (5.7)$$

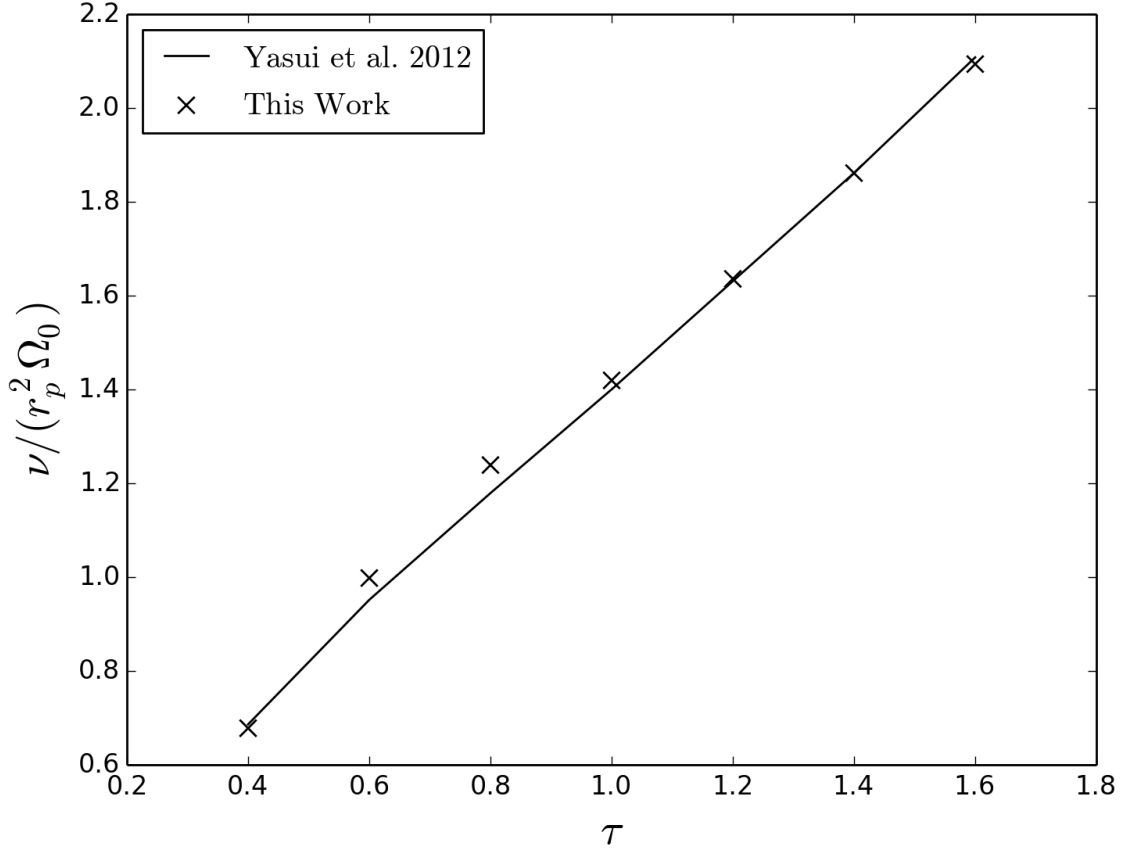


Figure 5.2: We plot the total viscosity,  $\nu$ , normalized by  $\Omega_0 r_p^2$  as a function of the dynamical optical depth of the ring. Our total viscosity calculations (translational and collisional) match those found by [Yasui et al. \(2012\)](#) (see their Fig. 1b). The simulations are for a velocity-dependent normal restitution coefficient with  $\epsilon_t = 0.5$ .

where  $B$  is the elevation angle of the observer,  $I$  is the measured intensity, and  $I_0$  is the unocculted intensity of the light source.

If particles are randomly distributed in the horizontal directions and the mutual separation is large enough,  $\tau_{\text{phys}}$  becomes independent of observational geometry and coincides with  $\tau_{\text{dyn}}$  (the limit of classic radiative transfer). If the mutual separation is comparable to the particle radius,  $\tau_{\text{phys}}$  becomes larger than  $\tau_{\text{dyn}}$ . This effect is called the volume filling factor effect (e.g., [Salo & Karjalainen 2003](#)). If the ring structure is not horizontally uniform due to wakes or waves,  $\tau_{\text{phys}}$  depends on the azimuthal angle of the observer. Usually,  $\tau_{\text{phys}}$  takes its minima when the line of sight is aligned to the wake direction (e.g., [Colwell et al. 2006](#); [Hedman et al. 2007](#)). [Fig 5.3](#) illustrates this principle.

We developed a ray-tracing code to derive  $\tau_{\text{phys}}$  using outputs of  $N$ -body simulations. The basic schemes employed in the code are similar to those given in [Salo and Karjalainen \(2003\)](#). Briefly, the algorithm is as follows:

- The simulated region is partitioned into two-dimensional sub-cells, with particles allocated by sub-cell.
- A ray is generated by randomly choosing  $x$  and  $y$  coordinates in the ring midplane, where  $z=0$ , and forming the unit vector  $\mathbf{n}$  directed towards the light source. In the Hill coordinate system,  $\mathbf{n}$  is defined by its components:

$$n_x = \cos \theta_s \sin B_s,$$

$$n_y = \sin \theta_s \sin B_s,$$

$$n_z = \cos B_s,$$

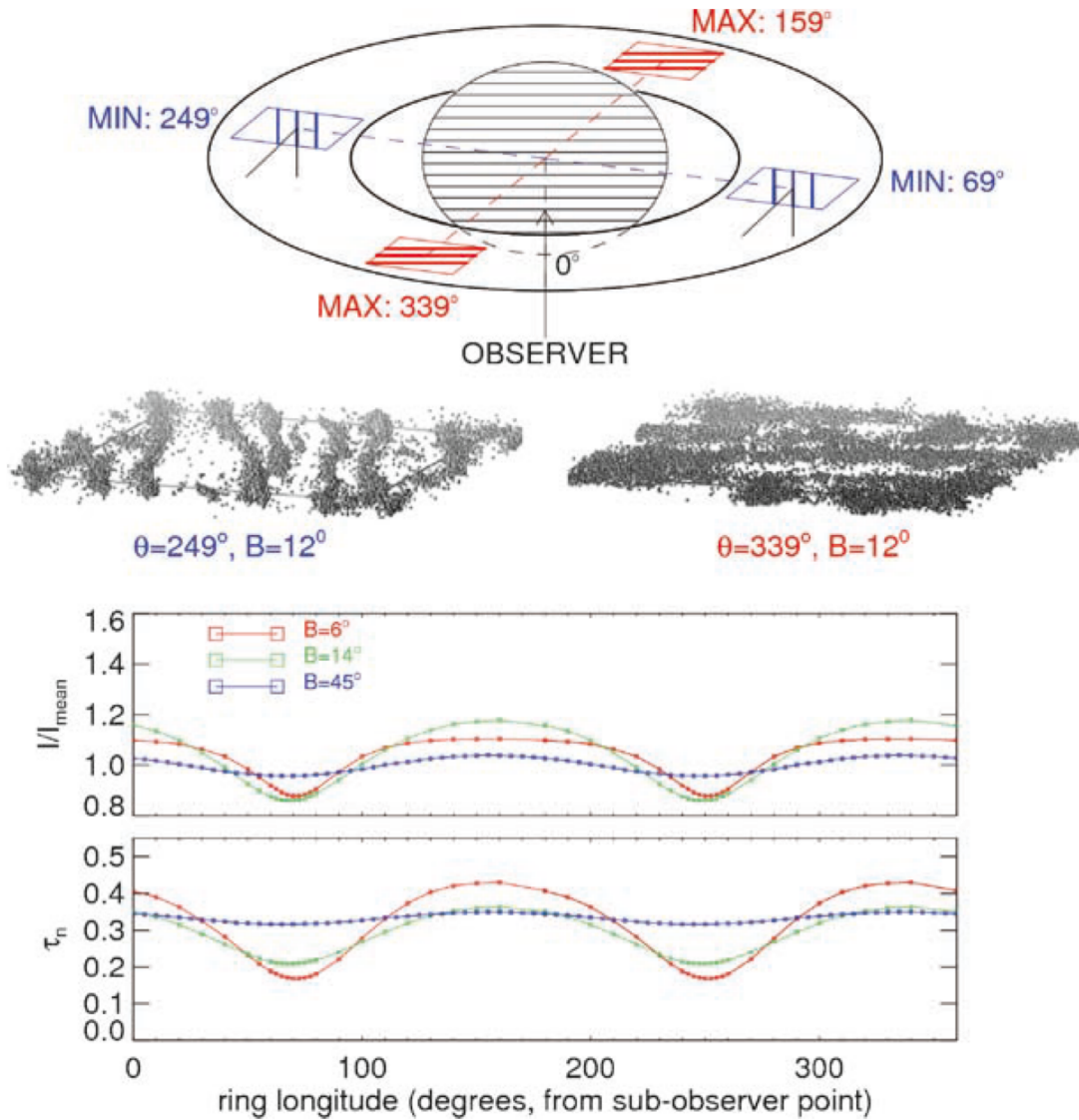


Figure 5.3: Schematic representation of azimuthal brightness asymmetry in the ring system due to the presence of wake structure. At low elevation angles,  $B$ , the wakes, which trail here by about  $21^\circ$  with respect to the observer's tangential direction, are seen along their long axis at ring longitudes,  $\theta$ , of  $69^\circ$  and  $249^\circ$ . Therefore, the rarefied regions are visible, reducing the total reflecting surface area. This corresponds to minimum brightness (top plot) or minimum optical depth (bottom plot). At longitudes  $90^\circ$  away, the rarefied regions are hidden, maximizing the total reflecting surface area. This corresponds to maximum brightness levels and optical depths. Source: Schmidt et al. (2009)

where  $\theta_s$  and  $B_s$  are the azimuthal and elevation angle of the light source.

- We first check whether the ray coming from the light source intersects any sub-cells, and then check whether the ray intersects any particles within an intersected sub-cell. If multiple sub-cells can be intersected by a single ray, then these sub-cells are checked in the order of which is intersected first by the ray's trajectory.
- If the ray passes through the simulated region without intersecting any particles, it may still intersect with a ghost particle. Therefore, if an intersection is still possible, the ray is regenerated with a new position given by the periodic boundary conditions of the shearing system. Intersections are still possible if

$$p_z < \max(z_i + r_i) \quad (5.8)$$

or

$$p_z > \min(z_i - r_i) \quad (5.9)$$

where  $p_z$  is the  $z$  coordinate of the ray,  $z_i$  is the  $z$  coordinate of any particle in the simulation, and  $r_i$  is the corresponding particle radius. Therefore, the algorithm compares the  $z$  coordinate of the ray to the maximum and minimum vertical extent of the simulated particles.

- We continue generating randomly positioned rays until we numerically converge on a value for the physical optical depth. The simulated physical optical depth is found by setting  $I_0$ , in Eq. 5.7, to the number of rays produced, and

$I$  to the number of rays that pass through the ring without intersecting any particles.

## 5.4 Results

We have performed simulations that explore the effects of particle density and friction on the collisional dynamics of the ring particles and the subsequent large-scale structure evolution. Each simulation was run for at least 100 orbits in order for the patch to safely reach collisional equilibrium. Since the surface properties of actual ring particles are not well constrained, we explored a wide range of friction properties. This allowed us to gauge the range of possible behaviors of large-scale structure formation. Furthermore, by matching collisional outcomes in our simulations to observations, we may be able to constrain the frictional (surface) properties of real ring particles.

Table 5.1–5.1 lists the simulations that were performed. Here we also summarize the outcome of each simulation by providing the equilibrium collisional and translational viscosities. Furthermore, we also give the Toomre  $Q$  of the ring, where  $Q$  is defined as:

$$Q = \frac{c_r \Omega}{\pi G \sigma}, \quad (5.10)$$

where  $c_r$  is the radial velocity dispersion, and  $\sigma$  is the surface density.  $Q$  attains a time-averaged equilibrium value of the order of 2 in the case of strong wake structure. Previous results have shown the emergence of strong wake structure when the radial

velocity dispersion due to collisions and gravitational encounters does not exceed that corresponding to  $Q \sim 2$  (Salo, 1995; Salo et al., 2001; Ohtsuki & Emori, 2000).

Table 5.1: Summary of ring patch parameters and simulations results.  $\rho$  is the ring particle internal density,  $r_p$  is the ring particle radius,  $\mu_s$  is the coefficient of static friction,  $\mu_r$  is the coefficient of rolling friction,  $\nu_{\text{coll}}$  is the collisional viscosity (in units of  $\Omega_0 r_p^2$ ),  $\nu_{\text{trans}}$  is the translational viscosity (in units of  $\Omega_0 r_p^2$ ), and  $Q$  is the Toomre parameter.

$\rho$ (g cm $^{-3}$ )	$r_p$ (m)	$\mu_s$	$\mu_r$	$\nu_{\text{coll}}$	$\nu_{\text{trans}}$	$Q$
0.45	1.0	0.0	0.0	5.70	8.29	1.34
0.45	1.0	0.0	0.2	5.64	8.23	1.31
0.45	1.0	0.2	0.0	8.88	14.12	1.86
0.45	1.0	0.2	0.2	9.91	16.41	2.09
0.45	1.0	0.4	0.0	9.24	16.32	2.07
0.45	1.0	0.4	0.2	18.89	30.81	2.65
0.45	1.0	0.6	0.0	13.98	20.98	2.30
0.45	1.0	0.6	0.2	17.81	28.21	2.58
0.45	1.0	0.8	0.0	13.12	21.06	2.43
0.45	1.0	0.8	0.2	20.75	40.96	3.44
0.45	1.0	1.0	0.0	12.97	20.08	2.04
0.45	1.0	1.0	0.2	20.35	40.86	3.22
0.60	0.75	0.0	0.0	6.81	14.41	2.34
0.60	0.75	0.0	0.2	6.98	15.65	2.25
0.60	0.75	0.2	0.0	10.97	22.43	2.53
0.60	0.75	0.2	0.2	10.71	20.04	2.71
0.60	0.75	0.4	0.0	10.96	21.10	2.48
0.60	0.75	0.4	0.2	13.34	24.81	2.96
0.60	0.75	0.6	0.0	7.80	15.07	3.05
0.60	0.75	0.6	0.2	16.67	34.48	3.09
0.60	0.75	0.8	0.0	10.51	20.48	2.67
0.60	0.75	0.8	0.2	14.57	25.74	3.13
0.60	0.75	1.0	0.2	11.82	21.10	3.32

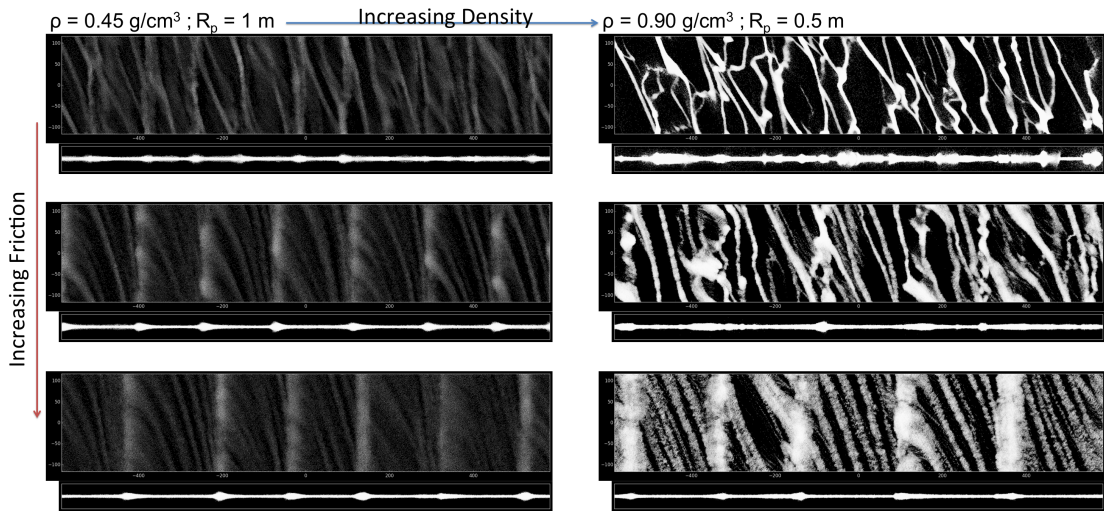


Figure 5.4: Snapshots of some of our simulations after 100 orbits of collisional and gravitational evolution. The larger images show the position of ring particles in radial ( $x$ ) and azimuthal ( $y$ ) space. The smaller image shows the positions of particles in radial and vertical ( $z$ ) space. The left and right columns show ring particles with internal densities of 0.45 and 0.9  $\text{g}/\text{cm}^3$ , respectively. When we allow the particles to interact with higher frictional forces (lower rows in the figure have higher friction), we find that the ring particles are better at maintaining azimuthal ( $y$ -direction) axisymmetric features, brought about by the viscous overstability. For lower friction, the patch is not viscous enough to be stable against self-gravity wakes (inclined features most prominent in top panels).

Table 5.1: Summary of ring patch parameters and simulations results, continued.

$\rho$ (g cm <sup>-3</sup> )	$r_p$ (m)	$\mu_s$	$\mu_r$	$\nu_{\text{coll}}$	$\nu_{\text{trans}}$	$Q$
0.75	0.60	0.0	0.0	7.45	22.19	2.60
0.75	0.60	0.0	0.2	7.45	20.62	2.73
0.75	0.60	0.2	0.0	12.01	26.76	2.95
0.75	0.60	0.2	0.2	14.03	28.32	3.14
0.75	0.60	0.4	0.0	13.43	30.97	2.92
0.75	0.60	0.4	0.2	16.52	32.17	3.22
0.75	0.60	0.6	0.0	13.47	27.77	2.85
0.75	0.60	0.6	0.2	17.02	32.20	2.99
0.75	0.60	0.8	0.0	13.87	30.43	2.99
0.75	0.60	0.8	0.2	17.68	32.26	2.93
0.75	0.60	1.0	0.0	14.29	31.33	2.70
0.75	0.60	1.0	0.2	16.06	28.80	2.91
0.90	0.50	0.0	0.0	7.45	22.19	1.816
0.90	0.50	0.0	0.2	7.45	20.62	2.155
0.90	0.50	0.2	0.0	12.01	26.76	2.49
0.90	0.50	0.2	0.2	14.03	28.32	2.59
0.90	0.50	0.4	0.0	13.43	30.97	2.94
0.90	0.50	0.4	0.2	16.52	32.17	3.27
0.90	0.50	0.6	0.0	13.47	27.77	3.86
0.90	0.50	0.6	0.2	17.02	32.20	3.74
0.90	0.50	0.8	0.0	13.87	30.43	3.73
0.90	0.50	0.8	0.2	17.68	32.26	4.01
0.90	0.50	1.0	0.0	14.29	31.33	4.24
0.90	0.50	1.0	0.2	16.06	28.80	4.33

#### 5.4.1 Correlation between Friction and Viscosity

Figure 5.4 shows snapshots of our simulations after 100 orbits of collisional and gravitational evolution. We find that when particles have higher surface friction, axisymmetric features become more prevalent. Visual inspection of multiple frames allows us to ascertain that these features are likely brought about by viscous overstability wakes. At lower friction values, the ring particles form self-gravity wake

structure that are inclined with respect to the orbital direction (inclined features most prominent in top panels of Figure 5.4).

The viscous overstability comes about by the combined effects of inelastic collisions and Keplerian shear, which lead to an energetic steady state. In this state, inelastic collisions cause overdense regions to develop. Due to energy input from the Keplerian shear, the particle flux is directed away from regions of high density. The mass in over-dense regions flows to under-dense regions; however, this mass flow overshoots due to the momentum of the particle flow, leading to new overdense regions. Studies show that this overstability develops for regions in the ring where the viscosity increases with optical depth beyond some critical rate (Salo et al., 2001; Daisaka et al., 2001; Rein & Latter, 2013):

$$\beta = \frac{d \ln \nu}{d \ln \tau} > \beta_{\text{cr}} \sim 1$$

where  $\nu$  is the viscosity, and  $\tau$  is the optical depth.

For moderately high-friction cases, we see that the patch also reaches an equilibrium state with characteristic viscous overstability pulsations. Unlike previous simulations that studied the overstability (Salo et al., 2001), we see very little sign of gravitational wakes in this case even for a moderately high internal particle density of  $0.45 \text{ g cm}^{-3}$ . Salo et al. (2001) showed that the viscous overstability is present when ring particles have low internal density ( $0.20\text{--}0.30 \text{ g cm}^{-3}$ ), and may be slightly featured (less prominent axisymmetric features) at intermediate internal densities ( $0.45 \text{ g cm}^{-3}$ ), and likely non-existent for particles with the density of actual water ice  $0.90 \text{ g cm}^{-3}$ . We find that, for sufficiently high surface friction, overstability

features may exist even for non-porous water ice with densities of  $0.90 \text{ g cm}^{-3}$  (see bottom-right panel of Figure 5.4).

Quantitatively, we can compare the change in the collisional viscosity of the patch with the Toomre  $Q$  parameter, as a function of particle static friction  $\mu_s$  (Figure 5.5). The  $Q$  parameter is a ratio of the particle’s radial velocity dispersion to the ring patch’s surface density. Self gravity wakes develop for  $Q < 2$ . A high friction value increases the viscosity of the patch, and inhibits the formation of self-gravity wakes.

#### 5.4.2 Correlation with Density

We studied the dependence of the collisional viscosity with density. We find that for sufficiently large friction values (here  $\mu_s = 1$ ), the viscosity stabilizes the disk against self-gravity wakes even for very dense particles. Previous results that did not include explicit treatment of friction and multi-contact physics (Salo et al., 2001; Hedman et al., 2014) have shown that the internal density of particles needs to be  $< 0.30 \text{ g cm}^{-3}$  for viscous overstability to develop. Here we find that even particles with  $0.90 \text{ g cm}^{-3}$  can exhibit the overstability.

To further test the influence of particle density on large-scale structure formation, we plotted the relationship between  $\rho$ , the friction parameters, and  $Q$  in Figure 5.6. We show the value of  $Q$  found in simulations with three different particle densities, for values of  $\mu_s$  ranging from 0.0–1.0, and for a rolling friction value of  $\mu_r = 0.2$ . Here, we see that  $Q$  rises most steeply with  $\mu_s$  for the lowest particle

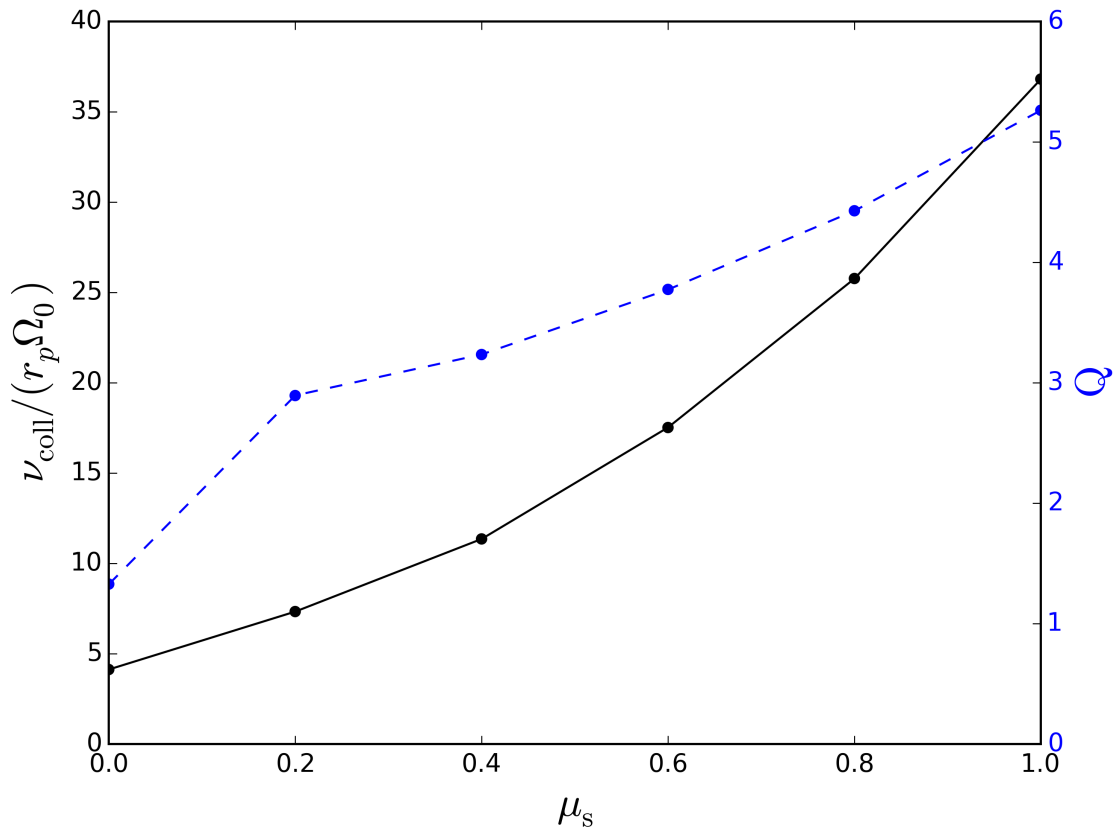


Figure 5.5: Quantitatively, we can compare the change in the collisional viscosity (left axis, solid black curve) of the patch with the Toomre  $Q$  parameter (right axis, dashed blue curve), as a function of particle static friction  $\mu_s$ . A high friction value increases the viscosity of the patch, and inhibits the formation of self-gravity wakes.

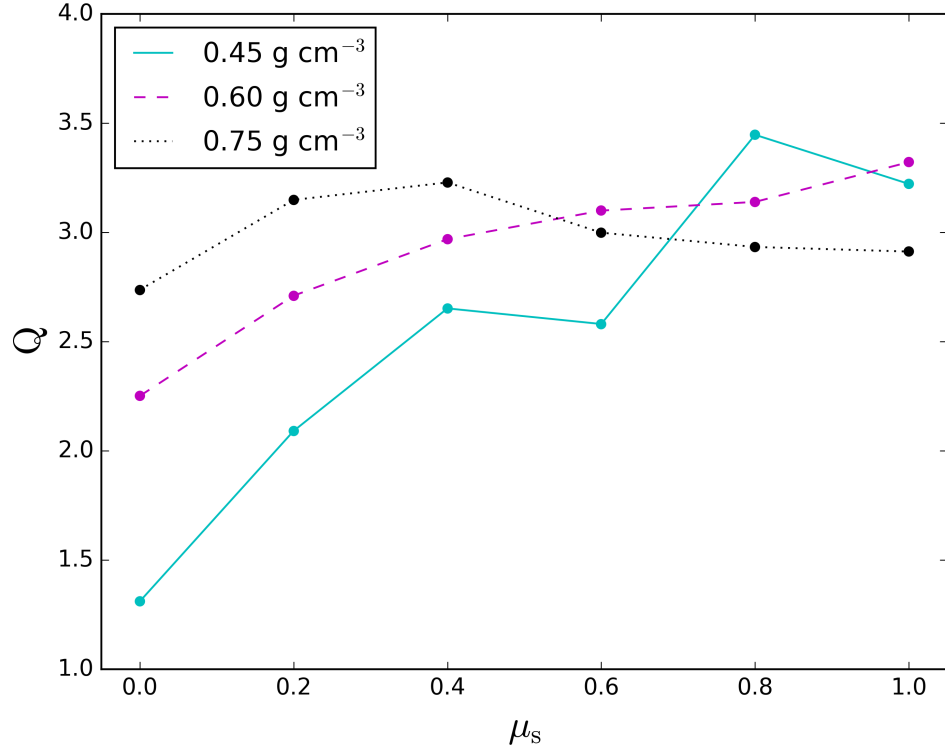


Figure 5.6: The relationship between particle density (denoted by different linestyles and colors), the static friction component, and Toomre  $Q$ . These are cases where  $\mu_r = 0.2$ . The solid cyan line represents cases with  $\rho = 0.45 \text{ g cm}^{-3}$  and  $r_p = 1.0 \text{ m}$ . The dashed magenta line represents cases with  $\rho = 0.60 \text{ g cm}^{-3}$  and  $r_p = 0.75 \text{ m}$ . The dotted black line represents cases with  $\rho = 0.75 \text{ g cm}^{-3}$  and  $r_p = 0.60 \text{ m}$ .

density. The friction parameter here acts to increase the viscosity of the patch, and subsequently drives the formation of large-scale structure and overstability wakes. At sufficiently high friction values, the value of  $Q$  seems to saturate at  $\sim 3$ .

### 5.4.3 Physical Optical Depth Measurements

Using the ray-tracing algorithm described in Section 2.3.2, we can generate synthetic optical depth profiles of our library of simulations, in order to compare with Cassini observations.

By varying the azimuthal observing angle,  $\theta$ , we are able to investigate the nature of the large-scale structure in our simulations. Structures generated by the viscous overstability are axisymmetric; therefore, the physical optical depth,  $\tau_{\text{phys}}$ , is at a minimum when  $\theta$  is aligned parallel to the azimuthal direction and at a maximum when  $\theta$  is aligned parallel to the radial direction.

In Fig. 5.7, we show our generated  $\tau_{\text{phys}}$  profiles for two different particle density cases, 0.45 and 0.60 g cm<sup>-3</sup>. In these figures,  $\theta = 0$  corresponds to an observing angle aligned with the radial direction facing inwards towards Saturn.  $\theta$  increases in a counterclockwise fashion from this initial geometry. For each simulation,  $\tau_{\text{phys}}$  is calculated for an elevation angle of  $B = 30^\circ$ , and for  $\theta$  ranging from 0 to  $2\pi$  sampled at  $4^\circ$  intervals. This value of  $B$  is chosen to match that of the Cassini spacecraft. Furthermore, intermediate values of  $B$  results in variations  $\tau_{\text{phys}}$  with  $\theta$ . As  $B$  approaches  $90^\circ$ , the viewing geometry will be less influenced by changes in  $\theta$ , resulting in a near-constant  $\tau_{\text{phys}}$ . For both particle density cases, we see that the amplitude of the  $\tau_{\text{phys}}$  variation decreases as a function of the friction parameters. This suggests that friction acts to create a larger dispersion in the physical location of particles in the patch. This is consistent with the idea that friction acts against self-gravitational clumping. For most of the cases seen here for both particle densities, we see that the minima are located at  $\theta$  values between  $\sim 90^\circ$  and  $110^\circ$ . This is consistent with observations of  $\sim 90^\circ$  to  $120^\circ$  tilts in the structure found in Saturn's dense rings (e.g. Colwell et al. 2007). The typical value is  $90^\circ$  for the outer B ring, indicating the existence of overstability features. Although the typical pitch angle seen in all of our simulations is consistent with observations, the average values of

$\tau_{\text{phys}}$  we measure ( $\sim 1$ ) are much lower than those for the outer B ring, which are typically a few factors larger than 1 and can be greater than 5. It is possible that inter-wake gaps are filled by small particles that are ignored in our simulations, but contribute most of the observed opacity.

We also find that for higher friction values, the minima are shifted towards  $90^\circ$ , or axisymmetry. This is true for both density cases. In order to obtain an accurate estimate of the azimuthal angle that coincides with a given minimum  $\tau_{\text{phys}}$ , a sinusoidal curve that best fits the data was generated using a least-squares minimization technique. For the case of  $0.45 \text{ g cm}^{-3}$ , we find minima at values of  $100.1^\circ$ ,  $93.6^\circ$ , and  $88.5^\circ$  for  $\mu_s = 0.6, 0.8, \text{ and } 1.0$ , respectively. For the case of  $0.60 \text{ g cm}^{-3}$ , we find minima at values of  $109.5^\circ$ ,  $103.8^\circ$ , and  $95.8^\circ$  for  $\mu_s = 0.6, 0.8, \text{ and } 1.0$ , respectively. The shift is more apparent in the top panel of Fig. 5.7, the lower-density case. This is expected, as larger particle densities tend to lead to stronger self-gravitational wakes. Hence, for similar friction values, lower-density particles are more strongly driven to axisymmetry and viscous overstability.

#### 5.4.4 Comparison with Cassini UVIS occultations

Finally, we attempt to compare the results of our simulations to Cassini UVIS stellar occultations (Colwell et al., 2006). Observations of stellar occultations by the UVIS instrument reveal the transparency of the ring as a function of observation geometry. These observations vary both the azimuthal observing angle,  $\theta$ , and the spacecraft elevation angle  $B$ . Therefore, in order to effectively compare our simu-

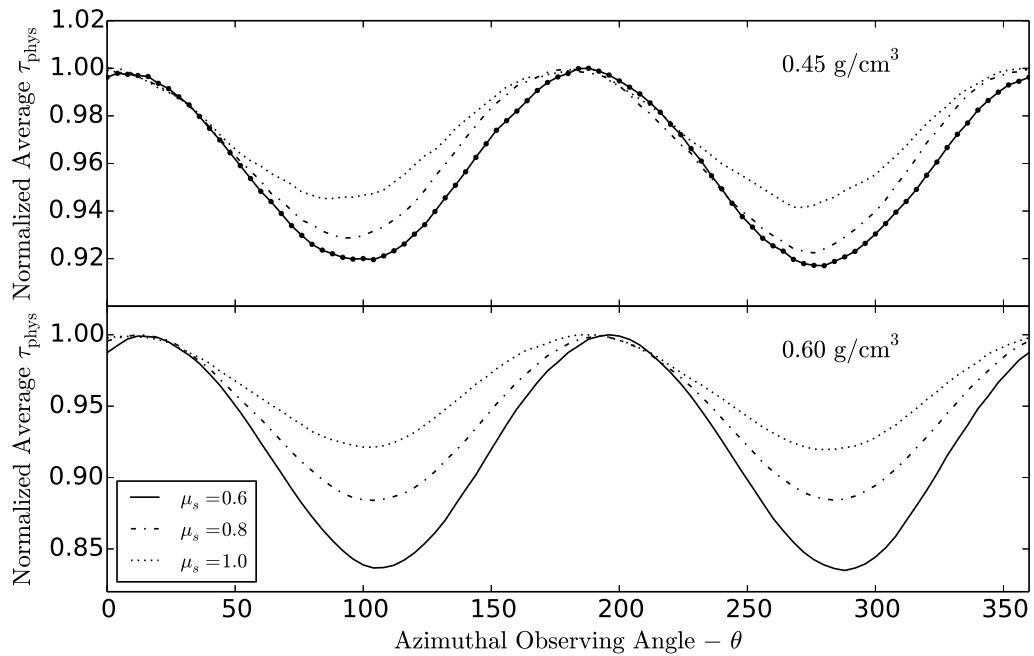


Figure 5.7: The normalized average physical optical depth as a function of observing angle ( $^{\circ}$ ) at an elevation  $B = 30^{\circ}$  for simulations with a particle density of  $0.45 \text{ g cm}^{-3}$  (top panel) and  $0.60 \text{ g cm}^{-3}$  (bottom panel). For both panels, the solid, dash-dotted, and dotted curves represent simulations where particles have static friction values of 0.6, 0.8, and 1.0, respectively. Individual data points are plotted on the solid line in the top panel to show the  $4^{\circ}$  sampling frequency that was used for each curve. An increase in the particle surface roughness evidently causes an observational shift from tilted self-gravity wake features to azimuthally coherent viscous overstability features.

lation data to observations, we calculate the average transparency of our simulated patch for unique combinations of  $\theta$  and  $B$ . The transparency,  $T$ , of the ring patch is defined as

$$T = e^{-\tau_{\text{phys}}/\mu}, \quad (5.11)$$

where  $\mu$  is the projection factor,  $\mu = |\sin(B)|$ . In Fig. 5.8, we plot  $T$  as a function of  $\mu$  for two particle densities and two different values of static friction  $\mu_s$ . For each value of  $\mu$ , we plot results for a range of the azimuthal observing angles,  $\theta$ . As expected, for larger elevation angles,  $B$ , the range of transparencies becomes smaller across the range of  $\theta$ . This is due to the fact that at high elevation angles, variation in  $\theta$  would result in very minimal changes to the observing geometry. Overall, we find that a simulation where particles have lower densities and higher friction ( $\rho = 0.45 \text{ g/cm}^3$  and  $\mu_s = 1.0$ ) is the best fit to the observations. Furthermore, in general, a higher value of static friction results in lower transparencies.

## 5.5 Conclusions & Future Work

We presented ring simulations that reveal the relationship between particle friction and large-scale structure in Saturn’s B ring. A comprehensive explanation of the interplay between the mechanisms of self-gravity and viscous overstability has remained elusive. It is understood that both play an important role in generating large-scale structure in Saturn’s rings. Here we have shown that it is possible that the surface properties of particles, here modeled through two friction parameters (static and rolling friction), may control whether a patch of ring particles exhibits

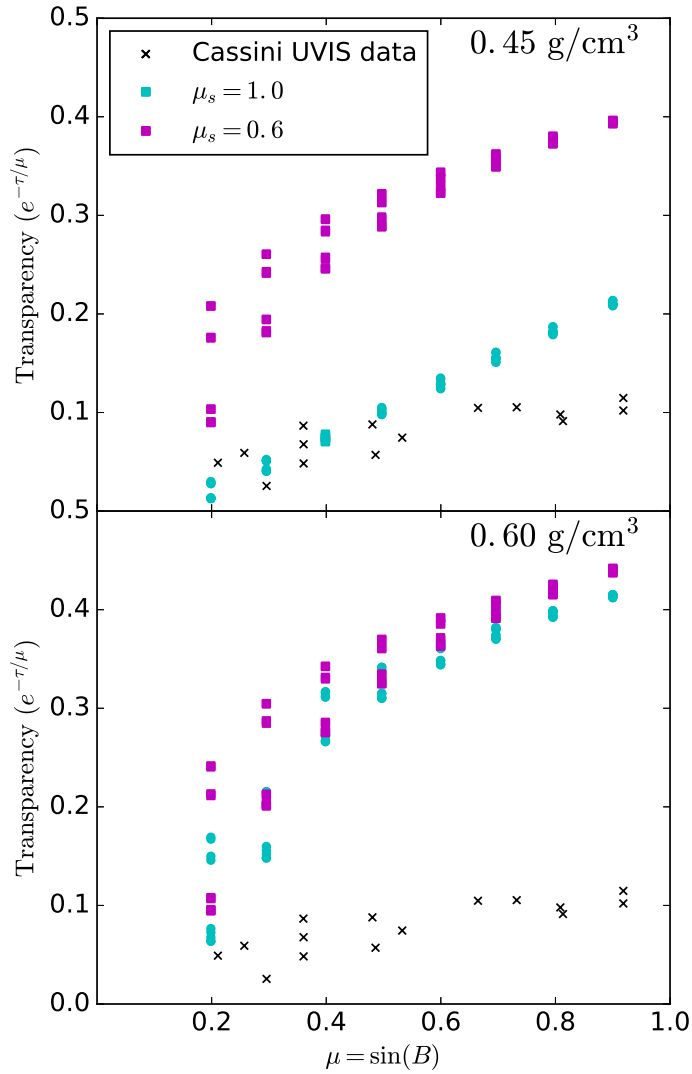


Figure 5.8: The transparency of the simulated data (circles and squares) is compared to Cassini UVIS stellar occultation data (crosses). The top and bottom panels plot transparency of two friction cases (cyan circles for  $\mu_s = 1.0$  and magenta squares for  $\mu_s = 0.6$ ) as a function of the projection factor for simulations with particle densities of  $0.45 \text{ g/cm}^3$  (top panel) and  $0.60 \text{ g/cm}^3$  (bottom panel), respectively. We find that higher values of friction lead to lower ring patch transparency.

self-gravitational wakes or axisymmetric overstable features, or both.

We find that higher interparticle friction increases the viscosity (collisional and translational), such that the ring particles become stable against self-gravitational perturbations. Furthermore, we have shown that the presence of axisymmetric features via viscous overstability does not necessarily require highly porous particles. In fact, non-porous particles may generate viscous overstability features if their surface roughness is sufficiently high.

This has important implications for the possible mass of the B ring itself. Previous studies (Robbins et al., 2010) have relied on similar simulations to estimate the masses of the A and B rings. Robbins et al. (2010) suggested an upper limit for ring particle density of  $0.45 \text{ g/cm}^3$ , based on comparisons of simulation data to ring opacity measurements. However, they did not include the effects of inter-particle friction. If highly frictional particles exist in the B ring, then axisymmetric features in the B ring may be produced by particles with densities as high as  $0.90 \text{ g/cm}^3$ , and current values for the mass of the B ring may be underestimated by at least a factor of 2.

We have performed comparisons to Cassini UVIS stellar occultation data and found that particles with lower densities and higher friction produce ring transparencies that best match the observations. This suggests that axisymmetric features are likely prevalent in the B ring, as both conditions of low densities and high friction are conducive to the generation of viscous overstability. However, the average physical optical depths measured for these simulations ( $\sim 1$ ) are much lower than those observed in the B ring ( $> 4$  in some locations). If we were to simulate a ring

patch with a larger size distribution of particles (and with more small particles in particular), the transparencies would likely be lower for all our cases. Simulations by [Robbins et al. \(2010\)](#) showed that for high particle densities ( $> 0.45 \text{ g/cm}^3$ ), a particle size distribution does lead to more opaque rings. However, this effect was not as pronounced for simulations with lower particle densities. Nevertheless, this suggests a possibility that particles with densities greater than  $0.45 \text{ g/cm}^3$  may still be able to produce features that are sufficiently opaque to match observations, with the caveat that they would need to have high surface roughness.

Since friction plays an important role in controlling the macroscopic properties of the ring, our simulations have shown that understanding the surface roughness of the ring particles is essential if observations of large-scale structures are to be used to interpret their physical properties (size, densities, etc.). Here, we have chosen to explore a wide range of the friction parameter space in order to understand the range of possible behaviors. The actual surface roughness of ice particles in a vacuum are unknown. So far, simulations have relied on experimental work ([Bridges et al., 1984](#)) that was performed on perfectly smooth and non-rotating ice spheres. There have been some experiments that have measured the friction properties of ice on ice. [Sukhorukov & Løsetl \(2013\)](#) conducted field tests on the friction of sea ice on sea ice in the Barents sea in temperatures of 253 to 271 K, and found that the coefficient of static friction can range from  $\sim 0.6$  to 1.26 depending on the time the ice is held together before sliding is allowed to begin (higher hold times result in higher friction). [Schulson & Fortt \(2012\)](#) measure the coefficient of kinetic friction of freshwater ice sliding slowly (with speeds up to 1 mm/s) at temperatures of 98 to

263 K. They found that the kinetic friction can range from 0.15 to 0.76 depending on the temperature and sliding speed. While these results can provide some ground truths to numerical studies, the environmental conditions they were conducted in do not match that found around Saturn (vacuum at temperatures that range from 20 to 40 K (Flasar et al., 2005)). Therefore, future experimental and theoretical studies should explore the collisional interaction of realistic ice particles in order to place better constraints on their surface properties.

Future work should consider a size distribution of particles (within a single simulation) and a wider range of initial geometric optical depths in order to better quantify the effect that particle surface roughness has on observable properties of the rings. Furthermore, recent studies (Hedman et al., 2014) have shown that axisymmetric features in the B ring are azimuthally coherent in length scales much larger than those simulated here. If inter-particle friction does indeed allow high-density particles to form overstabilities, then simulation with much larger azimuthal extents will have to be performed to show that such developed structures are stable in the long-term. Finally, we intend to study the effect of inter-particle cohesive forces on the formation of km-scale structure. Tremaine (2003) showed that cohesion can have an important role in creating structure in Saturn's ring and predicted the formation of shear-free ringlets. We will study the extent to which cohesive forces can enhance or diminish the generation of self-gravitational wakes and axisymmetric features, or if they generate separate unique large-scale features.

## Chapter 6: Conclusions & Future Work

### 6.1 Conclusions

Our study of granular physics in the Solar System has shown that granular matter behaves quite differently in low-gravity environments. In particular, we find surprising that the manner in which grains flow past each other is different for small solar system bodies compared to Earth. In Chapter 2, we conducted a study of vibration-driven size-segregation of grains to study the effectiveness of the Brazil-nut effect (BNE) in different boundary and gravity conditions that closely resemble those found on asteroids. While previous studies had shown that the classical BNE effect can occur in low-gravity environments, the studies were limited to containers with lateral boundaries. We were able to better mimic the asteroid environment by removing these lateral boundaries, using periodic boundary conditions (PBC). We were able to show that for a wide range of friction properties, the BNE occurs even when PBC are used. However, rather than granular convection, a void-filling mechanism drives the BNE when PBC are present. By analyzing the flow patterns of grains during the oscillatory driven motion, we were able to show that the vibration causes the granular system to dilate, creating void spaces in the medium. Due to the size difference between the large intruder and the surrounding grains, the smaller

grains have a higher probability of filling the void space created below the intruder. This allows the BNE to occur in a system without confining wall boundaries, which are otherwise required for granular convection to occur. Furthermore, we find hints that the void-filling mechanism may be more efficient in lower-gravity environments. Our study suggests that the BNE driven by a void-filling mechanism can occur on an asteroid, and it may be able to explain the presence of large boulders on their surfaces.

In Chapter 3, we studied low-speed impacts onto granular material in low-gravity environments in the context of the OSIRIS-REx mission to the asteroid Bennu. We demonstrated that the outcome of a sampling attempt by the TAGSAM varies depending on the properties of the regolith. By generating an atlas of simulation results, we will be able to develop maps of the sampleability of different regions of the surface of Bennu. When touchdown does occur in 2020, we will be able to reconstruct the response of the OSIRIS-REx spacecraft as it touches down on the surface. Furthermore, by comparing our synthetic accelerometer data to the actual behavior of the spacecraft, we may be able to derive the properties of the surface regolith.

We showed indications that granular material behaves in a more fluid-like manner in a low-gravity environment, and does not resist penetration as much as it would in  $1g$ . This was also demonstrated through low-speed impact experiments of an aluminum sphere onto dry sand. Our analysis shows that, compared to low-speed impacts on Earth, an impactor experiences less drag as it penetrates through a granular medium on an asteroid. The simulations suggest that the drag coefficient

varies as  $\log(g)$ . Further simulations and experiments are required to fully develop a coherent theory of granular impacts in low-gravity environments. Calibrating our code to low-gravity experiments will be an important next step to further elucidating such a theory. An important breakthrough in this process will be the development of an experimental apparatus that is able to replicate the gravity conditions on an asteroid. Some low-gravity experiments have been performed in Atwood-type machines ([Altshuler et al., 2014](#)), but the realistically achievable gravity level in these experiments are still orders of magnitude greater than that found on an asteroid. Developing a coherent theory of granular impacts in low gravity enables us to better predict the outcome of a robotic or human interaction on the surface of an asteroid.

In Chapter 4, we moved from discussions of cm-size particles on the surface or near-surface of small bodies to exploring the collisions of rubble piles. We studied the effect of initial rotation on the outcome of rubble-pile collisions by analyzing the properties of the largest remnant and material that is gravitationally bound to it. We found that the collisional mass loss is sensitive to the initial rotation period, with faster-rotating rubble-pile targets dispersing more mass. The mass of the largest remnant of head-on impacts is well described by the “universal law” for catastrophic disruption first put forward by [Leinhardt & Stewart \(2009\)](#), independent of initial pre-impact rotation. However, the actual interacting mass fraction of a rubble pile needs to be considered for oblique impacts to match the universal law. Furthermore, we developed a prescription that describes the change in the catastrophic disruption criteria of head-on equatorial impacts onto a rotating target. Finally, we found that dissipation and frictional effects combine to increase the catastrophic disruption

threshold in rubble-pile collisions. A logical next step for this study is to apply our revised mass-loss prescription to a larger study of proto-planetary disk evolution, where we can test whether the effects of pre-impact rotation drastically influence the growth of large planetesimals.

In Chapter 5, we studied large-scale structure in Saturn’s B ring. The physical properties of the icy particles that make up Saturn’s rings are poorly constrained, since even the highest-resolution Cassini images of the rings are unable to resolve individual ring particles. These properties must be inferred from the observable structures in the rings that are generated from the collective collisional, gravitational, and possibly electrostatic interactions of ring particles. Two types of km-scale macroscopic structures have been observed in the B ring: self-gravity wakes, which are tilted with respect to the azimuthal direction of the ring system, and axisymmetric viscous overstability structures. A comprehensive explanation of the interplay between the two mechanisms of self-gravity and viscous overstability has remained elusive. It is understood that both play an important role in generating large-scale structure in Saturn’s rings. We showed that the surface properties of particles controls whether a patch of ring particles exhibits self-gravitational wakes or axisymmetric overstable features, or both. We find that higher inter-particle friction increases the viscosity (collisional and translational), such that the ring particles become stable against self-gravitational perturbations. This allows particles with relatively high densities to form overstable features. This has important implications for the possible mass of the B ring, as previous studies have suggested that the presence of overstability features precludes the existence of non-porous particles

in the B ring. By comparing synthetic observational data generated from analyzing simulation output with Cassini UVIS stellar occultation data, we find that particles with lower densities and higher friction produce ring transparencies that best match the observations. However, the average physical optical depths measured for these simulations ( $\sim 1$ ) are only found in the innermost B1 portion of the B ring. Therefore, we expect that simulations with a larger size distribution of particles, or a larger optical depth, are necessary if we wish to study the higher-opacity regions of the B ring.

## 6.2 Future Work

In this section, we outline work that will build upon the results presented in this thesis. First, we discuss on-going work to study the interaction of the cube-shaped Mobile Asteroid Surface Scout (MASCOT) that will be deployed by the Hayabusa 2 mission to the asteroid Ryugu. Then, we discuss work that we have proposed to do on studying the plateaus in Saturn's C ring. These two applications further show the scope of possible problems that can be approached with numerical simulations of granular material. With each application, code improvements are required to enable the study of that application and to ensure that the software's performance and capabilities does not stagnate. Future possible improvements include a full treatment of polyhedral particles to model irregularly shaped granular materials. Such an implementation would enable even more applications of the code, such as studies of situations where grains may fracture or cases where the shape of

the particles are well constrained.

### 6.2.1 MASCOT lander

The Hayabusa 2 mission, a direct successor of the Hayabusa mission, is the second asteroid-sample-return mission of the Japan Aerospace Exploration Agency (JAXA) (Tsuda *et al.*, 2013). It is expected to reach the near-Earth asteroid Ryugu in July 2018. Hayabusa 2 will deploy a cube-shaped lander, MASCOT, that is expected to bounce and eventually settle on the asteroid surface. The purpose of the lander is to characterize the surface features of Ryugu using four instruments: a camera, a hyperspectral microscopic imager, a magnetometer and a radiometer. By studying the lander’s mechanical response to the surface, we may also be able to determine the mechanical properties of the asteroid’s regolith.

In collaboration with instrument designers at the German aerospace center (DLR) and the French space agency (CNES), we have been performing simulations in order to characterize the bouncing of the lander as a function of assumed regolith properties, in the gravitational environment of the target asteroid Ryugu (see Fig. 6.1). A key goal of this project is to determine the effective coefficient of restitution (eCOR) of a lander impacting the surface of an asteroid, as a function of both regolith properties and initial impact conditions (angle of approach, rotation velocity, impact speed, etc.). The effective coefficient of restitution is a measure of the ratio of the final linear and rotational impact to their initial values. Laboratory experiments by MASCOT designers have shown that the value of the eCOR can vary

quite wildly. For very special circumstances it can even be greater than unity. Our simulations have attempted to constrain the range of possible values, and attempt to find correlations with the initial conditions of the lander. Using simulations has the added benefit of testing whether a very-low-gravity environment affects the value of eCOR, compared to an Earth-gravity experiment. Preliminary results have shown that the eCOR is sensitive to the initial orientation of the lander.

Understanding how the eCOR can vary is important for ensuring spacecraft safety. By estimating the eCOR for an individual bounce, we can then predict subsequent impact conditions and formulate the spacecraft's future trajectory. Furthermore, we can measure the response of the regolith to the bouncing lander. The mass and speed of grains ejected by the impact depends on the impact conditions. If we are able to know the pre-impact state of MASCOT, we can measure the properties of the ejecta created in our simulations. The mass and speed of the ejecta also depends on the properties of the regolith. By generating an atlas of simulation results, and comparing with spacecraft observations of an impact event, we can then make some determination of the regolith properties.

### 6.2.2 The Plateaus in Saturn's C ring

We have shown that numerical simulations are a crucial tool for the study of large-scale structure in Saturn's rings. By recreating the conditions necessary for the formation of these macroscopic structures, the microscopic properties of the constituent ring particles can be inferred. Saturn's C ring exhibits peculiar

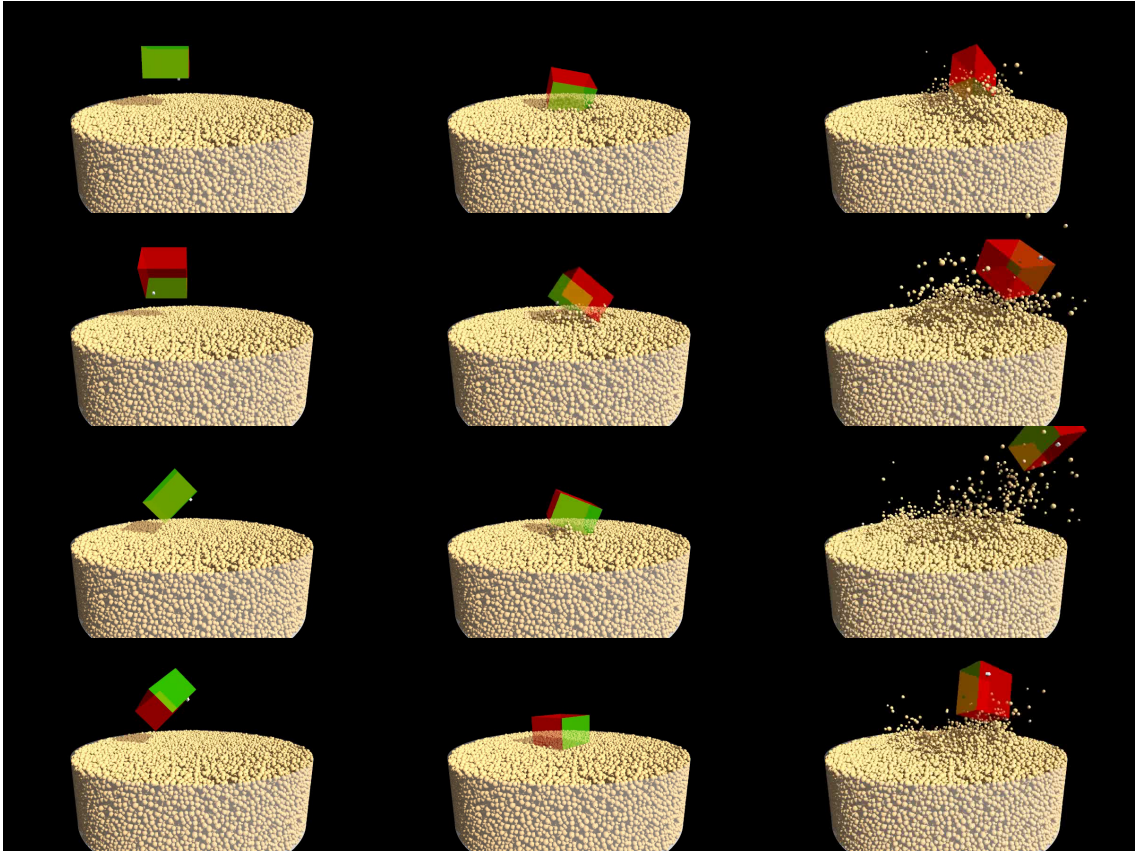


Figure 6.1: Snapshots at three different times (ordered by column) of four different simulations (ordered by row). For each row, MASCOT has a unique pre-impact orientation. From top to bottom these are: a flat orientation, where the lander impacts the surface on a flat face; edge-on-parallel, where the lander impacts the surface along an edge that is oriented parallel to the direction of motion; edge-on-perpendicular, where the edge is oriented perpendicular to the direction of motion; and a case where the corner of the lander touches the surface first. The post-collisional properties of MASCOT are sensitive to its initial orientation.

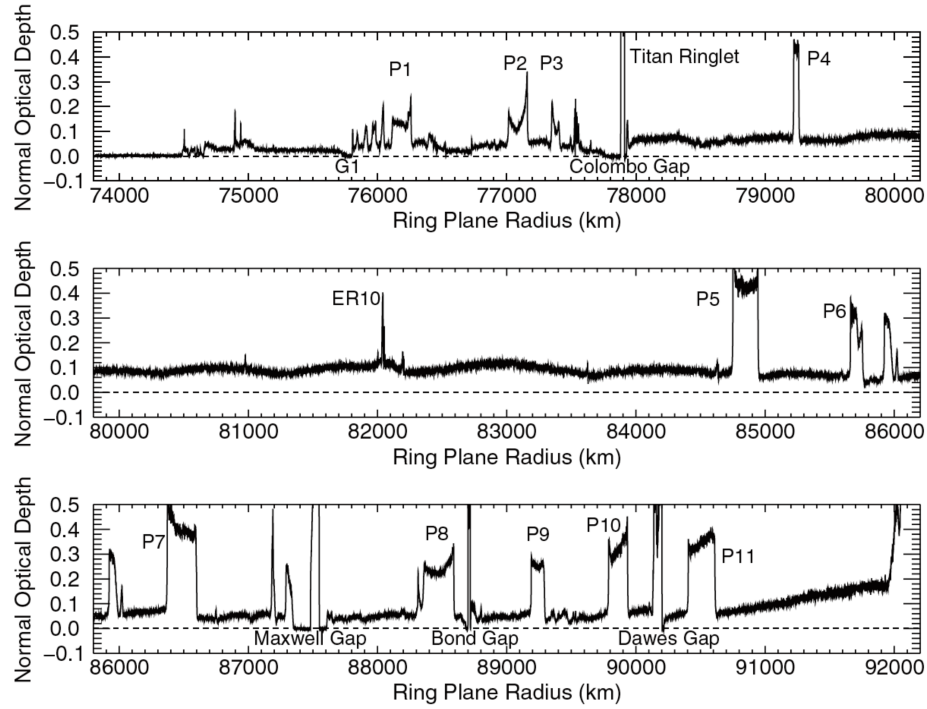


Figure 6.2: Radial profile of Saturn’s C ring from UVIS stellar occultation data. High optical depth regions (plateaus) are interspersed between lower optical depth regions. Source: [Colwell et al. \(2009\)](#).

structures, whose presence has eluded explanation. Figure 6.2 [Colwell et al. \(2009\)](#) shows the optical depth profile of the C ring, which displays broad regions of optical depth less than 0.1, interspersed with narrow “plateaus” (labeled P1 through P11 in the figure) with optical depths that are 3 to 5 times the optical depth of most of the C ring. [Hedman & Nicholson \(2014\)](#) have found that the surface mass densities of the plateaus are very similar to that of the surrounding regions, in spite of the very different optical depths. This implies that either the average particle size is much smaller in the plateaus or that the interior density of the particles is substantially lower in the plateaus.

Furthermore, high resolution-Cassini images of plateaus [Spitale & Porco \(2007\)](#) found narrow 10-km-long striations aligned with the orbital direction, which are similar to axisymmetric viscous overstability structures. It is possible that these features are a result of jamming transitions where the particles are temporarily locked up into narrow, low-shear zones where the thickness of the rings can locally increase due to particles moving vertically out of the ring plane. We intend to study this phenomenon by first studying the jamming transition more intently. Published work on granular flows shows that the jamming transition only occurs for specific combinations of particle density, friction and particle filling factors ([Otsuki & Hayakawa, 2011](#); [Grob et al., 2014](#)). By first determining these properties in laboratory-scale simulations, we will then be able to see if the jamming transition can occur in the context of a ring particle simulation. Reproducing the jamming transition and the associated gaps and ridges in the C ring plateaus, as well as the observed average optical depth and surface mass density, would allow us to place tight constraints on the particle properties in this part of Saturn's rings.

## Bibliography

- Abell, P. A., Barbee, B. W., Chodas, P. W., et al. 2015, in *Asteroids IV*, ed. P. Michel, F. E. DeMeo, & W. F. Bottke (University of Arizona Press), 855–880
- Altshuler, E., Torres, H., González-Pita, A., et al. 2014, *Geophysical Research Letters*, 41, 3032
- Asphaug, E. 2007, in *Lunar and Planetary Science Conference*, Vol. 38, Lunar and Planetary Science Conference, 2432
- Asphaug, E. 2010, *Chemie der Erde / Geochemistry*, 70, 199
- Asphaug, E., King, P. J., Swift, M. R., & Merrifield, M. R. 2001, in *Lunar and Planetary Science Conference*, Vol. 32, Lunar and Planetary Science Conference
- Barabási, A.-L., Albert, R., & Schiffer, P. 1999, *Physica A Statistical Mechanics and its Applications*, 266, 366
- Barnouin-Jha, O. S., Cheng, A. F., Mukai, T., et al. 2008, *Icarus*, 198, 108
- Benz, W., & Asphaug, E. 1999, *Icarus*, 142, 5
- Berry, K., Sutter, B., May, A., et al. 2016, in *Annual AAS Guidance and Control Conference*, Vol. 36, AAS/Division for Planetary Sciences Meeting Abstracts
- Biele, J., Ulamec, S., Maibaum, M., et al. 2015, *Science*, 349
- Binzel, R. P., Morbidelli, A., Merouane, S., et al. 2010, *Nature*, 463, 331
- Borderies, N., Goldreich, P., & Tremaine, S. 1985, *Icarus*, 63, 406
- Bottke, W. F., Brož, M., O’Brien, D. P., et al. 2015, in *Asteroids IV*, ed. P. Michel, F. E. DeMeo, & W. F. Bottke (University of Arizona Press), 701–724
- Bottke, W. F., Durda, D. D., Nesvorný, D., et al. 2005, *Icarus*, 179, 63
- Bottke, Jr., W. F., Cellino, A., Paolicchi, P., & Binzel, R. P., eds. 2002, *Asteroids III* (University of Arizona Press)
- Bottke, Jr., W. F., Vokrouhlický, D., Rubincam, D. P., & Nesvorný, D. 2006, *Annual Review of Earth and Planetary Sciences*, 34, 157
- Bridges, F. G., Hatzes, A., & Lin, D. N. C. 1984, *Nature*, 309, 333
- Canup, R. M. 2008, *Icarus*, 196, 518
- Cellino, A., Zappala, V., Davis, D. R., Farinella, P., & Paolicchi, P. 1990, *Icarus*, 87, 391
- Chapman, C. R. 1976, *Geochim. Cosmochim. Acta*, 40, 701
- Cheng, A. F., Izenberg, N., Chapman, C. R., & Zuber, M. T. 2002, *Meteoritics and Planetary Science*, 37, 1095
- Chesley, S. R., Ostro, S. J., Vokrouhlický, D., et al. 2003, *Science*, 302, 1739
- Colwell, J. E. 2003, *Icarus*, 164, 188
- Colwell, J. E., Cooney, J. H., Esposito, L. W., & Sremčević, M. 2009, *Icarus*, 200,

- Colwell, J. E., Esposito, L. W., & Sremčević, M. 2006, *Geophysical Research Letters*, 33, L07201
- Colwell, J. E., Esposito, L. W., Sremčević, M., Stewart, G. R., & McClintock, W. E. 2007, *Icarus*, 190, 127
- Cotto-Figueroa, D., Statler, T. S., Richardson, D. C., & Tanga, P. 2015, *The Astrophysical Journal*, 803, 25
- Daisaka, H., & Ida, S. 1999, *Earth, Planets, and Space*, 51, 1195
- Daisaka, H., Tanaka, H., & Ida, S. 2001, *Icarus*, 154, 296
- Delbo', M., dell'Oro, A., Harris, A. W., Mottola, S., & Mueller, M. 2007, *Icarus*, 190, 236
- Delbo, M., Mueller, M., Emery, J. P., Rozitis, B., & Capria, M. T. 2015, in *Asteroids IV*, ed. P. Michel, F. E. DeMeo, & W. F. Bottke (University of Arizona Press), 107–128
- Delbo, M., Libourel, G., Wilkerson, J., et al. 2014, *Nature*, 508, 233
- Dobrovolskis, A. R., & Burns, J. A. 1984, *Icarus*, 57, 464
- Dollfus, A., Geake, J. E., Mandeville, J. C., & Zellner, B. 1977, in *IAU Colloq. 39: Comets, Asteroids, Meteorites: Interrelations, Evolution and Origins*, ed. A. H. Delsemme, 243–251
- Dunham, D. W., Farquhar, R. W., McAdams, J. V., et al. 2002, *Icarus*, 159, 433
- Flasar, F. M., Achterberg, R. K., Conrath, B. J., et al. 2005, *Science*, 308, 975
- Forterre, Y., & Pouliquen, O. 2008, *Annual Review of Fluid Mechanics*, 40, 1
- Fujiwara, A., Kawaguchi, J., Yeomans, D. K., et al. 2006, *Science*, 312, 1330
- Garcia, R. F., Murdoch, N., & Mimoun, D. 2015, *Icarus*, 253, 159
- Gray, J. M. N. T., & Thornton, A. R. 2005, *Proceedings of the Royal Society of London Series A*, 461, 1447
- Grob, M., Heussinger, C., & Zippelius, A. 2014, *Physical Review E*, 89, 050201
- Güttler, C., von Borstel, I., Schräpler, R., & Blum, J. 2013, *Physical Review E*, 87, 044201
- Hedman, M. M., & Nicholson, P. D. 2014, *Monthly Notices of the Royal Astronomical Society*, 444, 1369
- . 2016, *Icarus*, 279, 109
- Hedman, M. M., Nicholson, P. D., & Salo, H. 2014, *The Astronomical Journal*, 148, 15
- Hedman, M. M., Nicholson, P. D., Salo, H., et al. 2007, *The Astronomical Journal*, 133, 2624
- Hill, G. W. 1878, *American Journal of Mathematics*, 1, 5
- Holsapple, K. A. 1994, *Planetary & Space Sciences*, 42, 1067
- . 2016, private communication
- Housen, K. R., & Holsapple, K. A. 1990, *Icarus*, 84, 226
- . 2011, *Icarus*, 211, 856
- Housen, K. R., Wilkening, L. L., Chapman, C. R., & Greenberg, R. 1979, *Icarus*, 39, 317
- Jaeger, H. M., Nagel, S. R., & Behringer, R. P. 1996, *Reviews of Modern Physics*, 68, 1259

- Jutzi, M., Michel, P., Benz, W., & Richardson, D. C. 2010, *Icarus*, 207, 54
- Kato, M., Iijima, Y.-I., Arakawa, M., et al. 1995, *Icarus*, 113, 423
- Katsuragi, H., & Durian, D. J. 2007, *Nature Physics*, 3, 420
- Knight, J. B., Jaeger, H. M., & Nagel, S. R. 1993, *Physical Review Letters*, 70, 3728
- Korycansky, D. G., & Asphaug, E. 2009, *Icarus*, 204, 316
- Kudrolli, A. 2004, *Reports on Progress in Physics*, 67, 209
- Lambe, T. W., & Whitman, R. V. 1979, *Soil Mechanics*, SI edition (Wiley, New York)
- Lay, T., & Wallace, T. C. 1995, *Modern Global Seismology* (Academic Press, San Diego)
- Leinhardt, Z. M., & Richardson, D. C. 2002, *Icarus*, 159, 306
- . 2005, *The Astrophysical Journal*, 625, 427
- Leinhardt, Z. M., Richardson, D. C., & Quinn, T. 2000, *Icarus*, 146, 133
- Leinhardt, Z. M., & Stewart, S. T. 2009, *Icarus*, 199, 542
- . 2012, *The Astrophysical Journal*, 745, 79
- Leinhardt, Z. M., Stewart, S. T., & Schultz, P. H. 2008, in *The Solar System Beyond Neptune*, ed. M. A. Barucci, H. Boehnhardt, D. P. Cruikshank, A. Morbidelli, & R. Dotson (University of Arizona Press), 195–211
- Levison, H. F., Thommes, E., & Duncan, M. J. 2010, *The Astronomical Journal*, 139, 1297
- Lissauer, J. J. 1993, *ARAA*, 31, 129
- Love, S. G., & Ahrens, T. J. 1996, *Icarus*, 124, 141
- Matsui, T., Waza, T., Kani, K., & Suzuki, S. 1982, *Journal of Geophysical Research*, 87, 10968
- Matsumura, S., Richardson, D. C., Michel, P., Schwartz, S. R., & Ballouz, R.-L. 2014, *Monthly Notices of the Royal Astronomical Society*, 443, 3368
- Merline, W. J., & Chapman, C. R. 2001, *Meteoritics and Planetary Science Supplement*, 36, A132
- Michel, P., Benz, W., & Richardson, D. C. 2004, *Planetary & Space Sciences*, 52, 1109
- Michel, P., Benz, W., Tanga, P., & Richardson, D. C. 2001, *Science*, 294, 1696
- Michel, P., DeMeo, F. E., & Bottke, W. F., eds. 2015a, *Asteroids IV* (University of Arizona Press)
- Michel, P., O'Brien, D. P., Abe, S., & Hirata, N. 2009, *Icarus*, 200, 503
- Michel, P., & Richardson, D. C. 2013, *Astronomy & Astrophysics*, 554, L1
- Michel, P., Richardson, D. C., Durda, D. D., Jutzi, M., & Asphaug, E. 2015b, in *Asteroids IV*, ed. P. Michel, F. E. DeMeo, & W. F. Bottke (University of Arizona Press), 341–354
- Michikami, T., Nakamura, A. M., Hirata, N., et al. 2008, *Earth, Planets, and Space*, 60, 13
- Miyamoto, H., Yano, H., Scheeres, D. J., et al. 2007, *Science*, 316, 1011
- Morris, A. J. W., Burchell, M. J., Price, M. C., Wozniakiewicz, P. J., & Cole, M. J. 2012, in *European Planetary Science Congress 2012, EPSC2012*
- Mukhopadhyay, S., Allen, B., & Brown, E. 2014, *ArXiv e-prints*, arXiv:1407.0719
- Murdoch, N., Rozitis, B., Green, S. F., et al. 2013, *Monthly Notices of the Royal*

- Astronomical Society, 433, 506
- Murdoch, N., Sánchez, P., Schwartz, S. R., & Miyamoto, H. 2015, in *Asteroids IV*, ed. P. Michel, F. E. DeMeo, & W. F. Bottke (University of Arizona Press), 767–792
- Nakamura, A. M., Setoh, M., Wada, K., Yamashita, Y., & Sangen, K. 2013, *Icarus*, 223, 222
- Nesvorný, D., Bottke, W. F., Vokrouhlický, D., Chapman, C. R., & Rafkin, S. 2010, *Icarus*, 209, 510
- Ohtsuki, K., & Emori, H. 2000, *The Astronomical Journal*, 119, 403
- Orlova, N. S. 1962, in *IAU Symposium, Vol. 14, The Moon*, ed. Z. Kopal & Z. K. Mikhailov, 411–414
- Otsuki, M., & Hayakawa, H. 2011, *Physical Review E*, 83, 051301
- Perera, V., Jackson, A. P., Asphaug, E., & Ballouz, R.-L. 2016, *Icarus*, 278, 194
- Perrine, R. P., & Richardson, D. C. 2012, *Icarus*, 219, 515
- Porco, C. C., Baker, E., Barbara, J., et al. 2005, *Science*, 307, 1226
- Pöschel, T., & Herrmann, H. J. 1995, *EPL (Europhysics Letters)*, 29, 123
- Pravec, P., Harris, A. W., Scheirich, P., et al. 2005, *Icarus*, 173, 108
- Rein, H., & Latter, H. N. 2013, *Monthly Notices of the Royal Astronomical Society*, 431, 145
- Richardson, D. C., Blum, J., Weinhart, T., et al. 2012, in *AAS/Division for Planetary Sciences Meeting Abstracts, Vol. 44, AAS/Division for Planetary Sciences Meeting Abstracts*, 105.06
- Richardson, D. C., Leinhardt, Z. M., Melosh, H. J., Bottke, Jr., W. F., & Asphaug, E. 2002, in *Asteroids III*, ed. W. F. Bottke, Jr., A. Cellino, P. Paolicchi, & R. P. Binzel (University of Arizona Press), 501–515
- Richardson, D. C., Michel, P., Walsh, K. J., & Flynn, K. W. 2009, *Planetary & Space Sciences*, 57, 183
- Richardson, D. C., Quinn, T., Stadel, J., & Lake, G. 2000, *Icarus*, 143, 45
- Richardson, D. C., Walsh, K. J., Murdoch, N., & Michel, P. 2011, *Icarus*, 212, 427
- Richardson, J. E., Melosh, H. J., & Greenberg, R. 2004, *Science*, 306, 1526
- Richardson, J. E., Melosh, H. J., Greenberg, R. J., & O’Brien, D. P. 2005, *Icarus*, 179, 325
- Robbins, S. J., Stewart, G. R., Lewis, M. C., Colwell, J. E., & Sremčević, M. 2010, *Icarus*, 206, 431
- Robinson, M. S., Thomas, P. C., Veverka, J., Murchie, S. L., & Wilcox, B. B. 2002, *Meteoritics and Planetary Science*, 37, 1651
- Rosato, A., Standburg, K., Prinz, F., & Swendsen, R. 1987, *Phys. Rev. Lett.*, 1038, L58
- Ryan, E. V. 2000, *Annual Review of Earth and Planetary Sciences*, 28, 367
- Salo, H. 1992, *Nature*, 359, 619
- . 1995, *Icarus*, 117, 287
- Salo, H., & Karjalainen, R. 2003, *Icarus*, 164, 428
- Salo, H., Schmidt, J., & Spahn, F. 2001, *Icarus*, 153, 295
- Sánchez, D. P., & Scheeres, D. J. 2012, *Icarus*, 218, 876
- Schmidt, J., Ohtsuki, K., Rappaport, N., Salo, H., & Spahn, F. 2009, in *Saturn*

- from Cassini-Huygens, ed. M. K. Dougherty, L. W. Esposito, & S. M. Krimigis (Springer), 413
- Schmidt, R. M., & Housen, K. R. 1987, *International Journal of Impact Engineering*, 5, 543
- Schröter, M., Ulrich, S., Kreft, J., Swift, J. B., & Swinney, H. L. 2006, *Physical Review E*, 74, 011307
- Schulson, E. M., & Fortt, A. L. 2012, *Journal of Geophysical Research (Solid Earth)*, 117, B12204
- Schwartz, S., Richardson, D., & Michel, P. 2012, *Granul. Matter*, 14, 363
- Schwartz, S. R., Michel, P., & Richardson, D. C. 2013, *Icarus*, 226, 67
- Schwartz, S. R., Michel, P., Richardson, D. C., & Yano, H. 2014, *Planetary & Space Sciences*, 103, 174
- Spitale, J., & Porco, C. C. 2007, in *Bulletin of the American Astronomical Society*, Vol. 39, AAS/Division for Planetary Sciences Meeting Abstracts #39, 460
- Stadel, J. G. 2001, PhD thesis, University of Washington
- Sukhorukov, S., & Løsetl, S. 2013, *Cold Regions Science and Technology*, 94, 1
- Sullivan, R. J., Thomas, P. C., Murchie, S. L., & Robinson, M. S. 2002, in *Asteroids III*, ed. W. F. Bottke, Jr., A. Cellino, P. Paolicchi, & R. P. Binzel (University of Arizona Press), 331–350
- Taguchi, Y.-H. 1992, *Physical Review Letters*, 69, 1367
- Takeda, T., & Ohtsuki, K. 2009, *Icarus*, 202, 514
- Tanaka, H., Ohtsuki, K., & Daisaka, H. 2003, *Icarus*, 161, 144
- Tancredi, G., Maciel, A., Heredia, L., Richeri, P., & Nesmachnow, S. 2012, *Monthly Notices of the Royal Astronomical Society*, 420, 3368
- Tiscareno, M. S., Perrine, R. P., Richardson, D. C., et al. 2010, *The Astronomical Journal*, 139, 492
- Tremaine, S. 2003, *The Astronomical Journal*, 125, 894
- Tsuda, Y., Yoshikawa, M., Abe, M., Minamino, H., & Nakazawa, S. 2013, *Acta Astronautica*, 91, 356
- Uehara, J. S., Ambroso, M. A., Ojha, R. P., & Durian, D. J. 2003, *Physical Review Letters*, 90, 194301
- Vincent, J.-B., Besse, S., Marchi, S., et al. 2012, *Planetary & Space Sciences*, 66, 79
- Wada, K., Senshu, H., & Matsui, T. 2006, *Icarus*, 180, 528
- Walsh, K. J., Richardson, D. C., & Michel, P. 2008, *Nature*, 454, 188
- Weidenschilling, S. J. 2011, *Icarus*, 214, 671
- Wisdom, J., & Tremaine, S. 1988, *The Astronomical Journal*, 95, 925
- Yanagisawa, M., & Hasegawa, S. 2000, *Icarus*, 146, 270
- Yano, H., Kubota, T., Miyamoto, H., et al. 2006, *Science*, 312, 1350
- Yasui, Y., Ohtsuki, K., & Daisaka, H. 2012, *The Astronomical Journal*, 143, 110
- Yeomans, D. K., Konopliv, A. S., & Barriot, J.-P. 1997, *Journal of Geophysical Research*, 102, 23775
- Yoshikawa, M., Kawaguchi, J., Fujiwara, A., & Tsuchiyama, A. 2015, in *Asteroids IV*, ed. P. Michel, F. E. DeMeo, & W. F. Bottke (University of Arizona Press), 397–418
- Yu, Y., Richardson, D. C., Michel, P., Schwartz, S. R., & Ballouz, R.-L. 2014, *Icarus*,

242, 82

Zhang, Y., Richardson, D., Barnouin, O., et al. 2016, submitted